CINÉTICA DA REAÇÃO DE CONVERSÃO DE ETANOL EM 1,3-BUTADIENO EMPREGANDO CATALISADORES MULTIFUNCIONAIS

Simoní Da Ros

Tese de Doutorado apresentada ao Programa de Pós-graduação em Engenharia Química, COPPE, da Universidade Federal do Rio de Janeiro, como parte dos requisitos necessários à obtenção do título de Doutor em Engenharia Química.

Orientadores: José Carlos Costa da Silva Pinto
Marcio Schwaab
Fábio Bellot Noronha

Rio de Janeiro
Abril de 2017

CINÉTICA DA REAÇÃO DE CONVERSÃO DE ETANOL EM 1,3-BUTADIENO EMPREGANDO CATALISADORES MULTIFUNCIONAIS

Simoní Da Ros

TESE SUBMETIDA AO CORPO DOCENTE DO INSTITUTO ALBERTO LUIZ COIMBRA DE PÓS-GRADUAÇÃO E PESQUISA DE ENGENHARIA (COPPE) DA UNIVERSIDADE FEDERAL DO RIO DE JANEIRO COMO PARTE DOS REQUISITOS NECESSÁRIOS PARA A OBTENÇÃO DO GRAU DE DOUTOR EM CIÊNCIAS EM ENGENHARIA QUÍMICA.

Examinada por:

_____
Prof. José Carlos Costa da Silva Pinto, Ph.D.

_____
Prof. Fábio Bellot Noronha, Ph.D.

_____
Prof. Marcio Schwaab, Ph.D.

_____
Prof. Cristiane Assumpção Henriques, Ph.D.

_____
Prof. José Maria Corrêa Bueno, Ph.D.

_____
Dr. Elias Tauchert, D.Sc.

RIO DE JANEIRO, RJ - BRASIL
ABRIL DE 2017

Da Ros, Simoní

Cinética da reação de conversão de etanol em 1,3-butadieno empregando catalisadores multifuncionais/ Simoní Da Ros. – Rio de Janeiro: UFRJ/COPPE, 2017.

XII, 213 p.: il.; 29.7 cm.

Orientador: José Carlos Costa da Silva Pinto

Marcio Schwaab

Fábio Bellot Noronha

Tese (doutorado) – UFRJ/ COPPE/ Programa de Engenharia Química, 2017.

Referências Bibliográficas: p. 183-193.

1. Cinética. 2. Catálise heterogênea. 3. Erro experimental. I. Pinto, José Carlos Costa da Silva Pinto *et al*. II. Universidade Federal do Rio de Janeiro, COPPE, Programa de Engenharia Química. III. Título.

A meus pais Jorge e Ligia.

AGRADECIMENTOS

A meus orientadores, José Carlos Pinto, Marcio Schwaab e Fabio Bellot Noronha, sem os quais este trabalho não teria sido realizado. Pelos ensinamentos, amizade, incontáveis discussões, paciência e oportunidades concedidas.

A todos os colegas, funcionários e professores do PEQ/COPPE/UFRJ, em particular ao pessoal do LMSCP.

Ao Instituto Nacional de Tecnologia (INT), em particular ao Laboratório de Catálise (LACAT/DCAP), pela infraestrutura técnica concedida. Aos professores Fabio Bellot Noronha, Alexandre Barros Gaspar e Marco André Fraga, por suas atuações para desenvolver o ambiente de pesquisa. A todos os profissionais do INT, em especial a Renata, Elaine e Sidnei, pela atenciosa atuação na caracterização dos catalisadores, na troca de cilindros, etc. A todos os amigos do LACAT, muito obrigada.

Ao Dr. Crisóstomo Raimundo Rabelo Neto e à Profª Elisa Barbosa-Coutinho pelos ensinamentos, amizade e colaborações na discussão do preparo dos catalisadores e das reações de conversão catalítica do etanol.

Aos parceiros da Arlanxeo, Marcus Moutinho, Luiz Nicolini e Elias Tauchert, pelo apoio técnico e financeiro ao trabalho.

Ao Conselho Nacional de Desenvolvimento Científico e Tecnológico, CNPq, pela bolsa de estudo concedida e por financiar o período sanduíche de um ano na Universidade de Bath.

A meu orientador de doutorado sanduíche, Matthew David Jones, pelos ensinamentos, amizade e incansável dedicação diária ao trabalho. Ao Prof. Davide Mattia, pelos ensinamentos e colaboração com o trabalho.

À Univeridade de Bath, pela oportunidade de atuar como pesquisador visitante no Departamento de Química, e ao Centro de Tecnologias Químicas Sustentáveis, pelo apoio técnico concedido. A todos os amigos do laboratório de tecnologias químicas sustentáveis, em especial ao *Jones group*, e ao Dr. Rémi Casting e a Dra. Gabriele Kociok-Köhnfor pela atenciosa ajuda com a caracterização dos catalisadores, muito obrigada.

A meus pais, Jorge e Ligia, e irmãs, Caroline e Fernanda, pelo amor, apoio, e por compreenderem minha ausência. A todas as pessoas que contribuíram de alguma forma para este trabalho, muito obrigada!

ACKNOWLEDGMENTS

I would like to thank my advisors, José Carlos Pinto, Marcio Schwaab and Fabio Bellot Noronha, for the taught lessons, friendship, uncountable discussions, patience and all the opportunities given to me. This work could not have been performed without them.

Thanks to all colleagues, professionals and professors from PEQ/COPPE/UFRJ, in particular to the people from LMSCP.

Thanks to the National Institute of technology (INT), in particular to the Catalysis Divison, (LACAT/DCAP), for the conceded technical infrastructure. Thanks to Professors Fabio Bellot Noronha, Alexandre Barros Gaspar and Marco André Fraga, for keeping the lab operation. Thanks to all professionals from INT, in particular to Renata, Elaine and Sidnei, for their carefull help with the catalyst characterization, cylinders change, etc. Thanks to all colleagues and friends from LACAT.

Thanks to Dr. Crisóstomo Raimundo Rabelo Neto and to Profª Elisa Barbosa-Coutinho, for the many taught lessons, friendship and collaboration.

Thanks to partners from Arlanxeo, Marcus Moutinho, Luiz Nicolini and Elias Tauchert, for the technical support and conceded scholarship.

Thanks to the Conselho Nacional de Desenvolvimento Científico e Tecnológico, CNPq, for the scholarship and for funding the sandwich period at the University of Bath.

Thanks to my advisor in the University of Bath, Matthew David Jones, for the many taught lessons, friendship and for his tireless diary dedication to the research. Thanks to Prof. Davide Mattia, for the taught lessons and collaboration.

Thanks to the University of Bath for the opportunity to work as a visiting researcher in the Chemistry Department, and thanks to the Centre for Sustainable Chemical Technologies for the technical support. Thanks to all friends from the CSCT lab, in especial to the *Jones's group* and to Dr. Rémi Casting and Dr. Gabriele Kociok-Köhnfor for the careful help with the catalyst characterization.

Thanks to my parents, Jorge and Ligia, and my sisters, Caroline and Fernanda, for all the love, support and for understanding my absence. Finally, thanks to all people that contributed somehow to this work.

Resumo da Tese apresentada à COPPE/UFRJ como parte dos requisitos necessários para a obtenção do grau de Doutor em Ciências (D.Sc.)

CINÉTICA DA REAÇÃO DE CONVERSÃO DE ETANOL EM 1,3-BUTADIENO EMPREGANDO CATALISADORES MULTIFUNCIONAIS

Simoní Da Ros

Abril/2017

Orientadores: José Carlos Costa da Silva Pinto

Marcio Schwaab

Fábio Bellot Noronha

Programa: Engenharia Química

Neste trabalho, a conversão catalítica em fase gasosa de etanol em 1,3-butadieno (1,3-BD) foi estudada empregando catalisadores heterogêneos do tipo $MgO\text{-}SiO_2$, dopados com ZrO_2 e ZnO, e sistemas $ZrO_2\text{-}ZnO/MgO\text{-}SiO_2$ modificados com metais alcalinos, preparados por co-precipitação. Pela primeira vez, a cinética deste sistema reacional foi investigada utilizando a informação contida na matriz de covariância das medidas experimentais, a qual permitiu indentificar uma mudança no mecanismo reacional com o aumento da temperatura: entre 300 e 400 ºC, a etapa lenta foi sugerida como a condensação do acetaldeído, enquanto que entre 400 e 450 ºC, a desidrogenação do etanol limitou o processo. Além disso, a caracterização da matriz de covariância das medidas experimentais, empregando distintas condições reacionais e catalisadores, demonstrou que tanto a temperatura da reação, quanto as características do catalisador afetaram as flutuações experimentais. Demonstrou-se que o método de co-precipitação foi eficiente para o preparo de catalisadores capazes de apresentar elevada produtividade à 1,3-BD. Além disso, a acidez dos catalisadores foi modificada pela adição de metais alcalinos (Na, K e Li), permitindo minimizar reações paralelas de desidratação do etanol à eteno e éter etílico. Assim, um novo catalisador foi desenvolvido, o qual permitiu aumentar a seletividade combinada para 1,3-BD e acetaldeído para 72 mol. %. Finalmente, as variáveis reacionais de operação, temperatura e velocidade espacial, foram investigadas com um planejamento estatístico, empregando o novo catalisador desenvolvido. Demonstrou-se que altos rendimentos à 1,3-BD podem ser obtidos empregando elevadas velocidades espaciais, desde que a pressão parcial de etanol seja também alta, aumentando assim o potencial de aplicação industrial deste processo.

Abstract of Thesis presented to COPPE/UFRJ as a partial fulfillment of the requirements for the degree of Doctor of Science (D.Sc.)

REACTION KINETICS OF THE ETHANOL CONVERSION INTO 1,3-BUTADIENE EMPLOYING MUTIFUNCTIONAL CATALYSTS

Simoní Da Ros

April/2017

Advisors: José Carlos Costa da Silva Pinto
Marcio Schwaab
Fábio Bellot Noronha

Department: Chemical Engineering

The catalytic conversion in gas phase of ethanol into 1,3-butadiene (1,3-BD) was investigated over the heterogeneous catalysts $MgO\text{-}SiO_2$, ZrO_2 and ZnO containing $MgO\text{-}SiO_2$, and alkali metal doped ZrO_2-ZnO/$MgO\text{-}SiO_2$ prepared by co-precipitation. For the first time, the kinetics of this reactional system was evaluated employing the information contained in the covariance matrix of experimental measurements, which allowed indentifying a modification of the mechanism as reaction temperature increased: from 300 to 400 ºC, the rate-limiting step was suggested as the acetaldehyde condensation, while at 450 ºC, ethanol dehydrogenation step limited the process. Besides, the characterization of the covariance matrix of experimental fluctuations, using different reaction conditions and catalysts, demonstrated that both reaction temperature and catalyst properties affected experimental fluctuations. It was also shown that the co-precipitation method was appropriate for preparation of catalysts able to achieve high 1,3-BD productivities. Moreover, catalyst acidity was modified through the addition of alkali metals (Na, K and Li), allowing for the minimization of parallel reactions of ethanol dehydration to ethene and diethyl ether. Thus, a new catalyst was developed, which allowed for the increasing of the combined 1,3-BD and acetaldehyde selectivity up to 72 mol %. Finally, the effects of reaction variables, temperature and spatial velocity, were investigated with help of a statistical design, employing the developed catalysts. Results indicated that high 1,3-BD yields may be achieved at high spatial velocities conditions, as long as ethanol partial pressure be kept high, improving the potential of industrial application of this process.

CONTENTS

INTRODUCTION

Dienes are important raw materials for organic syntheses, being used for the commercial production of many plastics and synthetic rubbers (VAABEL *et al*., 1973). In particular, the use of dienes as comonomers with conventional olefins allows for modification of the final polymer properties (as melting temperature, crystallinity, ductility and flexibility) (ODIAN, 2004).

Among the dienes, 1,3-butadiene (1,3-BD) is particularly important due to its widespread use for the production of distinct polymers. The main commercial application of 1,3-BD is the manufacture of styrene-butadiene rubber (SBR), which is used mainly for tires manufacture. Other 1,3-BD important commercial applications includes the polymerization into polybutadiene, which is also applied for tires manufacture, and the production of acrylonitrile-butadiene-styrene (ABS) resins (WHITE, 2007).

It is estimated that 95 % of the worldwide 1,3-BD production is achieved through thermal cracking of saturated hydrocarbons, using naphtha as a typical raw-material. Actually, 1,3-BD is normally obtained as a co-product of the ethylene production. The products of this process include hydrogen, ethene, propene and 1,3-BD, among other olefins (WHITE, 2007, JOHANN *et al*., 2007). These products are then separated through additional processing steps and a final stream constituted mainly by C4 compounds can be obtained. In order to use 1,3-BD in polymerizations, however, it is necessary to produce a highly pure 1,3-BD, since impurities presence may lead to catalyst deactivation and undesired parallel reactions (PETERS *et al*., 2010). Thus, expensive extractive distillation processes are required to separate 1,3-BD from its boiling point neighboring compounds (1-butene and 2-butene, for example) (HSU and LI, 2012).

The need for an alternative production route to 1,3-BD is exacerbated by the possible future shortfall of naphtha, due to the increasing importance of ethane feedstock, particularly in the U.S., as new shale gas reserves have been discovered since 2007, boosting the shale gas production over the last years (MAKSHINA *et al*., 2014;

BRUIJNINCX *et al*., 2013, GALADIMA and MURAZA, 2016). Whereas the use of ethane for ethene production is economically more favorable, ethane yields much lower amounts of 1,3-BD when compared with naphtha. For instance, whilst a naphtha cracker produces 16 lb of 1,3-BD per 100 lb of ethene, an ethane cracker produces only 2 lb, according to WHITE *et al*. (2007). The existence of technically recoverable deposits of shale gas widely distributed across the globe (especially in China, Argentina, Algeria, U.S, Canada, Mexico, Australia, South Africa, Russia and Brazil) (EIA, 2014) represents a future alternative for the ethene production from ethane cracking or from oxidative coupling of methane and simultaneously represents a threat for 1,3-BD production (GALADIMA and MURAZA, 2016, OBRADOVIC *et al*., 2016).

The ethanol conversion into 1,3-BD, conversely, constitutes a renewable and environmental friendly route for 1,3-BD production. This is mainly due to the availability of bioethanol, which is expected to significantly increase over the next few years from fermentation of sugar rich waste materials (CESPI *et al*., 2015, MAKSHINA *et al*., 2014, ANGELICI *et al*., 2013, POSADA *et al*., 2013). For example, 23.4 billion litres of bioethanol were produced in 2014 in Brazil (RENEWABLE FUELS ASSOCIATION, 2016). The use of ethanol as raw material presents some economical advantages (related to the cheap availability of bioethanol) and also brings some environmental benefits. During the sugar cane (or other renewable biomass source) growing cycle, solar energy, CO_2 and water are combined to produce polymer chains, allowing for fixation of atmospheric CO_2 in the plant in the form of cellulose, hemicellulose and sugar. Thus, the use of ethanol for 1,3-BD production in fact contributes for reduction of the CO_2 atmospheric composition (HUBER *et al*., 2006).

However, many aspects of this process still require improvement in order to increase the conversion of ethanol into 1,3-BD and avoid ethanol conversion into undesired co-products, although the ethanol to 1,3-BD reaction has been known since the beginning of the 20th century and employed industrially in the past. The ethanol to 1,3-BD conversion is achieved in the gas phase, employing solid catalysts, and can be operated at atmospheric pressure. Typical temperatures employed lie in the range between 250 and 450 ºC. However, reaction temperature, contact time and ethanol composition constitute important operation variables that affect catalyst performance and 1,3-BD yields (BHATTACHARYYA and GANGULY, 1962, NIIYAMA *et al*., 1972).

In particular, it has been established that the ideal catalyst for ethanol to 1,3-BD reaction must present suitable amounts, in terms of strength and distribution, of acid and basic sites, since the widely accepted reaction pathway involves different consecutives steps: (i) ethanol dehydrogenation, (ii) aldol condensation, (iii) Meerwein-Ponndorf-Verley (MPV) reduction of crotonaldehyde and (iv) crotyl alcohol dehydration (SUSHKEVICH *et al*., 2015, MAKSHINA *et al*., 2014). However, ethanol dehydration to ethene and diethyl ether (DEE) at acid sites can also constitute undesired parallel reactions.

As a consequence, materials with multifunctional properties have been studied, especially MgO-SiO_2 systems (JANSSENS *et al*., 2015, MAKSHINA *et al*., 2014). This is related to the fact that Mg-O pairs may contain Lewis acid and Brønsted basic sites, while the silanol groups act as Brønsted acid sites, which are necessary for ethanol dehydrogenation (DI COSIMO *et al*., 1998), acetaldehyde condensation (ORDOMSKY *et al*., 2010), crotonaldehyde reduction and crotyl alcohol dehydration to 1,3-BD.

In the present thesis, the development of new catalysts, based on Zr-Zn containing magnesium silica oxide, prepared by co-precipitation was investigated. The co-precipitation method can constitute an efficient preparation procedure for production of catalysts with homogeneous surface properties, allowing for control of the physical and chemical properties of the catalyst and specification of the structure-activity relationship. Despite that, rigorous studies of the co-precipitation method for production of these catalysts have not been reported yet. Moreover, the role of catalyst acidity on ethanol to 1,3-BD conversion, using the co-precipitation preparation method, was also investigated here, by modifying catalyst acidity through addition of alkali metals, such as Na, K and Li, to the final catalyst materials.

It must be emphasized that the ethanol to 1,3-BD reaction mechanism is still subject to debate and opinions disagree regarding the rate-limiting step. For instance, both the ethanol dehydrogenation and the aldol condensation have been suggested as the rate-limiting step over distinct catalysts. Some authors have yet ruled out the aldol condensation as the main path, suggesting instead that crotyl alcohol is produced through the reaction between an activated form of ethanol and acetaldehyde (CHIEREGATO *et al*., 2015).

Moreover, the effects of common reaction variables, such as temperature and contact time, on ethanol to 1,3-BD reaction performance have received little attention in this field (MAKSHINA *et al*., 2014). Few studies attempted to investigate the kinetic

aspects of this reaction, without sufficient support of statistical analyses (EZINKWO *et al*., 2014, JONES *et al*; 1949). However, in order to improve the catalyst properties it may be necessary to understand the kinetic mechanism and identify the rate-limiting step of the ethanol to 1,3-BD reaction.

Based on the previous remarks, this thesis also investigated the kinetics of the ethanol to 1,3-BD reactions over MgO-SiO_2 and alkali metal doped ZrO_2 and ZnO containing MgO-SiO_2 systems, allowing for identification of the rate-limiting step of the ethanol to 1,3-BD reaction, using two different approaches. In the first approach, the covariance matrix of experimental fluctuations of product compositions over MgO-SiO_2 systems was fully characterized and the kinetic information contained in the covariance matrix of experimental fluctuations was discussed. In the second approach, the kinetic effects of operation variables, such as temperature and ethanol feed flow rate, were investigated over a more active on catalyst activity K_2O:ZrO_2:ZnO/MgO-SiO_2 catalyst, using a full factorial design.

This work is organized as follows. Chapter 1 presents the literature review. Section 1.1 is focused on the 1,3-BD production methods. Section 1.2 describes catalysts already employed for the ethanol to 1,3-BD conversion; Section 1.3 presents the mechanism of ethanol to 1,3-BD conversion; Section 1.4 presents the thermodynamic aspects of this reaction; and Section 1.5 shows the importance of the characterization of experimental fluctuations and of experimental design techniques for purposes of kinetic analyses. In Chapter 2, the pursued objectives are highlighted. Chapter 3 describes the materials and methods used in the present thesis. Results and discussions are presented in Chapter 4, which is divided in five subsections. Section 4.1 describes the initial steps required for the synthesis of magnesium silica oxide based catalysts prepared by co-precipitation. Section 4.2 presents the characterization of experimental fluctuations and the kinetic information is discussed. Section 4.3 analyzes the role of the Mg to Si molar ratio and ZrO_2 and ZnO addition on the catalyst performance. Section 4.4 studies the effects of catalyst modification through alkali metal doping. Finally, Section 4.5 analyzes the effect of reaction variables on catalyst activity with help of experimental design techniques. Final conclusions and recommendations for future work are presented in Chapter 5. Finally, following the conclusions and suggestions chapter, references and appendices are provided.

1. LITERATURE REVIEW

1.1. Dienes and the 1,3-Butadiene Production

Dienes, or diolefins, are hydrocarbons which contain two carbon double bonds. They can be cyclic, as the α-cadinene (also known as the citronella oil), or acyclic, as the 1,3-butadiene (1,3-BD). Figure 1.1.1 (a-b) illustrates the α-cadinene cyclic and 1,3-BD acyclic structures.

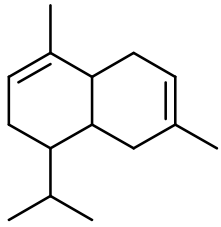

(a) α-cadinene

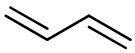

(b) 1,3-butadiene

(c) 1,4-pentadiene

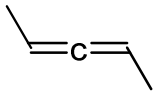

(d) 2,3-pentadiene

Figure 1.1.1 - Dienes: the citronella oil is a cyclic (a), whereas 1,3-BD (b), 1,4-pentadiene (c) and 2,3-pentadiene (d) are acyclic dienes.

Diene properties and reactivities are affected by the relative positions of the double bonds. For this reason, dienes are usually classified as conjugated, isolated or cumulated. Conjugated dienes present double bonds separated by only one single bond, as in the case of 1,3-BD. When dienes present double bonds separated by more than one single bond, they are classified as isolated, as 1,4-pentadiene. Finally, when the double bonds are adjacent to each other, as in 2,3-pentadiene, dienes are classified as cumulated (or allenes) (BRUICE, 2004).

Conjugated dienes are more stable than isolated dienes. Isolated dienes, in turn, are more stable than cumulated dienes. The higher stability associated to conjugated dienes is due to two main reasons. The first factor regards the hybridization of the orbitals. Whereas the single bond of a conjugated diene is formed from the overlap of two sp^2 orbitals, the single bond in an isolated diene is formed by the overlap of a sp^2 orbital with another sp^3 orbital. Thus, the single bond in the conjugated diene is shorter and stronger, when compared to the single bond of isolated dienes, as electron orbitals are closer to the nucleus (BRUICE, 2004). The second factor regards the π electron delocalization, which gives a partial double bond character to the single bond. For instance, due to the molecular orbital symmetry in 1,3-BD, the four π electrons are equally shared among the four carbons. On the other hand, 1,4-pentadiene does not present this molecular symmetry, so that π electrons are separated from each other and confined to the two carbons atoms that form the bond. The lowest stability of cumulated dienes is related to their intrinsic molecular orbital geometry (BRUICE, 2004).

Dienes are important raw materials for organic syntheses, being used for commercial production of many plastics and synthetic rubbers (VAABEL *et al*., 1973). In particular, the use of dienes as comonomers with conventional olefins allows for modification of the final polymer properties (as melting temperature, crystallinity, ductility and flexibility) (ODIAN, 2004). For instance, the copolymerization of propene with 1,5-hexadiene can improve the limited impact resistance at low temperatures of commercial isotatic polypropylenes (SHI *et al*., 2011, WANG *et al*., 2015).

Among the many dienes, 1,3-BD is the most important one, being used for production of distinct polymers. The main commercial application of 1,3-BD, both in volume and value, is the production of styrene-butadiene rubber (SBR), which is used mainly for tires manufacture, although this resin is also applied for production of other consumer goods, such as conveyor belts, industrial hoses, shoe heels and soles, adhesives, sealants, cable coatings, among others. Other 1,3-BD applications include the polymerization into polybutadiene, which is also applied for tires manufacture, and the production of acrylonitrile-butadiene-styrene (ABS) resins (ODIAN, 2004, WHITE, 2007).

It is estimated that 95 % of the worldwide 1,3-BD production is achieved through the thermal cracking of saturated hydrocarbons, normally naphtha (WHITE, 2007, JOHANN *et al*., 2007). 1,3-BD usually is a co-product of the ethylene production

process, when naphtha (or light gases, such as ethane, propane and butane) is fed into a furnace operated between 790 and 830 ºC, under continuous flow of steam. The output stream of this process contains hydrogen, ethene, propene and 1,3-BD, among other olefins. These products must then be separated through several additional steps, so that a final stream constituted mainly by C4 compounds can be obtained. 1,3-BD composition within this C4 stream depends on the plant operation and feedstock, but it is typically between 40 and 50 wt. % (WHITE, 2007).

In order to use 1,3-BD in polymerization, however, it is necessary to obtain highly pure 1,3-BD, since impurities may result in catalyst deactivation and undesired parallel reactions (PETERS *et al*., 2010). Thus, expensive extractive distillation processes are normally required to separate 1,3-BD from its boiling point neighboring compounds (1-butene and 2-butene, for instance) (HSU and LI, 2012).

Besides the high consumption of energy, other disadvantage related to the thermal cracking is the generation of large amounts of carbon dioxide (CO_2), normally released to the atmosphere (REN *et al*., 2008). CO_2 is the main greenhouse gas driver of climate change and the average CO_2 molar fraction in the atmosphere has increased since the start of the instrumental record in the late 1950s (HARTMANN *et al*., 2013), mostly due to combustion of fossil fuels. Thus, it is important to develope alternative ways to produce 1,3-BD.

The need for an alternative reaction route for 1,3-BD is exacerbated by the possible future shortfall of naphtha, since new shale gas reserves have been discovered since 2007 (MAKSHINA *et al*., 2014, BRUIJNINCX *et al*., 2013). Although the use of ethane for ethene production is economically favorable, ethane yields lower amounts of 1,3-BD, when compared to naphtha. For instance, whilst a naphtha cracker produces 16 lb of 1,3-BD per 100 lb of ethene, an ethane cracker produces only 2 lb, according to WHITE *et al*. (2007).

Alternative processes that may be used to produce 1,3-BD include the dehydrogenation of n-butanes and n-butenes. In 2007, BASF patented a process where 1,3-BD production occurs through two n-butane dehydrogenation steps. According to the inventors, this process allows for minimization of the formation of undesired co-products, while maximizing 1,3-BD yield and selectivity (JOHANN *et al*., 2007). Figure 1.1.2 illustrates the proposed process flow diagram. The initial feed stream,

which is constituted mainly of n-butane, is submitted to a non-oxidative catalytic dehydrogenation step, which occurs between 400 and 1100 ºC.

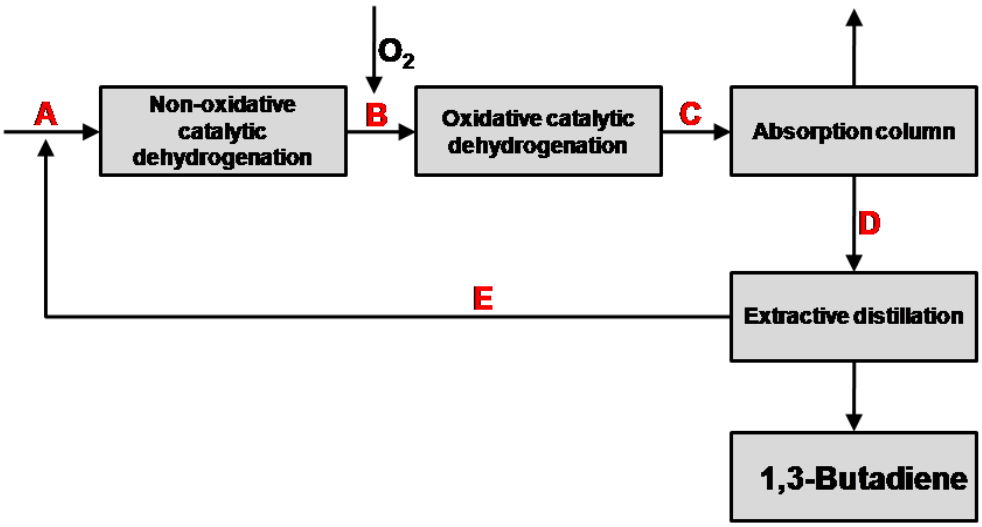

Figure 1.1.2 – Process flow diagram for the 1,3-BD production from n-butane dehydrogenation steps, according to the US2007/0167661 A1 patent (JOHANN *et al.*, 2007).

The catalyst employed in this step is preferentially a single or a bimetallic system involving Pt, K, Cs, La, Ce and Sn doped on ZrO_2 or SiO_2. Steam is used to increase the catalyst life. The output stream of the initial dehydrogenation step, *B*, contains unconverted n-butane, 1-butene, 2-butene, 1,3-BD, H_2, steam, methane, ethane, ethene, propane, propene, CO and CO_2. Thus, in the next step, the *B* stream is mixed with air and fed into an oxidative catalytic dehydrogenation zone, where 1-butene and 2-butene are dehydrogenated to 1,3-BD. The second dehydrogenation step is performed between 250 and 450 ºC and is preferentially carried out over one of the following catalyst systems: Mo-Bi-Fe-O, Mo-Bi-Fe-Cr-O e Mo-Bi-Fe-Zr-O. Whereas the steam may be removed by condensation, the remaining output stream, *C*, follows to an absorption column, which selectivity separates n-butane, 2-butene and 1,3-BD, generating the *D* stream. Finally, the *D* stream is sent to an extractive distillation column, resulting in a highly pure final stream of 1,3-BD. The remaining stream, *E*, contains n-butane and 2-butane and must be recycled.

According to the inventors, the coupling of two dehydrogenation steps is advantageous because allows for higher 1,3-BD yields and selectivities, when compared to the conventional cracking process. Moreover, the recycling of the *E* stream allows for

minimization of the amount of unreacted n-butane. Table 1.1.1 shows typical conversion and selectivities obtained for each dehydrogenation step.

Table 1.1.1 – Typical conversions and selectivities obtained in the n-butane dehydrogenation process (JOHANN *et al*., 2007).

Step	Conversion (%)	Selectivity (%)
Non-oxidative catalytic dehydrogenation	50,5 (n-butane)	98,4 (butenes and 1,3-BD)
Oxidative catalytic dehydrogenation	100 (1-butene) 92,7 (2-butene)	95,0 (1,3-BD)

However, the n-butane and n-butenes dehydrogenation process also presents the disadvantage of not being a green process. For this reason, distinct renewable routes for 1,3-BD production have been presented in the last decade. For instance, the US-0216958 patent (PETERS *et al*., 2010) describes the dehydration of 2,3-butanediol or 1,4-butanediol as a potential route for obtainment of 1,3-BD. 2,3-butanediol and 1,4-butanediol may be produced from sugar fermentation (PETERS *et al*., 2010), whereas 1,4-butanediol may be obtained from succinic acid hydrogenation, which in turn can also be a sugar fermentation product (DELHOMME *et al*., 2009). However, these processes are still very expensive due to the difficult separation of dialcohols and diacids from the fermentation mixture (PETERS *et al*., 2010).

Other renewable route for obtainment of 1,3-BD involves butanol (1-butanol, 2-butanol, isobutanol) dehydration into butene (1-butene, 2-butene, isobutene), followed by butene dehydrogenation into 1,3-BD (PETERS *et al*., 2010). Butanol can be produced from different renewable routes, such as biomass fermentation, or through photosynthesis, using genetically modified cyanobacteria or algae (PETERS *et al*., 2010). The butanol dehydration can then be catalytically performed over acid materials, such as alumina γ-Al_2O_3 and zeolites ZSM-5. The output stream from butanol dehydration is constituted mainly by 1-butene, *cis*-2-butene, *trans*-2-butene and isobutene. Non-oxidative or oxidative catalytic dehydrogenation can be carried out in the following step to convert the linear olefins into 1,3-BD (PETERS *et al*., 2010).

Among the renewable routes for 1,3-BD production, however, the ethanol conversion into 1,3-BD is described as the most advantageous both in economical and environmental terms. The use of ethanol as a renewable source can be very attractive for the production of different chemicals, such as ethene, propene, ethyl acetate, diethyl ether, acetaldehyde, ethylene oxide and 1,3-BD (POSADA *et al*., 2013). This is mainly due to the availability of bioethanol, which is expected to significantly increase over the next few years from fermentation of waste carbohydrate materials (second generation bioethanol) (CESPI *et al*., 2015, MAKSHINA *et al*., 2014, ANGELICI *et al*., 2013, POSADA *et al*., 2013). For example, 23.4 billion liters of bioethanol were produced in 2014 in Brazil (RENEWABLE FUELS ASSOCIATION, 2016).

In particular, the use of ethanol as a renewable raw-material for the production of 1,3-BD in Brazil presents many advantages, when compared to the previous routes based on production of C4 alcohols. Firstly, Brazil is the second largest worldwide ethanol producer, so that there is a large amount of ethanol available in the market. Secondly, the ethanol production is expected to increase in the next few years from fermentation of waste carbohydrate materials, contributing to reduction of ethanol prices. These factors suggest that Brazil is the most suitable place for the 1,3-BD production from ethanol, when compared to United Stated, China and Europe (POSADA et al., 2013).

The company Raízen, which was founded in 2011 through merger of Shell and Cosan, is planning to expand the ethanol production by at least 40 % until the end of 2017. According to the sustainability report of the company, Raízen has been improving the technology used in plantations to increase its efficiency (RAÍZEN SUSTAINABILITY REPORT, 2011-2012). Besides, Raízen also aims to commercialize the second generation ethanol in the near future. In order to do that, the company has been sending sugar-cane wastes to Canada since 2012, where pilot plants are being used for research and optimization of second generation ethanol production.

Figure 1.1.3 illustrates the global and Brazilian ethanol production from 2007 to 2015. It is possible to observe the continuous increase of the worldwide ethanol production, which is associated mainly to the use of ethanol as fuel (ANGELICI *et al*., 2013).

Besides the economical advantages discussed in the previous paragraphs, it is also important to emphasize the environmental benefits of the ethanol use as raw-

material. During the sugar cane (or other renewable source) growing cycle, solar energy, CO_2 and water are combined to produce polymer chains, allowing for fixation of the atmospheric CO_2 in the plant in the form of cellulose, hemicellulose and sugar. Therefore, the use of ethanol for 1,3-BD production in fact contributes to reduce the CO_2 atmospheric composition (HUBER *et al*., 2006).

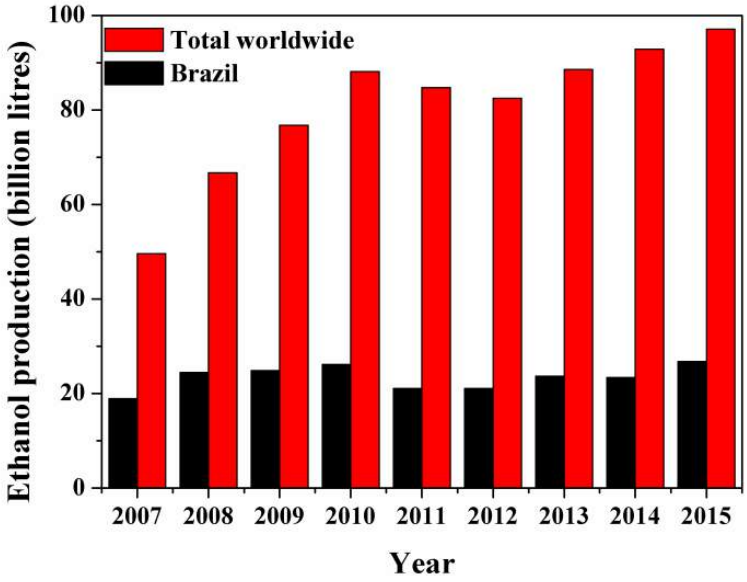

Figure 1.1.3 – Worldwide and Brazilian ethanol production from 2007 to 2015 (Data source: Renewable Fuels Association, 2016).

The ethanol to 1,3-BD reaction has been known since the beginning of the 20th century, although only in the last decade it received a more significant attention from the academic community (MAKSHINA *et al*., 2014, KLEIN *et al*., 2016). The next section describes what is known so far about the ethanol to 1,3-BD conversion, discussing the available technology in terms of both catalyst and production process.

1.2 1,3-Butadiene Production from Ethanol

The route most widely accepted to account for 1,3-BD production from ethanol involves five consecutive reactions (NIIYAMA *et al*., 1972, KVISLE *et al*.; 1988, JONES *et al*., 2011, MAKSHINA *et al*., 2012, SUSHKEVICH *et al*., 2014, GAO *et al*., 2014, SUSHKEVICH *et al*., 2015), as illustrated in Figure 1.2.1. Initially, ethanol is dehydrogenated to acetaldehyde. Then, 3-hydroxybutanal is formed from acetaldehyde self-aldolization. Next, 3-hydroxybutanal dehydrates to crotonaldehyde, which is reduced (Meerwein-Ponndorf-Verley (MPV) reduction) with ethanol to produce crotyl alcohol and acetaldehyde. Finally, crotyl alcohol is dehydrated to afford 1,3-BD.

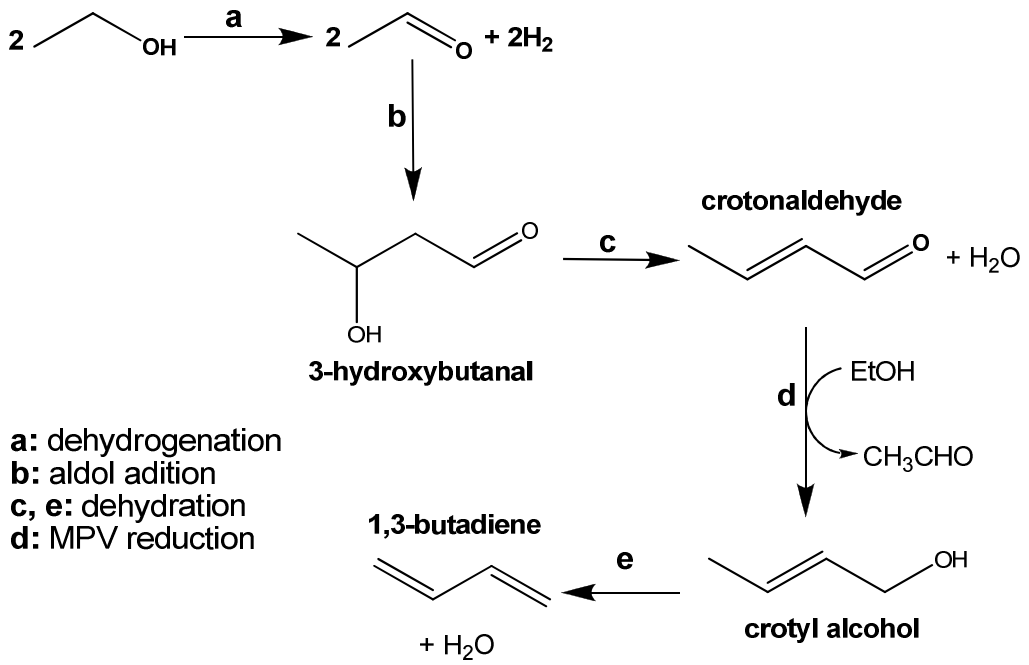

Figure 1.2.1 – Illustration of the reaction network that explains the conversion of ethanol into 1,3-BD (NIIYAMA *et al*., 1972).

The history of the ethanol to 1,3-BD conversion started in 1903, when IPATIEFF verified the 1,3-BD formation, although in low yields, when ethanol was passed over aluminium oxide (QUATTLEBAUM *et al*., 1947). Some years later, using ethanol and acetaldehyde in the feed, OSTROMISSLENSKY (1915) reported the 1,3-BD formation over alumina and clay. Over a bimetallic catalyst, constituted of zinc and

aluminium oxide, LEBEDEV observed 1,3-BD yields of approximately 18 % from pure ethanol. Thus, it was rationalized that whereas zinc oxide catalyzed ethanol dehydrogenation, aluminium oxide was involved in the dehydration steps of the overall reaction pathway. As LEBEDEV protected his invention (Patent 331482, 1930), the ethanol to 1,3-BD conversion is still currently cited as the "Lebedev process". The ethanol to 1,3-BD conversion was used industrially in Russia between 1940 and 1960 to attend rubber demand for 1,3-BD (QUATTLEBAUM *et al*., 1947, BHATTACHARYYA e GANGULY, 1962).

In the same period, researchers from the *Carbide and Carbon Chemicals Corporation* reported the 1,3-BD formation, using feeds mixtures of ethanol and crotonaldehyde and of ethanol and acetaldehyde over different metal oxides (SiO_2, Al_2O_3, Ta_2O_5/SiO_2, CdO/SiO_2, ZrO_2/SiO_2, Nb_2O_5/SiO_2 and $(CdO+ZrO_2)/SiO_2$). Among the analyzed materials, Ta_2O_5/SiO_2 was suggested as the most promising catalyst for the 1,3-BD formation, with 1,3-BD yields between 60 and 70 % (which were calculated based on the amounts of converted ethanol and acetaldehyde) (TOUSSAINT *et al*., 1947, QUATTLEBAUM *et al*., 1947). Using the same Ta_2O_5/SiO_2 catalyst, only traces of 1,3-BD were observed when pure ethanol was employed in the feed (KAMPMEYER and STAHLY, 1949).

A mixture of ThO_2 and ZrO_2 supported on SiO_2 was demonstrated as an active catalyst for the 1,3-BD formation from ethanol or from mixtures of ethanol and acetaldehyde, ethanol and crotonaldehyde and of ethanol and 3-hydroxybutanal (U.S. Patent 2438464, 1948). According to this patent, 1,3-BD yields ranged from 34 to 44 % based on the amounts of converted reactants at reaction temperatures between 432 and 460 ºC (SPENCE *et al*., 1948).

QUATTLEBAUM and coworkers (1947) started the discussion regarding the mechanism of the ethanol to 1,3-BD conversion. They suggested that crotonaldehyde was the main intermediate in the 1,3-BD reaction mechanism and observed that the Ta_2O_5/SiO_2 catalyst was able to convert acetaldehyde into crotonaldehyde and also to convert a mixture of crotonaldehyde and ethanol into 1,3-BD, acetaldehyde and water. According to the authors, 1,3-BD yields were higher when a mixture of ethanol and crotonaldehyde was used, instead of a mixture of ethanol and acetaldehyde, in the feed.

Around 1940, ethanol to 1,3-BD conversion process was responsible for 60 % of the total amount of 1,3-BD produced within the United States (CORSON *et al*. 1949).

There, *Carbide and Carbon Chemicals Corporation* operated the process commercially utilizing two steps. In the first step, ethanol was dehydrogenated into acetaldehyde, with an efficiency of 92 %. In the following step, the produced acetaldehyde and a recycle stream containing ethanol and acetaldehyde were fed into a second reactor, where 2 wt. % of Ta_2O_5 supported on SiO_2 was used as catalyst, to produce 1,3-BD. The 1,3-BD selectivity was reported as equal to 64 %, whereas the 1,3-BD yield was equal to 35 %.

In order to increase the 1,3-BD yields, STAHLY *et al*. (1948) reported that ethyl acetate (a co-product of the reaction system) could be kept in the recycle stream of ethanol and acetaldehyde, leading to the improvement of the 1,3-BD productivity by 2 %.

CORSON *et al*. (1949) evaluated the effect of eight variables on the 1,3-BD yields from the conversion of ethanol and acetaldehyde feeds using a Ta_2O_5/SiO_2 catalyst. The investigated variables were the catalyst average particle size, reactor bed length and diameter, feed flow rate, ethanol to acetaldehyde feed ratio (EtOH/AcH), reaction temperature and pressure, time on stream (TOS), and the catalyst tantalum content.

The commercial catalyst was constituted of a mixture of different particles sizes: 16 % were greater than 4.76 mm (4 mesh); 81 % were between 2.38 and 4.76 mm (4-8 mesh); and 3 % were smaller than 2.38 mm (8 mesh). Then, it was investigated how these different particle sizes could affect the overall 1,3-BD yield. In order to do that, the authors performed 16 experiments using the commercial catalyst and reported the average 1,3-BD yield of 35.6 ± 2.5 %. Table 1.2.1 shows the yields obtained when the catalyst was fractioned in different particle sizes.

Table 1.2.1 - Evaluation of average particle size of the Ta_2O_5/SiO_2 catalyst on the ethanol and acetaldehyde conversion to 1,3-BD (CORSON *et al*., 1949).

Average particle size (mm)	1,3-BD yield
Higher than 4.76	23
Between 2.38 and 4.76	40
Lower than 2.38	36

Reaction conditions: 350 ºC, EtOH/AcH = 2.75, LHSV = 0.4 h^{-1}, atmospheric pressure.

The reported weighted average of Table 1.2.1 was 37.2 % and it was concluded that the screening of catalyst particle sizes was not necessary. However, the lower yields

(23 %) observed when bigger particle sizes were employed suggested the occurrence of internal pore size diffusion limitations, a point not commented by the authors. The catalyst bed dimensions were also reported as not important in the evaluated range, as shown in Table 1.2.2, suggesting that the system could be affected by thermodynamic constraints.

The feed flow rate effect, on the other hand, was shown to be very important. Whereas the 1,3-BD yield increased linearly with the contact time (from ≈ 23 to ≈ 36 %), the 1,3-BD selectivity was nearly constant at around 70 %, as the contact time was increased from 2.7 to 4.5 s. Additional increase of the contact time up to 13 s, nevertheless, reduced the 1,3-BD selectivity to 60 %, suggesting that 1,3-BD could be converted to other products inside the reactor. The effect of feed flow rate was evaluated at 350 ºC, EtOH/AcH feed ratio of 2.75, at atmospheric pressure and time on stream (TOS) of 8 h.

Table 1.2.2 - Evaluation of catalyst bed dimension over Ta_2O_5/SiO_2 on the ethanol and acetaldehyde conversion to 1,3-BD (CORSON *et al*., 1949).

Bed length (cm)	Bed diameter (cm)	1,3-BD selectivity (%)	1,3-BD yield (%)
5.08	2.54	64	27
25.4	2.54	63	34
30.48	0.89	63	34
30.48	2.54	64	36
30.48	5.08	62	32
533.4	7.62	63	33

Reaction conditions: 350 ºC, EtOH/AcH feed ratio of 2.75, LHSV equal to 0.4 h^{-1}, atmospheric pressure, TOS of 8 h.

The influence of the ethanol to acetaldehyde (EtOH/AcH) feed ratio on 1,3-BD yield was also investigated at different temperatures and spatial velocities. At 350 ºC, liquid hourly space velocity of 0.4 h^{-1} and atmospheric pressure, the 1,3-BD yield increased from 30 to 40 % as the EtOH/AcH feed ratio was decreased from 3 to 2. The 1,3-BD selectivity, in turn, ranged from 60 to 70 %, presenting its highest value at the EtOH/AcH feed ratio of 2.5. Whereas the increase of the AcH feed content was beneficial to 1,3-BD yield, a faster rate of carbonization was verified, as suggested by the final carbon content of the catalyst. Besides, further decrease of the EtOH/AcH feed ratio to 1 resulted in 1,3-BD yield and selectivity of 29 and 52 %, respectively.

Figure 1.2.2 illustrates the faster rate of catalyst activity decay when the EtOH/AcH feed ratio was equal to 1. Whereas the feed ratio of 1 resulted in a loss of 38 % of yield from 8 to 16 h of time on stream, the feed ratio of 2.75 led to 1,3-BD yields nearly constant at 21 %. Similar trends were observed for 1,3-BD selectivity.

The same group of researchers analyzed the effect of the EtOH/AcH feed ratio (specifically at ratio conditions of 2, 2.75 and 3) on 1,3-BD yields at 300 and 400 ºC. At liquid hourly space velocity of 0.4 h^{-1} and atmospheric pressure, the 1,3-BD yield increased with the AcH feed content in both temperatures. The highest value was approximately equal to 45 % (with 1,3-BD selectivity of 57 %) at EtOH/AcH feed ratio of 2 and reaction temperature of 400 ºC. The 1,3-BD selectivity, on the other hand, exhibited a very non-linear behavior with temperature, with highest value observed at 350 ºC (CORSON *et al*., 1949).

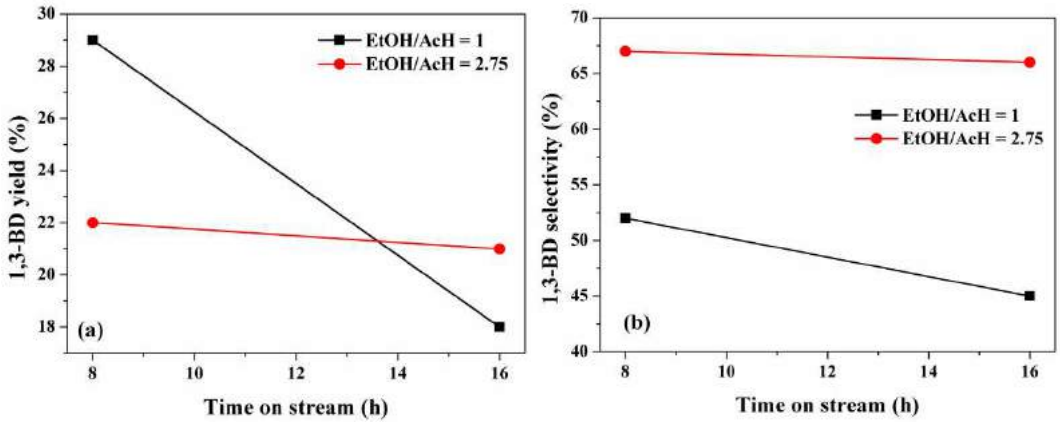

Figure 1.2.2 – Effect of the EtOH/AcH feed ratio on 1,3-BD yield and selectivity as a function of the time on stream. Reactions were performed at 350 ºC, liquid hourly space velocity of 1 h^{-1} and atmospheric pressure (CORSON *et al*., 1949).

Figure 1.2.3 illustrates the stability of the Ta_2O_5/SiO_2 catalyst, which was investigated at 350 ºC, liquid hourly space velocity of 0.4 h^{-1}, EtOH/AcH feed ratio of 2.75 and atmospheric pressure. Reaction was operated in cycles of 120 h, assumed to be equal to 1 operation week in the Figure 1.2.3. Catalyst was submitted to 1 day of regeneration between each cycle, which was performed by burning off the carbonaceous deposit at 400 ºC in an air-nitrogen stream. Whereas catalyst activity was reduced after 1 year of consecutive operation cycles and regeneration steps, the overall 1,3-BD selectivity was reported as approximately constant and equal to 64 %. The loss of

activity was associated with carbon deposition on catalyst surface, which was estimated as equal to 2 % per operation week.

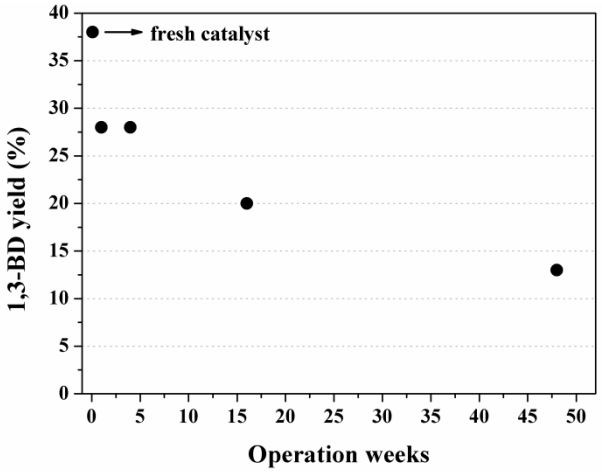

Figure 1.2.3 – Effect of consecutive operation and regeneration cycles on 1,3-BD yield over the Ta_2O_5/SiO_2 catalyst. Reaction conditions: 350 ºC, liquid hourly space velocity of 0.4 h^{-1}, EtOH/AcH feed ratio of 2.75 and atmospheric pressure (CORSON *et al.*, 1949).

Among the different tantalum contents investigated, Figure 1.2.4, 2 wt. % was described as the ideal content due to the high 1,3-BD yield that was obtained (36 % at 350 ºC).

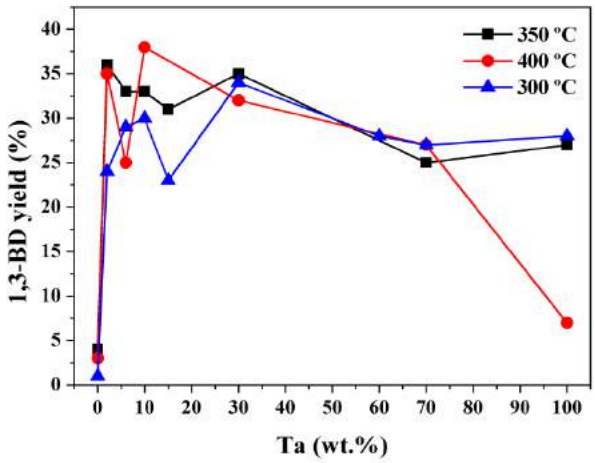

Figure 1.2.4 – Effect of tantalum content of the Ta_2O_5/SiO_2 catalyst and on 1,3-BD yield. Reaction conditions: liquid hourly space velocity of 0.4 h^{-1}, EtOH/AcH feed ratio of 2.75, atmospheric pressure and TOS = 8 h (CORSON *et al.*, 1949).

Finally, the effect of operation pressure was investigated. Higher pressures caused the significant decrease of the 1,3-BD yield; however, according to the authors, the amount of 1,3-BD produced per catalyst gram was largely increased, although higher liquid hourly space velocities were used with higher pressures in order to avoid carbonization. Thus, it is not clear whether the rise in productivity and reduction in yield of 1,3-BD resulted from increase of pressure or spatial velocity (CORSON *et al*., 1949).

Inspired in the proposed mechanism for the ethanol to 1,3-BD conversion, where the intermediate crotonaldehyde is reduced by ethanol, and taking into account that the initial EtOH/AcH feed ratio (between 2.75 and 1, according to CORSON *et al*., 1949) decreases along the bed length, KAMPMEYER E STAHLY (1949) evaluated the effect of introducing feed side streams (pure ethanol and mixtures of acetaldehyde). According to the authors, co-feeding of ethanol and acetaldehyde along the catalyst bed can be beneficial for the process. However, reported changes of 1,3-BD yield and selectivity were small, with optimum yield of 37 % at 68 % of 1,3-BD selectivity. In this study, the lack of dehydrogenation capacity of the Ta_2O_5/SiO_2 catalyst was confirmed by the fact that a feed comprising pure ethanol could not produce significant amount of AcH, with traces of 1,3-BD. Besides, a feed comprising only acetaldehyde resulted in significant amounts of crotonaldehyde, supporting the hypothesis that ethanol is required for the crotonaldehyde reduction and production of 1,3-BD.

CORSON and coworkers (1950) investigated the use of a large number of different catalytic systems for the two-step American process and the one-step Lebedev process. Table 1.2.3 illustrates catalytic data reported using pure ethanol in the feed over different materials. One must note the different catalytic performances at similar Mg to Si ratios depending on the catalyst preparation procedure (entries 22-33, Table 1.2.3).

The authors stressed that the optimal temperature of the two-step process was lower than for the one-step process (350 and 425 ºC, respectively). Furthermore, the two-step process allowed for higher 1,3-BD selectivities than the one-step process (64 and 56 %, respectively). The authors also verified that the catalytic system that led to the best performance in the one-step process (entry 1, Table 1.2.3) did not perform well in the two-step process. Figure 1.2.5 illustrates the catalytic performance over the 2 wt. % $Cr_2O_2/MgO\text{-}SiO_2$ catalytic system employed in the one-step process at 400 and 425 ºC.

Table 1.2.3 – 1,3-BD yield (Y_{BD}) over different catalytic systems using pure ethanol as feed (92 wt.%). Reactions at 425 ºC, TOS of 3 h, atmospheric pressure, liquid hourly space velocity of 0.6 h^{-1} (CORSON *et al.*, 1950).

Entry	Catalyst [a]	Y_{BD} (%)	Entry	Catalyst	Y_{BD} (%)
1	59%MgO-2%Cr_2O_3-39%SiO_2	39	18	$MgCO_3$	12
2	60%MgO-2%Ta_2O_5-38%SiO_2	34	19	TiO_2	10
3	1.1%CuO on 2%Ta_2O_5-98%SiO_2	25	20	38% V_2O_5-12% $AgNO_3$-50%SiO_2	11
4	9.5%ZrO_2-90.5%SiO_2	23	21	1%TiO_2-9%ZrO_2-90%Al_2O_3	10
5	10%ZnO-90%SiO_2	20	22	99%$MgCO_3$-1%SiO_2	11
6	45%MgO-2%Ta_2O_5-53%SiO_2	20	23	98%$MgCO_3$-2%SiO_2	20
7	21%MgO-2%Ta_2O_5-77%SiO_2	18	24	95%$MgCO_3$-5%SiO_2	28
8	1%TiO_2-9%ZrO_2-90%Al_2O_3	17	25	95%$MgCO_3$-5%SiO_2	14
9	57%Sb_2O_3-38%Al_2O_3-5%SiO_2	17	26	95%$MgCO_3$-5%SiO_2	13
10	4.6% V_2O_5-95.4%SiO_2	14	27	90%$MgCO_3$-10%SiO_2	15
11	2%Ta_2O_5-98%SiO_2	16	28	80%$MgCO_3$-20%SiO_2	10
12	2%PbO-98%Al_2O_3	18	29	80%$MgCO_3$-20%SiO_2	17
13	10-%CdO-90%SiO_2	10	30	70%MgO-30%SiO_2	15
14	30%PbO-70%SiO_2	10	31	50%$MgCO_3$-50%$MgSiO_2$	21
15	1.1%Ta_2O_5-98.9%SiO_2	13	32	50%MgO-50%SiO_2	11
16	30%Sb_2O_3-70%Al_2O_3	14	33	46%$MgCO_3$-54%SiO_2	14
17	75%SiO_2-24.7%ZrO_2-0.3%Sb_2O_3	13			

[a] All % are in weight.

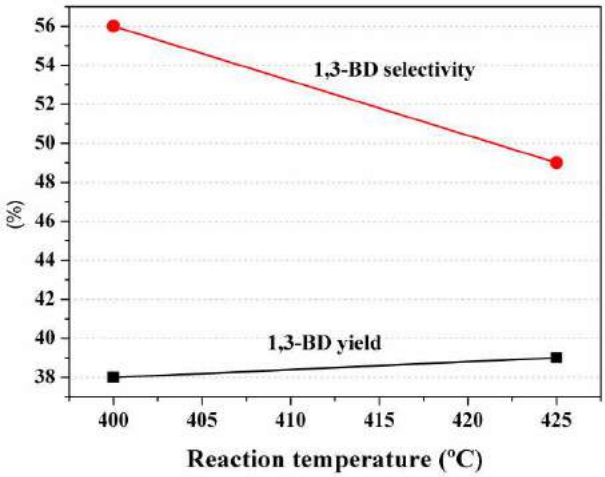

Figure 1.2.5 – Catalytic performance of the ethanol conversion over the 2 wt. % Cr_2O_2/MgO-SiO_2 catalyst, using diluted ethanol (92 wt. %) in the feed, with liquid hourly space velocity of 0.4 h^1, atmospheric pressure and TOS of 8 h (CORSON *et al.*, 1950).

According to CORSON and coworkers (1950), the catalysts employed in the Lebedev process also presented a much lower life time (≈ 12 h) than the catalysts used in the two-step process (≈ 120 hours) requiring more frequent regeneration cycles. These authors reported the use of 612 catalyst combinations for the two-step process, involving 40 elements from Periodic Table. The authors verified that the combination of

the elements Hf-SiO_2, Cu-Ta-SiO_2, Zr-Ta-SiO_2, Mg-Ta-SiO_2, Ag-Ta-SiO_2, Th-Zr-SiO_2 and Zr-SiO_2 allowed for yields as high as obtained with the industrial Ta_2O_5/SiO_2 catalyst (1,4-BD selectivity of 64 % and yield of 35 %). Thus, it was suggested that future research should study mixtures of Hf, Zr and Ta supported on silica.

Finally, according to CORSON *et al*., (1950), whereas the two-step process could result in a 1,3-BD purity of 98 %, the 1,3-BD produced by the Lebedev process presented lower purity, around 80 %. Taking all these arguments into account, the authors concluded that the future of the ethanol to 1,3-BD conversion should surely involve the two-step process and that efforts should be driven to improve the two catalytic stages separately.

Nevertheless, some researchers defended the one-step Lebedev process, due to its higher simplicity for industrial applications (BHATTACHARYYA and GANGULY, 1962a). Thus, different single, binary and ternary metal oxides were studied using pure ethanol as feed (BHATTACHARYYA and GANGULY, 1962a-b). The single metal oxides MgO, Al_2O_3, ThO_2, ZrO_2, SiO_2, Fe_2O_3, TiO_2, Cr_2O_3, CaO, ZnO, NiO, Co_2O_3, CuO, SrO and BaO were prepared through thermal decomposition of the respective metal hydroxides, which in turn were prepared through precipitation of soluble salts using distinct precipitating agents, such as ammonium, sodium and potassium hydroxides. Single metal oxides prepared through thermal decomposition of the corresponding carbonates were also evaluated. Table 1.2.4 shows the performance of the single metal oxides that allowed for production of the highest 1,3-BD yields.

The high yields presented in Table 1.2.4 were probably obtained due to the high catalyst weight employed. The authors explained that previous runs were performed with different catalyst loadings in order to define an optimal amount. The total ethanol conversion increased with the catalyst mass, as expected, whereas the 1,3-BD yield either passed through a maximum or became constant when the catalyst mass was increased until 20 g.

Thus, results presented in Table 1.2.4 could actually be close to the equilibrium condition, hiding relevant catalyst performance information. Regardless of this point, single metal oxides from Table 1.2.4 were investigated at different reaction temperatures, ethanol flow rates and ethanol concentrations. Temperatures ranged from 350 to 450 ºC. For all single metal oxides, temperature changed the 1,3-BD yield non-linearly and higher 1,3-BD yields were observed between 400 and 425 ºC. The flow rate

also exerted a non linear influence on 1,3-BD yield. In a general way, higher yields were achieved at lower flow rates, as expected (BHATTACHARYYA and GANGULY, 1962a).

Table 1.2.4 – 1,3-BD yields over different single metal oxides using ethanol as feed (92 wt.%). Reactions were performed using 20 g of catalyst, at atmospheric pressure (BHATTACHARYYA and GANGULY, 1962a).

Catalyst	Temperature (ºC)	Feed rate (ml / h·g)	1,3-BD yield
ThO_2	400	1.256	36.1
ZrO_2	450	1.256	35.5
Fe_2O_3	425	0.938	29.8
MgO	425	1.256	27.4
Al_2O_3	400	1.256	24.0

The effect of ethanol composition was investigated using aqueous diluted mixtures. Figure 1.2.6 illustrates the effect of ethanol composition on 1,3-BD selectivity (a) and 1,3-BD yield (b).

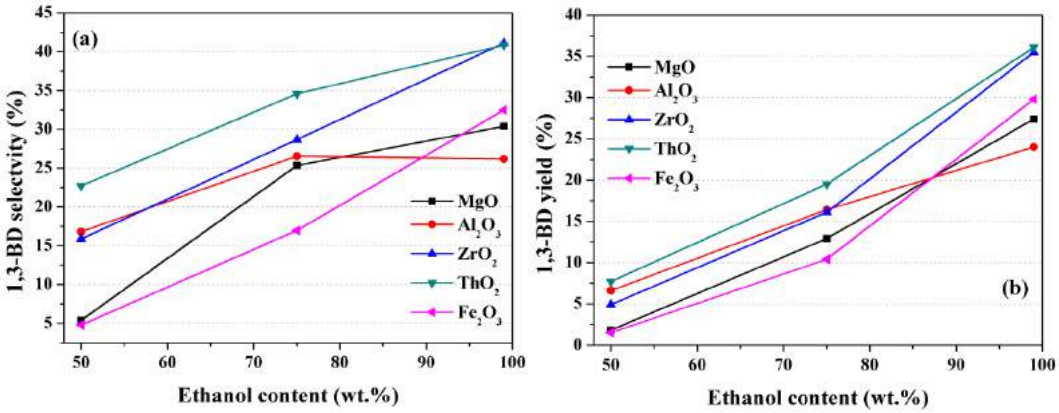

Figure 1.2.6 – Effect of ethanol composition on 1,3-BD selectivity (a) and 1,3-BD yield over single metal oxides. Mixtures of ethanol and water were employed. Reaction temperature and flow rates as described at Table 1.2.4 (BHATTACHARYYA and GANGULY, 1962a).

Reduction of the ethanol content (through dilution in water) caused the decrease of both the 1,3-BD selectivity and yield. However, the reduction in yield was more pronounced when the ethanol content decreased from 98 to 75 %, when compared with the reduction of selectivity. The reaction temperature and feed flow used for reactions

investigating the ethanol composition effect were not clearly reported, but it is believed that reactions were performed at the reaction temperature and feed flow rate described in Table 1.2.4. The authors also emphasized the fact that higher water contents in the feed increased the yields of carbonyl compounds, acids and esters, but results were not presented (BHATTACHARYYA and GANGULY, 1962a). Finally, among the evaluated preparation methods, those that employed precipitation with aqueous ammonia and nitrates resulted in better performances.

The performances of binary metal oxides Al-Mg, Al-Zr, Al-Cr, Al-Ca, Al-Mn, Zr-Cr, Al-Si, Al-Fe, Al-Zn, Al-Ni, Zr-Fe and Th-Fe and the ternary metal oxides Al-Cr-Fe, Al-Mg-Zn, Al-Zn-Cr and Al-Ni-Fe, were studied by BHATTACHARYYA and GANGULY (1962b) in the ethanol to 1,3-BD reaction. Different metal compositions were evaluated, resulting in 65 binary metal and 40 ternary metal oxides. The most promising catalyst was reported to be a mixture of ZnO and Al_2O_3, at the proportion of Al_2O_3:ZnO equal to 60:40, resulting in a 1,3-BD yield of 55.8 % at 425 ºC and 1.874 $mL_{EtOH}/h \cdot g$. Figure 1.2.7 illustrates the 1,3-BD yields obtained over some of the binary metal oxides, as reported by BHATTACHARYYA and GANGULY (1962b), as a function of the metal composition.

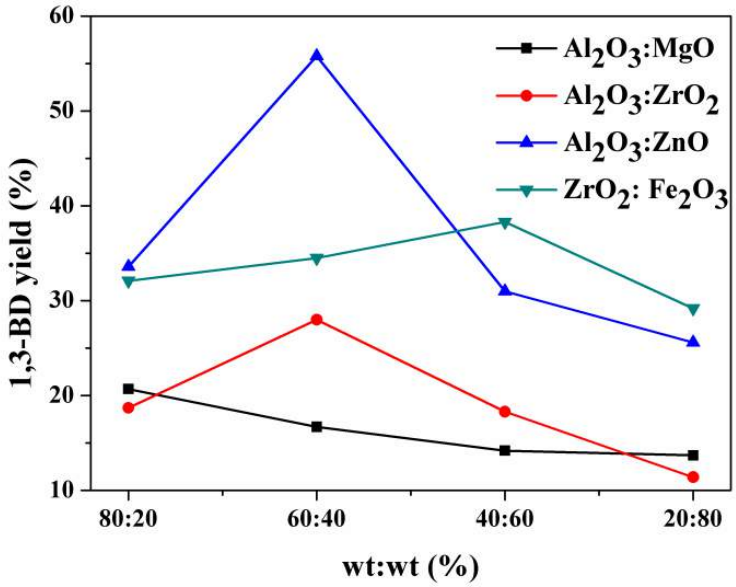

Figure 1.2.7 – Effect of the metal oxide composition of binary systems on 1,3-BD yield. Reactions were performed using 20 g of catalyst, 1 atm, at 400, 425, 425, and 450 ºC for Al_2O_3:MgO, Al_2O_3:ZrO_2, Al_2O_3:ZnO and ZrO_2:Fe_2O_3 catalysts, respectively (BHATTACHARYYA and GANGULY, 1962b).

The effect of the preparation procedure on the 1,3-BD production from ethanol was also investigated. The mechanical mixture of single oxides at the best composition observed for each binary metal oxide prepared by co-precipitation (through thermal decomposition of hydroxides prepared by co-precipitation of nitrates) was performed for comparison. For all systems, the 1,3-BD yield was significantly lower for samples prepared through mechanical mixture, when compared with the analogous mixtures obtained by co-precipitation (BHATTACHARYYA and GANGULY, 1962b). These results are also in line with the observation of BHATTACHARYYA and GANGULY (1962b), showing that binary metal oxides were in general more active than single metal oxides, since higher 1,3-BD yields were achieved.

The effect of the reaction variables on 1,3-BD yields was also assessed over the most promising binary and ternary metal oxides. Both reaction temperature and ethanol flow rate exerted a non linear effect on 1,3-BD yield for all systems, as illustrated in Figure 1.2.8 for Al_2O_3:ZnO and Al_2O_3:MgO binary systems.

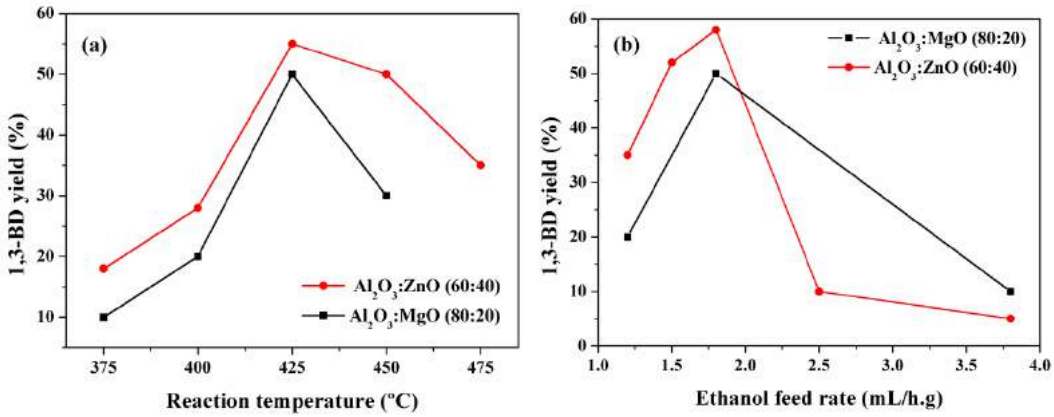

Figure 1.2.8 – Effect of reaction temperature (a) and ethanol feed flow rate (b) on 1,3-BD yield over Al_2O_3:MgO and Al_2O_3:ZnO binary metal oxides. Reactions were performed using 20 g of catalyst, at 1 atm, using ethanol as feed (92 wt. %) (BHATTACHARYYA and GANGULY, 1962b). Lines were drawn for clarity only.

The authors also stressed that the most promising composition verified for the Al_2O_3:ZnO material (60:40) was different from the previously reported value for the Lebedev process. According to BHATTACHARYYA and GANGULY (1962b), the optimal proportion was equal to 25:75. However, the Al_2O_3:ZnO system presented very poor stability, as the 1,3-BD yield decreased from 55 to 10 % after approximately 2.5

reaction hours. The stabilities of the other investigated systems were not reported (BHATTACHARYYA and GANGULY, 1962b).

Based on the previous paragraphs, it seems clear that both the composition and the preparation procedure can modify the catalyst properties and 1,3-BD yields. At this point, it is important to note that, although active materials have been indentified for production of 1,3-BD from ethanol, product distributions had not been reported at this literature stage. Besides, as access to catalyst characterization techniques were rather limited, catalysts had been poorly characterized, impairing the proper understanding of catalyst property effects on 1,3-BD formation.

The study of the ethanol to 1,3-BD reaction in a fluidized bed reactor was reported by BHATTACHARYYA and AVASTHI (1963). In this study, the single metal oxides Al_2O_3, Fe_2O_3, ZrO_2 and ThO_2 and the binary metal oxides Al_2O_3-ZnO, Al_2O_3-CaO, Al_2O_3-MgO and Al_2O_3-Cr_2O_3 were investigated. Molar compositions of the output stream for other products were reported, Table 1.2.5. It is worthwhile to note that the best catalyst presented by the authors (the Al_2O_3-ZnO 60:40 system), showed very high selectivities for other ethanol dehydration products, such as ethene.

Table 1.2.5 - Experimental results reported by BHATTACHARYYA and AVASTHI (1963) for selected samples. Reactions were performed at 425 ºC, using ethanol 99 % as feed in a fluidized bed reactor.

Catalyst	Composition (mol.%) of output stream					1,3-BD selectivity (mol.%)[a] (excluding H_2)	1,3-yield [b]
	1,3-BD	Unsaturated hydrocarbons (as C_2H_4)	H_2	CO_2	Saturated hydrocarbons (as CH_4)		
Al_2O_3	13.5	64.5	15.5	2	2.4	16	25.9
Al_2O_3-ZnO (60:40)	16.40	61.14	10	8	16.1	16	72.8
Al_2O_3-MgO (80:20)	15.2	12.8	49.4	4	16.5	31	35.2

[a] Calculated as $y_{BD}/\Sigma y_i$. [b] Although presenting similar 1,3-BD molar composition, different yields were achieved by different reaction conditions employed such as catalyst weight, which were equal to 24.3, 52 and 23.4 g for the samples Al_2O_3, Al_2O_3-ZnO (60:40) , and Al_2O_3-MgO (80:20), respectively.

BHATTACHARYYA and AVASTHI (1963) also investigated the effects of reaction variables (such as temperature, ethanol feed composition and flow rate and time on stream) on 1,3-BD yields. According to the authors, the Al_2O_3-ZnO presented the best catalytic performance among the investigated catalysts, achieving 72.8 % of

1,3-BD yield, with ethanol conversion of 99.4 % at 425 ºC. Thus, the use of fluidized bed reactors was suggested as an excellent alternative to improve the 1,3-BD yields, allowing for higher yields when compared to the fixed bed operation (73 and 56 %, respectively). Besides, reported productivities (in $g_{BD}/h \cdot L_{cat}$) were much higher during the fluidized bed operation than observed for fixed bed reactions.

Nevertheless, it must be noted that, employed catalyst weight and ethanol flow rates were higher in the fluidized bed operation (for instance, whereas 20 g of catalyst and ethanol flow rate of 1.88 mL/g·h were used for fixed bed reactions, 52 g of catalyst and ethanol feed rate of 2.6 mL/g·h were used for fluidized bed reactions). Moreover, regardless the probable different compositions and contact times employed in the reaction runs, the stability of the Al_2O_3-ZnO was confirmed to be poor. According to the authors, this catalyst was stable during 1 reaction hour only. Although it was stressed that the catalyst could be completely reactivated by calcination in air flow at 375 ºC during 60 min, the 1,3-BD yield fell from 55 to 38 % after three operation and regeneration cycles. The use of the fluidized bed, however, could be further investigated, as it allows for more efficient heat transfer, which can be beneficial for the endothermic 1,3-BD reaction formation.

The catalytic activity of single metal oxides Al_2O_3, ZrO_2 and ThO_2 and binary metal oxides Al_2O_3-ZnO, Al_2O_3-ThO_2, Al_2O_3-ZrO_2, ZrO_2-SiO_2 and MgO-SiO_2 was later evaluated in a fluidized bed reactor using ethanol and acetaldehyde as feed (BHATTACHARYYA and AVASTHI, 1966). In this case, at the EtOH/AcH feed ratio of 2.75, it was observed that the use of the fluidized bed reactor could lead to higher 1,3-BD yields, but to lower 1,3-BD selectivities, when compared to the operation in fixed bed. For instance, between 350 and 400 ºC, 1,3-BD yields ranged from 31 to 43 %, whereas 1,3-BD selectivities ranged from 33 to 48 %. CORSON *et al*. (1950) reported 1,3-BD yields around 35 % at selectivities of 64 % when mixtures of ethanol and acetaldehyde were used as feed over a fixed bed of Ta_2O_5/SiO_2. Besides, the poor catalyst stability with the ethanol and acetaldehyde co-feeding in the fluidized bed was ratified. According to the authors, Al_2O_3, ZrO_2 and ThO_2 had to be recycled after 30 min of time on stream, leading to much lower 1,3-BD yields after only three regeneration cycles. For instance, for the ZrO_2 catalyst, 1,3-BD yields fell from 38 to 10 % after 3 reaction and regeneration cycles.

As stressed by the authors, given the higher reaction enthalpy of the ethanol to 1,3-BD reaction (+23.63 kcal/mol), when compared to the enthalpy of converting mixtures of ethanol and acetaldehyde to 1,3-BD (+7.11 kcal/mol), it was expected that the higher heat transfer efficiency achieved by the fluidized operation would cause the improvement of the ethanol to 1,3-BD conversion in the one-step process (BHATTACHARYYA and AVASTHI, 1966).

Some years later, NIIYAMA *et al*. (1972) studied the catalytic activity of the $MgO\text{-}SiO_2$ system for the ethanol to 1,3-BD reaction, being the pioneers to attempt to establish correlations between basic and acid catalyst features and catalyst activity. These authors also contributed with the mechanism discussion, by performing reactions with different possible intermediates in the feed. 1,3-BD was the main carbonaceous product observed from the ethanol conversion when reactions were performed at 380 ºC, over the $MgO\text{-}SiO_2$ (75:25) system, at atmospheric pressure, using 1 g of catalyst, and 100 mL/min of H_2 as carrier gas. The authors observed the production of ethene, diethyl ether (DEE) and acetaldehyde (AcH). The effect of contact time on products yield is illustrated in Figure 1.2.9. As expected, higher contact times led to higher 1,3-BD yields, whereas the acetaldehyde yields were reduced.

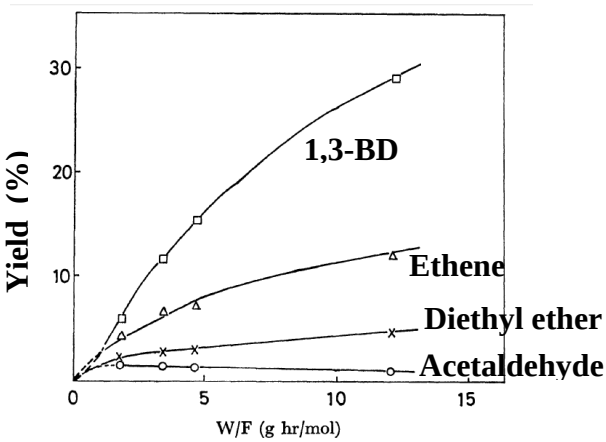

Figure 1.2.9 – Effect of contact time on products yield from ethanol conversion at 380 ºC over the $MgO\text{-}SiO_2$ (75:25) system, at 1 atm, using 1 g of catalyst, and 100 $mL \cdot min^{-1}$ of H_2 as carrier gas (Printed and adapted from NIIYAMA *et al*., 1972, Copyright (1972), with permission from the Chemical Society of Japan).

By co-feeding ethanol and acetaldehyde or ethanol and crotonaldehyde, it was observed that the 1,3-BD yield increased from 11 %, when pure ethanol was used as feed, to 31 %, when ethanol and acetaldehyde were used as feed, and to 36 % when

ethanol and crotonaldehyde were used as feed. Based on these results, the authors suggested that the rate-limiting step should be the ethanol dehydrogenation. However, in fact, data presented by the authors were not sufficient to prove their hypothesis, as the acetaldehyde condensation could not be discarded as rate-limiting step since the co-feeding of ethanol and crotonaldehyde also improved the 1,3-BD yield. In order to investigate the reaction mechanism, the possible participation of 1,3-butanediol as an intermediate was also ruled out, since a feed comprising pure 1,3-butanediol resulted in traces of 1,3-BD (NIIYAMA *et al*., 1972).

These authors also investigated the effect of different MgO to SiO_2 compositions on the catalytic activity for the ethanol conversion. The authors observed a significant increase of the 1,3-BD formation rate (in $mol \cdot m^{-2} \cdot h^{-1}$) as the MgO content increased from 25 to 85 % (in fact, as a decrease in the catalyst surface area is expected with the increase of the Mg content, if the formation rate in $mol \cdot g^{-1} \cdot h^{-1}$ is kept constant or is reduced in a smaller proportion, when compared to the surface area, the 1,3-BD formation rate in $mol \cdot m^{-2} \cdot h^{-1}$ would increase anyway). In line with this trend, the ethene formation rate started to decrease when the SiO_2 content was reduced from 50 to 15 %; that is, the increase of the MgO content until 85 % caused the increase of the 1,3-BD formation rate and simultaneously suppressed the ethene formation. However, both pure SiO_2 and pure MgO were not 1,3-BD active. Measures of pyridine adsorption suggested that MgO-SiO_2 (50:50) was the most acidic among the samples, with acidity decreasing with the increase of the MgO content. The catalyst basicity, in turn, which was assessed by boron trifluoride adsorption, showed a linear correlation with the MgO content; that is, the basicity increased continuously with the MgO content. It is important to note the identification of crotonaldehyde among the main reaction products when ethanol was passed over MgO.

NIIYAMA *et al*. (1972) also investigated the effect of poisoning acidic and basic sites by adding pyridine and phenol into the reaction system. According to the authors, the phenol adsorption can involve Brønsted basic sites, as illustrated in Figure 1.2.10, explaining the observed reduction in the 1,3-BD yield with phenol co-feeding. On the other hand, pyridine presented a dual effect on 1,3-BD yield. When a small amount of pyridine was inserted into the reaction system, the 1,3-BD yield increased. A further increase of the pyridine content, nevertheless, reduced the 1,3-BD yield. According to the authors, the adsorption of pyridine on Lewis acid sites could raise the electron

density of the nearest oxide ions, as illustrated in Figure 1.2.10, contributing to increase the concentration of basic sites. However, a surface containing high concentrations of pyridine could lead to reduction of concentrations of the acid sites, explaining the harmful effect on 1,3-BD yield when higher pyridine content was added into the reaction system.

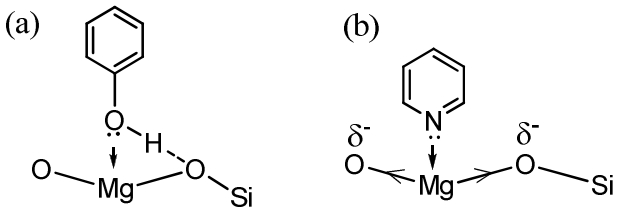

Figure 1.2.10 – Illustration of phenol (a) and pyridine (b) adsorption over Lewis acid-Brønsted basic sites of the MgO-SiO_2 system (NIIYAMA *et al*., 1972).

OHNISHI *et al*. (1985) reported the synthesis of a catalyst that was able to convert 100 % of ethanol with 87 % of yield to 1,3-BD. The catalyst was constituted of 0.1 wt.% Na_2O containing MgO-SiO_2 (1:1) system, which was prepared from $Mg(OH)_2$ and SiO_2. The MgO-SiO_2 (1:1) was calcined at 500 ºC under N_2 atmosphere during 3 h, then impregnated with NaOH and recalcined at the same previous conditions. However, these results have not been achieved by other researchers (KVISLE *et al*., 1988).

The system MgO-SiO_2 was investigated by KVISLE *et al*. (1988), who verified the thermal stability of this catalyst during 10 h (using 200 mg of catalyst, at 350 ºC and atmospheric pressure). The catalyst employed by KVISLE *et al*. (1988) was prepared by wet-kneading of precipitates obtained during the synthesis of the MgO and SiO_2. Specifically, magnesium nitrate was dissolved in water and the magnesium hydroxide was precipitated using ammonium hydroxide. The resulting gel was filtrated and washed with water. This material was wet-kneaded at equal molar proportion with the similar gel obtained from the synthesis of SiO_2, which in turn was prepared by using tetraethylorthosilicate diluted into ethanol, treated with nitric acid and ammonium hydroxide. Finally, the wet mixture was dried and calcined at 500 ºC for 4h (0.5 ºC/min).

It was observed that both 1,3-BD yield and selectivity could be increased through addition of small amounts of O_2 in the feed stream (KVISLE *et al*., 1988). This

may occur due to the dissociative adsorption of oxygen on the catalyst surface which can lead to the formation of additional Brønsted basic sites, contributing to ethanol dehydrogenation (a deeper discussion regarding the reaction mechanism and the possible role of active sites is presented in the next section). Among the main reaction products, ethene, 1,3-BD, AcH, DEE, methane, propane, propanal and acetone were described (KVISLE *et al.*, 1988).

Different compositions and flow rates of ethanol were also evaluated and, according to the authors, the increase of the ethanol flow rate from $8 \cdot 10^{-6}$ to $16 \cdot 10^{-6}$ and to $32 \cdot 10^{-6}$ $L \cdot h^{-1}$, respectively, led to reduction of 1,3-BD yield, suggesting a positive effect of higher contact times on 1,3-BD yield, as expected.

The highest 1,3-BD yield was obtained when AcH was co-fed with ethanol, at the EtOH:AcH proportion of 80:20. In this case, the reported 1,3-BD yield was equal to 33 % at the ethanol conversion of 48 % and 1,3-BD selectivity of 68 %. The authors observed that AcH addition improves 1,3-BD yield and suppresses the ethanol dehydration to ethene, also raising 1,3-BD selectivity. The effect of reaction temperature was analyzed using a feed stream containing ethanol and crotonaldehyde (70 vol. % of ethanol). The 1,3-BD composition at the output stream increased with temperature from 200 to 325 ºC, leveling off from 325 to 400 ºC. Figure 1.2.11 illustrates the compound distribution as a function of reaction temperature at the output stream. AcH presented the highest composition throughout the evaluated temperature range. Ethene composition rose significantly from 350 to 400 ºC, being similar to the 1,3-BD composition at 400 ºC.

By performing experiments of desorption at programmed temperatures over used catalysts samples (under helium flow), the authors observed ethene and acetaldehyde as the major desorption products, suggesting the excess of oxygenated species containing two carbons on the catalyst surface. Thus, it was suggested that the rate-limiting step for the ethanol to 1,3-BD conversion was the acetaldehyde condensation (KVISLE *et al.*, 1988).

Synthetic hectorites were also used for the ethanol conversion into 1,3-BD (SUZUKI *et al.*, 1988). These materials are found naturally in a mineral form. According to the authors, the unit formula of hectorite can be described as $Mg_{16/3}Li_{2/3}Si_8O_{20}(OH,F)_4M_{2/3}$, where M is a metallic cation. Thus, it is believed that

such structure might present acid and basic active sites, suitable for the 1,3-BD formation.

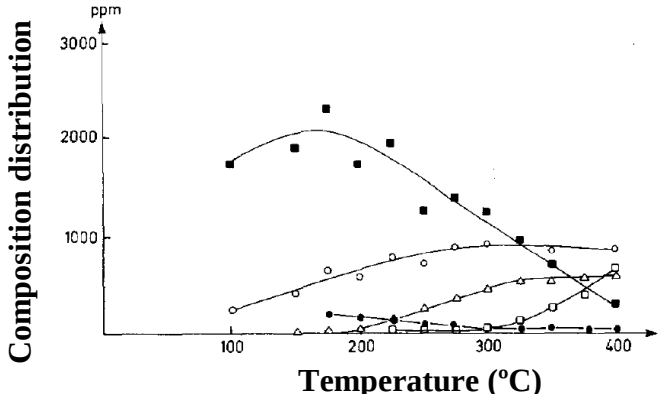

Figure 1.2.11 – Effect of reaction temperature on the output stream composition from reactions over $MgO\text{-}SiO_2$ (1:1) at atmospheric pressure and ethanol and crotonaldehyde co-feeding (70 vol.% of ethanol). Symbols denote: (■) ethanol, (○) acetaldehyde, (Δ) 1,3-butadiene, (□) ethene and (●) crotonaldehyde (Reprinted and adapted from KVISLE *et al.*, 1988, copyright (1988), with permission from Elsevier).

The authors prepared five different silicates (using SiO_2, Na_2O, $MgCl_2 \cdot 6H_2O$, HCl, water, and NH_4OH or NaOH solutions as precipitating agent). The precipitates were dissolved in water and solutions of $LiOH \cdot 2H_2O$, NaOH or KOH were added. Acid fluorhidric (10 vol. %) was added to two samples. After the calcination of samples, they were evaluated in terms of the conversion of 2-propanol and ethanol.

In both cases, the use of NaOH as precipitating agent resulted in lower dehydration product yields, which might be related with the residual Na content. For samples not containing acid fluorhidric, 2-propanol and ethanol conversions decreased in the following order: Li > Na > K. Dehydration products also reduced according to the same order. According to the authors, the role of alkali metal cations would be acting as Lewis acid sites. Thus, the higher dehydration capacity of the Li containing sample was associated to a higher electrostatic field, as the result of its smaller atomic radius; that is, stronger Lewis acidity was suggested for the Li containing samples. Dehydrogenation sites were ascribed to oxygen anions bound to Mg cations, since no clear relationship among alkali metals and acetaldehyde or acetone yields, in the case of ethanol and 2-propanol conversion, could be observed. However, such hypothesis cannot explain why the combined 1,3-BD and acetaldehyde yields were reduced in the order Li > Na > K. In fact, prepared samples could contain different acid and basic sites concentrations, which

were not properly characterized. However, the beneficial effect of increasing the contact time on 1,3-BD yield was also confirmed. The highest reported 1,3-BD yield was equal to 20 % at 375 ºC. Other products observed in the case of ethanol conversion were ethene, DEE, AcH, propene and butenes (SUZUKI *et al*., 1988).

Nickel magnesium silicates were active for the conversion of ethanol into 1,3-BD (KITAYAMA *et al*., 1996). Samples were prepared by mixing hydrophilic fumed silica (Aerosil 380, powder) and $Mg(OH)_2$ at different proportions, followed by the resulting powder impregnation with an aqueous solutions of $Ni(NO_3)_2$ and calcination at 400 ºC for 2 h. By keeping the nickel content fixed, it was observed that an optimal Mg to Si ratio might be defined, as shown in Figure 1.2.12 (a).

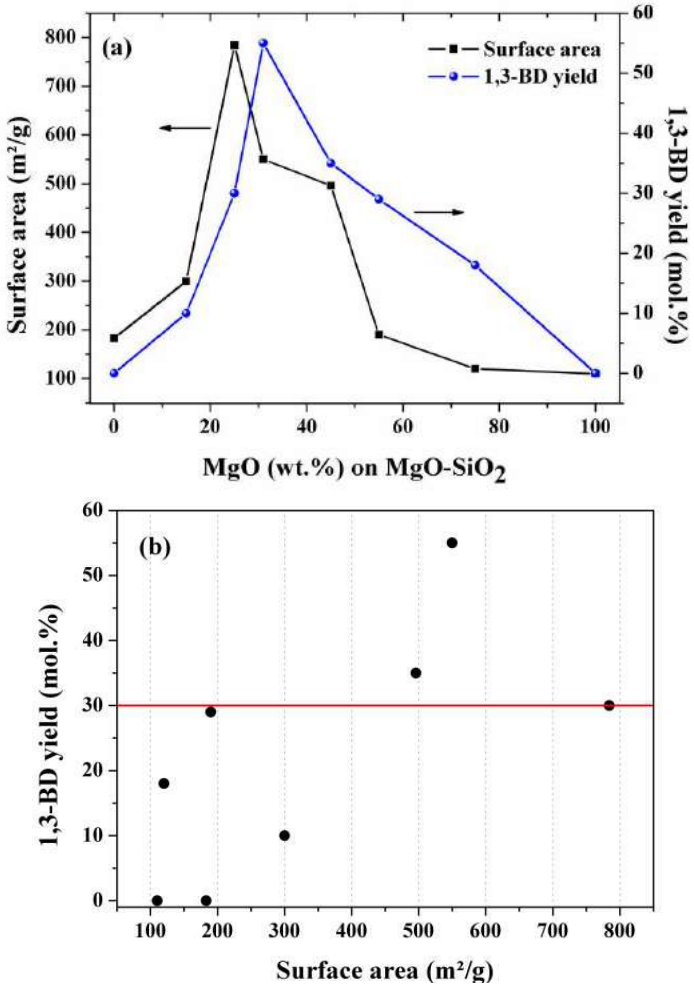

Figure 1.2.12 – Effect of the MgO content of NiO containing MgO-SiO_2 samples on 1,3-BD yield and samples surface area (a). 1,3-BD yield as a function of surface area (b) (Data from KITAYAMA *et al*., 1996).

It was stressed that the method of synthesis was successful to produce materials with high surface area, as shown in Figure 1.2.12(a), and that this catalyst property might have contributed to the higher 1,3-BD yields.

However, it was also emphasized the importance of the acid-basic sites distribution, which would be closely related to the Mg to Si ratio, since the maximum in surface area did not match exactly the highest 1,3-BD yield. In fact, approximately the same 1,3-BD yield was observed for samples presenting very different surface areas (in m^2/g), as illustrated in Figure 1.2.12(b). It was also verified that NiO/SiO_2 and NiO/MgO were not 1,3-BD active, producing only acetaldehyde from ethanol.

Hydroxyapatites ($Ca_{10}(PO_4)_6(OH)_2$) were also used for the ethanol conversion due to its acid-basic properties (TSUCHIDA *et al*., 2008). By varying the Ca/P ratio, the increase of basic and the reduction of acidic sites concentrations were verified as the Ca content was increased from 1.59 to 1.67 (observed by NH_3 and CO_2 adsorption, followed by temperature programmed desorption experiments). However, these materials presented very low surface areas, ranging from 27 to 40 $m^2 \cdot g^{-1}$. Ethene selectivity (in C wt. %) was correlated with the Ca content; that is, the reduction of the ethene formation was observed when the Ca content was increased. 1,3-BD formation was observed for a single sample, which contained the acid to basic catalyst site ratio close to 1.

The 1,3-BD selectivities (in C wt. %) were reported as 4.9 and 13.8 % at 10 and 20 % of ethanol conversions, respectively, which were achieved at 320 and 350 ºC, with contact time of 1.78 s. At these reaction conditions ethene was the main carbon product. The continuous increase of catalyst basicity, however, did not cause the increase of 1,3-BD production. Instead, high butanol selectivities were verified, which were confirmed by coupled gas chromatography-mass spectrometry (GC-MS) of the reaction output stream. According to the authors, butanol formation would be favored on hydroxyapatite samples due to the higher Ca-O (0.239 nm) distance, when compared to Mg-O (0.210 nm). This higher distance would allow the hydrogen released during ethanol dissociative adsorption to be trapped on catalyst surface instead of desorbing as molecular hydrogen in the gas phase. These trapped hydrogens would be involved in the hydrogenation of the crotonaldehyde, resulting in 1-butanol.

Sepiolites, a crystalline magnesium silicate found naturally as a mineral, was also studied to convert ethanol (GRUVER *et al*., 1995). The effect of the partial

substitution of Si and Mg atoms by Al atoms was investigated. These authors also evaluated the effect of silver addition on Al-containing sepiolites. According to the authors, silver introduced Lewis acidity on the catalyst samples, which caused the increase of both acetaldehyde and 1,3-BD yields, at costs of further ethanol dehydration to ethene and diethyl ether. A positive effect of contact time on yields was observed at 280 ºC. Besides, an induction period (which can be understood as the contact time required for the start of the 1,3-BD formation, given the consecutive character of the reaction kinetics) was observed for both 1,3-BD and for ethene, suggesting that these compounds should not be primary products but formed from acetaldehyde and diethyl ether conversion, respectively. These authors also stressed the possibility that 1,3-BD formation could involve ethene, through the Prins reaction, which will be explained in the next section.

The exchange of magnesium atoms from sepiolite by metals (Mn, Zn, Ni, Co, V and Cu) was reported by KITAYAMA *et al.*, (2002), who also aimed to synthesize a bifunctional catalyst for the ethanol to 1,3-BD conversion. All transition metals resulted in high 1,3-BD yields, in comparison to the magnesium silicate sepiolite precursor, which showed no activity for 1,3-BD formation. Moreover, among the metals, Co, Zn and Cu were pointed as the most promising metals to convert ethanol into 1,3-BD, since they resulted in higher yields.

JONES *et al*. (2011) investigated the role of bi and tri metallic systems (Zr/Zn, Co/Zn, Cu/Zn, Co/Zr, Cu/Co, Co/Mn, Ce/Zr, Hf/Zn, Mn/Zr, Cu/Mn, Mn/Zn and Cu/Zr/Zn) supported over SiO_2 on the ethanol conversion. The catalysts were initially evaluated at 375 ºC and contact time of 2.3 s. Among the bimetallic systems, those containing CuO or ZnO showed higher ethanol dehydrogenation capacity. However, samples also presented high selectivities for ethene and diethyl ether (DEE). Besides, the $ZrZn/SiO_2$ catalyst resulted in the best performance among the bimetallic samples, achieving 1,3-BD selectivity of 38.9 % at 46 % of ethanol conversion, as shown in Figure 1.2.13. It is rationalized that ZnO is active for the dehydrogenation of ethanol, whereas the ZrO_2 is active for the crotonaldehyde Meerven-Ponndorf-Verley reduction.

Trying to improve the catalytic activity of the $ZrZn/SiO_2$ system, silicas with different pore diameter sizes (40, 60 150 Å), prepared at distinct calcination temperatures (300 and 500 ºC), were investigated. Whereas calcination temperature did not exert a significant effect on catalytic activity, 1,3-BD selectivity raised from 28 to

48 % when the SiO_2 pore diameter size was increased from 40 to 150 Å, although no clear effect of the pore size on ethanol conversion was observed. The silicon environments of the samples containing different SiO_2 pore diameter sizes were evaluated by nuclear magnetic resonance (^{29}Si NMR). A higher proportion of Q^4 species was observed for the sample with pore diameter size of 150 Å, suggesting a lower concentration of Si-O-Zr or Si-O-Zn linkages on this sample. Indeed, the surface composition measured by X-ray photoelectron spectroscopy (XPS) indicated that the 150 Å sample presented half of the Zr content observed for the 40 and 60 Å samples. Thus, it was not clear if the positive effect on 1,3-BD selectivity resulted from the pore size or the Zr content effect, or both.

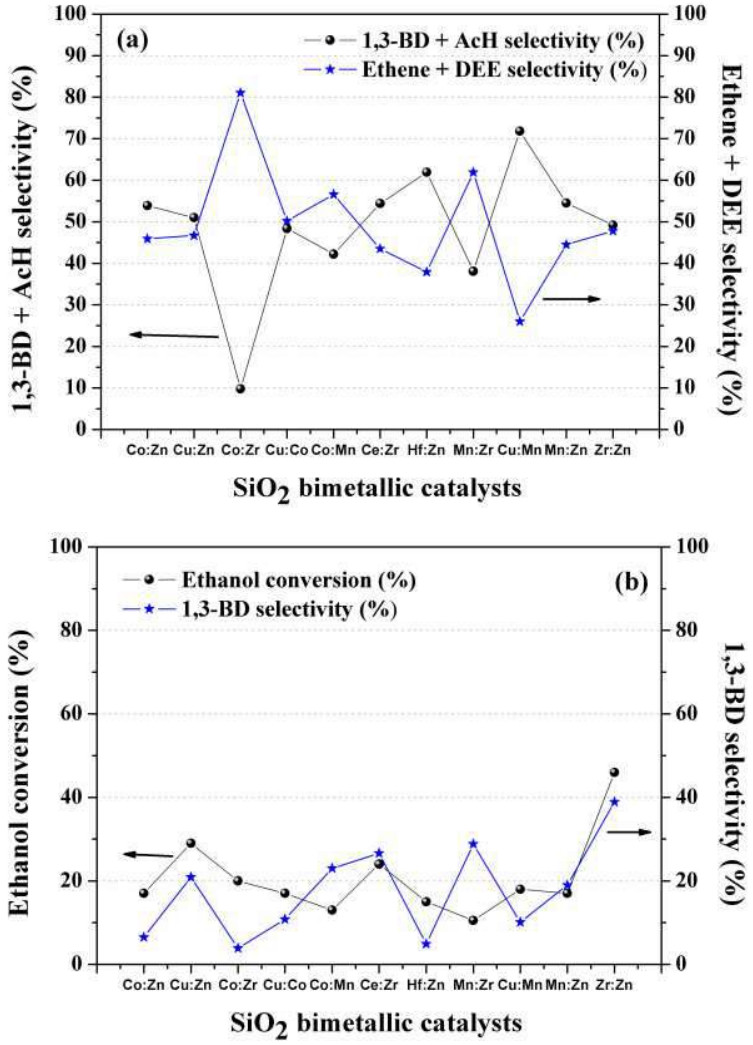

Figure 1.2.13 – Catalytic activity of bimetallic systems supported on SiO_2: (a) Comparison between the combined selectivities of 1,3-BD and AcH, and ethene and DEE; (b) Comparison between ethanol conversions and 1,3-BD selectivities. Data from JONES *et al*. (2011). Reaction at 375 ºC and contact time of 2.3 s (1 g of catalyst).

The addition of Cu, resulting in the trimetallic system $CuZrZn/SiO_2$, produced the highest 1,3-BD selectivity, reported as equal to 67.4 %, at ethanol conversion of 45 %. This result was obtained over the SiO_2 of 150 Å pore diameter, whereas the same system over the SiO_2 of 60 Å pore diameter presented 33 % of 1,3-BD selectivity at 27 % of ethanol conversion, supporting the positive effect of the SiO_2 pore diameter size observed for the bimetallic systems. Washing the catalyst with NaOH suppressed 1,3-BD formation, supporting the hypothesis that both basic and acid sites are needed for on the overall reaction pathway. Finally, the effect of co-feeding ethanol and acetaldehyde (AcH) was shown to give rise for the 1,3-BD selectivity in the case of the bimetallic $ZrZn/SiO_2$ system, but no clear effect was observed over the trimetallic catalyst.

Mg-Al mixed oxides derived from hydrotalcites were also evaluated for the ethanol conversion into 1,3-BD (LEÓN *et al*., 2011a-b). Hydrotalcites present crystalline structure, with a global formula as $(Mg_6Al_2(CO_3)(OH)_{16}\cdot 4(H_2O))$. Thus, mixed oxides obtained from the thermal decomposition of hydrotalcites are reported to contain both basic and acidic features. As these materials also present high surface area, they are expected to behave as active catalysts for different reactions (PÉREZ, 1997).

LEÓN and coworkers (2011a) studied catalyst synthesis variables during the preparation of Mg-Al mixed oxides derived from hydrotalcites. In this study, the Mg/Al ratio was fixed at 3. The effect of keeping the pH constant, or allowing it to be varied during the precipitation, was evaluated. Moreover, the use of Na_2CO_3 and K_2CO_3 was analyzed in terms of the compensation anion. According to the authors, allowing the pH to vary during the precipitation and using Na_2CO_3 as the compensation anion favors the 1,3-BD formation. This result is associated to different distributions of acid and basic sites generated from the distinct preparation methods. However, the mixed Mg-Al oxides resulted in high ethene selectivities, denoting the undesirable strong acid feature of these systems.

In order to overcome this drawback, aluminum atoms were replaced by Fe^{3+} in the Mg-Al mixed oxides derived from hydrotalcites (LÉON *et al*., 2011b). This was performed by adding a $Fe(NO_3)_3.9H_2O$ solution to the aluminum and magnesium nitrate solutions during the hydrotalcite precipitation. Experiments of NH_3-TPD suggested that this approach allowed for success reduction of the catalyst acidity. Thus, it was stressed that the choice of the metal could constitute the right way to adjust acid-basic properties

in these systems, in order to improve 1,3-BD yields. The 1,3-BD selectivities reported over the Fe containing Mg-Al mixed oxides were rather low, below 16 %. In fact, crotonaldehyde, butanal, butenes and butanols were also detected in significant amounts.

The effect of the Mg/Al ratio of these mixed oxides had been previously investigated for the ethanol conversion into 1,3-BD (DI COSIMO *et al*., 1998). It was observed, as expected, that the increase of the aluminum content caused reduction of the AcH yield and increase of the ethene formation. Thus, as observed for the $MgO\text{-}SiO_2$ systems, the acid basic properties of Mg-Al mixed oxides could be modified by changing the Mg/Al ratio. However, employing Mg/Al molar ratios between 0.5 and 9, the authors identified n-butanol, AcH, butanal, ethene and DEE as the major reaction products.

The addition of different transition metals on the $MgO\text{-}SiO_2$ system resulted in significant improvement of the 1,3-BD formation from ethanol (MAKSHINA *et al*., 2012). These authors studied five different preparation methods for this system. In the first one, MgO and SiO_2 were mixed mechanically. In the second one, $Mg(OH)_2$ and SiO_2 were mixed mechanically. Wet-kneading of $Mg(OH)_2$ and tetraethyl-orthosilicate was the third method. Impregnation of SiO_2 with an aqueous solution of magnesium nitrate was the fourth method. Finally, in the fifth method, MgO and SiO_2 were wet-kneaded using ethanol. Besides, by employing the fifth method, at the Mg/Si molar ratio of 2, eight catalysts were prepared, each of them containing one of the following transition metals: Cr; Mn; Fe; Co; Ni; Cu; Zn; and Ag. One additional catalyst series was prepared by using the second method at different Mg/Si molar ratios and also by adding different silver contents. Finally, a second additional series, where SiO_2 was impregnated with an aqueous solution of magnesium nitrate (at the Mg/Si ratio of 2) and then with an aqueous solution of zinc nitrate, was tested. The effect of the Mg/Si molar ratio was also studied, from 1 to 3. All catalyst samples were calcined at 500 ºC during 4 h, and reactions were performed at 350 and 400 ºC, at atmospheric pressure and spatial velocity of $0.18 \cdot 10^6\ g_{cat} \cdot s \cdot mol_{etOH}^{-1}$.

As reported by KVISLE *et al*. (1988) and GRUVER *et al*. (1995), MAKSHINA *et al*. (2012) also reported an initial time period before observation of stable catalytic activity. In the study of MAKSHINA *et al*. (2012), this time was approximately equal to 1 hour. After this, catalytic activity was described to be stable during 7 hours.

The effect of the Mg/Si molar ratio, employing the different preparation methods, did not result in large variations on the 1,3-BD selectivity, which fluctuated mainly between 10 and 15 %, although the ethanol conversion was omitted. It was stressed that the simpler MgO-SiO_2 system could not produce satisfactory 1,3-BD yields. Similar surface areas and X-ray diffractograms were observed for samples containing similar Mg/Si ratios and prepared by the different methods. The only exception was the system prepared by impregnation of the SiO_2 with the aqueous solution of magnesium nitrate. This method in particular resulted in lower surface area and lower 1,3-BD selectivity (8 %) (MAKSHINA *et al*., 2012).

Regarding the transition metal addition on the MgO-SiO_2 precursor, a clear relationship between the transition metal electronegativity and the 1,3-BD selectivity was verified. The higher was the electronegativity, the higher was the 1,3-BD yield. The only exceptions were Ag and Mn. No significant change of 1,3-BD selectivity and ethanol conversion was reported for samples containing different silver contents. However, the effect of the Mg/Si molar ratio was more pronounced for silver containing systems, contrasting with results obtained for simpler MgO-SiO_2 samples. In this case, the Mg/Si most promising content was equal to 2. Moreover, samples prepared by impregnation and containing different zinc contents resulted in similar performances, as observed for simpler MgO-SiO_2 samples (MAKSHINA *et al*., 2012).

According to the authors, the most promising performances were obtained over Ag/MgO-SiO_2 and Cu/MgO-SiO_2 samples. These materials resulted in approximately 60 % of 1,3-BD selectivity at ethanol conversion of 97 % (the 1,3-BD productivity, in $g_{BD} \cdot g_{cat}^{-1} \cdot h^{-1}$, being equal to 0.07 and 0.06 at 350 ºC). By increasing reaction temperature until 400 ºC and the ethanol feed composition, 0.20 $g_{BD} \cdot g_{cat}^{-1} \cdot h^{-1}$ could be achieved by these catalysts; however, at the cost of lower 1,3-BD selectivities (44 and 49 %).

Following the suggestions by JONES *et al*. (2011) and MAKSHINA *et al*. (2012), LEWANDOWSKI *et al*. (2014) extended the study of transition metals addition over the MgO-SiO_2 precursor, however by using simultaneously Zr and Zn. The effect of the Mg/Si molar ratio was evaluated in this case between 1 and 19. At 325 ºC and spatial velocity of 0.3 h^{-1}, after 3 h of reaction, 1,3-BD selectivity increased with Mg/Si molar ratio from 1 to 3, being reduced with the continuous increase of the Mg/Si molar ratio over simpler MgO-SiO_2 systems. As reported by KITAYAMA *et al*. (1996),

LEWANDOWSKI *et al*. (2014) also observed the reduction of the catalyst surface area with higher MgO contents (higher Mg/Si ratios). When the $MgO\text{-}SiO_2$ samples containing Zr and Zn were evaluated, however, 1,3-BD selectivities increased continuously with the Mg/Si ratio. It should be mentioned that a fixed amount of Zr and Zn was added to the samples, equal to 1,5 and 0.5 wt.% for Zr and Zn, respectively. Thus, a maximum 1,3-BD selectivity of 68.7 % was quantified at the ethanol conversion of 30 %. Besides, for the $ZrZn/MgO\text{-}SiO_2$ sample at the Mg/Si molar ratio of 5.7, slight improvement of the 1,3-BD selectivity was observed when the SiO_2 with pore diameter size of 150 Å was employed (selectivity raised from 63 to 68 %).

The patent WO-015340 (ORDOMSKIY *et al*., 2012) reported a large list of possible new catalysts for 1,3-BD production from ethanol and from mixtures of ethanol and AcH. The mixed oxides described by this patent included $Ag/MgO\text{-}SiO_2$, $Ag/TiO_2\text{-}SiO_2$, $Ag/ZrO_2\text{-}SiO_2$, $Au/MgO\text{-}SiO_2$, $Au/TiO_2\text{-}SiO_2$, $Au/ZrO_2\text{-}SiO_2$, $Co/MgO\text{-}SiO_2$, $Co/TiO_2\text{-}SiO_2$ and $Co/ZrO_2\text{-}SiO_2$. These systems could be modified through addition of alkali metals or Ce, Sn or Sb. According to the refereed patent, 1,3-BD yields as 70 % or higher could be obtained over these materials.

Probably inspired by results provided by JONES *et al*. (2011) regarding the effect of the pore diameter size on the 1,3-BD yields, CHAE et al. (2014) investigated the use of ordered mesoporous silica supported tantalum oxide on the conversion of mixtures of ethanol and AcH. Ordered mesoporous silica with different pore morphology, size and crystal sizes were evaluated in respect to the ability to produce 1,3-BD and to the thermal stability as a function of the time on stream. SBA-15, KIT-6 and MMS silicas were employed. These silicas present pores with ordered geometry, and they are synthesized by using special polymers as “structure builders”, which act as templates for the silica polymerization, being removed during the subsequent calcination process. Such silicas present higher surface area and pore structure organization, when compared with common commercial silicas. For instance, the SBA-15 is characterized by its hexagonal channels, with 5 to 9 nm of diameter. The wall thickness of SBA-15 contributes for its thermal stability. In the KIT-6 material, the channels are orderly connected and the MMS presents cylindrical channels with thinner walls, when compared to the SBA-15 and KIT-6.

CHAE *et al*. (2014) used 2 wt.% of Ta_2O_5 supported over the special silicas, although commercial silicas were also evaluated for comparison. Besides, SBA-15

samples containing different pore sizes were prepared by using different temperatures during the synthesis. At 350 ºC, both the catalytic activity and the thermal stability of the ordered mesoporous silicas containing Ta_2O_5 were superior, when compared to the commercial silicas, as illustrated in Figure 1.2.14. The best performances of the remarkable silicas could be associated to their exceptional textural properties; for instance, the surface areas ranged between 580 and 805 $m^2 \cdot g^{-1}$ (CHAE *et al.*, 2014). However, characterization of acid and basic properties was not reported.

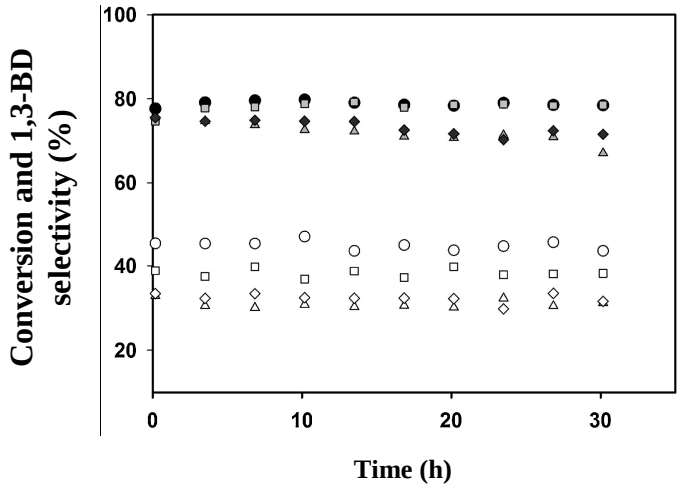

Figure 1.2.14 – Total conversion of ethanol and AcH (empty symbols) and 1,3-BD selectivity (in C mol.%) (full symbols) for Ta_2O_5/SBA-15 (circles), Ta_2O_5/KIT-6 (square) and Ta_2O_5/SiO_2 (triangle and diamond) (Reprinted and adapted from CHAE *et al.*, 2014, copyright (2014), with permission from Elsevier).

These authors also verified a linear and positive correlation among reactants conversion, 1,3-BD selectivity and catalyst pore size over a series of Ta_2O_5/SBA-15 samples. At 10 h of time on stream, 1,3-BD selectivity (in C mol. %) was reported as equal to 80 % at conversion level of 47 % over the Ta_2O_5/SBA-15 system. On the other hand, the Ta_2O_5/SiO_2 sample presented 75 % of 1,3-BD selectivity at 33 % of conversion.

The addition of H_2O_2 to a feed comprising pure ethanol, over ZnO/γ-Al_2O_3 catalysts, was reported to present a positive effect on the thermal catalyst stability as a function of the time on stream (EZINKWO *et al.*, 2014). An increase of the 1,3-BD selectivity with the H_2O_2 addition was claimed. The increase of the life time of the catalyst was reported from 48 to 120 h; that is, when no H_2O_2 was employed, the catalyst started to show deactivation signals after 48 h of time on stream; when H_2O_2

was employed, deactivation started after 120 h. Reactions were performed at atmospheric pressure, between 390 and 420 ºC, using different spatial velocities between 1.2 and 4.4 h^{-1} and different ethanol to H_2O_2 feed ratios.

According to EZINKWO *et al*. (2014), the role of H_2O_2 could be associated to the production of radicalar $OH^{\bullet}$ species, which would re-oxidize active sites on the catalyst surface, improving 1,3-BD selectivity. 1,3-BD yields ranged from 18 to 24.5 % and 1,3-BD selectivities ranged between 42 and 55 %. Nevertheless, the effect of H_2O_2 on yields and selectivities was not very pronounced. For instance, an increase from 18.1 to 18.2, or from 20 to 22.3 was described for 1,3-BD yields when H_2O_2 was added into the feed. Thus, the most significant effect of the H_2O_2 could be in fact associated to the increase of catalyst life time.

Catalyst preparation variables were also studied by ANGELICI *et al*. (2014, 2015), who evaluated different preparation methods for the SiO_2-MgO system. This group compared the mechanical mixing of MgO and SiO_2 with three wet-kneading methods, by using different sources of SiO_2 and two precipitation methods. It was claimed that the wet-kneading method was more appropriate, because this method resulted in a lower acid sites concentration. Besides, the addition of CuO into the SiO_2-MgO system was reported to be very beneficial to the 1,3-BD yield and selectivity. According to these authors, 1,3-BD selectivity raised from 30 to 50 %, while the ethanol conversion raised from 50 to 80 % when SiO_2-MgO samples containing CuO were tested (reactions were performed at 425 ºC, and spatial velocity of $0.149 \cdot 10^6\ g_{cat} \cdot s \cdot mol_{etOH}^{-1}$).

At this point, it can be noted that, given the fact that the reaction pathway of ethanol transformation into 1,3-BD involve acid and basic catalysis, a very large set of different metal oxides might be applicable to this reaction, as emphasized in the previous discussion. In order to facilitate the comparison among catalytic activities over different systems described in this section, Tables 1.2.6 and 1.2.7 were organized. Table 1.2.6 presents catalytic results over selected systems employing only ethanol as feed, whereas Table 1.2.7 includes data where mixtures of ethanol and AcH were used.

Table 1.2.6 – Overview of catalytic activities for ethanol conversion (X), 1,3-BD selectivity (S), and 1,3-BD yield (Y), and main reaction conditions employed (temperature (T), contact time (τ) and ethanol feed composition ($\tilde{x}_{etOH}$)).

Catalyst	*T (ºC)*	*τ* (s) or *W/F* ($g_{cat}/(mol_{etOH}/s)$)	$\tilde{x}_{etOH}$ (mol.%)	*X (%)*	*S* [a] *(%)*	*Y (%)* [b]	*Ref.*
Al_2O_3-ZnO	400	NI	NI	-	-	18	1
ZrO_2 - SiO_2 ThO_2 - SiO_2	432-460	NI	NI	NI	34-44	NI	2
MgO-SiO_2 -Cr_2O_3	425	NI	82	NI	NI	39	3
MgO-SiO_2 -Ta_2O_5	420	NI	82	NI	NI	34	
Al_2O_3-ZnO (60:40)	425	1.875 $ml_{etOH}/h \cdot g_{cat}$		94.4	NI	55.8	4
MgO-SiO_2(1:1) (A)	350	1.1 x 10^6 $g_{cat}/(mol_{etOH}/s)$	1,6	50	84	42	5*
MgO-SiO_2(1:1) (B)				98	2	2	
MgO-SiO_2(1:1) (C)				71	7	5	
MgO-SiO_2(1:1)-Na_2O (0,1 wt %)				100	87	87	
MgO-SiO_2(1:1)-K_2O (0.1 wt.%)				80	87	70	
MgO-SiO_2 (Mg/Si = 0,83)	350	5.2 x 10^6 $g_{cat}/(mol_{etOH}/s)$	3,06	53	30	16	6
MgO-SiO_2 (Mg/Si = 0,63)				62	24	15	
Hectorites	325-400	$6 \cdot 10^5$ $g_{cat}/(mol_{etOH}/s)$	9.68	13-46	NI	4-20.7[c]	7
MgO-SiO_2(2:3)-NiO (10 wt %)	280	288	NI	58	90	52	8
$Ca_{10}(PO_4)_6(OH)_2$	320-350	1.78	16.4	50	23	-	9
MnO_2/sepiolite	280	NI	NI	92.5	-	55.5	10
Zr/Zn-SiO_2	375	$0.35 \cdot 10^5$ $g_{cat}/(mol_{etOH}/s)$	NI	48	47.9	NI	11
Zr/Zn/Cu-SiO_2				44.6	67.4		
MgO-SiO_2	350	$0.18 \cdot 10^6$ $g_{cat}/(mol_{etOH}/s)$	NI	NI	16	NI	12
Ag-MgO-SiO_2				97.5	58.2		
Cu-MgO-SiO_2				97.1	56.3		
Au-ZrO_2-SiO_2	325	$0.55 \cdot 10^6$ $g_{cat}/(mol_{etOH}/s)$	NI	47.2	72	34	13
MgO-SiO_2				45	40	18	
ZrO_2-SiO_2				17	48	8	
γ-Al_2O_3-ZnO	395	818	NI	NI	55[c]	24.5[c]	14
Mixed oxide derived from hydrotalcite (Mg/Al = 3)	450	$6.7 \cdot 10^{-5}$ $g_{cat}/(mol_{etOH}/s)$	5,5	≈ 85	≈ 23	NI	15
Fe-Mg/Al mixed oxide derived from hydrotalcite	230-480			≈ 50	≈ 15	NI	16
MgO-SiO_2 (Mg/Si = 3)	325	12000	NI	35	43.6	NI	17
MgO-SiO_2-ZnZr (Mg/Si = 19)				30	68.7		

NI = no information. *10 min of reaction; (A), (B) and (C) represent different preparation methods;
[a] Reported yields based in the amount of reactant consumed were assumed as selectivity; [b] Yields are based in the amount of reactant fed; [c] Calculation formula was not reported.

Table 1.2.7 – Overview of catalytic activities for ethanol and AcH conversion (X), 1,3-BD selectivity (S), and 1,3-BD yield (Y), and main reaction conditions employed (temperature (T), contact time (τ) and ethanol feed composition ($\tilde{x}_{etOH}$)).

Catalyst	*T (ºC)*	*τ* (s) or *W/F* ($g_{cat}/(mol_{etOH}/s)$)	*Ethanol/ AcH molar ratio*	*X (%)*	*S* [a] *(%)*	*Y* [b] *(%)*	*Ref.*
Ta_2O_5 - SiO_2	330	$6.02 \cdot 10^{-4}$	3.03	30	60	NI	21
	325	$4.90 \cdot 10^{-4}$	3.04	39	71	NI	19
	350	4.5	2.5	55	64	35	18
MgO-SiO_2 -Cr_2O_3	400			70	33	23	
MgO-SiO_2 -Ta_2O_5	400			90	30	27	
Ta_2O_5 -SiO_2	350	NI	2.75	50	69	34	3
Hf - SiO_2	300			45	64	29	
Zr - SiO_2	300			47	64	30	
MgO-SiO_2 (Mg/Si = 0.83)	350	5.2×10^6 $g_{cat}/(mol_{etOH}/s)$	5	48	68	33	6
Zr/Zn-SiO_2	375	$0.70 \cdot 10^5$ $g_{cat}/(mol_{etOH}/s)$	4	45	66	NI	11
Cu-ZrO_2-SiO_2	325			63.4	71	45	
Au-ZrO_2-SiO_2	325			38	82	31	
Ag-TiO_2-SiO_2	325			49	72	35	
Ag-Ta_2O_2-SiO_2	325			46.5	71	33	
Ag-ZrO_2-SnO_2-SiO_2	325			48	75	36	
Ag-ZrO_2-SbO_2-SiO_2	325	$0.55 \cdot 10^6$ $g_{cat}/(mol_{etOH}/s)$	NI	50	76	38	13
Ag-ZrO_2-CeO_2-SiO_2	325			50.6	81	41	
Ag-ZrO_2-Na_2O-SiO_2	325			58	72	42	
Ag-ZrO_2-CeO_2-Al_2O_3-SiO_2	325			46	74	34	
Ag-ZrO_2-CeO_2-SiO_2	325			56	78	44	
Ta -SBA-15	350	$0.11 \cdot 10^6$ $g_{cat}/(mol_{etOH}/s)$	2.5	46.9	80	-	20

NI = no information. [a] Reported yields based in the amount of reactant consumed were assumed as selectivity; [b]Yields are based in the amount of reactant fed; [c] Calculation formula was not reported.

Table 1.2.8 shows references indicated as "Ref" in the right column of Tables 1.2.6 and 1.2.7.

Table 1.2.8 – References from Tables 1.7 and 1.8.

Number	*Reference*	*Number*	*Reference*
1	Lebedev, 1930	12	Makshine *et al*., 2012
2	Spence *et al*., 1948	13	Ordomskiy *et al*., 2012
3	Corson *et al*., 1950	14	Ezinkwo *et al*., 2014
4	Bhattacharyya e Ganguly, 1962b	15	León *et al*., 2011-a
5	Ohnishi *et al*., 1985	16	León *et al*., 2011-b
6	Kvisle *et al*., 1988	17	Lewandowski *et al*., 2014
7	Suzuki *et al*., 1988	18	Corson *et al*., 1949
8	Kitayama *et al*., 1996	19	Quattlebaum *et al*., 1947
9	Tsuchida *et al*., 2008	20	Chae *et al*., 2014
10	Kitayama *et al*., 2002	21	Toussaint *et al*., 1947
11	Jones *et al*., 2011		

1.2.1 Final Comments

Based on the previous discussion, it can be seen that materials with multifunctional properties have been studied, especially $MgO\text{-}SiO_2$ systems (JANSSENS *et al*., 2015; MAKSHINA *et al*., 2014). This is related to the fact that Mg-O pairs may act as Lewis acid-Brønsted basic sites and to the fact that silanol groups act as a Brønsted acid sites, which are necessary for ethanol dehydrogenation (DI COSIMO *et al*., 1998), acetaldehyde condensation (ORDOMSKY *et al*., 2010), crotonaldehyde reduction and crotyl alcohol dehydration to 1,3-BD. However, due to the presence of acid sites in these systems, ethanol dehydration to ethene and diethyl ether are significant competitive reactions.

Therefore, efforts have been dedicated to the design of catalysts that are able to suppress these undesirable parallel reactions. For instance, the addition of metals and/or metal oxides based on Cu, Zr, Zn and Ag to the $MgO\text{-}SiO_2$ system has been shown to be beneficial to 1,3-BD yield (MAKSHINA *et al*., 2012, ORDOMSKY *et al*., 2010, ANGELICI *et al*., 2014, LEWANDOWSKI *et al*., 2014, LARINA *et al*., 2015). In particular, a synergic effect between ZrO_2 and ZnO has been shown to exist (JONES *et al*., 2011; LEWANDOWSKI *et al*., 2014). ZnO may support ethanol dehydrogenation and ZrO_2 is expected to assist aldol condensation and crotonaldehyde reduction (JONES *et al*., 2011, SUSHKEVICH *et al*., 2014, LEWANDOWSKI *et al*., 2014, LARINA *et al*., 2015, SEKIGUCHI *et al*., 2015, BAYLON *et al*., 2016).

Conversely, both catalyst composition and catalyst preparation method were shown to be of paramount importance for 1,3-BD formation, since different acid-basic features may be obtained, depending on synthesis conditions (OCHOA *et al*., 2015, ANGELICI *et al*., 2015, LEWANDOWSKI *et al*., 2014, BAERDEMAEKER *et al*., 2015). Due to this, different optimum Mg-to-Si molar ratios have been reported for 1,3-BD formation, depending on the employed synthesis procedure (MAKSHINA *et al*., 2012, OCHOA *et al*., 2015, LEWANDOWSKI *et al*., 2014).

Among the catalyst preparation procedures, different methods have been investigated, such as physical mixtures of MgO and SiO_2 (KVISLE *et al*., 1988, MAKSHINA *et al*., 2012), wet-kneading (NIIYAMA et al., 1972, KVISLE *et al*., 1988, JONES *et al*., 2011, MAKSHINA *et al*., 2012), sol-gel (OCHOA *et al*., 2015, HAN *et al*., 2015), impregnation (MAKSHINA *et al*., 2012) and co-precipitation (ANGELICI *et al*., 2014, LEÓN *et al*., 2011a-b). Whereas it has been proven that a physical mixture

between precursor oxides is not suitable for 1,3-BD formation, since the resulting catalysts show similar features to single MgO and SiO_2 phases, wet-kneading methods have been the most widely discussed preparation methods in the literature, with less attention being dedicated to sol-gel and co-precipitation methods (MAKSHINA *et al*., 2014).

In the wet-kneading preparation procedure, MgO and SiO_2 are usually mixed at the desired molar ratio in the presence of water, dried and calcined. Besides the specific features of the MgO and SiO_2 precursors employed and their molar ratio, the amount of water, time, ageing temperature, drying and calcination procedure represent some of the preparation steps that may affect the catalysts behavior (MAKSHINA *et al*., 2014). As observed by energy dispersive X-ray (EDX) and transmission electron microscopy (TEM) analyses, materials prepared by wet-kneading are usually heterogeneous in terms of composition and morphology (KVISLE *et al*., 1988, ANGELICI *et al*., 2014, ANGELICI *et al*., 2015). These materials are generally constituted by ¨islands¨ of MgO and SiO_2, and a limited amount of amorphous magnesia hydrosilicate phase (ANGELICI *et al*., 2014, 2015). These unique characteristics are described as the key factor for the conversion of ethanol into 1,3-BD, since an intrinsic basic-acid sites distribution is obtained on these materials (ANGELICI *et al*., 2014, 2015).

Using a sol-gel method, OCHOA *et al*. (2015) observed that the Mg to Si molar ratio affected the number, strength and distribution of basic-acid sites, the surface area and the crystalline structure of the catalysts, impacting on product distribution. As described previously, a comparison between wet-kneading and a co-precipitation method, at similar Mg:Si ratios, showed that the former is more suitable for ethanol conversion into 1,3-BD (ANGELICI *et al*., 2014, ANGELICI *et al*., 2015). However, the co-precipitation method may constitute an efficient preparation procedure for production of catalysts with homogeneous properties, allowing for better control of the physical and chemical properties of the catalyst and facilitating the determination of structure-activity-relationships. Despite that, a rigorous study based on the co-precipitation method has not been reported.

In the next section, a deeper discussion regarding the overall reaction pathway is presented, and the possible role of the different active sites on the different reaction steps is discussed.

1.3 Mechanism of Ethanol Conversion into 1,3-Butadiene

As discussed in the previous sections, the route most widely accepted to account for 1,3-BD production from ethanol involves five consecutive reactions, which are illustrated in Figure 1.2.1. Initially, ethanol is dehydrogenated to acetaldehyde. Then, 3-hydroxybutanal is formed from acetaldehyde self-aldolisation. Next, 3-hydroxybutanal dehydrates to crotonaldehyde, which is reduced (Meerwein-Ponndorf-Verley (MPV) reduction) with ethanol to produce crotyl alcohol and acetaldehyde. Finally, crotyl alcohol is dehydrated to afford 1,3-BD (NIIYAMA *et al*., 1972).

In the first step, ethanol is dehydrogenated to acetaldehyde (AcH). This step involves basic sites. FRANCKAERTS and FROMENT (1964) studied the kinetics of ethanol dehydrogenation over an oxide, including Cr_2O_3, CoO and CuO. It was concluded that the surface reaction limits the kinetics and that ethanol adsorption occurs non-dissociatively on two adjacent sites. DI COSIMO *et al*. (1998) described the ethanol dehydrogenation step as involving pairs of Brønsted basic and Lewis acid sites, as illustrated in Figure 1.3.1, where B denotes one Brønsted basic site and A denotes one Lewis acid site. GRUVER et al. (1995) also stated that ethanol dehydrogenation could involve Lewis acid sites.

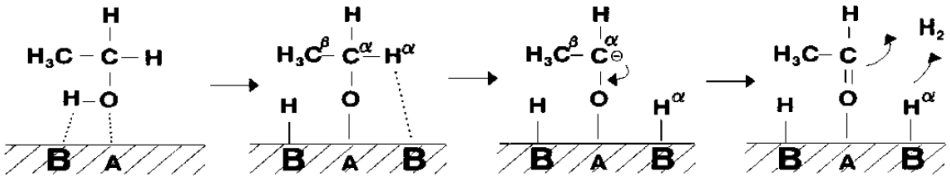

Figure 1.3.1 – Mechanism of ethanol dehydrogenation over Mg-Al mixed oxides derived from hydrotalcites, according to DI COSIMO *et al*. (1998).

In step 2, aldol addition takes place, producing 3-hydroxybutanal, as shown in Figure 1.3.2. The basic site is responsible for the proton abstraction from the α carbon of acetaldehyde. This originates the enolate ion, which, in turn, attacks the carbonyl carbon of a second acetaldehyde molecule, resulting in one alkoxide ion. Finally, the

alkoxide ion abstracts the proton from the basic site, producing 3-hydroxibutanal and releasing the basic site (BASTIANI, 2001).

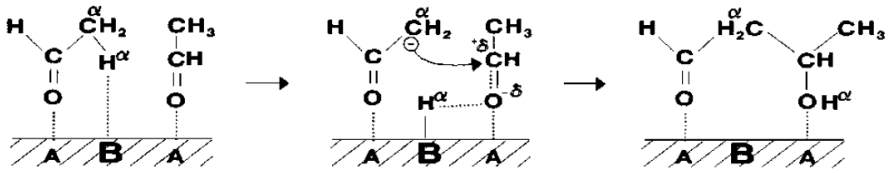

Figure 1.3.2 – Mechanism of 3-hydroxibutanal formation from acetaldehyde over Mg-Al mixed oxides derived from hydrotalcites, according to DI COSIMO *et al*., (1998).

In step 3, 3-hydroxybutanal is dehydrated to crotonaldehyde (2-butenal) (for each compound, the commonest name employed in the literature was kept throughout this text in order to facilitate the reading). This step benefits from the stability of the resulting product, due to the double bond conjugation. Therefore, it is believed that this step occurs very fast. In the presence of basic sites and at high temperatures, the dehydration of 3-hydroxybutanal, as illustrated in Figure 1.3.3, could involve the formation of an enolate ion, through proton abstraction from the α carbon by the basic site, and the subsequent crotonaldehyde formation, through hydroxyl elimination from the hydroxide ion (CAREY, 2001). However, the 3-hydroxibutanal dehydration could also occur over acid sites, as shown in Figure 1.3.4. In this case, Brønsted (route 1) and Lewis (route 2) acid sites could be involved (KALSI, 2006).

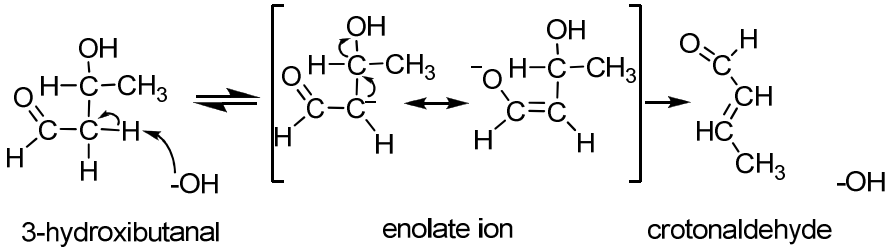

Figure 1.3.3 – Suggested mechanism for crotonaldehyde formation from 3-hydroxibutanal dehydration, involving basic sites (CAREY, 2001).

In step 4, crotonaldehyde is reduced through the carbonyl group, producing crotyl alcohol (2-butenol) and acetaldehyde, as shown in Figure 1.3.5. The reaction is known as the *Meerwein-Ponndorf-Verley* (MPV) mechanism and involves the formation of a cyclic intermediate (not shown in the figure) from the adjacent

adsorption of ethanol and crotonaldehyde. Ethanol allows the hydride transfer from the ethanol carbonyl carbon to the crotonaldehyde carbonyl carbon (DI COSIMO *et al*., 2004).

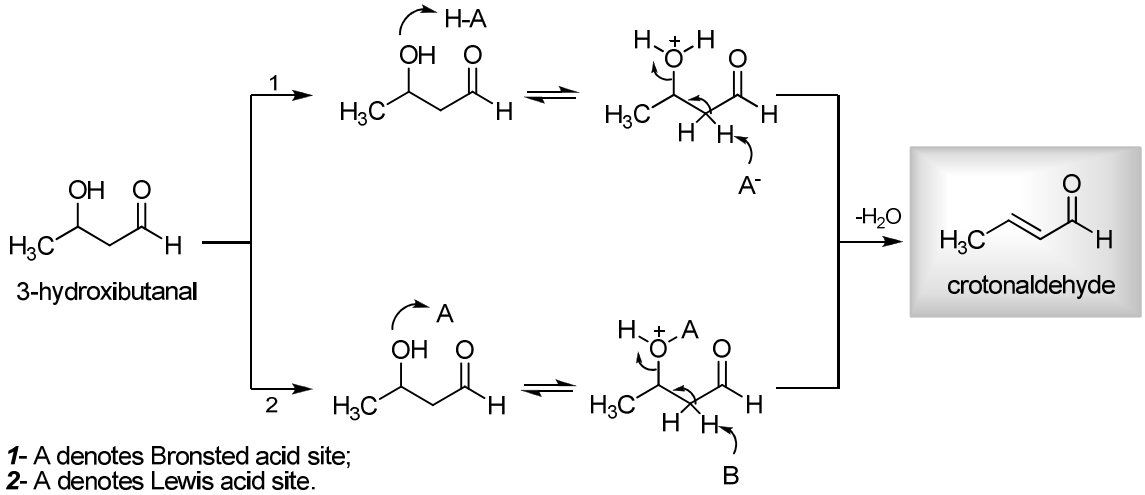

Figure 1.3.4 – Suggested mechanism for crotonaldehyde formation from 3-hydroxibutanal dehydration, involving Brønsted and Lewis acid sites (KALSI, 2006).

The *"Meerwein-Ponndorf-Verley reduction"* was described in 1920 for homogenous reactions, explaining the carbonyl reduction of aldehydes and cetones resulting from the hydride transfer from an alcohol formed over aluminum isopropoxide (or other metallic alkoxides), used as a catalyst (KURTI and CZAKÓ, 2005). Thus, a similar mechanism is hypothesized in the case of heterogeneous catalysis, with adsorption on a Lewis acid site.

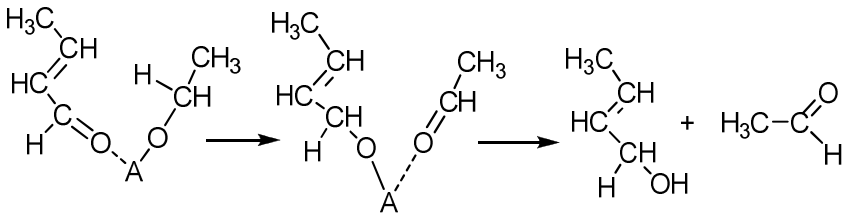

Figure 1.3.5 – Suggested mechanism for the *Meerwein-Ponndorf-Verley* reduction of crotonaldehyde, involving Lewis acid sites (KVISLE *et al*., 1988).

Finally, in the last step, crotyl alcohol is dehydrated over acid sites resulting into 1,3-BD and water, as shown in Figure 1.3.6. Once again, Brønsted (route 1) and Lewis (route 2) acid sites may dehydrate crotyl alcohol.

This global five-step mechanism was initially suggested by QUATTLEBAUM *et al.* (1947), who verified experimentally that higher 1,3-BD yields were achieved when crotonaldehyde and ethanol were used in the feed, when compared to a feed stream that contained acetaldehyde and ethanol, using a SiO_2 or Ta_2O_5/SiO_2 catalysts.

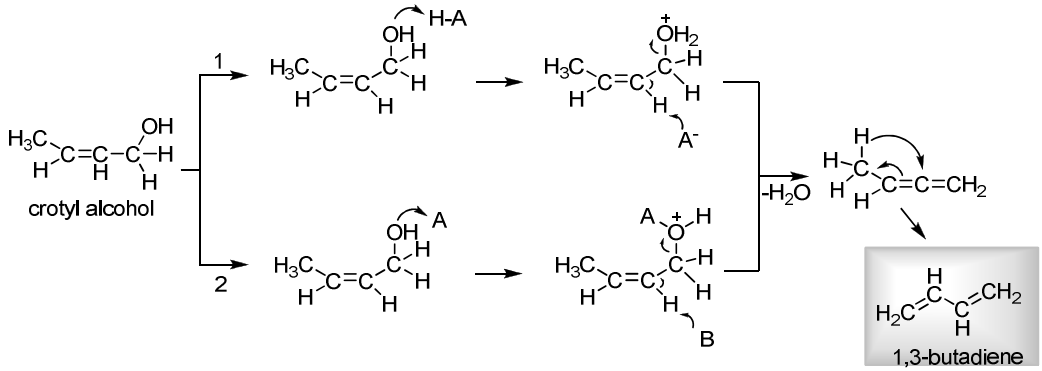

Figure 1.3.6 – Suggested mechanism for the crotyl alcohol dehydration, producing 1,3-BD. In the figure, B denotes a basic site.

With the Ta_2O_5/SiO_2 catalyst, the authors also observed that a feed stream containing pure acetaldehyde would be converted into crotonaldehyde, which was not observed in significant quantities when ethanol and acetaldehyde were passed over the catalyst. This suggests that crotonaldehyde was rapidly converted into crotyl alcohol (presumably by an MPV process) and subsequently to 1,3-BD. However, some reports have recently ruled out the aldol condensation as the main path, suggesting instead that crotyl alcohol is produced through the reaction between an activated form of ethanol and acetaldehyde (OCHOA *et al.*, 2015, CHIEREGATO *et al.*, 2015).

Some researchers suggested that 1,3-BD could also be produced from the hydrogenation of the carbonyl group from 3-hydroxibutanal, via 3-hydroxibutanol (1,3-butanediol) dehydration (JONES *et al.*, 2011). However, this pathway has been ruled out by TOUSSAINT *et al.* (1947) and NIIYAMA *et al.* (1972), who verified experimentally traces of 1,3-BD when 3-hydroxibutanol was used as reactant.

A different mechanism was also defended by GRUVER *et al.* (1995), who described the 1,3-BD formation based on the reaction between acetaldehyde and ethene, the so called Prins reaction, as shown in Figure 1.3.7. However, ANGELICI *et al.* (2013) discussed the low probability for this reaction pathway, since it involves the generation of a highly unstable primary carbocation from ethene.

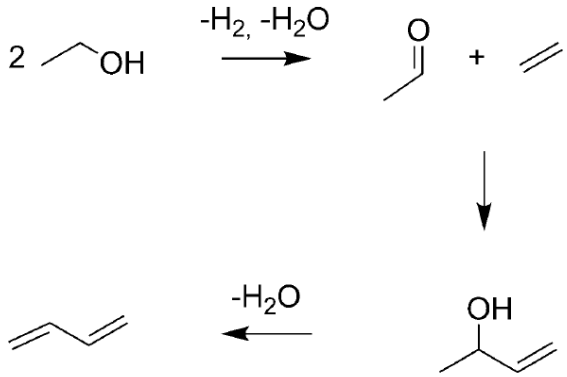

Figure 1.3.7 – Suggested reaction pathway for 1,3-BD formation from acetaldehyde and ethene (GRUVER *et al.*, 1995, ANGELICI *et al.*, 2013).

Thus, it can be said that the ethanol to 1,3-BD reaction mechanism is still subject to debate. Furthermore, opinions also disagree regarding the rate-limiting step. For instance, considering the overall reaction pathway, as presented in Figure 1.2.1, the aldol condensation step has been suggested to be the most probable rate-limiting step over Ta_2O_5-SiO_2 (JONES *et al.*, 1949), Ag/Zr/SiO_2 (SUSHKEVICH *et al.*, 2014), Ag/MgO-SiO_2 (JANSSENS *et al.*, 2015), Zn/MgO-SiO_2 (LARINA *et al.*, 2015).and Al_2O_3-ZnO (BHATTACHARYYA and SANYAL, 1967) catalysts, whereas the ethanol dehydrogenation (NIIYAMA *et al.*, 1972) and the aldol condensation (KVISLE *et al.*, 1988) have been pointed to be the rate-limiting step over MgO-SiO_2 catalysts.

1.3.1 Final Comments

Based on the previous discussion, it seems clear that both acid and basic sites are important for the reaction pathway, which also depends on the strength and distribution of sites on the catalyst surface. Since no agreement regarding the rate-limiting step has been settled, the design of unequivocal catalyst properties for increase of 1,3-BD yields is not possible yet. Besides, it is important to note that there is no fundamental mathematical model available to explain the reaction kinetics in published material, impairing the proper quantification of the rate-limiting step and the design, optimization and control of industrial reactors for ethanol conversion into 1,3-BD.

1.4 Thermodynamics of the Ethanol to 1,3-BD Conversion

This section is dedicated to discussing some thermodynamic aspects of the ethanol to 1,3-BD conversion. In order to evaluate the reaction feasibility, Gibbs energy changes and compositions at the equilibrium state were calculated. A description of the employed methodology and hypotheses assumed to perform the simulations can be found in Appendix A.

As discussed in the previous section, five reaction steps are required to describe the ethanol to 1,3-BD conversion. However, since thermodynamic properties for 3-hydroxybutanal, crotonaldehyde and crotyl alcohol are not available (ANGELICI *et al.*, 2013), the feasibility of the reaction system was studied taking into account reactions **1** and **2** of Table 1.4.1. In fact, the overall reaction pathway could be described as shown in Eq. (1.4.1):

$$2CH_3CH_2OH \rightarrow C_4H_6 + 2H_2O + H_2 \qquad (1.4.1)$$

Table 1.4.1– Reaction set considered for calculations of Gibbs energy changes and compositions.

Reaction		*Initial number of mols*
$CH_3CH_2OH \rightarrow CH_3CHO + H_2$	(1)	$CH_3CH_2OH_{in} = 2$
$CH_3CH_2OH + CH_3CHO \rightarrow C_4H_6 + 2H_2O$	(2)	$CH_3CH_2OH_{in} = 1$ $CH_3CHO_{in} = 1$
$CH_3CH_2OH \rightarrow C_2H_4 + H_2O$	(3)	$CH_3CH_2OH_{in} = 2$
$2CH_3CH_2OH \rightarrow (C_2H_5)_2O + H_2O$	(4)	$CH_3CH_2OH_{in} = 2$

In this case, however, the thermodynamics of the ethanol dehydrogenation to acetaldehyde (AcH) would not be considered. Thus, reaction **1** and **2** were used to evaluate the thermodynamic feasibility, even though it is known that reaction 2 does not occur exactly as described.

Table 1.4.1 also shows the ethanol dehydration reactions, which comprise the main competitive steps. For the simulations, reaction temperature was assumed to vary

from 25 to 500 ºC at atmospheric pressure. Figure 1.4.1 shows the Gibbs energy changes for reactions 1-4 (Table 1.4.1), which were computed separately. Values are in good agreement with those reported previously (MAKSHINA *et al.*, 2014, ANGELICI *et al.*, 2013).

From Gibbs energy changes, the ethanol to 1,3-BD conversion is favorable and the ethanol conversion at equilibrium is nearly full above 250 ºC, reaction **2,** as shown in Figures 1.4.1 and 1.4.2. Ethanol dehydrogenation becomes favorable around and above 300 ºC, reaction **1**, as shown in Figure 1.4.1, with ethanol conversion of 97 and 99 % at 450 and 500 ºC, respectively, as shown in Figure 1.4.2. Ethanol dehydration to ethene is favorable throughout the analyzed temperature range, with full conversion slightly above 200 ºC, reaction **3**, as shown in Figures 1.4.1 and 1.4.2. Ethanol dehydration to diethyl ether (DEE) is also favorable, with Gibbs energy changes ranging from -14 to -3 kJ/mol, from 25 to 500 ºC, and ethanol equilibrium conversion decreasing with the temperature increase, reaction **4**, as shown in Figures 1.4.1 and 1.4.2.

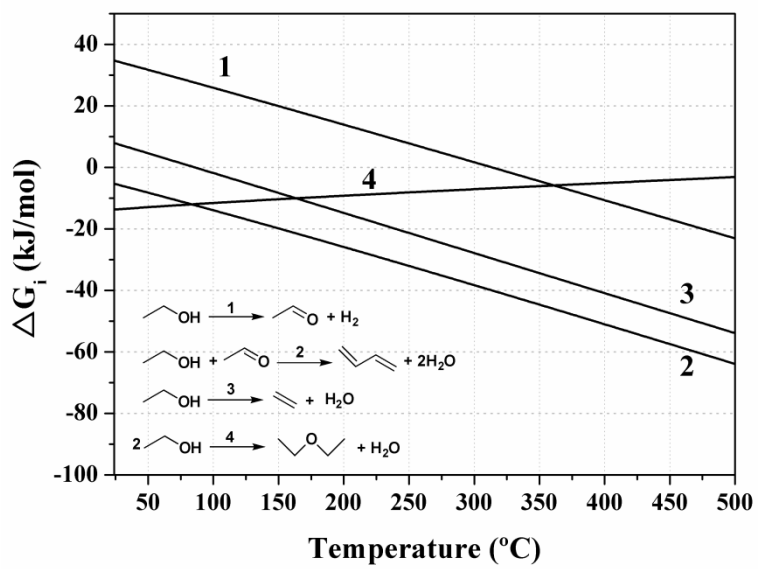

Figure 1.4.1 - Gibbs energy change (ΔG_i) as a function of temperature for reactions 1-4 in Table 1.4.1 at atmospheric pressure and initial compositions described in Table 1.4.1.

The thermodynamics of AcH to 1,3-BD conversion, involving the AcH aldol addition to 3-hydroxybutanal, dehydration to crotonaldehyde, the MPV reduction of crotonaldehyde by ethanol and, finally, the crotyl alcohol dehydration to 1,3-BD steps, has been reported previously (MAKSHINA *et al.*, 2014, ANGELICI *et al.*, 2013,

BHATACHARIA and SANVYAL, 1967). These authors calculated the thermodynamic properties of 3-hydroxybutanal, crotonaldehyde and crotyl alcohol with help of group contribution method (POILING *et al*., 2001).

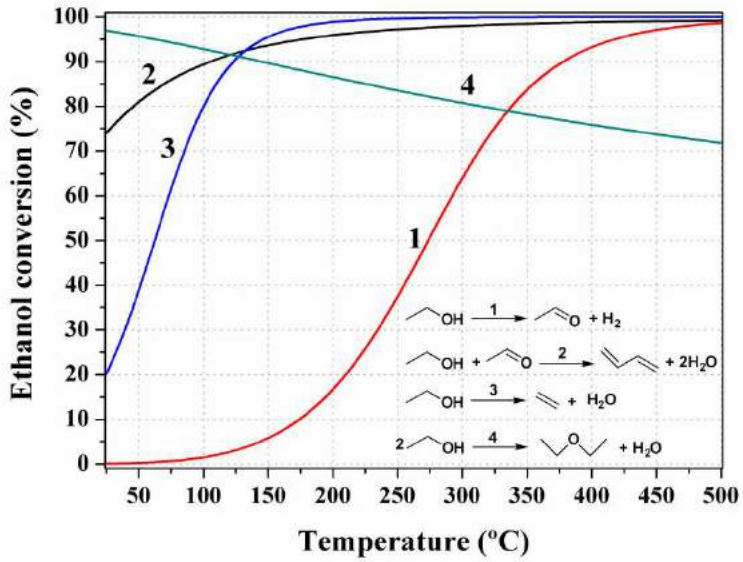

Figure 1.4.2 - Ethanol equilibrium conversions for reactions in Table 1.4.1 at atmospheric pressure and initial compositions as described in Table 1.4.1.

According to the literature, the 3-hydroxybutanal formation is thermodynamically unfavorable (positive Gibbs energy changes were reported between 100 and 500 ºC) (MAKSHINA *et al*., 2014, ANGELICI *et al*., 2013). However, its subsequent dehydration to crotonaldehyde is highly favorable. Thus, even though the overall AcH to crotonaldehyde reaction is thermodynamically less favorable at higher temperatures, the temperature increase cause the increase of the ethanol dehydrogenation rate, so that the AcH in excess can contribute to the aldol addition (MAKSHINA *et al*., 2014, ANGELICI *et al*., 2013).

Moreover, the crotonaldehyde MPV reduction by ethanol was also described to present low Gibbs energy change values (≈ 0) (MAKSHINA *et al*., 2014, ANGELICI *et al*., 2013). However, it was observed that an excess of ethanol (higher ethanol to crotonaldehyde ratios) can shift crotonaldehyde conversion to higher values. Finally, the crotyl alcohol dehydration to 1,3-BD was found to be thermodynamically favored (MAKSHINA *et al*., 2014).

When all reactions in Table 1.4.1 are considered simultaneously (or, when the following compounds are allowed to be present at the equilibrium: ethanol, ethene,

DEE, H_2O, AcH, H_2 and 1,3-BD), ethanol conversion is complete above 250 ºC. Figure 1.4.3(a) shows the molar fractions of products and the ethanol conversion for this scenario, using a feed of comprising 2 mols of ethanol. Figure 1.4.3(b) shows the composition distribution excluding water and hydrogen. This figure emphasizes that ethene is the most thermodynamically stable product. Thus, ethanol dehydration must be suppressed kinetically in order to increase the 1,3-BD yield (MAKSHINA *et al.*, 2014), by tuning catalyst active sites.

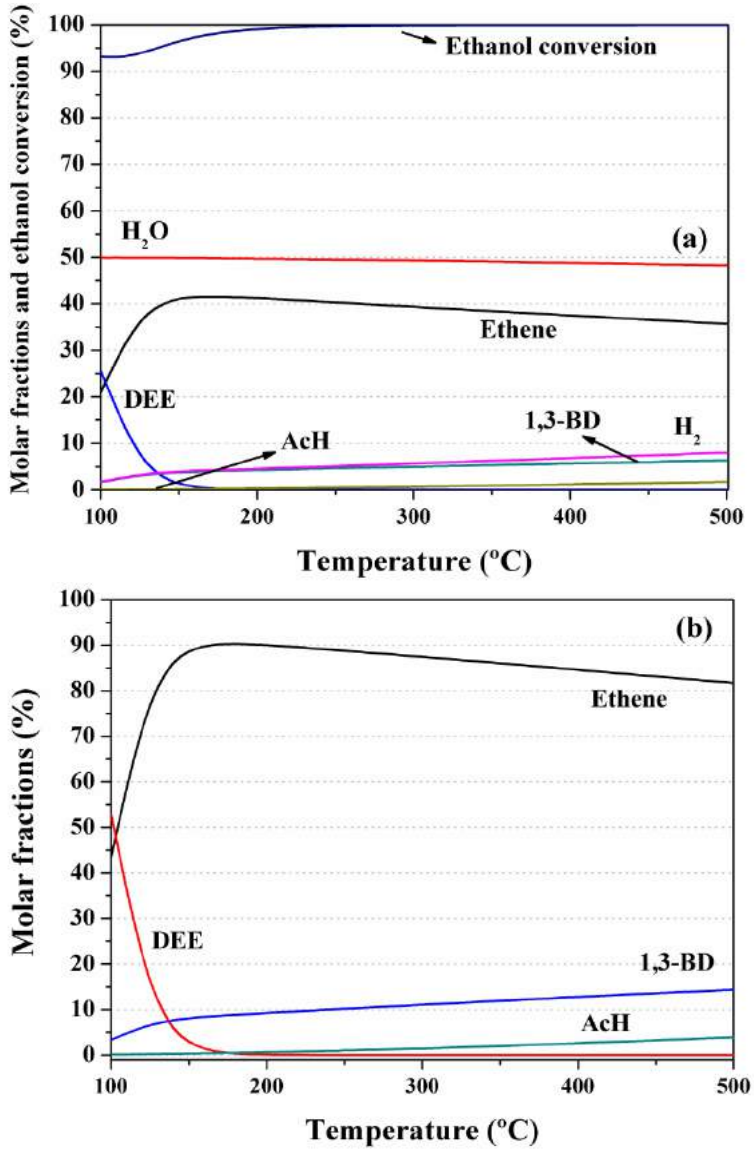

Figure 1.4.3 – Equilibrium composition at 1 atm, using pure ethanol as reactant (2 mols). The following compounds were allowed to be present at the equilibrium: ethanol, ethene, DEE, H_2O, AcH, H_2 and 1,3-BD. In (a), molar fractions were calculated excluding ethanol; in (b), molar fractions were calculated excluding ethanol, water and hydrogen.

The effect of AcH addition to the ethanol feed was reported as thermodynamically insignificant, when equilibrium compositions obtained from feed streams containing a mixture of ethanol and AcH (at the ethanol to AcH molar ratio of 3) and pure ethanol were compared to each other (MAKSHINA *et al*., 2014).

However, as data presented by MAKSHINA *et al*. (2014) showed a slight increase of the 1,3-BD molar fraction when AcH was mixed considered with ethanol in the feed stream, and as experimental data indicates that co-feeding of ethanol and AcH can enhance the 1,3-BD yield (CORSON *et al*., 1949, JONES *et al*.; 2011), the effect of the ethanol to AcH molar fraction on equilibrium compositions was also evaluated here. For these calculations, all compounds in Table 1.4.1 were allowed to vary simultaneously, and the initial number of mols was always equal to 2. Thus, for instance, at the AcH composition of 20 mol %, 0.4 mols of AcH and 1.6 mols of ethanol were used as initial reactants in the simulations. Figure 1.4.4 shows a point of maximum for the number of 1,3-BD mols produced as a function of the AcH content in the feed.

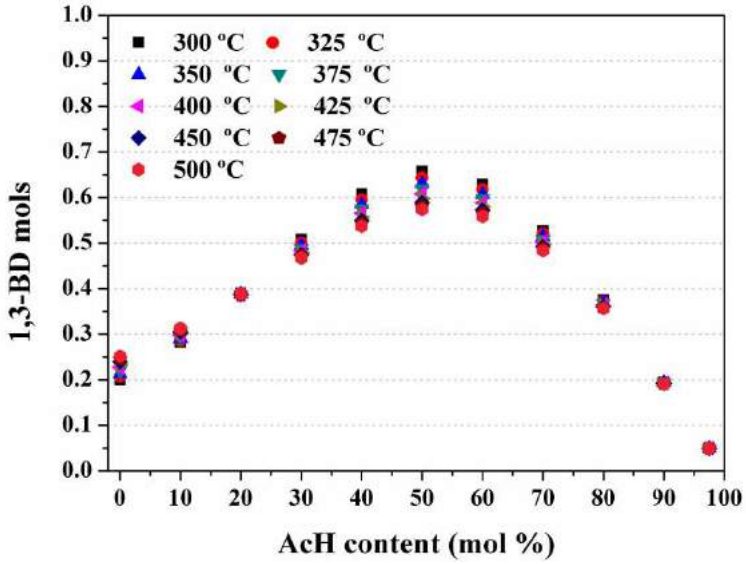

Figure 1.4.4 – Effect of the AcH feed content (0 % represents pure ethanol = 2 mols) on 1,3-BD mols produced at different temperatures at 1 atm. The following compounds were allowed to be present at the equilibrium: ethanol, ethene, DEE, H_2O, AcH, H_2 and 1,3-BD.

It could be expected that the 1 to 1 ethanol to AcH feed ratio would result in the higher 1,3-BD formation, given the stoichiometry of reaction 2 (Table 1.4.1). However, one must note that all compounds in Table 1.4.1 were considered simultaneously in the equilibrium calculations. Thus, co-feeding of AcH shifts the ethanol conversion to 1,3-

BD, suppressing ethene formation at equilibrium. Besides, one must note that the number of 1,3-BD mols represented in the *y* axis of Figure 1.4.4 is also a measure of the 1,3-BD yield.

Even though aldol condensation, MPV reduction of crotonaldehyde and crotyl alcohol dehydration reactions were not considered in the simulations (due to lack of thermodynamic properties for these compounds), results presented in Figure 1.4.4 are in agreement with experimental observations in the sense that there is an optimum ethanol to AcH molar ratio (CORSON *et al*., 1949, JONES *et al*., 2011). However, as commented in Section 1.2, a higher rate of carbonization (coke formation leading to catalyst deactivation) was observed when higher AcH contents were used experimentally (CORSON *et al*., 1949).

Figure 1.4.5 shows a comparison between Gibbs energy changes for the ethanol to 1,3-BD conversion considering three overall reactions. Here, the overall reaction pathway Eq. (1.4.1) was included as reaction **1**. Its feasibility is confirmed by the negative values obtained in the temperature range studied. The Prins reaction, which was suggested as a possible route to produce 1,3-BD (GRUVER *et al*, 1995) from AcH and ethene, is indicated as reaction **3**. It can be seen that such pathway is thermodynamically possible within the temperature range, but less probable because of the much lower 1,3-BD yields and selectivities.

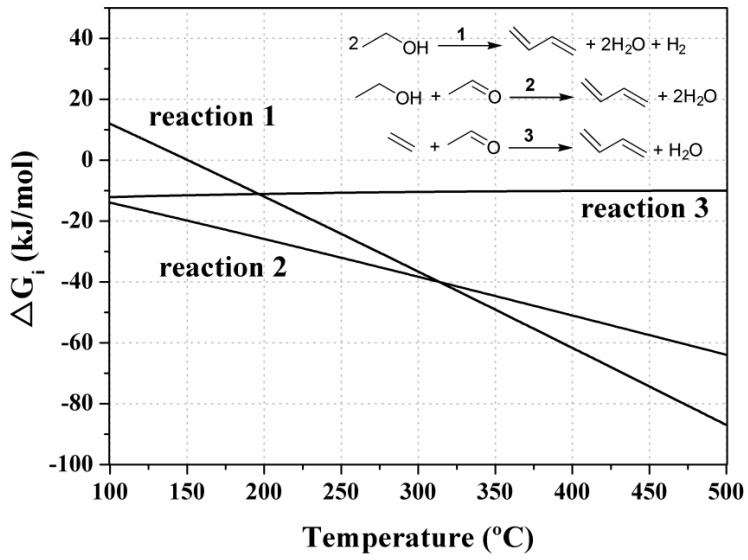

Figure 1.4.5 - Gibbs energy changes as a function of temperature at atmospheric pressure and using pure ethanol in the feed.

Equilibrium compositions were also studied considering the presence of butene in the reaction system, as described in Table 1.4.2. Butene formation must be kinetically avoided, since formation of butene is thermodynamically more favorable than formation of 1,3-BD, as shown in Figure 1.4.6 and also indicated by MAKSHINA *et al*. (2014).

Table 1.4.2 – Alternative reaction set considered for equilibrium composition calculations.

$CH_3CH_2OH + CH_3CHO \rightarrow C_4H_6 + 2H_2O$	(1)
$CH_3CH_2OH \rightarrow CH_3CHO + H_2$	(2)
$CH_3CH_2OH \rightarrow C_2H_4 + H_2O$	(3)
$2CH_3CH_2OH \rightarrow (C_2H_5)_2O + H_2O$	(4)
$C_4H_6 + H_2 \rightarrow C_4H_8$	(5)

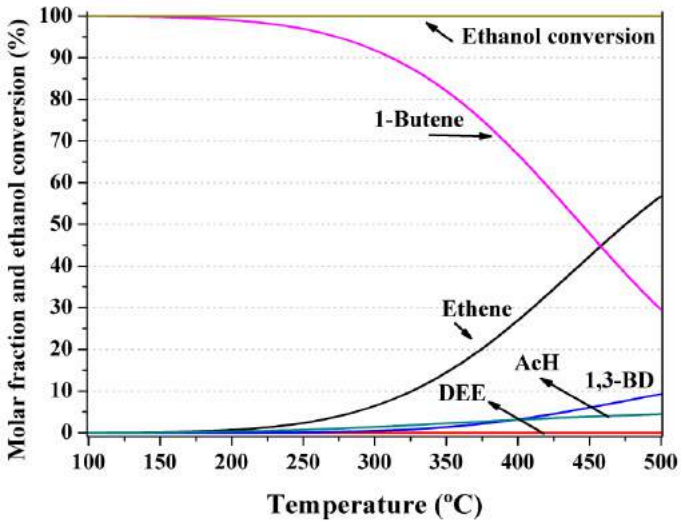

Figure 1.4.6 – Equilibrium composition at 1 atm, using 2 mols of ethanol as reactant. All compounds in Table 1.4.2 were allowed to vary simultaneously. Molar fractions were calculated excluding ethanol, water and hydrogen.

A thermodynamic consideration is necessary for crotonaldehyde reduction. Particularly, it was evaluated whether H_2 could affect the crotonaldehyde reduction step through a competitive reaction step. BHATTACHARYYA and SANYAL (1967) reported Gibbs energy changes at 380 and 460 ºC, as shown in Table 1.4.3. ANGELICI *et al*. (2013) presented Gibbs energy change for the same reactions at 400 and 425 ºC, as shown in Table 1.4.4. Thus, it has been agreed that the crotonaldehyde reduction by ethanol constitutes the most probable route.

Co-feeding of ethanol and crotonaldehyde resulted in higher AcH amounts than expected when AcH is produced only through ethanol dehydrogenation. Thus, this was described as an experimental evidence for the occurrence of MPV reduction by ethanol, since this route produces AcH, explaining the AcH excess (BHATTACHARYYA and SANYAL, 1967).

Table 1.4.3 – Gibbs energy changes for the crotonaldehyde reduction by ethanol and hydrogen, as reported by BHATTACHARYYA and SANYAL (1967).

Reaction	***ΔG (kJ/mol)***		
	25 ºC	380 ºC	460 ºC
$C_3H_5CHO + CH_3CH_2OH \rightarrow C_4H_6 + CH_3CHO + H_2O$	7.1	-30.5	-38.9
$C_3H_5CHO + H_2 \rightarrow C_4H_6 + H_2O$	-	-21.3	-20.9

Table 1.4.4 – Gibbs energy changes for the crotonaldehyde reduction by ethanol and hydrogen, as reported by ANGELICI *et al*. (2013).

Reaction	***ΔG (kJ/mol)***		
	25 ºC	400 ºC	425 ºC
$C_3H_5CHO + CH_3CH_2OH \rightarrow C_4H_6 + CH_3CHO + H_2O$	2.2	-1.2	-1.4
$C_3H_5CHO + H_2 \rightarrow C_4H_6 + H_2O$	-32.5	9.0	11.9

Although values reported by different authors present some discrepancies, probably associated to the different calculation methods employed, the important information is that the reaction that involves H_2 presents less negative Gibbs energy changes, so that this competitive route is less favorable.

Finally, Figure 1.4.7 shows the effect of undesired products on 1,3-BD thermodynamic yield, Y_{BD}, calculated with Eq. (1.4.2), where $N_{BD,out}$ is the number of 1,3-BD mols at the equilibrium and $N_{EtOH,in}$ is the initial ethanol number of mols.

$$Y_{BD}(\%) = \frac{\mathrm{N_{BD,out}} \cdot 200}{N_{EtOH,in}} \qquad (1.4.2)$$

These calculations were performed using the Gibbs energy minimization method, described in Appendix A. When AcH, 1,3-BD, H_2, H_2O, ethene, diethyl ether

and 1-butene are considered as reaction products, the 1,3-BD thermodynamic yield is the smallest possible, equal to 13 % at 500 ºC (line *a*, Figure 1.4.7).

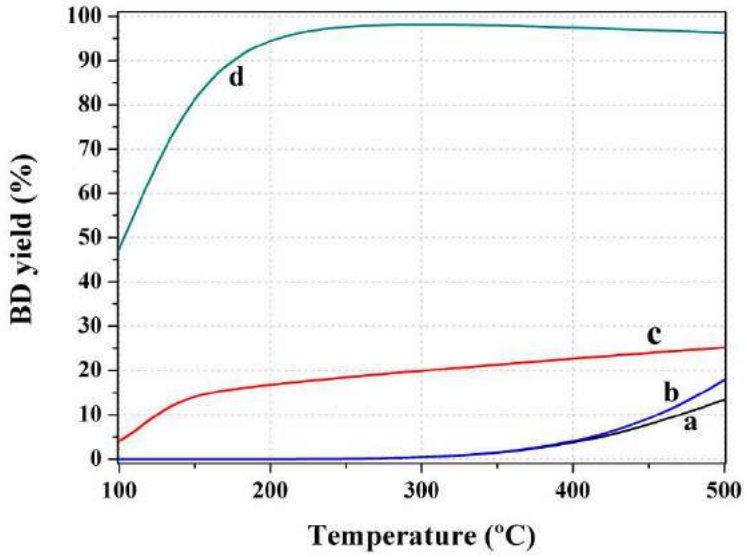

Figure 1.4.7 –Equilibrium 1,3-BD yields at atmospheric pressure using 2 mols of ethanol as reactant. Compounds considered in the simulation: (a) ethanol, AcH, 1,3-BD, H_2, H_2O, ethene, DEE, and 1-butene; (b) ethanol, AcH, 1,3-BD, H_2, H_2O, and 1-butene; (c) ethanol, AcH, 1,3-BD, H_2, H_2O, ethene and DEE; (d) ethanol, AcH, 1,3-BD, H_2, H_2O. 1,3-BD yield was calculated as Eq. (1.4.2).

If ethene and DEE formation can be avoided, 1,3-BD yield reaches 18 % at 500 ºC (line *b*). On the other hand, if the formation of 1-butene can be suppressed, then 1,3-BD yield reaches 25 % at 500 ºC (line *c*). Finally, when formation of ethene, DEE and 1-butene is not allowed, 1,3-BD becomes the most favored containing carbon product (line *d*).

1.4.2 Final Comments

This chapter showed that the ethanol to 1,3-BD conversion is thermodynamically feasible. It was verified that co-feeding of acetaldehyde can lead to increase of 1,3-BD yield at thermodynamic equilibrium. Furthermore, the reaction temperature window with higher yields is between 350 and 500 ºC. However, ethene and butene formation is more favored. Thus, ethanol dehydration and butene formation must be suppressed kinetically in order to obtain higher 1,3-BD yield.

1.5 Experimental Fluctuations and Experimental Design

1.5.1 Experimental Fluctuations Characterization

As discussed in the previous sections, in order to produce 1,3-BD from ethanol, special catalysts are required, as the conversion of ethanol into 1,3-BD involves a complex network of consecutive reactions, which must be promoted by distinct active sites. The ideal catalyst should contain both basic and acidic sites, distributed homogeneously throughout the catalyst surface (MAKSHINA *et al*., 2012). However, ethanol dehydration to ethene and diethyl ether are also expected to constitute an undesired competitive reaction, due to the presence of acidic sites on the catalyst surface. Thus, considerable effort has been concentrated on the careful catalyst design (MAKSHINA *et al*., 2014) for proper balancing of obtained reaction products, with much less attention dedicated to effects of operation variables (such as temperature, pressure and compositions) on the overall process performance for a particular catalyst.

In spite of that, the appropriate design, optimization and control of the overall reaction process require the adequate description of reaction phenomena with help of mathematical models, in order to represent the underlying relationships among independent (for instance, reaction temperature, feed concentration and residence time) and dependent variables (for instance, ethanol conversion and 1,3-BD selectivity). Besides, the kinetic mechanism can be better understood when more fundamental rate equations can be proposed, allowing for estimation of kinetic parameters and equilibrium constants (FROMENT *et al*., 2011).

During the model building process, model parameters must be estimated using the available experimental data. This process involves the minimization of an objective function that measures the distance between model predictions and observed experimental results. When experimental data follow the normal distribution and the independent variables are known with good precision, the objective function can usually be written in the form (SCHWAAB *et al*., 2008, BARD, 1974):

$$S(\boldsymbol{\theta}) = (\mathbf{y}^{*} - \mathbf{y}^{\mathbf{e}})^{T} \mathbf{V}^{-1} (\mathbf{y}^{*} - \mathbf{y}^{\mathbf{e}}) \tag{1.5.1}$$

where $\mathbf{y}^*$ is the vector of model responses, $\mathbf{y}^e$ is the vector of experimental responses and $\mathbf{V}$ is the covariance matrix of experimental fluctuations. Since model responses must be described as functions of the independent variables, $\mathbf{x}^*$, and of the model parameters, $\boldsymbol{\theta}$, as

$$\mathbf{y}^* = f(\mathbf{x}^*, \boldsymbol{\theta}) \tag{1.5.2}$$

the minimization of Eq. (1.5.1) in fact requires the determination of the parameter values that lead to the point of minimum of the objective function defined by Eq. (1.5.1). However, as the experimental data contain unavoidable experimental uncertainties, parameter estimates are also uncertain to some extent. The parametric uncertainties are usually calculated with help of the covariance matrix of the parameter estimates, $\mathbf{V}_\theta$, defined as

$$\mathbf{V}_\theta = [\mathbf{B}^T \mathbf{V}_y^{-1} \mathbf{B}]^{-1} \tag{1.5.3}$$

where $\mathbf{B}$ is the sensitivity matrix that contains the first derivatives of the model responses in respect to the model parameters (SCHWAAB *et al.*, 2008, BARD, 1974). As the model parameters are uncertain, model predictions are also subject to uncertainties, which can be calculated in the form (LARENTIS *et al.*, 2003, SCHWAAB *et al.*, 2008b):

$$\mathbf{V}_y = \mathbf{B} \mathbf{V}_\theta \mathbf{B}^T \tag{1.5.4}$$

As a consequence, the precise determination of experimental fluctuations is of fundamental importance for model building and evaluation of model adequacy, although careful determination of experimental errors is frequently overlooked in most kinetic studies.

It is also important to emphasize that available experimental data can often be explained by different mechanistic interpretations, particularly during the initial steps of investigations performed in the field of catalysis (FROMENT *et al.*, 2011,

KNÖZINGER *et al*., 1973). In this case, experimental design techniques can be employed for discrimination among rival models (SCHWAAB *et al*., 2006 and 2008b). The main idea behind these techniques is to perform experiments at conditions that can lead to the maximum difference among the responses of the rival models, making model discrimination easier. In order to do that, different design criteria have been proposed in the literature (SCHWAAB *et al*., 2006 and 2008b, ALBERTON *et al*., 2011). For instance, SCHWAAB *et al*. (2006) proposed the use of a discriminating function between rival models *m* and *n* that takes into account the probabilities P_m and P_n for the analyzed models to be the correct ones, in the form:

$$D_{m,n}(\mathbf{x}) = (P_m P_n)^z [\hat{\mathbf{y}}_m(\mathbf{x}) - \hat{\mathbf{y}}_n(\mathbf{x})]^T \mathbf{V}_{m,n}^{-1} \times [\hat{\mathbf{y}}_m(\mathbf{x}) - \hat{\mathbf{y}}_n(\mathbf{x})] \tag{1.5.5}$$

where *z* is a parameter used to modulate the relative importance of the rival models, $\hat{\mathbf{y}}_m$ is a vector of response variables for model *m* and $\mathbf{V}_{m,n}$ is defined as

$$\mathbf{V}_{m,n} = 2\mathbf{V}(\mathbf{x}) + \mathbf{V}_m(\mathbf{x}) + \mathbf{V}_n(\mathbf{x}) \tag{1.5.6}$$

where $\mathbf{V}$ is the covariance matrix of experimental fluctuations and $\mathbf{V}_m$ is the covariance matrix of model responses calculated for model *m* with Eq. (1.5.4). In order to find the maximum value of Eq. (1.5.5) (and the best set of experimental conditions for model discrimination), independent variables $\mathbf{x}$ must be manipulated with help of a numerical procedure. Once more, the detailed characterization of experimental fluctuations, contained in the covariance matrix $\mathbf{V}$, is of paramount importance during the model building process.

Usually, experimental fluctuations are assumed to be independent from each other and constant throughout the experimental region. These hypotheses allow for significant simplification of the objective function defined in Eq. (1.5.1), as the matrix $\mathbf{V}$ becomes diagonal and independent of the experimental conditions. However, it has been demonstrated that the use of such assumptions with no previous experimental evidence may lead to inconsistent kinetic conclusions (LARENTIS *et al*., 2003). Additionally, the proper characterization of the covariance matrix is fundamental for computation of accurate kinetic parameters (LARENTIS *et al*., 2003, ALBERTON *et al*., 2009).

It is also important to observe that characterization of *V* can also allow for detailed observation of local kinetic phenomena, defined here as microkinetic analysis (LARENTIS *et al*., 2003). The idea is simple and appealing: if the experimental fluctuations are not independent and are not constant (which can only be assured if detailed characterization of error fluctuations is performed), then the fluctuations of the distinct analyzed variables affect one another, revealing the underlying local reaction mechanism. The use of the words *"local"* and *"microkinetic"* can be justified by the low magnitude of the error fluctuations when replicates are performed. For instance, these error fluctuations can be present due to small deviation in the catalyst mass used in replicates and, since catalyst mass affect all reactions simultaneously, the deviations in the replicates are connected with the particular reaction mechanism that is occurring on the catalyst surface. As a consequence, the covariance matrix of error fluctuations contains information about the experimental errors and about the underlying kinetic mechanism, which can be used for model building and kinetic interpretation (LARENTIS *et al*., 2003).

1.5.2 Experimental Design

As commented in the previous section, experimental data can often be explained by different mechanistic interpretations. In this case, it is necessary to design new experiments to discriminate among candidate models. Figure 1.5.1 illustrates the process of experimental sequential design which might be used for this purpose (SCHWAAB and PINTO, 2011, ALBERTON, 2010).

In the first stage, an initial set of experiments is performed, allowing the parameter estimation of the model candidates. Then, the quality of each model is evaluated. If more than one model is able to explain experimental data satisfactorily, it is necessary to perform new experiments. These new experiments are usually performed sequentially and designed according to a discrimination criterion. The new experiment is then carried out and the information obtained is added into the initial experimental set. Models parameters are re-estimated and the model quality is checked again. The process stops when only one model can adjust experimental data or when it is concluded that discrimination cannot be achieved. In this case, proposed models, ranges

of independent variables and the magnitude of the experimental fluctuations must be revised (SCHWAAB and PINTO, 2011).

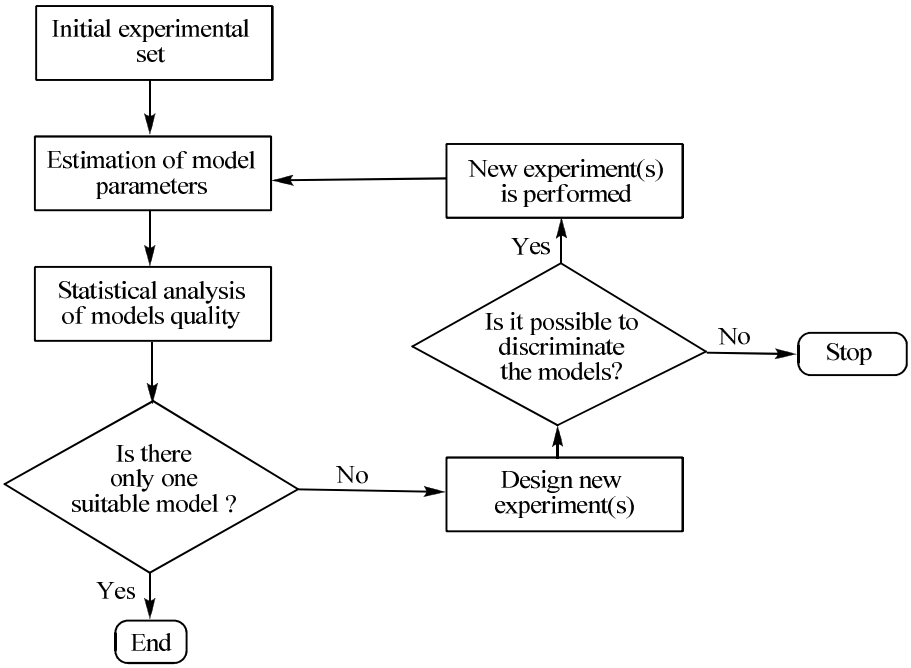

Figure 1.5.1 – Sequential experimental design steps for model discrimination (SCHWAAB and PINTO, 2011).

Some previous studies have investigated the kinetic aspects of the ethanol to 1,3-BD conversion; however, without sufficient support of statistical analyses (JONES *et al.*, 1949, EZINKWO *et al.*, 2014). Furthermore, the effects of common reaction variables, such as temperature and contact time, on ethanol to 1,3-BD reaction performance have been usually studied using the "change-one-factor-at-a-time" method; that is, one variable is changed while the other experimental conditions are kept constant (KVISLE *et al.*, 1988, MAKSHINA *et al.*, 2012, SUSHKEVICH *et al.*, 2014, JANSSENS *et al.*, 2015, BHATTACHARYYA and SANYAL, 1967, BHATTACHARYYA and GANGULY 1962a-b). Based on this method, it has been found that temperature exerts an important nonlinear effect on 1,3-BD yields, as observed with different catalysts (SUSHKEVICH *et al.*, 2014, LARINA *et al.*, 2015, JANSSENS *et al.*, 2015, BHATTACHARYYA and GANGULY 1962a-b). Similar studies have shown that the weight hourly spatial velocity (WHSV) also modifies 1,3-BD yields and selectivities (SUSHKEVICH *et al.*, 2014, LARINA *et al.*, 2015, JANSSENS *et al.*, 2015, BHATTACHARYYA and SANYAL, 1967,

BHATTACHARYYA and GANGULY 1962a-b). Usually, enhancement of 1,3-BD selectivities (SUSHKEVICH *et al*., 2014, LARINA *et al*., 2015) and yields (LARINA *et al*., 2015, BHATTACHARYYA and SANYAL, 1967) could be observed when the WHSV was reduced, suggesting the positive effect of contact times on reaction yields, as one might already expect. However, nonlinear effects of ethanol flow rates on 1,3-BD yields were verified over different single and binary metal oxides (such as MgO, ZrO_2, Al_2O_3-MgO, Al_2O_3-Fe_2O_3, Al_2O_3-Cr_2O_3 and ZrO_2-Fe_2O_3) (BHATTACHARYYA and GANGULY 1962a-b).

One of the main drawbacks associated with the "change-one-factor-at-a-time" method is the fact that the influence observed for the particularly analyzed variable may not be the same when some of the remaining experimental conditions change (NELE *et al*., 1999). This can occur because variables may interact with each other, resulting in unexpected nonlinear effects (NELE *et al*., 1999). Such interaction effects can only be identified when variables are investigated and manipulated simultaneously. Statistical experimental design techniques, such as factorial designs, overcome this drawback, allowing for identification and quantification of the distinct main variable effects and variable interaction effects.

In a factorial design, experimental conditions are uniformly distributed over the experimental region and, after the definition of experimental conditions for each variable, all possible combinations among variable experimental conditions are defined as experiments. In its simplest structure, the factorial design defines two levels of observation for each variable and combines the defined levels among all variables. In this case, for instance, the study of two variables results in four experiments, the study of three variables results in eight experiments, and the number of experiments increases with the number of variables, as defined in Eq.(1.5.7) (SCHWAAB and PINTO, 2011).

$$NE = NL^{NX} \tag{1.5.7}$$

In order to make easier the calculation of variable effects, variables are normalized, modifying the upper and lower experimental conditions to +1 and -1. When two levels are employed for each variable, only linear and interaction effects can be quantified. Thus, additional experiments must be designed in order to verify the existence of non-linear effects (BOX *et al*., 1978, SCHWAAB and PINTO, 2011).

The use of factorial designs presents the particular advantage of allowing the maximization of the information content of the experimental data set, as variable effects can be computed with minimum uncertainty (EDGAR *et al*., 2001, LARENTIS *et al*., 2001). In this case, mathematical models can be developed to correlate with maximum efficiency the independent (such as reaction temperature, feed concentration and contact time) and dependent variables (such as ethanol conversion and 1,3-BD selectivity), making data interpretation easier and more robust.

Besides, the phenomenological approach usually leads to very large number of model parameters, making their estimation difficult (LARENTIS *et al*., 2001, PINTO *et al*., 2011, SCHWAAB *et al*., 2008). For this reason, the empirical modelling of reaction data, with help of sound statistical tools, may be much more efficient for analysis and optimisation of complex catalytic processes, as the use of empirical mathematical tools is relatively simple and much less time consuming (LARENTIS *et al*., 2001, CALLEJA *et al*., 1995). Regardless, the initial set of experiments designed statistically may be used afterwards as the initial set of experiments, as illustrated in Figure 1.5.1.

1.5.3 Final Comments

Despite the clear importance of the characterization of the covariance matrix of experimental fluctuations, as required by the parameter estimation procedures used for model building and experimental design techniques used for model discrimination, no proper characterization of experimental fluctuations involved in the ethanol to 1,3-BD conversion has been performed yet. Besides, no proper mathematical modeling of this reaction system has been developed yet. Experimental design techniques, such as factorial designs, can be very useful to quantify the effects of independent variables on the dependent variables. Regardless, no work has employed this technique for investigation of the ethanol to 1,3-BD reaction.

2. OBJECTIVES

Two main objectives were pursued in the present work. The first objective was to develop new catalysts for the ethanol to 1,3-BD conversion. The second main objective was to study the reaction kinetics and identify the reaction rate-limiting step.

Within the first main objective, the most important specific objectives are described below.

1.1 To study the co-precipitation method for the preparation of magnesium silica oxide catalysts with different Mg-to-Si molar ratios, for use in ethanol to 1,3-BD reactions;

1.2 To investigate the possible advantages of doping magnesium silica oxide catalysts with dehydrogenating metal oxides, such as ZnO and ZrO_2;

1.3 To evaluate the role of catalyst acidity on ethanol to 1,3-BD conversion, while using the co-precipitation catalyst preparation method, by modifying catalyst acidity through addition of alkali metals, such as Na, K and Li, to the final materials.

Within the second main objective, the most important specific objectives are described below.

1.1 To characterize the covariance matrix of experimental fluctuations of product compositions from ethanol conversion reactions performed over $MgO\text{-}SiO_2$ systems, determining the effect of reaction conditions and catalyst properties on the covariance matrix of experimental fluctuations and analyzing the kinetic information contained in the covariance matrix of experimental fluctuations.

1.2 To evaluate the effects of operation variables, such as temperature and ethanol flow rate, on reaction performance with help of a full factorial design technique, with emphasis on the 1,3-BD productivity (in $g_{BD}/g_{cat}.h$), an important variable for real industrial applications.

3. MATERIALS AND METHODS

3.1 Catalyst Preparation

3.1.1 MgO-SiO_2 preparation

In a typical synthesis, catalysts at the Mg:Si molar ratio of 25:75, 50:50, 75:25 and 95:5 were prepared by co-precipitation. For the 50:50 material, 9.01 g of SiO_2 (Sigma-Aldrich, purity of 99.8 %, average particle size between 0.2-0.3 μm and surface area equal to 200 ± 25 m^2/g, code product S5505) was dissolved in 100 mL of 1.2 M NaOH solution (Sigma-Aldrich, purity of 99 %). The mixture was kept under heating (100 ºC) under vigorous stirring until complete SiO_2 dissolution. The solution was cooled and 42.4 g of Na_2CO_3 (Sigma-Aldrich, purity of 99.9 %) were added. A $Mg(NO_3)_2 \cdot 6H_2O$ solution (Sigma-Aldrich, purity of 99 %) was added drop-wise into this mixture under constant stirring at 25 °C (38.85 g of $Mg(NO_3)_2 \cdot 6H_2O$ in 200 mL). The pH was maintained at 10.5 by adding appropriate quantities of 1.2 M NaOH solution and, at the end of the process, the solution volume was adjusted to 600 mL with addition of deionized water. The resulting mixture was stirred for 2 h and aged for 22 h at 25 °C. Finally, the mixture was filtrated and washed with 7.5 L of boiling water. The precipitate was dried at 80 °C for 24 h before grinding. Materials were calcined in air at 500 °C for 4 h, using a heating rate of 5 °C/min. For the different Mg to Si molar ratios, the combined Mg and Si concentration was always equal to 0.5 M. Variations from this method were studied as described in Section 4.1. Otherwise, the method employed was performed as described above. Samples were labeled as MgO-SiO_2-*x*, where *x* represents the Mg:Si molar ratio.

3.1.2 ZnO and ZrO_2 containing MgO-SiO_2 systems

In order to produce materials with 1.5 and 0.5 wt. % of Zr(IV) and Zn(II), respectively, 0.57 g of $ZrO(NO_3)_2 \cdot H_2O$ (Sigma-Aldrich, purity of 99 %) and 0.24 g of $Zn(NO_3)_2 \cdot 6H_2O$ (Sigma-Aldrich, purity of 98 %) were dissolved in 50 mL of deionized water, and the solution was added to 10 g of the MgO-SiO_2-*x* system. The solution was stirred at room temperature until the mixture was completely dry. Finally, the solid was calcined in air at 500 °C for 5 h. These samples were labeled as ZrZn/MgO-SiO_2-*x*, where *x* represents the Mg:Si molar ratio.

3.1.3 Alkali metals addition

ZrZn/MgO-SiO_2-*(50:50)* catalysts were modified through addition of alkali metals. For the Na doping, the appropriate volume of 1.2 M NaOH solution was added to the final catalyst drop-wise. For instance, in order to produce materials with 1.2 wt. % of Na, 1.321 mL of the 1.2 M NaOH solution were added to 3.0 g of catalyst with help of a volumetric pipette. The mixture was kept under stirring during 1 h at 25 °C before drying at 80 °C for 5.5 h and finally calcined in air at 500 °C for 5 h (5ºC/min). KOH (Sigma-Aldrich, containing 10 wt. % of water) and $LiOH \cdot H_2O$ (Alfa Aesar, purity of 99 %, product code A15519) were used instead of NaOH for comparison. The overall catalyst preparation procedure is illustrated in Figure 3.1.1. Samples were labelled as *y-Me*/ZrZn/MgO-SiO_2-*(50:50)*, where *y* denotes the content of the alkali metal *Me* in weight %.

3.1.4 K_2O:ZrO_2:ZnO/MgO-SiO_2 (50:50) preparation

As it will be discussed in Section 4.3, one catalyst with superior 1,3-BD activity was produced when potassium was used as the alkali metal. Besides, it was verified that the removal of calcination steps 1 and 3 from Figure 3.1.1 resulted in a catalyst that presented the best performance to 1,3-BD. Thus, for the sake of clarity, the preparation of this catalyst is illustrated in Figure 3.1.2.

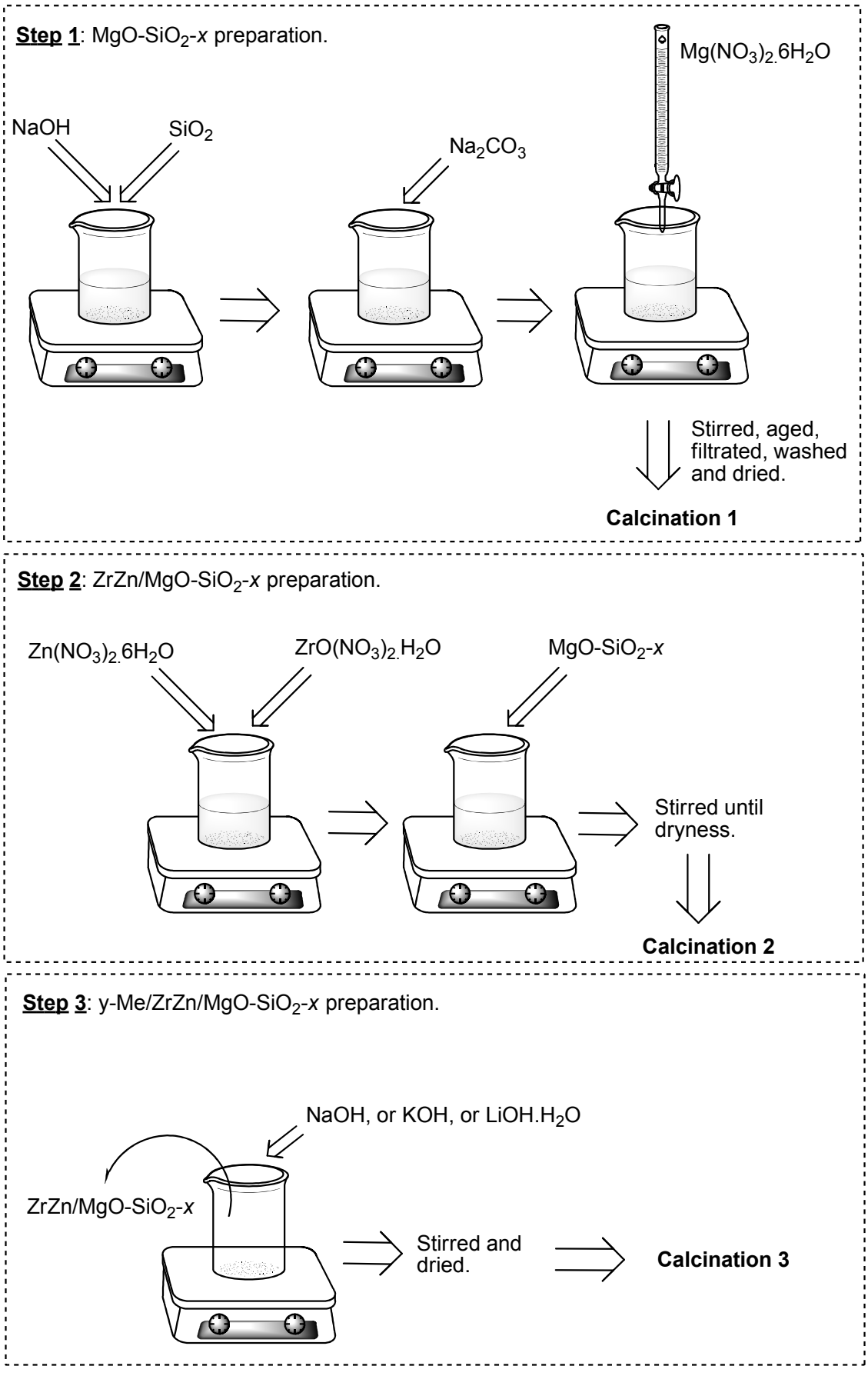

Figure 3.1.1 – Schematic representation of the catalyst preparation.

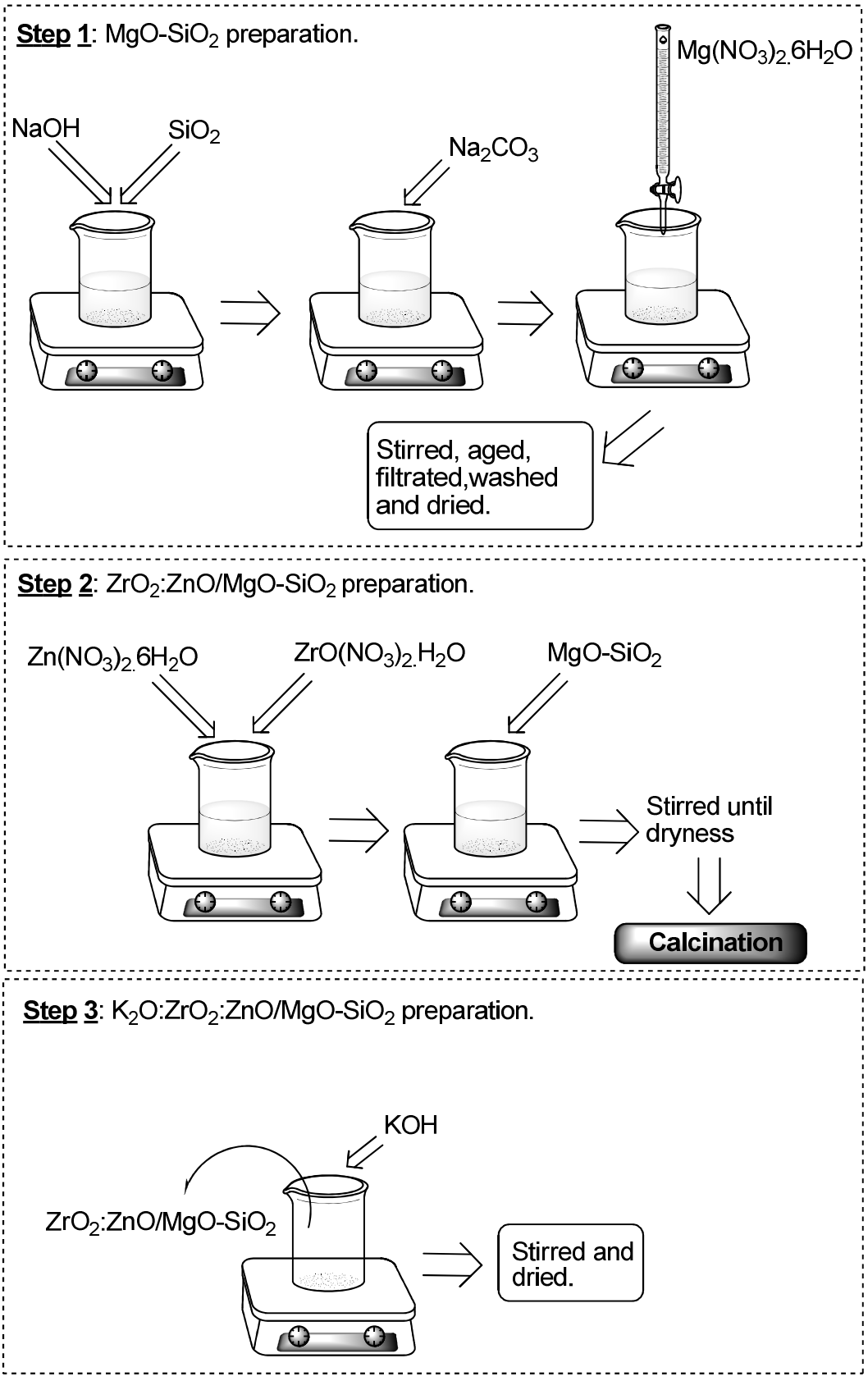

Figure 3.1.2 - Schematic representation of the K_2O:ZrO_2:ZnO/MgO-SiO_2-(50:50) catalyst preparation procedure.

3.1.5 Other catalysts

In order to compare the performance of catalysts prepared in the present with catalysts reported previously in the literature, two other catalysts were prepared, which were described as suitable materials for the ethanol to 1,3-BD reaction (JONES *et al*., 2011, MAKSHINA *et al*., 2012).

The first catalyst was constituted by CuO, ZrO_2 and ZnO containing silica, labelled as CuZrZn/SiO_2, which was suggested for the ethanol to 1,3-BD reaction by JONES *et al*., (2011) and BAERDEMAEKER *et al*., (2015). In order to produce a final material loaded with 1 wt. % of Cu, 1 wt. % of Zr and 0.5 wt. % of Zn, 0.327, 0.387 and 0.239 g of $Cu(CO_2CH_3)_2 \cdot H_2O$ (Sigma-Aldrich, purity of 99%), $ZrO(NO_3)_2 \cdot H_2O$ (Sigma-Aldrich, purity of 99 %), and $Zn(NO_3)_2 \cdot 6H_2O$ (Sigma-Aldrich, purity of 98 %), respectively, were added to 200 mL of deionized water. After complete dissolution of the metal salts, under constant stirring, 10 g of SiO_2 (Davisil grade 645, 35-65 Mesh, with pore diameter of 150 Å and purity of 99 %) were added to the solution. The slurry mixture was kept under stirring until the water was evaporated. The powder was then dried in an oven at 80 ºC during three hours before being calcined at 500 ºC for 5 hours, using a heating rate of 5 ºC/min.

The second catalyst was constituted by CuO containing MgO-SiO_2 system. The preparation procedure was adaptated from MAKSHINA *et al*. (2012). In this procedure, 8.0 g of MgO (Sigma-Aldrich, purity of 99%) and 5.96 g of SiO_2 (Davisil grade 635, with pore diameter of 60 Å, 35-65 Mesh and purity of 99%) were added to 42 mL of deionized water at room temperature. The slurry mixture was kept under stirring until the water was evaporated before being dried at 80 ºC during four hours. In a separated becker, 0.991 g of $Cu(CO_2CH_3)_2 \cdot H_2O$ (Sigma-Aldrich, purity of 99%) were dissolved in 60 mL of deionized water under constant stirring. To this mixture, the previously ground MgO-SiO_2 powder was added and the resulting mixture was stirred until the water was evaporated. The dried powder was finally calcined at 500 ºC during 4 hours, using a heating rate of 5 ºC/min. One must to note that similar Mg to Si molar ratio, equal to 2, and Cu to Si molar ratio, equal to 0.05, were employed, as suggested by MAKSHINA *et al*. (2012).

3.2 Catalyst Characterization

3.2.1 Physical Characterization

Scanning electron microscopy (SEM) and energy-dispersive X-ray spectroscopy (EDX) analyses were carried out on a JEOL6480LV at 20 kV. Energy-dispersive X-ray spectroscopy was carried out *in-situ* during the SEM analyses. At least 5 different spots were selected for detailed characterization, in order to evaluate the homogeneity of elements within catalyst particles. Powder samples were dispersed over a carbon tape and kept within a vacuum chamber during 24 h before analysis. Copper was used as the element for analysis optimization, Appendix F.

Measurements of static adsorption of N_2 at -196 °C were obtained using a Micromeritics 3Flex instrument. Samples were degassed at 150 °C under vacuum for 2 h prior to analysis. The specific surface area was calculated using the Brunauer, Emmett and Teller (BET) model using data in a relative pressure (p/p_0) range between 0.01 and 0.2. The pore size distributions were calculated from the adsorption data using the Barrett-Joyner-Halenda (BJH) model (ROUQUEROL *et al*., 1999).

Powder X-ray diffraction (pXRD) was performed on a BRUKER D8-Advance diffractometer using CuKα (λ = 1.5406 Å) radiation. Intensities were measured with a 0.02° step size and a measuring time of 0.3 s per point. All samples were analyzed between Bragg angles from 5 to 80 º, but diffractograms are presented in the present thesis starting from 15 º, in order to avoid the diffraction interference observed between 10 and 15 º, which was attributed to the employed polymethyl methacrylate (PMMA) sample holder, Appendix B.

3.2.2 Chemical Characterization

^{29}Si solid-state MAS NMR was performed using a Varian VNMRS 400 MHz spectrometer, operating at a resonance frequency of 79.44 MHz with a spinning rate of 6 kHz. 1000 scans were accumulated with a recycle time of 60 s and the pulse length of 4.5 μs . The ^{29}Si{^{1}H} CP MAS NMR spectra were recorded on the same spectrometer. 4000 scans were accumulated with a recycle time of 1 s. The CP contact time was 3.0 ms. The ^{29}Si chemical shifts are referenced to tetramethylsilane.

^{7}Li solid-state MAS NMR was performed using a Varian VNMRS 400 MHz spectrometer, operating at a resonance frequency of 155.405 MHz with a spinning rate of 14 kHz at room temperature. 500 scans were accumulated with a recycle time of 2 s and pulse length of 1.0 μs.

Acidity of samples was determined by temperature programmed desorption of ammonia (NH_3-TPD) experiments in a Setsys Evolution TGA Setaram system coupled with an *in-line* mass spectrometer (MS), OmniStar™ Pfeiffer Vacuum Quadrupole, for measurement of the outgas composition. The release of ammonia (m/z = 15) was monitored. The signal m/z equal to 15 was used in order to avoid interference by the fragmentation of water molecules. Samples (100 mg) were exposed to NH_3 for 48 h at room temperature before TPD experiment. In this procedure, samples were kept within a closed chamber containing an opened flask of ammonium hydroxide solution (Sigma Aldrich, 28 % NH_3 in H_2O, purity of 99.9 %). Pure argon, 100 mL/min, was used as sweep gas. Before starting the analysis, the analytical chamber was purged from ambient air using argon flow at 200 mL/min for 40 min. The NH_3-TPD analyses were started by heating the sample at 10 °C/min from room temperature to 700 °C and maintaining that temperature for 0.5 h, under argon.

In situ infrared spectroscopy (IR) spectra were recorded on a PerkinElmer Frontier spectrometer. Measurements were performed by accumulating 15-30 scans at a resolution of 4 cm^{-1}. $CHCl_3$ was used as molecular probe for basicity evaluation (TAMURA *et al.*, 2012), whereas NH_3 was used as molecular probe for acidity assessment. For the basicity evaluation, samples (50 mg) were exposed to $CHCl_3$ (3 drops, Sigma Aldrich, purity of 99.9 %) at 20 ºC. MgO (Sigma-Aldrich, purity of 99%) was also used for comparison. For the acidity assessment, samples (100 mg) were exposed to NH_3 for 48 h at room temperature before IR measurements. In this procedure, samples were kept within a closed chamber containing an opened flask of ammonium hydroxide solution (Sigma Aldrich, 28 % NH_3 in H_2O, purity of 99.9 %).

Basicity of catalyst samples was also assessed by temperature programmed desorption of CO_2 (CO_2-TPD). A flow system coupled with an *in-line* mass spectrometer, Prisma™ Pfeiffer Vacuum Quadrupole, was used to measure the outgas composition. The release of CO_2 (m/z = 44) was monitored. Prior to adsorption, the sample (200 mg) was pre-treated with helium flow (60 mL/min) for 1 h at 500 ºC (10 ºC/min). Samples were then exposed to CO_2 flow (60 mL/min, pure) for 0.5 h at

100 ºC. CO_2 excess was removed with helium flow at 100 °C for 1.5 h. The CO_2-TPD analyses were performed by heating the sample at rate of 10 °C/min from 100 to 700 °C and maintaining the temperature of 700 °C for 0.5 h, under helium.

X-ray fluorescence (XRF) was used to quantify the bulk chemical composition of samples. Powdered samples (300 mg) were pressed at 27 kN/cm² to provide disks with diameters of 18 mm. The disks were then analyzed by XRF under vacuum, using a RIX 3100 RIGAKU spectrometer. Metal loadings were also assessed by inductively coupled plasma optical emission spectroscopy (ICP-OES) by the MEDAC LTD Analytical and Chemical Consultancy services.

Thermogravimetric analyses of selected used catalysts were carried out in a Setsys Evolution TGA Setaram system coupled with an in-line mass spectrometer, OmniStar™ Pfeiffer Vacuum Quadrupole, for measurement of the outgas composition. Samples (20 mg) were heated from room temperature to 1000 ºC under air flow (100 mL/min), using a heating rate of 20 ºC/min.

Thermogravimetric analyses of used catalysts were also carried out in a *SDT Q600 TA Instruments*. Samples (10 mg) were heated from room temperature to 1000 ºC under air flow (100 mL/min), using a heating rate of 20 ºC/min.

3.3 Catalytic Reactions – Unit 1

Two catalytic units were employed. The first one is named here as Unit 1, while the second one is named as Unit 2.

In Unit 1, isothermal catalytic reactions were performed in a flow quartz packed-bed reactor at atmospheric pressure, as illustrated in Figure 3.3.1. The inner diameter of the catalytic bed was equal to approximately 1 cm. The reactor was kept within an electrical furnace and a thermocouple was kept next to the catalytic bed for temperature control. Nitrogen was used as diluent (15 ml/min, mass flow controller MKS). Quartz wool was used before and after the catalyst bed in order to fix the catalyst particles. Before the experiments, the catalyst sample (100 mg) was pre-treated with nitrogen flow for 1 h at 500 ºC (5 ºC/min). Reactions were then performed between 300 and 450 ºC, using an ethanol weight hourly space velocity (WHSV) of 0.8 h^{-1}. The WHSV was defined as the ratio between the ethanol mass flow rate and the catalyst mass. The

ethanol mass flow rate was measured at the inlet feed condition (20 ºC). The ethanol molar fraction in the inlet reactor stream (gas phase) was equal to 6 % on these runs. The ethanol was fed into the reactor with help of an ethanol saturator containing ethanol (99.9 % v/v) at 20 ºC, through which N_2 was bubbled. The gas mixture containing ethanol and N_2 from the ethanol saturator outlet was heated up to 160 ºC before feeding the reactor.

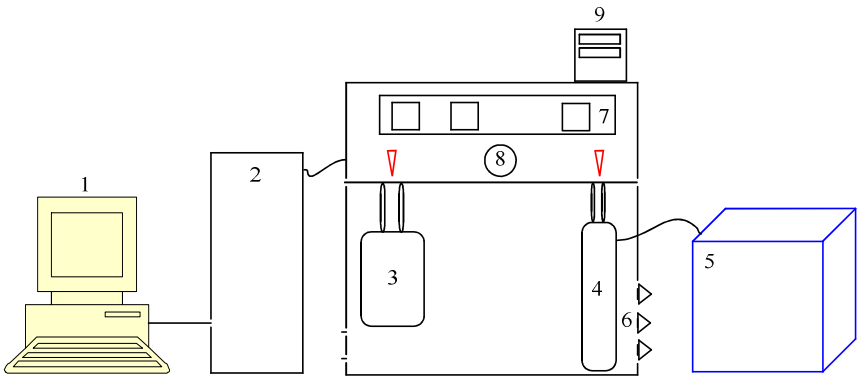

Figure 3.3.1 – Schematic representation of the Unit 1 catalytic reaction. Number *1* denotes the computer used for data acquisition; *2* represents the gas chromatograph; *3* is the reactor furnace; *4* is the ethanol saturator; *5* is the isothermal batch used to keep the ethanol saturator temperature constant; *6* represents valves for N_2 stream inlet; *7* represents temperature controllers; *8* is a barometer and *9* is a digital temperature reader connected to a thermocouple kept close to the wall of the ethanol saturator.

The reactor output stream was analyzed after 0.5 h of time on stream (TOS) using gas chromatography with help of an Agilent 3000A Micro GC instrument, equipped with three channels, each one containing a thermal conductivity detector and a column. The first channel contained a molecular sieve column (Molsieve 5Å, Agilent, 3 m m long 0.32 mm diameter, 10 μm of aluminosilicate stationary phase), which was used to separate light gases, such as H_2, CO, and N_2. In this column, Argon was used as the carrier gas. The second channel contained a Plot Q (HP-*PLOT/Q*) column with length of 8 m, diameter of 0.32 mm and 10 μm of polystyrene-divinylbenzene stationary phase. This channel was used to separate C1-C4 compounds, such as CO_2, ethene, ethane, propane, propene, 1,3-butadiene, butene (1-butene, *cis*- and *trans*-2-butene), besides water, and the carrier gas was Helium. Finally, the third channel contained an OV-1 column (Agilent, 14 m long, 0.15 mm of diameter, 2 μm of dimethylpolysiloxane

stationary phase), which was used to separate oxygenated compounds, such as acetaldehyde, ethanol, diethyl ether, crotonaldehyde and crotyl alcohol.

Before reaction experiments, ethanol and all possible reaction products were calibrated in the Micro GC instrument, as detailed in the next section. Appendix C presents the employed chromatographic method and Appendix D presents experimental data used for calibration.

3.4 Characterization of Experimental Fluctuations

The characterization of experimental fluctuations of ethanol to 1,3-BD conversion reactions was performed using the catalytic reaction Unit 1, described in the previous section.

The term "experimental fluctuation" is used here to represent the total intrinsic experimental variability associated with composition measurements of unconverted ethanol and reaction products in the reactor outlet stream. Therefore, experimental fluctuations comprise the intrinsic fluctuations of both the analytic chromatographic system and the reaction process, which are related to the composition measurements, Figure 3.4.1.

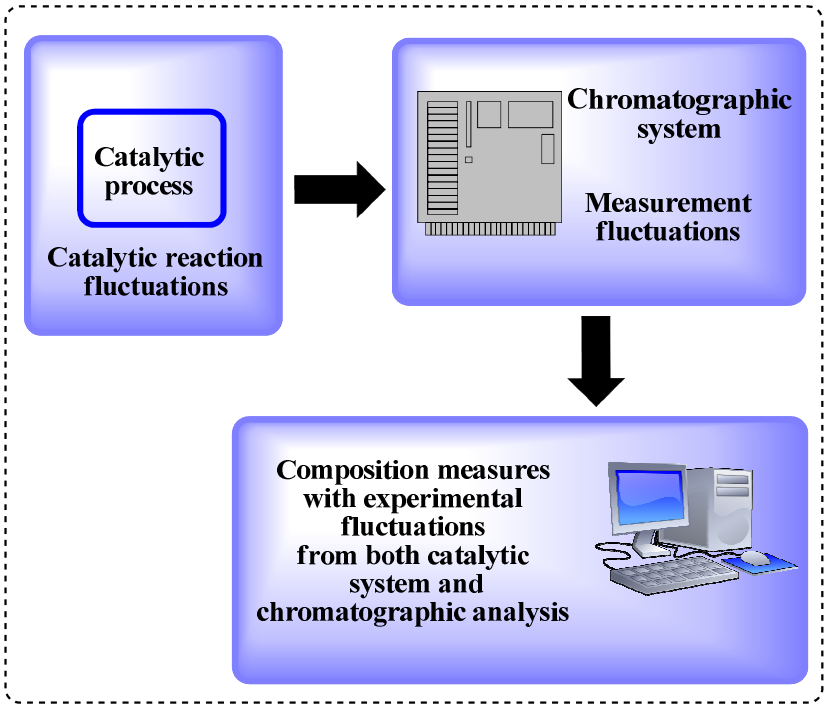

Figure 3.4.1 - Illustration of experimental fluctuations of composition measurements.

The intrinsic experimental fluctuations related to the analytic chromatographic system are referred here as the chromatographic measurement fluctuations (or only measurement fluctuations), while the intrinsic experimental fluctuations related to the catalytic experiments are referred here as the catalytic reaction fluctuations. However, catalytic reaction fluctuations cannot be determined independently from measurement fluctuations, since measurements obtained from process outputs present variability components originated from both catalytic and chromatographic systems and are, therefore, measures of the total experimental fluctuations. Thus, in order to discriminate measurement fluctuations from catalytic reaction fluctuations, both fluctuations were determined.

Chromatographic measurement fluctuations were calculated through replication of chromatographic analysis at different composition conditions, as shown in Table 3.4.1. In these replicate runs, chemical compounds were fed into the measuring system with help of a saturator (for ethanol and diethyl ether analyses) or gas cylinders (for 1,3-BD, acetaldehyde, ethene, butene and hydrogen analyses).

Table 3.4.1 - Molar fractions of ethanol, H_2, and main carbon containing products used for characterization of measurement fluctuations and GC calibration.

	Molar Fractions (%) [a]					
Ethanol [b]	5.80	4.26	2.10	0.89	0.53	
1,3-Butadiene [c]	5.03	1.80	0.68	0.36	0.20	0.10
Acetaldehyde [d]	72.26	66.65	24.73	16.29		
Ethene [e]	7.94	2.70	2.03	1.09	0.53	0.34
Diethyl ether [f]	49.47	28.34	13.49	7.86	4.30	
Hydrogen [g]	13.80	7.01	1.84			

[a] Molar fractions were modified by varying N_2 flow rate. **[b]** Ethanol was kept in a saturator at 20 ºC and N_2 was used as diluent. The saturator outlet stream was mixed with a second N_2 stream, which had its flow rate varied. **[c]** A gas mixture constituted by 2-butene (1.91 %), 1-butene (2.90 %) and 1,3-butadiene (5.03 %) was used. **[d]** Pure acetaldehyde was diluted with N_2. **[e]** A gas mixture constituted by ethane (4.99 %), ethene (7.94 %), propane (12.28 %), propene (2.00 %) and n-butane (2.97 %) was used. **[f]** As described for ethanol, but the saturator temperature was kept at 16 ºC. **[g]** A gas mixture constituted by H_2 (13.8 %), carbon monoxide (7.9 %) and carbon dioxide (6.2 %) was used. All gas cylinders mixtures were diluted in N_2.

At least three replicates were performed for each composition condition. These experiments were used simultaneously to calibrate the GC instrument and to estimate measurement fluctuations. It must be emphasized that these tests were not performed under reaction conditions.

From these composition measurements, variances were calculated for each composition condition using Eq. (3.4.1), where s_{ij}^2 is the variance of observed molar fractions of compound *i* at condition *j*, y_{ij}^k is the *k*-th observation of the molar fraction of compound *i* at composition condition *j*, $\bar{y}_{ij}$ is the average of observed molar fractions of compound *i* at composition condition *j* and *NR* is the number of replicates.

$$s_{ij}^2 = \frac{\sum_{k=1}^{NR}(y_{ij}^k - \bar{y}_{ij})^2}{NR-1} \tag{3.4.1}$$

Thus, it was possible to correlate compositions with the respective measurement fluctuations.

For characterization of catalytic reaction fluctuations, three experiments were performed for each reaction condition. The reaction conditions employed distinct temperatures. Specifically, reaction replicates were performed at 300, 350, 400 and 450 ºC. The covariance matrix of catalytic reaction fluctuations of composition measurements at each reaction condition was computed with Eq. (3.4.1) and Eq. (3.4.2), where s_{ij}^2 is the variance of observed molar fractions of compound *i* at reaction condition *j*, ξ_{il}^j denotes the covariance of observed molar fractions of compounds *i* and *l* at reaction condition *j*, y_{ij}^k is the *k*-th observation of the molar fraction of compound *i* at reaction condition *j*, $\bar{y}_{ij}$ is the average of observed molar fractions of compound *i* at reaction condition *j* and *NR* is the total number of replicates.

$$\xi_{il}^j = \frac{\sum_{k=1}^{NR}(y_{ij}^k - \bar{y}_{ij})(y_{lj}^k - \bar{y}_{lj})}{NR-1} \tag{3.4.2}$$

Finally, the correlation matrix of observed compositions at each reaction condition was calculated with Eq. (3.4.3), where ρ_{il}^j represents the correlation coefficient of observed molar fractions for compounds *i* and *l* at reaction condition *j*.

$$\rho_{il}^j = \frac{\xi_{il}^j}{s_{ij} \cdot s_{lj}} \tag{3.4.3}$$

At this point, it must be noted that the dimension of the covariance matrix of catalytic reaction fluctuations which must be used for parameter estimation can be much bigger than that one defined in the previous paragraph for the covariance matrix of

catalytic reaction fluctuations of composition measurements at each reaction condition. For instance, let us assume that the vector of model responses $\boldsymbol{y}^*$ from Eq. (1.5.1) is defined taking into account two compounds (for instance, ethanol and 1,3-BD) and four different reaction conditions. In this case, assuming yet that only the average values (obtained from replicates) for each compound molar fraction would be used for parameter estimation, the full covariance matrix of catalytic reaction fluctuations (used for minimization of the objective function defined by Eq. (1.5.1)) would contain 8 rows and 8 columns (SCHWAAB and PINTO, 2007), as illustrated below.

$$V = \begin{bmatrix}
s^2_{EtOH,T_1} & \xi^{T_1}_{EtOH,BD} & \chi^{T_1,T_2}_{EtOH,EtOH} & \chi^{T_1,T_2}_{EtOH,BD} & \chi^{T_1,T_3}_{EtOH,EtOH} & \chi^{T_1,T_3}_{EtOH,BD} & \chi^{T_1,T_4}_{EtOH,EtOH} & \chi^{T_1,T_4}_{EtOH,BD} \\
\xi^{T_1}_{BD,EtOH} & s^2_{BD,T_1} & \chi^{T_1,T_2}_{BD,EtOH} & \chi^{T_1,T_2}_{BD,BD} & \chi^{T_1,T_3}_{BD,EtOH} & \chi^{T_1,T_3}_{BD,BD} & \chi^{T_1,T_4}_{BD,EtOH} & \chi^{T_1,T_4}_{BD,BD} \\
\chi^{T_2,T_1}_{EtOH,EtOH} & \chi^{T_2,T_1}_{EtOH,BD} & s^2_{EtOH,T_2} & \xi^{T_2}_{EtOH,BD} & \chi^{T_2,T_3}_{EtOH,EtOH} & \chi^{T_2,T_3}_{EtOH,BD} & \chi^{T_2,T_4}_{EtOH,EtOH} & \chi^{T_2,T_4}_{EtOH,BD} \\
\chi^{T_2,T_1}_{BD,EtOH} & \chi^{T_2,T_1}_{BD,BD} & \xi^{T_2}_{BD,EtOH} & s^2_{BD,T_2} & \chi^{T_2,T_3}_{BD,EtOH} & \chi^{T_2,T_3}_{BD,BD} & \chi^{T_2,T_4}_{BD,EtOH} & \chi^{T_2,T_4}_{BD,BD} \\
\chi^{T_3,T_1}_{EtOH,EtOH} & \chi^{T_3,T_1}_{EtOH,BD} & \chi^{T_3,T_2}_{EtOH,EtOH} & \chi^{T_3,T_2}_{EtOH,BD} & s^2_{EtOH,T_3} & \xi^{T_3}_{EtOH,BD} & \chi^{T_3,T_4}_{EtOH,EtOH} & \chi^{T_3,T_4}_{EtOH,BD} \\
\chi^{T_3,T_1}_{BD,EtOH} & \chi^{T_3,T_1}_{BD,BD} & \chi^{T_3,T_2}_{BD,EtOH} & \chi^{T_3,T_2}_{BD,BD} & \xi^{T_3}_{BD,EtOH} & s^2_{BD,T_3} & \chi^{T_3,T_4}_{BD,EtOH} & \chi^{T_3,T_4}_{BD,BD} \\
\chi^{T_4,T_1}_{EtOH,EtOH} & \chi^{T_4,T_1}_{EtOH,BD} & \chi^{T_4,T_2}_{EtOH,EtOH} & \chi^{T_4,T_2}_{EtOH,BD} & \chi^{T_4,T_3}_{EtOH,EtOH} & \chi^{T_4,T_3}_{EtOH,BD} & s^2_{EtOH,T_4} & \xi^{T_4}_{EtOH,BD} \\
\chi^{T_4,T_1}_{BD,EtOH} & \chi^{T_4,T_1}_{BD,BD} & \chi^{T_4,T_2}_{BD,EtOH} & \chi^{T_4,T_2}_{BD,BD} & \chi^{T_4,T_3}_{BD,EtOH} & \chi^{T_4,T_3}_{BD,BD} & \xi^{T_4}_{BD,EtOH} & s^2_{BD,T_4}
\end{bmatrix}$$

This matrix shows, besides the covariances among reaction compounds at the same reaction temperature, the existence of covariances among variables measured at different temperatures (χ_{il}^{j}). It is usually assumed that these covariances χ_{il}^{j} are equal to zero, since experiments at different conditions may be assumed to be independent, but this is not necessarily true and can depend on the process analytics and operational procedures.

3.5 Catalytic Reactions - Unit 2

For experiments carried out in the catalytic reaction Unit 2, catalytic tests were performed using a flow quartz packed-bed reactor at atmospheric pressure. The inner diameter of the catalytic bed was equal to 1.8 cm and quartz wool was used before and after the catalyst bed in order to fix the catalyst particles. The reactor was kept within a *Carbolite* electrical furnace and Argon was used as the carrier gas (8 mL/min). Ethanol was fed with a Harvard Apparatus PHD 2000 programmable infusion syringe pump

(Harvard Apparatus, UK). In all experiments, ethanol 92 wt. % in distilled water was employed. Figure 3.5.1 illustrates the catalytic Unit 2, showing the infusion pump (left) coupled to the reactor system (right).

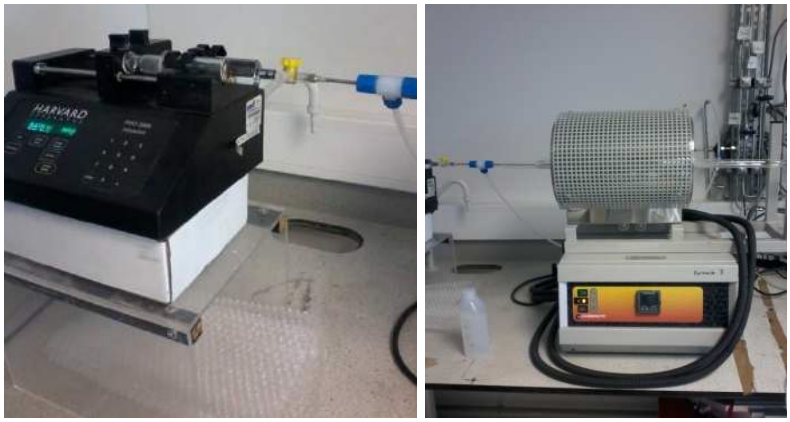

Figure 3.5.1 – Catalytic reaction Unit 2: ethanol feed pump and reactor system.

The ethanol WHSV was varied in the range from 0.3 to 2.5 h^{-1} through modification of the ethanol flow rate, keeping catalyst mass (2.0 g) and carrier gas flow rate fixed. The investigated WHSV range corresponded to ethanol molar fractions between 0.41 and 0.85. The contact time (calculated as the ratio between the catalyst volume and the total gas flow at the reaction temperature) ranged from 1.3 to 5.3 s. Reaction temperature ranged from 300 to 400 °C. Both WHSV and temperature ranges were consistent with the majority of the reaction conditions used in the literature.

The exhaust gases were analyzed after 3 h of time on stream (TOS) with help of a gas chromatograph (Agilent 7890A) coupled to a mass spectrometer (Agilent 5975C with triple axis detector) instrument. Gas samples (30 mL) were collected from the outlet reactor stream using a SGE gas tight syringe of 50 mL. The compounds were separated chromatographically using a HP-PLOT/Q column, with length of 30 m and diameter of 0.53 mm diameter. Quantification of compositions was performed using a flame ionization detector (FID). The mass spectrometer detector was used to confirm the identity of reaction products. The GC was calibrated as detailed in Appendix D, whereas the chromatographic method is detailed in Appendix C. Carbon balances were typically better than 90 %.

Ethanol conversion (X), selectivity (S), yield (Y), and 1,3-BD productivity (P_{BD}, in $g_{BD}/g_{cat}\cdot h$) were calculated with Eq. (3.5.1), (3.5.2), (3.5.3) and (3.5.4),

respectively, where $N_{EtOH,in}$ and $N_{EtOH,out}$ represent the number of mols of ethanol that were added and collected, respectively; N_i denotes the number of mols of the product *i*; *NP* is the total number of products; and *r* is the ratio between the number of carbons of the product *i* and of ethanol. For 1,3-BD, for instance, *r* is equal to 2. Finally, m_{cat} denotes the catalyst mass and *t* is the total reaction time.

$$X(\%) = \frac{(N_{EtOH,in} - N_{EtOH,out}) \cdot 100}{N_{EtOH,in}} \quad (3.5.1)$$

$$S_i(\%) = \frac{N_i}{\sum_{i=1}^{NP} N_i} \cdot 100 \quad (3.5.2)$$

$$Y_i(\%) = \frac{r \cdot N_i}{N_{EtOH,in}} \cdot 100 \quad (3.5.3)$$

$$P_{BD} = \frac{N_{BD} \cdot 54}{(m_{cat} \cdot t)} \quad (3.5.4)$$

3.6 Experimental Design

The effect of the experimental reaction variables, temperature and WHSV, on the catalyst performances were investigated with help of a two-level factorial design, with four central point experiments. These experiments were performed using the catalytic reaction Unit 2. The statistical design approach was chosen to allow for simultaneous and precise quantification of the main effects of temperature and WHSV, their interaction effect and to study any potential non-linear effects present on catalyst activity (NELE *et al*., 1999, LARENTIS *et al*., 2011, BOX *et al*., 2005). The experimental variables, z_i, were normalized within the [−1, +1] interval, according to Eq. (3.6.1). z_i represents the actual value of variable *i*, z_{ic} denotes the actual value of variable *i* at the central condition (equal to 350 ºC and 0.93 h^{-1} for temperature and WHSV, respectively), Δz_i is equal to 25 ºC and 0.31 h^{-1} for temperature and WHSV, respectively, and x_i is the normalized value of variable *i*.

$$x_i = \frac{z_i - z_{ic}}{\Delta z_i} \qquad (3.6.1)$$

Table 3.6.1 shows the experimental design matrix, with normalized and actual values of reaction conditions. Four experiments at central condition (Exps. 5-8, Table 3.6.1) were carried out in order to evaluate the experimental error and to test for the evidence of non-linear effects. Two additional axial experiments, −2 and +2, were performed for each variable (Exps. 9-12), to allow for improved quantification of nonlinear effects (NELE *et al*., 1999). Besides, Experiments 13 and 14, at conditions -1 and +1, were performed to evaluate the prediction capability of the proposed models. Finally, additional experiments were performed to assess the system behavior at higher WHSV values (Exps. 15-18).

Table 3.6.1 - Matrix of experimental conditions: actual and normalized variable values.

Experiment	Temperature (ºC) z_1 (x_1)	WHSV (h^{-1}) z_2 (x_2)
1	325 (-1)	0.62 (-1)
2	325 (-1)	1.24 (+1)
3	375 (+1)	0.62 (-1)
4	375 (+1)	1.24 (+1)
5	350 (0)	0.93 (0)
6	350 (0)	0.93 (0)
7	350 (0)	0.93 (0)
8	350 (0)	0.93 (0)
9	300 (-2)	0.93 (0)
10	400 (+2)	0.93 (0)
11	350 (0)	0.31 (-2)
12	350 (0)	1.55 (+2)
13	325 (-1)	0.93 (0)
14	375 (+1)	0.93 (0)
15	325 (-1)	2.49 (+5)
16	350 (0)	2.49 (+5)
17	375 (+1)	2.49 (+5)
18	400(+2)	2.49 (+5)

Ethanol conversions, product selectivities, molar fractions of reaction products, 1,3-BD yields and 1,3-BD productivities were selected as response or dependent variables to assess reaction temperature and WHSV effects. Models with the general

form of Eq. (3.6.2) - a classic structure used in factorial designs (NELE *et al*., 1999, LARENTIS *et al*., 2011, BOX *et al*., 2005) - were then applied to correlate dependent variables, y_i, with the reactions conditions, using the independent normalized variables, x_i.

$$y_i = b_0 + b_1 x_1 + b_2 x_2 + b_{12} x_1 x_2 + b_{11}\left(x_1^2 - \lambda_1\right) + b_{22}\left(x_2^2 - \lambda_2\right) \tag{3.6.2}$$

The parameters of Eq. (3.6.2), b_1 and b_2, b_{12}, b_{11} and b_{22}, are related to the linear, interaction and quadratic effects of temperature and WHSV, respectively, while b_0 is the independent bias parameter. Finally, λ_i is a constant used to guarantee the orthogonality of the design matrix, calculated as shown in Eq. (3.6.3), where *NE* is the total number of experiments. Parameters from Eq. (3.6.2) were estimated using least-squares estimation procedure (PINTO and SCHWAAB, 2008, BARD, 1974).

Statistical significance of the estimated model parameters was evaluated with the standard t-test (PINTO and SCHWAAB, 2007). Whenever parameter significance was lower than 5%, the parameter and respective variable effect were regarded as statistically insignificant and were removed from Eq. (3.6.2). Besides, fit quality was always verified by comparing experimental variance with Eq. (3.6.2) prediction variance using the standard F-test (BOX *et al*., 1978), in order to avoid overparameterized solutions. For all obtained models, experimental variances were always statistically equal to prediction variances, supporting the satisfactory statistical quality of the computed models.

$$\lambda_i = \frac{1}{NE}\sum_{j=1}^{NE} x_{ij}^2 \tag{3.6.3}$$

4. RESULTS AND DISCUSSION

4.1 Effect of co-precipitation variables used for preparation of $MgO-SiO_2$ systems on catalytic activity

Initially, Mg-Al mixed oxides derived from hydrotalcites were prepared with Mg/Al ratios of 3 and 5. These catalysts were selected because the co-precipitation method used for preparation is well defined (LEON *et al*. 2011a, DI COSIMO *et al*., 1998, PÉREZ, 1997). Thus, these materials were prepared and evaluated in terms of the catalytic activity. As observed previously (LEON *et al*. 2011a-b, DI COSIMO *et al*., 1998), and expected, the products distribution from ethanol conversion over Mg-Al mixed oxides derived from hydrotalcites was large, containing, among other minor compounds, carbon dioxide, ethene, ethane, butene (*cis* and *trans*) propene, acetaldehyde (AcH), diethyl ether (DEE), butanol and 1,3-BD. This means that 1,3-BD selectivities obtained were low, leading to very low yields compared to other major products, such as butanol and ethene. The poor activity of these materials for ethanol to 1,3-BD conversion is related to the strong acidity feature of Lewis acid sites of Al^{+3} species (DI COSIMO *et al*., 1998). The catalyst preparation method by co-precipitation was, however, successful and allowed for preparation of the target materials, as illustrated in the pXRD diffractograms presented in the Appendix E.

Therefore, the co-precipitation method was adapted to prepare $MgO-SiO_2$ systems. Figure 4.1.1 illustrates the initial tested A-D procedures. All runs used the same stirring time after the end of the precipitation (2 h) and the same aging time (22 h). Moreover, all runs used the same Mg to Si molar ratio of 1, and the combined Mg and Si metals concentration was 0.5 M (0.075 mols of Si and 0.075 mols of Mg were mixed into 300 mL of the preparation solution).

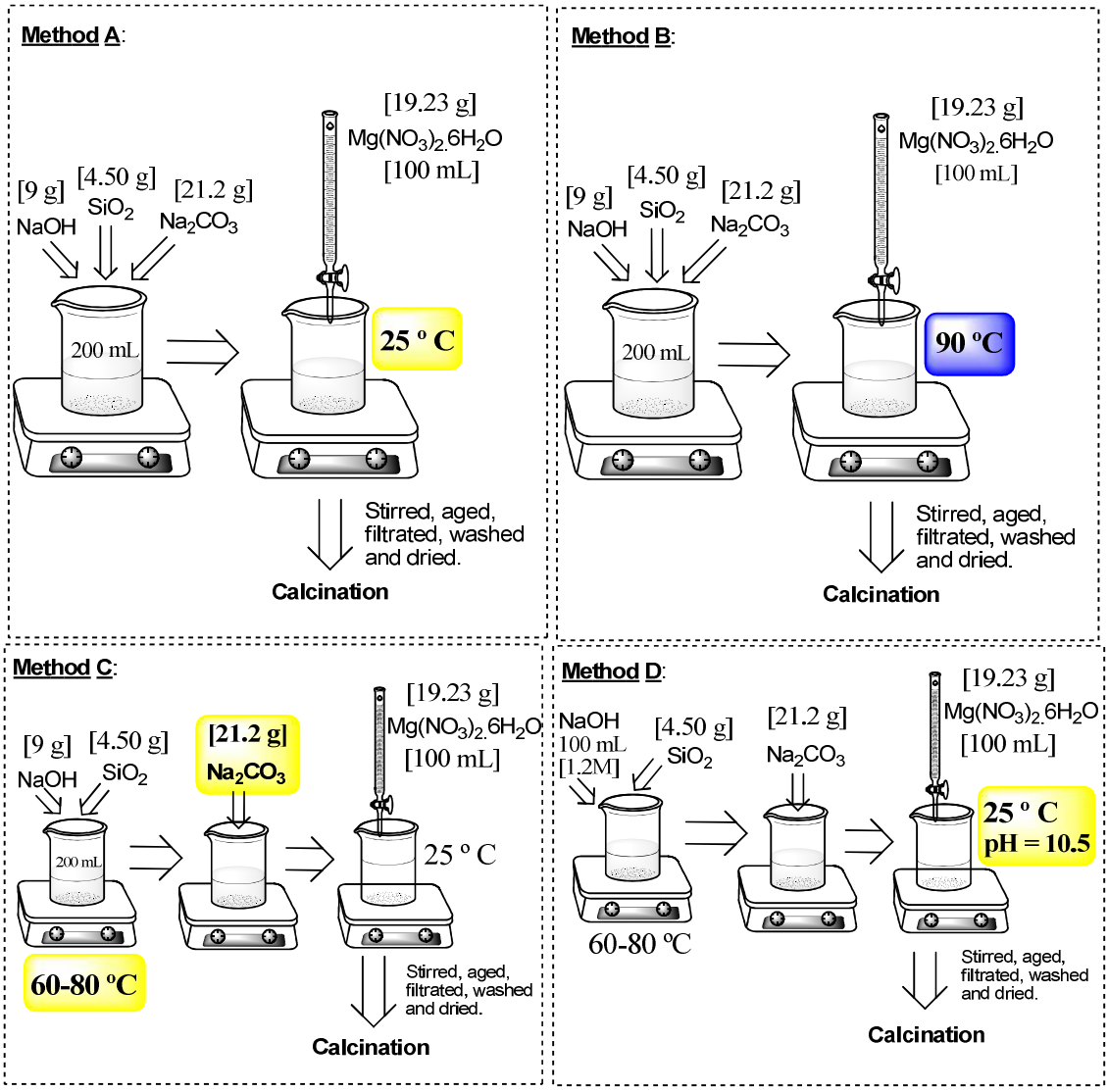

Figure 4.1.1 - MgO-SiO_2-(50-50) preparation methods. The final volume was always completed to 300 mL with distilled water in methods A-D. Calcination was performed at 500 ºC for 4 h (5 ºC/min), under air flow (50 mL/min). All employed flasks were made of polypropylene.

Initially, NaOH, SiO_2 and Na_2O_3 were mixed simultaneously in 200 mL of distillated water, Methods A-B, Figure 4.1.1. The aqueous magnesium nitrate solution was added to the previous mixture under stirring in a dropwise manner. Thus, Methods A and B were distinct in respect to the precipitation and stirring temperature. In Method A, precipitation and stirring were performed kept at 25 ºC, while in method B, this temperature was raised to 90 ºC. Method B was performed in order to verify if a higher temperature could result in higher number of structural defects, improving catalytic activity.

It was observed in the methods A and B, however, that the initial mixtures were not completely clear before the start of the precipitation process, no matter the length of time used to stir the solution. This could indicate that the SiO_2 was not completely dissolved. In order to achieve a final homogeneous material, Method C was designed. In Method C, the SiO_2 was mixed with the NaOH under heated stirring. After observing the complete dissolution of the powder, the solution was cooled and the Na_2CO_3 was added.

It is worth noting that in Methods A-C, after the aging time, the resulting mixture was filtrated and washed with boiling distilled water until constant pH value of the filtrate. The replicates indicated that the pH value of the washing water never returned back to neutral, even after an entire week of washing. It was verified, however, that 7.5 L of distillated water would be enough to remove the sodium residual from the final $MgO\text{-}SiO_2$ hydroxide (no sodium was found by XRF analysis of the powder samples); therefore, this volume of water was used in the preparations.

One must also note that in Methods A-C the pH of the precipitation was allowed to vary. The starting amount of NaOH was sufficient to keep the pH basic (around 12.5 at the beginning of the precipitation step) during the precipitation step. Thus, the effect of controlling the pH during the precipitation was also investigated, by keeping this value close to 10.5 during the magnesium nitrate solution addition step, through addition of small quantities of 1.2 M NaOH solution, Method D, Figure 4.1.1. Since the pH controls the concentrations of Mg^{2+} and OH^- species on solution, the control of precipitation pH should result in a more homogenous final structure, as illustrated in Eq. (4.1.1-4.1.5) (SZCZERBA *et al*., 2013, LI *et al*., 2014).

$$SiO_2 + 2OH^- \rightarrow H_2SiO_4^{2-} \quad (4.1.1)$$

$$SiO_2 + OH^- + H_2O \rightarrow H_3SiO_4^- \quad (4.1.2)$$

$$SiO_2 + OH^- \rightarrow HSiO_3^- \quad (4.1.3)$$

$$HSiO_3^- + Mg^{2+} + 2OH^- + H_2O \rightarrow MgHSiO_4 \cdot 2H_2O \quad (4.1.4)$$

$$2Mg^{2+} + H_3SiO_4^- + H_2SiO_4^{2-} \rightarrow Mg\text{-}Si\text{-}O\text{-}H_{solid} \quad (4.1.5)$$

Table 4.1.1 shows catalytic results for ethanol conversion at 350 ºC over catalyst samples from different batches prepared using methods A-D. Each entry represents a different reaction experiment.

Table 4.1.1 - Catalytic results over $MgO\text{-}SiO_2$-(50:50) systems prepared according to methods A-D. Reaction conditions: 350 ºC, WHSV of 0.8 h^{-1}, contact time of 0.2 s, ethanol molar fraction at the feed of 6 %, atmospheric pressure and TOS of 0.5 h. Before reactions, samples were pre-treated *in situ* with nitrogen flow (15 mL/min) for 1 h at 500 ºC (5 ºC/min).

Entry	Catalyst	Molar fraction of the output stream (%)[a]					
		1,3-BD	AcH	Ethene	DEE	Butene	Ethanol
1	$MgO\text{-}SiO_2$ -A 1º batch	0.06	0.05	0.09	0.04	0.004	5.31
2	$MgO\text{-}SiO_2$ -A 1º batch	0.04	0.04	0.30	0.12	0.002	5.30
3	$MgO\text{-}SiO_2$ -A 1º batch	0.03	0.03	0.25	0.09	0.002	5.13
4	$MgO\text{-}SiO_2$ -A 1º batch	0.05	0.05	0.30	0.11	0.004	5.58
5	$MgO\text{-}SiO_2$ -A 1º batch	0.04	0.04	0.30	0.12	0.002	5.36
6	$MgO\text{-}SiO_2$ -A 2º batch	0.03	0.03	0.30	0.11	0.002	5.15
7	$MgO\text{-}SiO_2$ -A 3º batch	0.02	0.04	0.17	0.07	0.002	5.56
8	$MgO\text{-}SiO_2$ -B 1º batch	0.02	0.02	0.07	0.04	0.001	5.42
9	$MgO\text{-}SiO_2$ -C 1º batch	0.15	0.08	0.80	0.16	0.016	4.19
10	$MgO\text{-}SiO_2$ -C 1º batch	0.03	0.07	0.18	0.07	0.002	5.28
11	$MgO\text{-}SiO_2$ -C 1º batch	0.03	0.03	0.19	0.09	0.001	5.41
12	$MgO\text{-}SiO_2$ -D 1º batch	0.12	0.12	0.40	0.15	0.011	4.95
13	$MgO\text{-}SiO_2$ -D 1º batch	0.03	0.03	0.49	0.20	0.001	4.90
14	$MgO\text{-}SiO_2$ -D 2º batch	0.14	0.14	0.35	0.14	0.013	4.81
15	$MgO\text{-}SiO_2$ -D 2º batch	0.02	0.03	0.47	0.18	0.002	5.09
16	$MgO\text{-}SiO_2$ -D 2º batch	0.02	0.03	0.49	0.19	0.002	5.05
17	$MgO\text{-}SiO_2$ -D 3º batch	0.06	0.05	0.62	0.22	0.004	4.81
18	$MgO\text{-}SiO_2$ -D 3º batch	0.05	0.04	0.53	0.20	0.004	5.08
19	$MgO\text{-}SiO_2$ -D 3º batch	0.04	0.04	0.50	0.20	0.004	4.95

[a] Molar fractions do not sum 100 % due to N_2 (inert gas) and water molar fractions, which were omitted. The employed catalytic unit was the Unit 1.

In Table 4.1.1, the main carbon containing products and ethanol molar fractions at the output stream are presented. The presentation of product molar fractions, rather than products selectivities and ethanol conversion, is justified by the high number of compounds, which leads to high variability of the final selectivities and impairs the observation of significant effects related to the different preparation methods.

Entries 1-5 in Table 4.1.1 represent reaction replicates obtained with the same catalyst batch prepared with Method A. This means that experimental fluctuations observed for entries 1-5 represent a measure of the catalytic reaction fluctuations. Taking this variability into account, reactions described in entries 9, 12 and 14 contain significantly different products molar fractions and could suggest that the preparation method exerts significant effect on the catalyst performance. However, data from entries 9, 12 and 14 were obtained when the hydroxide precursor was calcined and catalytically tested right after the preparation procedure and this higher activity was not reproducible after the first test for the same catalyst sample. Thus, it can be suggested that the fresh catalyst may present instable activity for the 1,3-BD formation and data collected for entries 9, 12 and 14 could not be regarded as the true performances for the MgO-SiO_2 catalysts.

Assuming normal distribution of experimental data with 95 % level of confidence, 1,3-BD and AcH molar fractions could vary inside the interval presented in Eq. (4.1.6) and (4.1.7), for samples prepared with Method A (the mean confidence interval was built using the t-student distribution with 4 degrees of freedom and data from entries 1-5) (PINTO and SCHWAAB, 2007). In Eq. (4.1.6-4.1.7), s_{yi} is the standard deviation and N is the number of replicates. Assuming the same intrinsic catalytic reaction fluctuation to build confidence intervals for molar fractions obtained with the other preparation methods, it can be concluded that all intervals present intersections, suggesting no significant effect of the preparation methods on the final 1,3-BD and AcH molar fractions (excluding results described in entries 9, 12 and 14 of Table 4.1.1).

$$\overline{y}_{BD} = \overline{y}_{BD} \pm \frac{t \cdot s_{y_{BD}}}{\sqrt{N}} \rightarrow \overline{y}_{BD} \pm \frac{2.78 \cdot s_{y_{BD}}}{\sqrt{5}} \rightarrow 0.03 < \overline{y}_{BD} < 0.06 \qquad (4.1.6)$$

$$\overline{y}_{AcH} = \overline{y}_{AcH} \pm \frac{t \cdot s_{y_{AcH}}}{\sqrt{N}} \rightarrow \overline{y}_{AcH} = \overline{y}_{AcH} \pm \frac{2.78 \cdot s_{y_{AcH}}}{\sqrt{5}} \rightarrow 0.03 < \overline{y}_{AcH} < 0.05 \qquad (4.1.7)$$

The higher activity of the fresh catalyst could be associated to some remaining MgO on the catalyst surface, which could produce stronger basic sites, boosting the 1,3-BD formation (SZCZERBA *et al.*, 2013). With some days of catalyst aging, however,

MgO might have been hydrated, as described in Eq. (4.1.8-4.1.10) (SZCZERBA *et al.*, 2013).

$$MgO_{(s)} + H_2O_{(l)} \rightarrow MgOH^+_{(surface)} + OH^-_{(aq)} \quad (4.1.8)$$

$$MgOH^+_{(surface)} + OH^-_{(aq)} \rightarrow MgOH^+OH^-_{(surface)} \quad (4.1.9)$$

$$MgOH^+OH^-_{(surface)} \rightarrow Mg^{2+}_{(aq)} + 2OH^-_{(aq)} \quad (4.1.10)$$

On the surface of the MgO grains, Mg^{2+} and OH^- ions formed due to MgO hydration could react with $Si(OH)_4$ species, producing more Mg-O-Si linkages (Eq. 4.1.1-4.1.5) (SZCZERBA *et al.*, 2013). As the residual MgO is consumed, however, the resulting structure would become stable over time, resulting in the overall catalytic performance observed in entries 1-8, 10-11, and 15-19 of Table 4.1.1.

It should be noted that experiments using higher times on stream suggested no reaction instability from 30 min to 1, 2 and 3 h of reaction. Moreover, it must be noted that these results do not seem to be related with the induction period, as cited in the literature review (which can be understood as the contact time required for the start of the 1,3-BD formation, given the consecutive character of the reaction kinetics), since similar contact times were used in the reaction runs.

Thus, it can be concluded that the MgO-SiO_2 system at the Mg to Si molar ratio of 1 presented similar overall catalytic performances with respect to the 1,3-BD and acetaldehyde molar fractions, regardless the preparation methods considered (A-D). Conversely, the preparation method presented a clear effect on the amounts of produced ethene and diethyl ether, which were higher for the samples prepared by the Method D. It suggests that the smaller amount of NaOH added during the Method D, when compared with Methods (A-C), resulted in catalysts with higher acidity. However, the Method D was selected for further studies because: i) it allows for easier removal of residual sodium; ii) the higher acidity of the MgO-SiO_2 system is expected to allow for easier observation of the catalytic effects of the addition of dehydrogenating metal oxides ZrO_2 and ZnO into the starting MgO-SiO_2 material; iii) the precipitation with pH control is expected to lead to more homogeneous final structures.

By using Method D, it was verified that increasing the final calcination temperature up to 600 and 700 ºC would not result in any significant improvement of

the final 1,3-BD yields, as shown in Figure 4.1.2(a). Moreover, MgO-SiO_2-(50:50) samples calcined at higher temperatures also resulted in lower ethene yields, as shown in Figure 4.1.2(b), suggesting that catalyst activity was reduced as the calcination temperature was increased. Ethanol conversion was also slightly reduced, as shown in Figure 4.1.2(c), giving additional support to the previous hypothesis. The reduction of activity could be related to sinterization of catalyst particles during exposition to higher calcination temperature, resulting in lower surface areas. Indeed, this was verified, as shown in Figure 4.1.2(d). Therefore, the calcination temperature equal to 500 ºC was kept in the following studies.

More details regarding physical and chemical properties of the MgO-SiO_2 catalyst samples prepared by the co-precipitation method will be presented in the following sections.

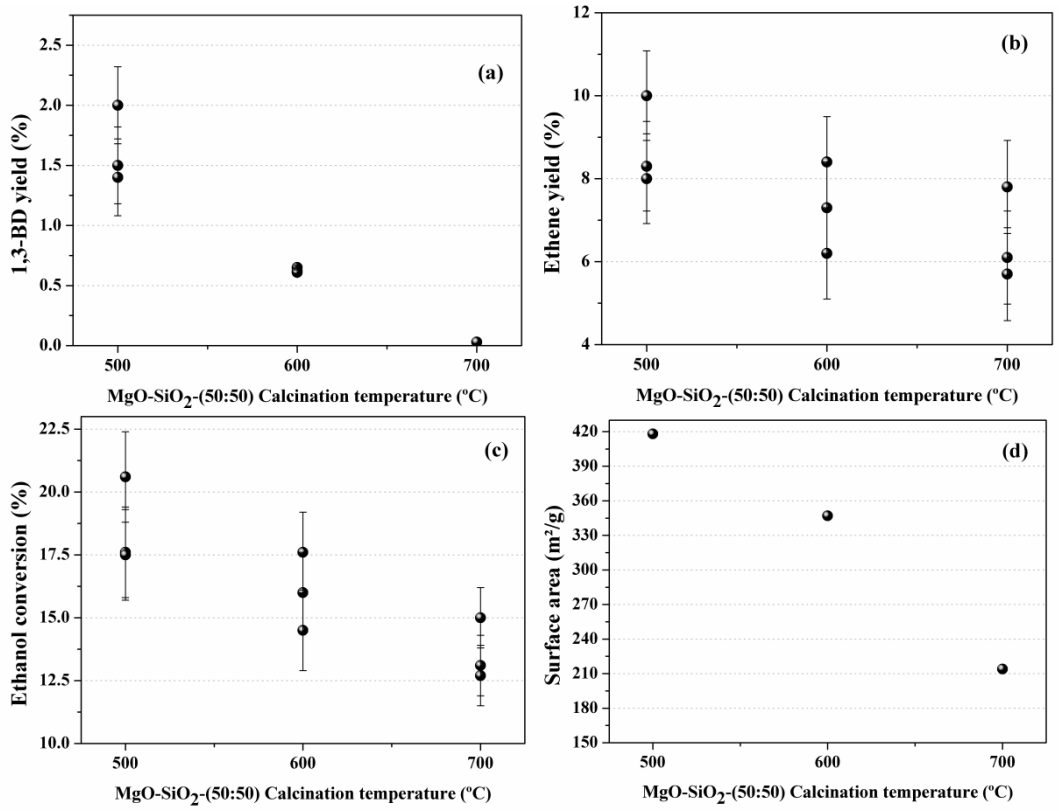

Figure 4.1.2 – Effect of the calcination temperature employed for preparation of the MgO-SiO_2-(50:50) systems using Method D on 1,3-BD yields (a); ethene yield (b); ethanol conversion (c); surface area (d). Reaction conditions: 350 ºC, WHSV of 0.8 h^{-1}, contact time of 0.2 s., ethanol molar fraction at the feed of 6 %, atmospheric pressure, and TOS of 0.5 h. Before reactions, samples were pre-treated *in situ* with N_2 (15 mL/min) for 1 h at 500 ºC (5 ºC/min). The catalytic unit employed was Unit 1.

4.1.1 Conclusions

The co-precipitation method was shown to be robust for preparation of MgO-SiO_2 systems, which resulted in similar average compositions of 1,3-BD and acetaldehyde in the outlet reactor stream.

Higher catalyst activity was observed when the catalyst was prepared and tested immediately after preparation, suggesting the occurrence of initial aging effects on the final oxide. These results, however, could not be considered as the true catalytic performances, because the same materials presented the average (and lower) catalytic performances when tested some days later. Thus, it is emphasized the importance of performing reaction replicates in order to evaluate the catalyst stability. It must be noted that care was taken in order to avoid the use of the catalyst right after its preparation procedure and no catalytic instability, as a result of catalyst aging, was observed in the experiments described in the following sections.

Higher calcination temperatures decreased the catalyst activity, being especially harmful for the 1,3-BD yields. This result was likely related to the sinterization of particles when higher temperatures were employed, as suggested by the reduction of the specific surface areas of the samples.

In the next section, the microkinetics of ethanol to 1,3-BD reactions over the MgO-SiO_2 catalysts was investigated through characterization of the experimental fluctuations. In order to do that, two MgO-SiO_2 catalyst systems (with Mg:Si molar ratios of 50:50 and 95:5, prepared with Method D) were studied, since these catalysts are employed widely for converting ethanol into 1,3-BD due to their intrinsic characteristic multifunctional properties (MAKSHINA *et al*., 2012, LEWANDOWSKI *et al*., 2014). Particularly, the effects of reaction temperature and catalyst properties on the covariance matrix of experimental fluctuations were investigated, as discussed in the next section.

4.2 Microkinetics of the ethanol to 1,3-butadiene conversion based on characterization of experimental fluctuations

4.2.1 Catalyst Properties

The effects of the Mg:Si molar ratio of MgO-SiO_2 catalysts prepared by co-precipitation on the performances of ethanol to 1,3-BD reactions were investigated and they are discussed in Section 4.3. In this section, the two catalysts employed for characterization of experimental fluctuations (with the Mg:Si molar ratios of 50:50 and 95:5) will be discussed in respect to their properties in order to highlight their very distinct features.

Figure 4.2.1 shows the diffraction patterns for samples MgO-SiO_2-(50:50) and MgO-SiO_2-(95:5). While diffraction patterns indicated amorphous features for the MgO-SiO_2-(50:50) sample, with broad peaks (at 25-30°, 33-39° and 58-62°) that are characteristic of magnesium silicate hydrates (BREW and GLASSER, 2005, LI *et al.*, 2014), the MgO-SiO_2-(95:5) sample presented diffractions at Bragg angles of 37º, 43º and 62º, suggesting the presence of MgO periclase phase (JANSSENS *et al.*, 2015).

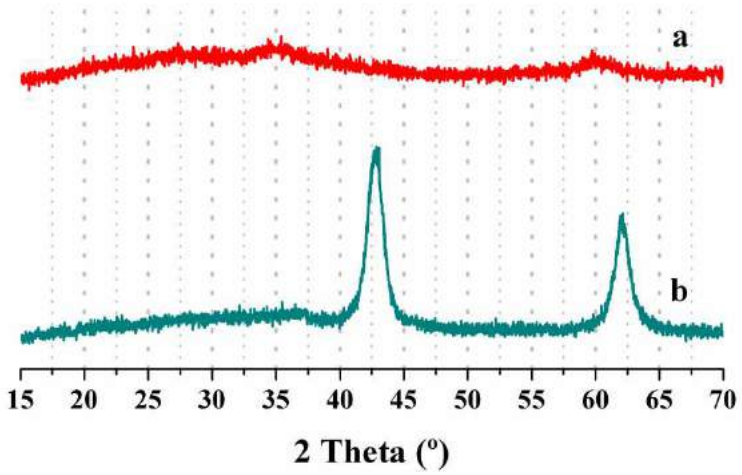

Figure 4.2.1 - XRD patterns of a) MgO-SiO_2-(50:50) and b) MgO-SiO_2-(95:5).

Surface areas were equal to 418 and 190 m^2/g, as determined for the MgO-SiO_2-(50:50) and MgO-SiO_2-(95:5) samples, respectively. To avoid internal pore diffusion limitations, catalysts particles were always grinded until sizes smaller than 53 μm.

The chemical composition estimated by XRF presented satisfactory agreement between nominal and measured Mg:Si molar ratios, as described in Table 4.2.1.

Table 4.2.1 - Chemical composition of samples, as determined by XRF.

Sample	*Mg:Si molar ratio*	
	Nominal	*Measured*
MgO-SiO_2-(50:50)	50:50	57:43
MgO-SiO_2-(95:5)	95:5	92:8

Finally, CO_2-TPD experiments were used to assess the basicity of catalyst samples. A huge difference in the *m/z* signal attributed to CO_2 was observed, as shown in Figure 4.2.2, indicating a higher concentration of basic sites for the MgO-SiO_2-(95:5) system, as expected. A desorption peak of CO_2 was also observed at temperatures above 500 ºC, Appendix F, indicating the presence of strong basic sites in the samples.

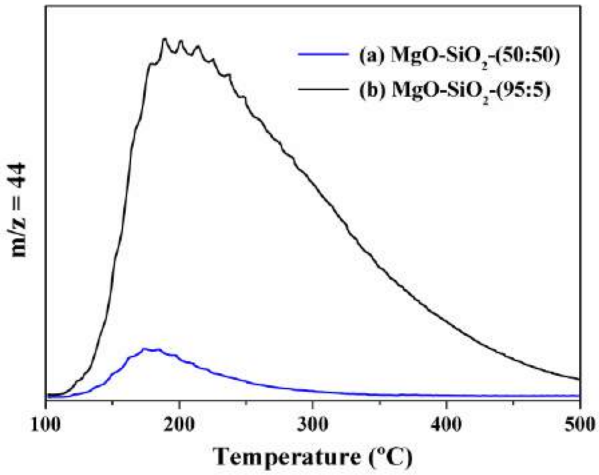

Figure 4.2.2 - CO_2-TPD profiles for the MgO-SiO_2-(50:50) (a) and MgO-SiO_2-(95:5) (b) samples.

4.2.2 Catalytic Reactions

The two catalysts, MgO-SiO_2-(50:50) and MgO-SiO_2-(95:5), were used to perform the ethanol reactions at reaction temperatures of 300, 350, 400 and 450 ºC. Thermogravimetric analyses of used catalysts indicated no significant catalyst

deactivation due to coke formation, as shown in Figure 4.2.3. Moreover, blank tests performed without the catalyst resulted in ethanol conversion approximately equal to zero (< 2 %, even at 450 ºC), suggesting that homogeneous gas phase reactions along the output lines were not important.

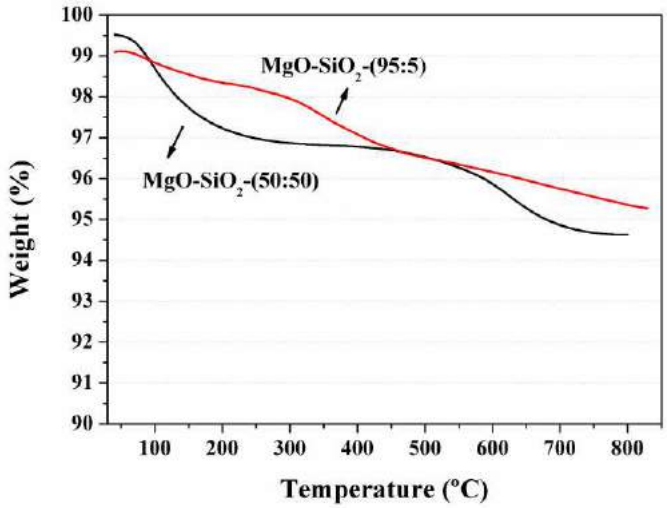

Figure 4.2.3 - Thermogravimetric analyses of used catalysts MgO-SiO_2-(50:50) and MgO-SiO_2-(95:5).

The main observed carbon containing products were ethene, 1,3-BD, acetaldehyde (AcH) and diethyl ether (DEE). In addition, traces of ethane, 1-butene, 2-butene, propene and CO_2 were also detected. Molar fractions of unconverted ethanol, main carbon containing products and hydrogen in the output stream are presented in Tables 4.2.2-4.2.3. It must be noted that molar fractions were selected as representative output variables because they were quantified directly through GC analyses, allowing for simpler discrimination between chromatographic measurement and catalytic reaction fluctuations.

Taking this into account, this section aims to present the experimental data used for characterization of catalytic reaction fluctuations. Table 4.2.4 presents the catalyst performances in terms of yields at distinct reaction temperatures, including carbon balances, which were typically better than 90 % for reactions performed with the MgO-SiO_2-(50:50) system. Average selectivities obtained over the MgO-SiO_2-(50:50) catalyst are shown in Table 4.2.5.

Table 4.2.2 - Output stream molar fractions of unconverted ethanol, main carbon containing products and hydrogen obtained with the MgO-SiO_2-(50:50) system (TOS of 0.5 h, WHSV of 0.8 h^{-1}, ethanol molar fraction at the feed equal to 6 %).

Reaction Temperature (ºC)	Molar fractions (%) [a]					
	Ethanol	1,3-BD	AcH	H_2	Ethene	DEE
300						
	5.621	0.048	0.070	0.031	0.063	0.080
	5.977	0.006	0.014	0.012	0.056	0.073
	5.836	0.009	0.018	0.029	0.053	0.072
350						
	4.813	0.061	0.053	0.086	0.617	0.219
	5.075	0.048	0.040	0.066	0.529	0.199
	4.949	0.043	0.041	0.084	0.499	0.202
400						
	1.941	0.193	0.087	0.249	2.785	0.160
	2.629	0.175	0.077	0.209	2.434	0.151
	2.412	0.178	0.085	0.241	2.418	0.195
450						
	0.139	0.289	0.093	0.376	4.403	0.008
	0.655	0.264	0.105	0.338	4.137	0.017
	0.250	0.295	0.096	0.374	4.354	0.015

[a] Molar fractions do not sum 100 % due to nitrogen (inert gas) and water molar fractions, which were omitted.

Table 4.2.3 - Output stream molar fractions of unconverted ethanol, main carbon containing products and hydrogen obtained with the MgO-SiO_2-(95:5) system (TOS of 0.5 h, WHSV of 0.8 h^{-1}, ethanol molar fraction equal to 6 %).

Reaction Temperature (ºC)	Molar fractions (%) [a]					
	Ethanol	1,3-BD	AcH	H_2	Ethene	DEE
300						
	5.271	0.012	0.031	0.063	0.015	0.003
	5.308	0.012	0.034	0.059	0.014	0.003
	5.309	0.010	0.028	0.060	0.016	0.004
350						
	4.617	0.084	0.088	0.254	0.077	0.006
	4.702	0.071	0.087	0.225	0.081	0.008
	4.681	0.074	0.087	0.237	0.076	0.006
400						
	3.126	0.319	0.208	0.810	0.262	0.008
	3.220	0.291	0.193	0.733	0.283	0.011
	3.101	0.299	0.197	0.765	0.257	0.009
450						
	0.838	0.601	0.238	2.146	0.645	0.002
	0.961	0.583	0.237	2.006	0.689	0.009
	0.909	0.591	0.237	2.018	0.632	0.008

[a] Molar fractions do not sum 100 % due to nitrogen (inert gas) and water molar fractions, which were omitted.

Table 4.2.4 - Catalytic results over the MgO-SiO_2-(50:50) system, for 0.5 h of time on stream (WHSV of 0.8 h^{-1}, ethanol feed molar fraction equal to 6 %).

Catalyst	T (ºC)	X (%)	Yield (mol %)[a]					Carbon Balance (%)
			1,3-BD	AcH	Ethene	DEE	Butene	
MgO-SiO_2-(50:50)								
		6.7	1.53	1.12	1.01	2.59	0.06	97.1
	300	3.7	0.19	0.22	0.87	2.28	0.00	97.5
		3.9	0.28	0.28	0.85	2.30	0.00	96.9
		20.6	1.95	0.86	9.96	7.07	0.14	97.8
	350	17.6	1.50	0.63	8.31	6.25	0.14	96.7
		17.5	1.36	0.66	7.97	6.45	0.11	95.6
		65.5	6.21	1.40	44.92	5.17	0.94	90.6
	400	55.3	5.50	1.21	38.26	4.73	0.77	92.3
		58.1	5.67	1.35	38.57	6.21	0.81	91.6
		97.4	9.35	1.50	71.01	0.26	1.61	87.5
	450	88.4	8.31	1.65	65.02	0.52	1.43	88.6
		95.5	9.42	1.52	69.45	0.49	1.57	87.8

[a] Product yields were calculated with Equation (3.5.3).

Table 4.2.5 - Average molar based selectivities obtained over the MgO-SiO_2-(50:50) system, for 0.5 h of time on stream (WHSV of 0.8 h^{-1}, ethanol molar fraction equal to 6 %).

Reaction temperature (ºC)	Selectivity average (mol %)*			
	1,3-BD	AcH	Ethene	DEE
300	9.2	15.7	31.9	41.9
350	5.8	5.2	63.6	24.1
400	6.0	2.7	83.8	5.6
450	5.9	2.0	89.4	0.28

*Only carbon containing products were considered.

The average values of molar fractions of the main products in the output stream are plotted as functions of the reaction temperature in Figure 4.2.4 for catalysts MgO-SiO_2-(50:50) and MgO-SiO_2-(95:5). The vertical bars represent the absolute standard deviations, which were calculated with the replicates.

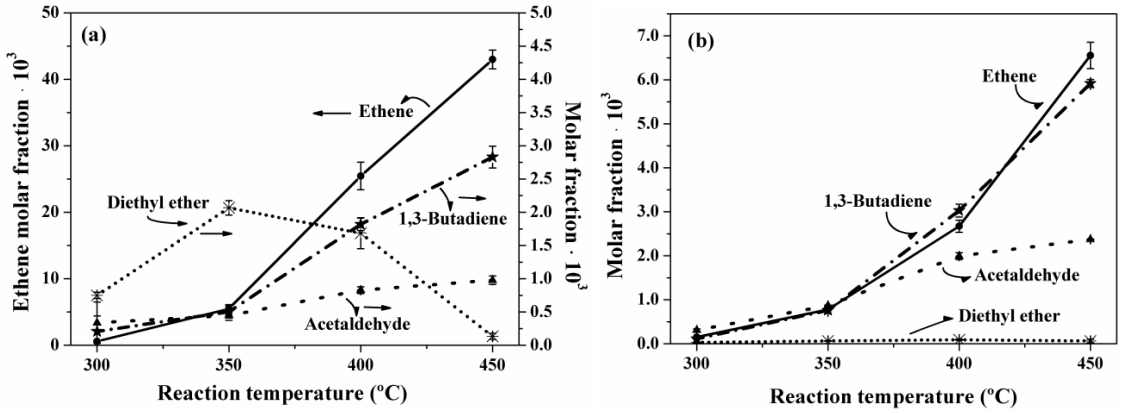

Figure 4.2.4 – Distribution of main carbon containing products: Ethene (●), 1,3-butadiene (★), diethyl ether (✳) and acetaldehyde (▲), for catalyst MgO-SiO_2-(50:50) (a) and MgO-SiO_2-(95:5) (b) as functions of reaction temperature (TOS = 0.5 h, feed rate of 0.8 g_{EtOH} g_{cat}^{-1} h^{-1}). Lines were drawn for clarity.

For catalyst MgO-SiO_2-(50:50), ethene was the main observed product from 350 to 400 ºC (left axis), while DEE was the main product at 300 ºC. Average ethanol conversion ranged from 4.7 %, at 300 ºC, to 93.8 %, at 450 ºC, with standard deviation equal to 1.7 % and 4.8 %, respectively. For catalyst MgO-SiO_2-(95:5), a different product distribution was obtained. In this case, the amounts of produced ethene were significantly smaller, when compared to the previous catalyst, although the amounts of 1,3-BD were similar. These results were in agreement with the higher basicity observed through CO_2-TPD characterizations for the MgO-SiO_2-(95:5) catalyst, as shown in Figure 4.2.1. The average ethanol conversion ranged from 6.2 %, at 300 ºC, to 83.0, at 450 ºC, with standard deviation equal to 3.4 % and 1.3 %. As expected, higher 1,3-BD, AcH and ethene molar fractions were observed with the increasing reaction temperature for both catalysts.

It is important to observe that the existence of mass transfer limitation effects in the catalytic experiments could be neglected, as shown in Figure 4.2.5, after estimation of the apparent activation energies. When pore diffusion limitations are important, experimentally apparent activation energies determined are expected to be approximately one half of the true value (FROMENT *et al*., 2011). Thus, a slope change in the Arrhenius plot may suggest that diffusion effects are present. Moreover, apparent activation energy values smaller than 20 kJ/mol, may also be an indication of existence of diffusion limitations (PEREGO and PERATELLO, 1999). Apparent activation

energy for the ethanol consumption was estimated as 60.2 and 51.6 kJ/mol for the MgO-SiO_2-(50:50) and MgO-SiO_2-(95:5) catalysts, respectively, as shown in Figure 4.2.5, suggesting that reaction rates were not limited by diffusional resistance. Linear correlation coefficients were equal to 0.99.

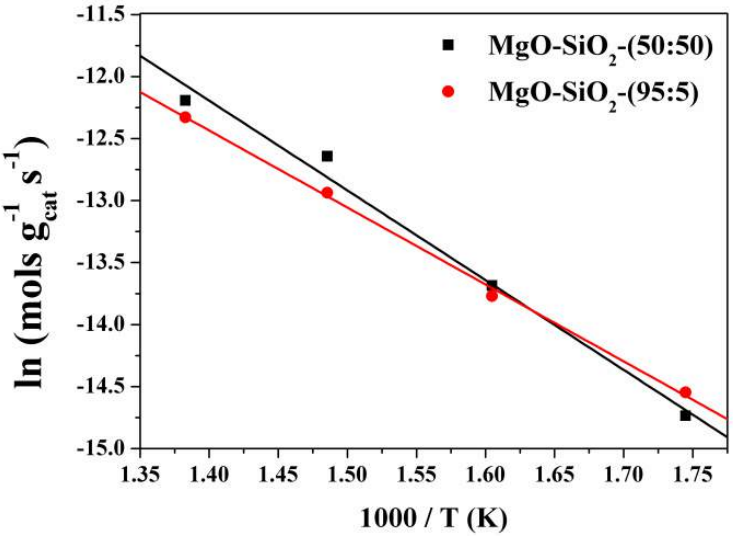

Figure 4.2.5 - Arrhenius plot for the ethanol consumption reaction, from 300 to 450 ºC.

However, in order to better evaluate the existence of mass transfer limitations presence, it is suggested that more detailed experiments be conducted. For assessing external transport limitations, it is advised to perform experiments varying the flow velocity, but keeping spatial time constant. In order to do this, both catalyst mass and reactant molar flow must be changed simultaneously. Then, if conversion remains constant in the experimental range, the conclusion is that there is no external transport limitation (FROMENT *et al*., 2011).

In order to assess internal mass transfer limitation, catalyst with different particle sizes should be used, and conversion should be measured at constant spatial time. If conversion varies by decreasing the particle size, it means that pore diffusion is important. On the other hand, constant conversion indicates chemical kinetic control. However, given the small scale of the reactor (100 mg of catalyst) and the small particle sizes employed in this study (< 53 μm), more detailed experiments evaluating mass transfer limitations were not performed.

4.2.3 Characterization of Chromatographic Measurement Fluctuations

Measurement fluctuations (experimental fluctuations from chromatographic analysis) were first determined to differentiate them from catalytic reaction fluctuations. In order to do this, compounds were analyzed chromatographically using distinct molar fraction compositions, using at least three replicates (see Section 3.4). It must be emphasized that these tests were not performed under reaction conditions and that the compounds were fed directly into the gas chromatograph equipment.

Figure 4.2.6 shows the effect of the average molar fraction on the respective variance of molar fraction measurements for ethanol (a), 1,3-BD (b), AcH (c), hydrogen (d), ethene (e) and DEE (f). The increase of variance could be observed as the average molar fraction increased, resulting in the relative molar fraction variance (variance divided by the square of the molar fraction) being approximately constant. This clearly shows that the assumption of constant measurement fluctuations can be indeed a very poor assumption for quantitative data analysis.

An empirical equation was then developed to describe molar fraction variance as a function of the average molar fraction. Data was fitted well by a quadratic function as $y = a \cdot x^2$, shown in Figure 4.2.6 as a line, where y represents the variance, x denotes the average molar fraction, and a is an empirical parameter, which is different for each compound and has the same definition of the relative molar fraction variance.

The effect of average molar fraction on its variance can possibly be associated with modification of the equilibrium states during the chromatographic separation, as the molar fraction increases, due to column overloading and different retention strengths for each solute (HARRIS, 2006). Change of the equilibrium states can result in wider chromatogram bandshapes, leading to an increase of the chromatographic variance (HARRIS, 2006).

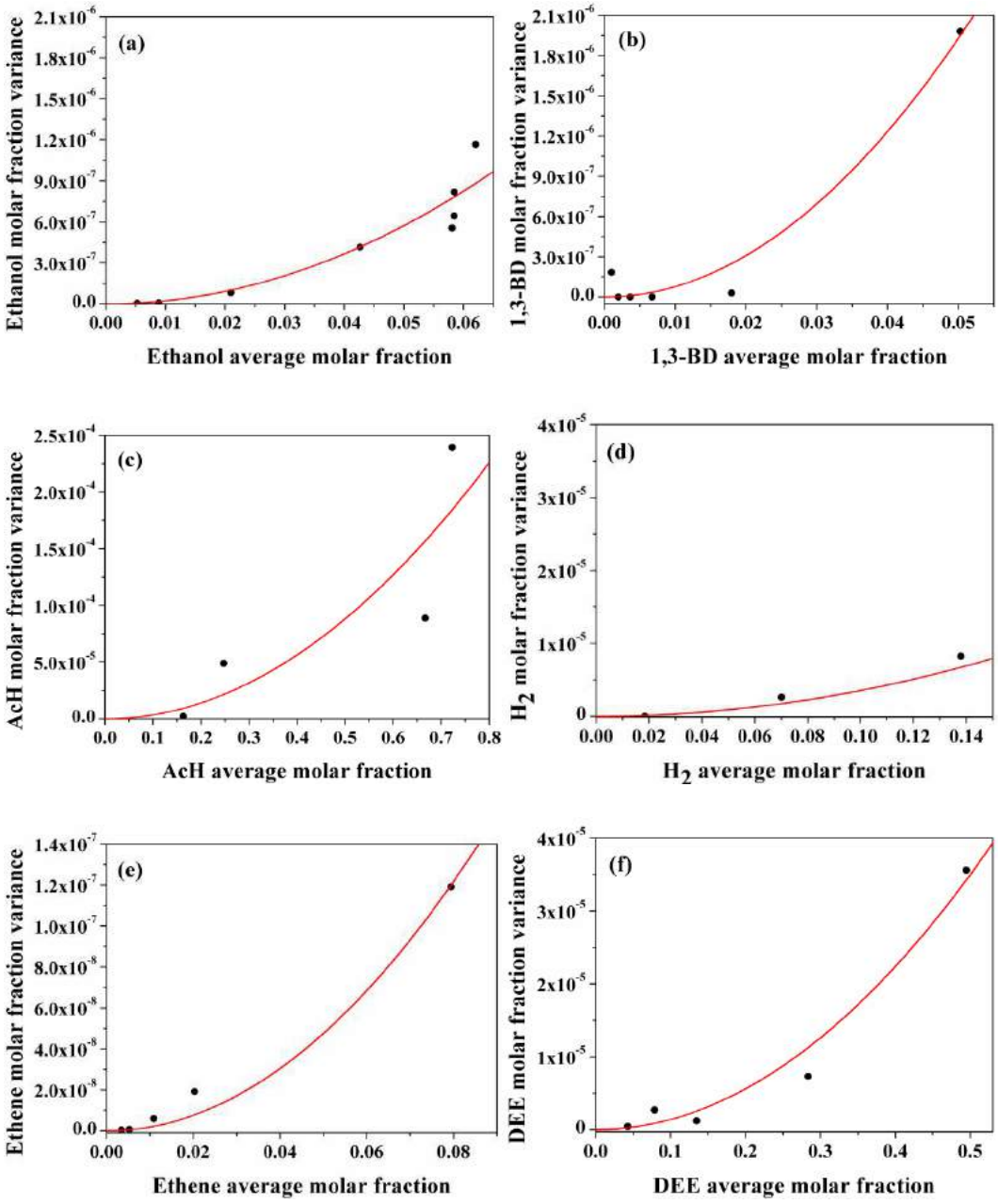

Figure 4.2.6 - Variance of molar fraction as function of average molar fraction from chromatographic analyses for ethanol (a), 1,3-BD (b), AcH (c), H_2 (d), ethene (e) and DEE (f): (●) experimental values, (-) empirical model.

4.2.4 Characterization of Catalytic Reactions Fluctuations

Variances of molar fractions measurements in the output stream were calculated with data presented in Tables 4.2.2 and 4.2.3 and using Eq. (3.4.1) at each reaction temperature. The obtained variances were statistically different at distinct reaction

temperatures and for the different catalysts, as verified with the standard F-test (BOX *et al*., 1978). This is very surprising, given the small number of degrees of freedom (equal to 2). For instance, for both catalysts, ethene molar fraction variance at 300 ºC was very different from the one obtained at 450 ºC. Acetaldehyde molar fraction variance obtained over the MgO-SiO_2-(95:5) catalyst at 400 ºC was also very different from the value obtained at 450 ºC. Moreover, variances among different compounds were very different. Consequently, the commonly used hypothesis of constant experimental error throughout the experimental region should not be applied for this reaction system. In other words, the diagonal of the covariance matrix V, as illustrated in the Section 3.4, has values that are statistically different.

Since the different reaction temperatures and catalysts lead to different ethanol conversions and product compositions, one might wonder whether molar fraction variances were different because of the molar fraction effect on chromatographic measurement fluctuations (as explained in Section 4.2.3) or because of the distinct catalytic reaction fluctuations. However, with help of the standard F-test (BOX *et al*., 1978), it can be concluded that catalytic reaction fluctuations cannot be explained only by the chromatographic measurement fluctuations, as illustrated in Figures 4.2.7 to 4.2.12. Consequently, it can also be concluded that there is at least one additional source of fluctuations in the reaction runs, other than the chromatographic measurement ones, and that this is related to the reaction phenomena itself, such as unavoidable fluctuation of catalyst activities (LARENTIS *et al*., 2003; ALBERTON *et al*., 2009).

Figures 4.2.7-4.2.12 show variances of molar fraction measurements obtained during catalytic reactions as functions of the average molar fraction for each compound. Each point is related to one reaction temperature for catalysts MgO-SiO_2-(50:50) (a) and MgO-SiO_2-(95:5) (b). In these figures, the empirical equations obtained to explain the chromatographic measurement fluctuations were plotted as continuous lines in order to allow for better visualization of the differences observed between variances from measurement and from catalytic reactions fluctuations. It must be emphasized that all molar fractions obtained during reaction experiments were in the same experimental range used to characterize the chromatographic measurement fluctuations and to build the respective empirical models, so that the empirical models provide good references of chromatographic measurement fluctuations in the analyzed ranges of molar fractions obtained during the reaction runs.

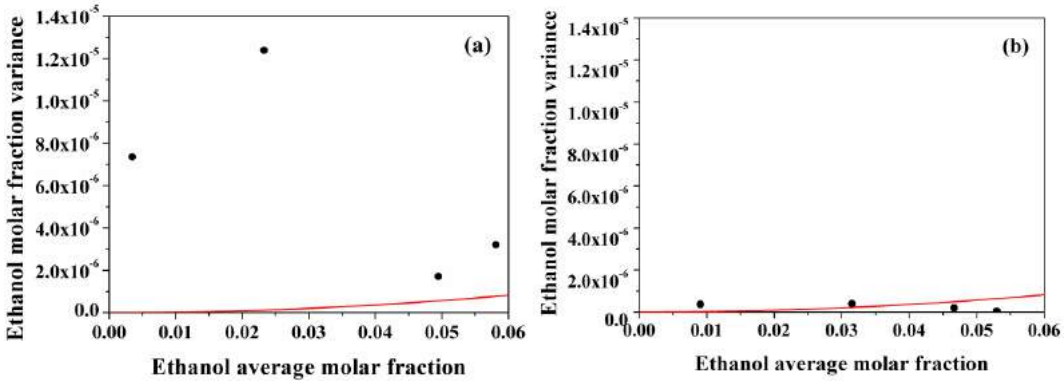

Figure 4.2.7 – Variances of ethanol molar fractions for catalytic reactions (●) and chromatographic measurement fluctuation model (-) as functions of ethanol average molar fractions for catalysts MgO-SiO_2-(50:50) (a) and MgO-SiO_2-(95:5) (b).

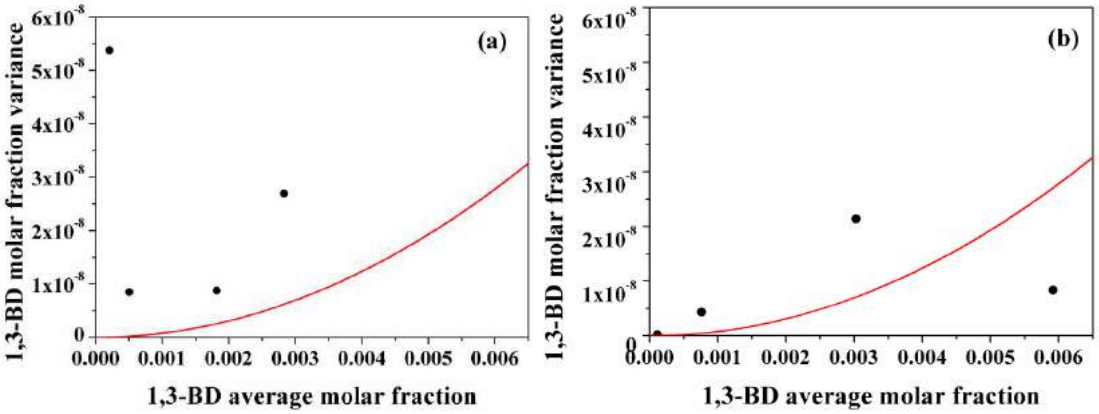

Figure 4.2.8 – Variances of 1,3-BD molar fractions for catalytic reactions (●) and chromatographic measurement fluctuation model (-) as functions of 1,3-BD average molar fractions for catalysts MgO-SiO_2-(50:50) (a) and MgO-SiO_2-(95:5) (b).

Whereas chromatographic measurement fluctuations increased with the respective average molar fraction, the same behavior was not observed for variances resulting from catalytic reactions. For instance, ethanol molar fractions variances in the output stream tended to decrease with the increase of the average molar fraction; that is, variances were reduced for low conversion values, as observed in reactions performed at 300 and 350 ºC, illustrated in Figure 4.2.7.

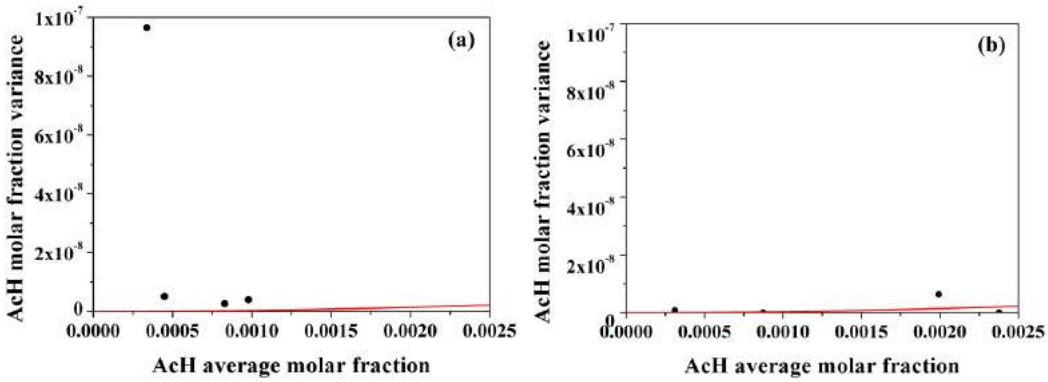

Figure 4.2.9 – Variances of AcH molar fractions for catalytic reactions (●) and chromatographic measurement fluctuation model (-) as functions of AcH average molar fractions for catalysts MgO-SiO_2-(50:50) (a) and MgO-SiO_2-(95:5) (b).

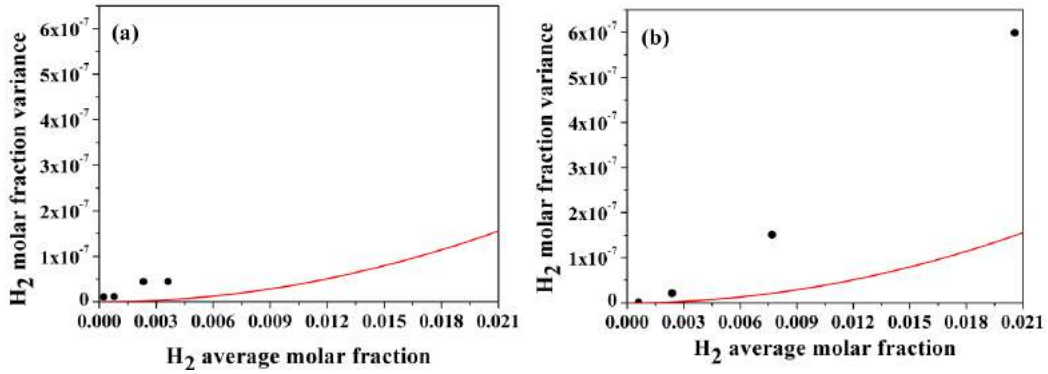

Figure 4.2.10 – Variances of hydrogen molar fractions for catalytic reactions (●) and chromatographic measurement fluctuation model (-) as functions of hydrogen average molar fractions for catalysts MgO-SiO_2-(50:50) (a) and MgO-SiO_2-(95:5) (b).

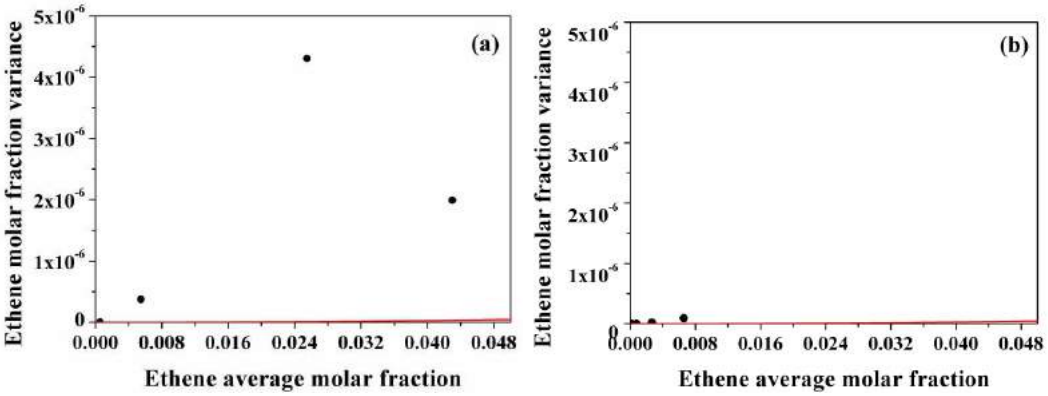

Figure 4.2.11 – Variances of ethene molar fractions for catalytic reactions (●) and chromatographic measurement fluctuation model (-) as functions of ethene average molar fractions for catalysts MgO-SiO_2-(50:50) (a) and MgO-SiO_2-(95:5) (b).

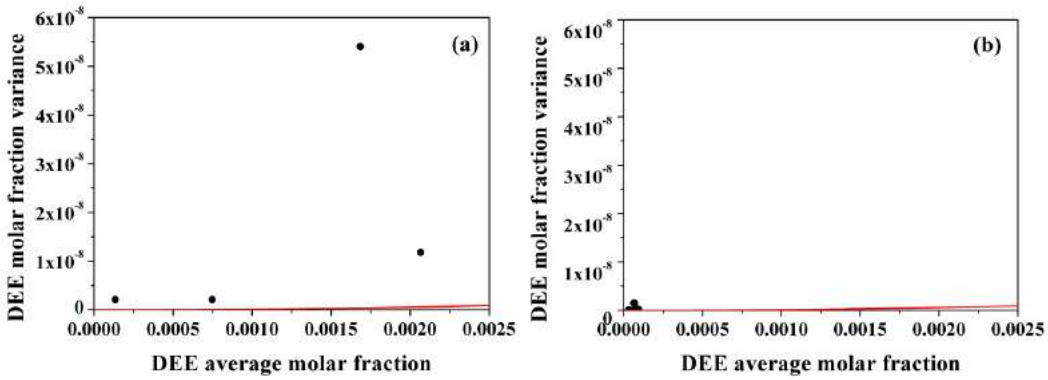

Figure 4.2.12 – Variances of DEE molar fractions for catalytic reactions (●) and chromatographic measurement fluctuation model (-) as functions of DEE average molar fractions for catalysts MgO-SiO_2-(50:50) (a) and MgO-SiO_2-(95:5) (b).

Moreover, whilst variances obtained with the MgO-SiO_2-(50:50) catalyst were higher than variances observed for chromatographic analyses, variances obtained with the MgO-SiO_2-(95:5) catalyst were similar to them, as observed in Figures 4.2.7(b), 4.2.8(b) and 4.2.9(b). Therefore, reaction conditions, including catalyst properties, may result in completely different experimental fluctuation behavior. These results indicate once more that catalytic reaction fluctuations should not be regarded as constant throughout the analyzed experimental region during quantitative data analysis.

In order to emphasize the variance differences associated with the catalyst properties, Figure 4.2.13 shows variances of ethanol molar fraction measurements obtained with catalysts MgO-SiO_2-(50:50) and MgO-SiO_2-(95:5). Dotted lines represent the upper and bottom 95% normal confidence limits for the assumption of similar variances, clearly indicating that variances were consistently lower for catalyst MgO-SiO_2-(95:5) and that at least one pair of variances could not be regarded as similar for both catalysts. It should be noted that variances were obtained for ethanol molar fractions of similar orders of magnitude, as one can visualize in Tables 4.2.2 and 4.2.3. Moreover, if catalyst properties did not exert any significant influence on variances of ethanol molar fractions, dots would be expected to be evenly distributed above and below the reference solid line in all cases, which could not be observed in the analyzed reaction runs. Therefore, it seems reasonable to assume that variances of ethanol molar fractions in the output stream depend on the analyzed catalyst.

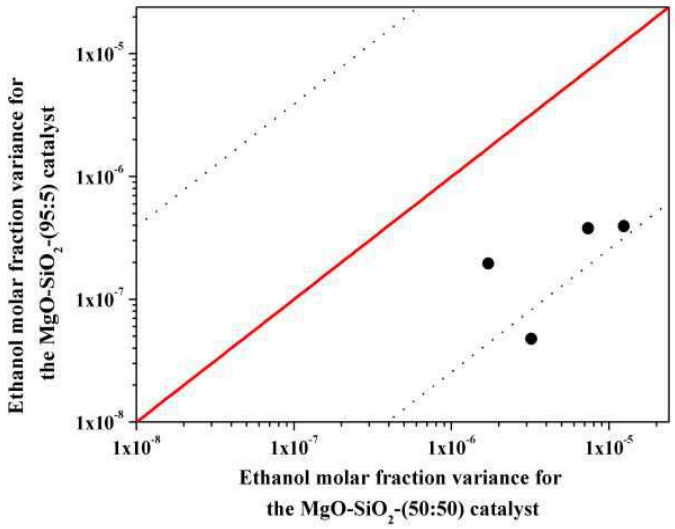

Figure 4.2.13 – Variances of ethanol molar fractions for catalysts MgO-SiO_2-(50:50) and MgO-SiO_2-(95:5).

Consequently, the larger catalytic reaction fluctuations observed in runs performed with catalyst MgO-SiO_2-(50:50) may contain significant amount of information about the reaction mechanism (LARENTIS *et al*., 2003, CERQUEIRA *et al*., 1999, RAWET *et al*., 2001). On the other hand, given the much lower fluctuation content in runs performed with catalyst MgO-SiO_2-(95:5), which were similar to the chromatographic measurement fluctuations, it may not be possible to obtain information about the reaction mechanism using the covariance matrix of catalytic reaction fluctuations for this catalytic system. Explaining why catalytic reaction fluctuations became much less important when the Mg:Si molar ratio was changed from 50:50 to 95:5 is beyond the scope of this work. However, a possible solution to allow the kinetic analysis of catalytic reaction fluctuations for the MgO-SiO_2-(95:5) system would be the determination of reaction conditions that would result in output compositions in the range where chromatographic measurement fluctuations attain the smallest possible values.

4.2.5 Principal Component Analysis

It must be noted that the mechanistic interpretation based on the information contained in the covariance matrix of catalytic reaction fluctuations is only possible if it is assumed that the observed fluctuations of outlet stream compositions are governed by

common sources of deviation, such as the intrinsic variability of catalyst activity. If fluctuations were governed by chromatographic measurement fluctuations, for instance, mechanistic interpretation of the covariance matrix would not make any sense, explaining why catalytic data obtained with the MgO-SiO_2-(95:5) catalyst cannot be used for kinetic interpretation.

In order to investigate whether fluctuations might have been induced by common sources of error, standard Principal Component Analysis (PCA) was performed with help of the software STATISTICA (STATSOFT INC., 1995). PCA results are presented in Table 4.2.6.

Table 4.2.6 - Principal directions of fluctuation, computed with standard PCA tools. Numbers represent correlations coefficients between the factor (eigenvector) and the original direction of variable fluctuation.

	Temperature							
	300 ºC		350 ºC		400 ºC		450 ºC	
	Factor 1	Factor 2	Factor 1	Factor 2	Factor 1	Factor 2	Factor 1	Factor 2
Ethene	**-0.93**	0.38	**-0.93**	-0.38	**-0.88**	0.48	**0.99**	0.02
1,3-BD	**-0.99**	0.10	**-0.91**	-0.41	**-0.95**	0.30	**0.94**	0.35
AcH	**-0.99**	0.10	**-0.99**	-0.09	**-0.93**	-0.37	**-0.99**	-0.01
Ethanol	**0.97**	0.25	**0.94**	-0.35	**0.99**	-0.14	**-0.99**	0.01
DEE	**-0.98**	0.20	**-0.99**	-0.004	-0.14	**-0.99**	**-0.75**	0.66
H_2	-0.68	**-0.73**	-0.69	**0.73**	**-0.92**	-0.39	**0.99**	0.15
Eigenvalue	5.20	0.79	5.03	0.97	4.39	1.60	5.41	0.59
Explained Variance (%)	86.7	13.3	83.9	16.1	73.2	26.8	90.2	9.8

Numbers in bold denote correlation coefficients higher than 0.7.

According to the standard PCA procedure, the eigenvalues and eigenvectors of the covariance matrices of catalytic reaction fluctuations were computed at each particular experimental condition and ordered in series of decreasing magnitudes. Assuming that catalytic reaction fluctuations follow the normal probability distribution, the confidence regions of data fluctuations can be described by a hyper-ellipsoid in the measured variable space, whose axes may have different sizes and do not necessarily coincide with the coordinate axes of the analyzed measurement space (SCHWAAB *et al*., 2008). In this case, the eigenvectors can be understood as the directions of variable fluctuation while the eigenvalues represent the relative importance of fluctuations along the distinct directions. Thus, if some of the eigenvalues present much larger magnitudes

than the remaining ones, this can possibly indicate that few sources of fluctuation perturb the measurements and that variable fluctuations respond simultaneously to few perturbations.

PCA results presented in Table 4.2.6 support the hypothesis that few common sources of fluctuation perturb the experimental system, as only one direction concentrates the largest part of the experimental variance for all reaction temperatures (for instance, at 450 ºC, 90 % of the experimental variance was due to one fluctuation direction). This common source of catalytic reaction fluctuations can be associated with different variables that characterize the experimental setup (ALBERTON *et al*., 2009). For instance, the most important source of fluctuation is expected to be the unavoidable variation of catalyst activity as a result of fluctuations of the reaction temperature, feed composition, catalyst mass or flow pattern in the catalyst bed.

Regardless of the true most important source of catalytic reaction fluctuations, the PCA shows that the covariance matrix of catalytic reaction fluctuations obtained through experimental replication can be valuable for interpretation of the ethanol to 1,3-BD reaction (LARENTIS *et al*., 2003). Moreover, PCA results highlight the relationship between the main reactant (ethanol) and the remaining products. From 300 to 400 °C, the vector coefficients of ethanol and of the other compounds have opposite signs, clearly indicating the roles of reactants and products. However, at 450 ºC these relationships vary, indicating that important mechanistic changes occur in the temperature range from 400 to 450 ºC, as discussed in the following sections.

4.2.6 Microkinetic Analysis of the Covariance Matrix of Catalytic Reaction Fluctuations

Molar fraction determined in the output stream obtained with catalyst MgO-SiO_2-(50:50), shown in Table 4.2.2, were used to compute the covariance matrix of composition measurements at each analyzed reaction condition using Eq. (3.4.1) and Eq. (3.4.2). Afterwards, the respective correlation matrix was calculated with Eq. (3.4.3). It could be clearly observed that molar fraction variances of the different compounds were not independent (correlation coefficients were significantly different from zero) and that the patterns of the observed correlations were different at distinct reaction temperatures, suggesting modification of the reaction mechanism with the

increase of reaction temperature. Based on the calculated correlation coefficients, it seems clear that the common assumption of independent fluctuations (and diagonal covariance matrix of catalytic reaction fluctuations) should be avoided.

4.2.6.1 Correlations between Ethanol and Reaction Products

Figure 4.2.14 shows the correlation coefficients between ethanol and the remaining reaction products. It can be seen that correlation coefficients change smoothly and steadily as temperature increases, supporting the physical interpretation of obtained correlation values (LARENTIS *et al.*, 2003).

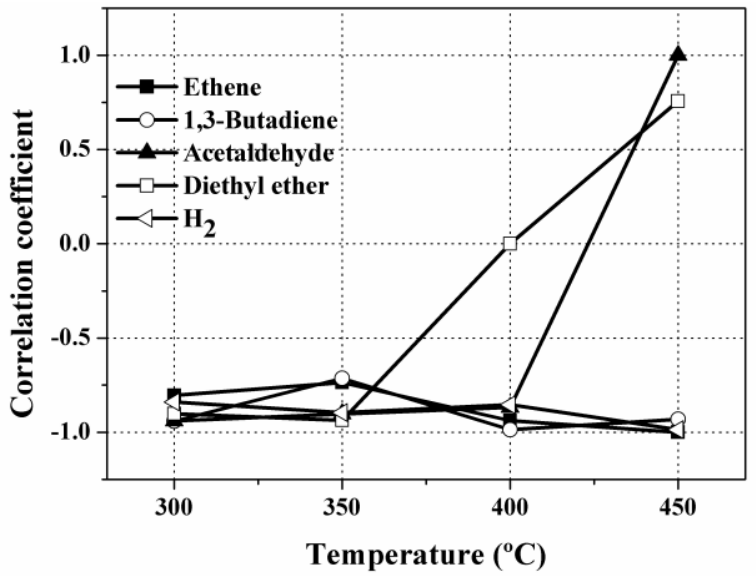

Figure 4.2.14 - Correlation coefficients between molar fractions of ethanol and of the major reaction products.

The correlation coefficient between ethanol and ethene showed negative values for all reaction temperatures, ranging from -0.7 to -1.0, indicating the strong negative correlation between ethanol and ethene molar fractions. Therefore, the amounts of ethanol and ethene fluctuate in opposite directions, as might already be expected, since ethene is a major product of ethanol dehydration, as described in Eq. (4.2.1).

$$C_2H_5OH \rightarrow C_2H_4 + H_2O \qquad (4.2.1)$$

Negative correlation coefficients for all reaction temperatures were also observed between ethanol and hydrogen and ethanol and 1,3-BD for similar reasons.

However, for AcH and DEE, ethanol correlation coefficients were negative at lower temperatures and strongly positive at 450 ºC, indicating a possible change in the mechanism.

Ethanol dehydrogenation is favored thermodynamically as reaction temperature increases, being favorable in all reaction temperatures investigated in this study, as shown in Section 1.4 and also discussed by other researchers (MAKSHINA *et al*., 2014, ANGELICI *et al*., 2013). Thus, negative correlation coefficients between ethanol and AcH would be expected as ethanol is consumed in order to produce acetaldehyde, Eq. (4.2.2), as it was observed for correlation coefficients at temperatures ranging from 300 to 400 ºC.

$$C_2H_5OH \rightarrow CH_3CHO + H_2 \qquad (4.2.2)$$

Nevertheless, AcH can also be produced in the proposed reaction pathway in the crotyl alcohol formation step, (step d, Figure 4.2.15, which is adapted from Figure 1.2.1 in order to illustrate ethanol dehydration to ethene and diethyl ether) where crotonaldehyde is reduced by ethanol.

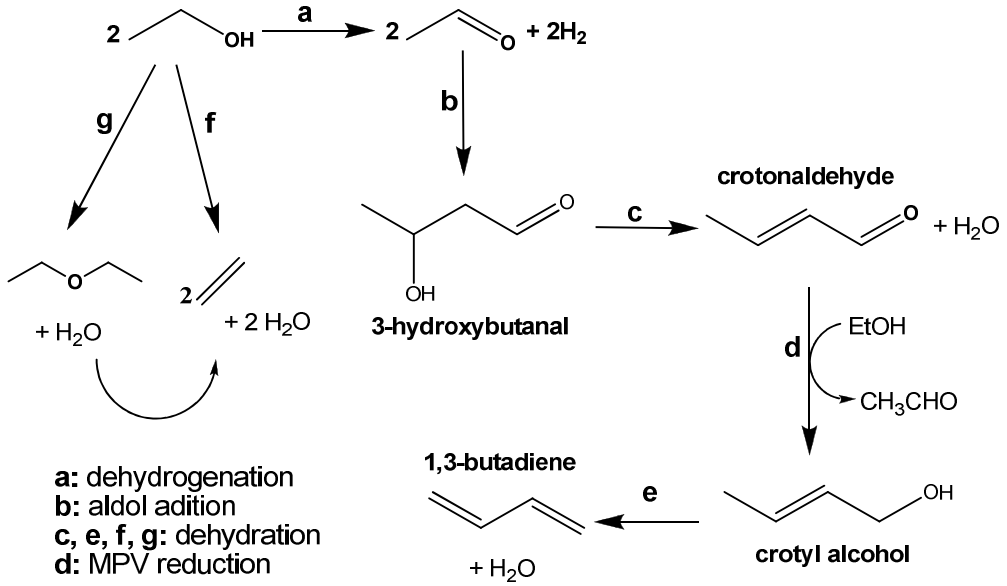

Figure 4.2.15 – Schematic representation of the reaction network (NIIYAMA *et al*., 1972, SUSHKEVICH *et al*., 2014).

Whereas aldol addition is an endergonic reaction in the analyzed temperature range, becoming more endergonic as reaction temperature increases (MAKSHINA *et al*., 2014), 3-hydroxybutanal dehydration to crotonaldehyde is favorable in the analyzed temperature range, becoming more favorable as the reaction temperature increases. As discussed by MAKSHINA *et al*. (2014), AcH formation is favored thermodynamically at higher temperatures and the excess of AcH in the system can contribute to AcH condensation. Therefore, the positive correlation coefficient between AcH and ethanol at 450 ºC suggests that the rate of the rate determining step, which is probably related to the 3-hidroxybutanal formation from AcH, increases at this temperature, resulting in higher rates of AcH consumption. As a consequence, ethanol and AcH molar fractions tend to fluctuate in the same direction at such reaction condition.

In order to understand the behavior of the correlation coefficients between molar fractions of ethanol and DEE, it is convenient to analyze first the correlation coefficients between ethene and DEE.

4.2.6.2 Correlations involving Ethene and DEE

Figure 4.2.16 shows the correlation coefficients between ethene and the remaining compounds. It is possible to verify the strong linear relationship between the amounts of DEE and ethene, which was positive at 300 and 350 ºC and became negative as reaction temperature increased. It is well-known that DEE formation from ethanol, Eq. (4.2.3), is an exothermic reaction, while ethene formation from ethanol dehydration, Eq. (4.2.1), is an endothermic reaction (ANGELICI *et al*., 2013).

$$2C_2H_5OH \rightarrow (C_2H_5)_2O + H_2O \quad (4.2.3)$$

$$(C_2H_5)_2O \rightarrow 2C_2H_4 + H_2O \quad (4.2.4)$$

Thus, the increase of reaction temperature favors the ethene formation and leads to decrease of DEE production. However, the strong negative relationship between ethene and DEE observed at 450 ºC can also be explained by DEE dehydration to ethene, Eq. (4.2.4) (SUSHKEVICH *et al*., 2014) and Figure 4.2.15. It must be noted that

even under kinetic regime, thermodynamic effects may contribute to changes on reaction rates, as equilibrium constants depend on temperature.

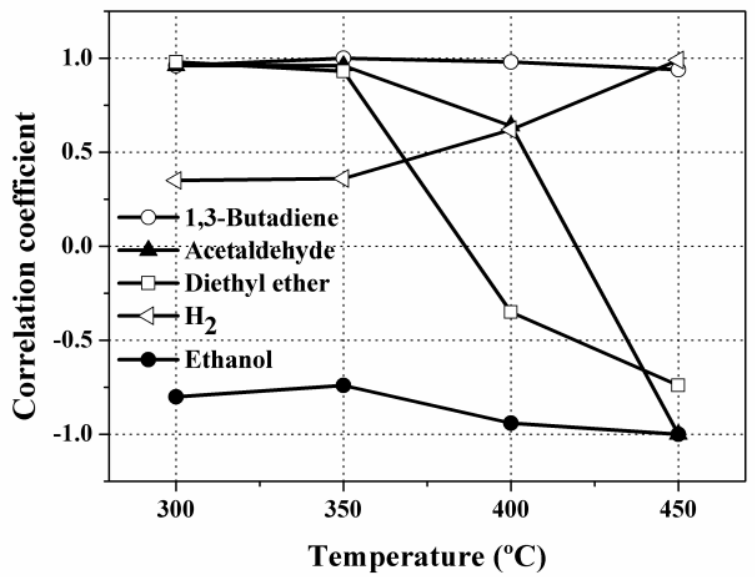

Figure 4.2.16 - Correlation coefficients between molar fractions of ethene and of the remaining major compounds.

Thus, at lower temperatures, both ethene and DEE are formed from ethanol. As reaction temperature increases, DEE can dehydrate to ethene and the production rate of DEE directly from ethanol decreases in respect to production rate of ethene. Both facts can explain why the amounts of ethene and DEE change in opposite directions at 400 and 450 ºC. Therefore, the positive correlation coefficient observed between ethanol and DEE at 400 and 450 ºC can be understood as fluctuations that take place along the same direction because of the small oscillations of the reaction activity.

As illustrated in Figure 4.2.14, the correlation coefficient between ethanol and 1,3-BD showed negative values at all reaction temperatures, as expected because 1,3-BD is the most important final product of the consecutive reactions starting from ethanol. Moreover, 1,3-BD and ethene are both final products in two independent parallel reaction sequences from ethanol (see Figure 4.2.15), which can explain the positive correlation coefficients between ethene and 1,3-BD molar fractions at all reaction temperatures, as shown in Figure 4.2.16. The positive correlation coefficients may also indicate that ethene and 1,3-BD do not compete for ethanol molecules, possibly suggesting the existence of excess of ethanol in the reacting system.

Furthermore, the Prins reaction, which has been described as a possible route for 1,3-BD formation from ethene and AcH (GRUVER *et al*., 1995), according to Eq. (4.2.5), does not seem to occur in large extent due to the positive correlations between ethene and 1,3-BD, even though this reaction is thermodynamically possible at the analyzed temperature range, as demonstrated in the Section 1.4.

$$C_2H_4 + CH_3CHO \rightarrow C_4H_6 + H_2O \quad (4.2.5)$$

As ethene and 1,3-BD are, respectively, reactant and product in Eq. (4.2.5), the significant occurrence of this reaction would probably lead to negative correlation coefficients between molar fractions of these two compounds (when 1,3-BD is produced, leading to higher 1,3-BD molar fractions, ethene is consumed, leading to lower ethene molar fractions). This finding is in accordance with the conclusions presented by SUSHKEVICH *et al*. (2014), who also ruled out the Prins reaction from experimental results for different ethanol conversions.

Similarly to 1,3-BD, hydrogen is also a final product, in the sense that it is not consumed by other side reactions after formation at the analyzed reaction conditions. As a consequence, the correlation coefficient between ethene and hydrogen molar fractions presented the same trends of correlation coefficients between 1,3-BD and ethene molar fractions. On the other hand, correlation coefficients observed between AcH and ethene showed trends that were similar to the ones observed for correlation coefficients between ethene and DEE. This can be rationalized in terms of the rates of acetaldehyde consumption when the reaction temperature increases, while ethene molar fractions remain high.

Figure 4.2.17 shows the correlation coefficients between DEE and the other analyzed compounds. As DEE is formed at lower temperatures, correlation coefficients between DEE and the other products are also positive. At higher reaction temperatures, correlation coefficient values become negative, indicating modification of the relative rates of some of the reactions. The molar fraction of the final products, 1,3-BD, hydrogen and ethene, show negative correlation coefficients with DEE molar fraction at 450 ºC, probably because the latter is dehydrated to ethene. On the other hand, ethanol and AcH molar fractions show positive correlation coefficients with DEE, as ethanol,

AcH and DEE might be being consumed at high rates at the highest reaction temperature.

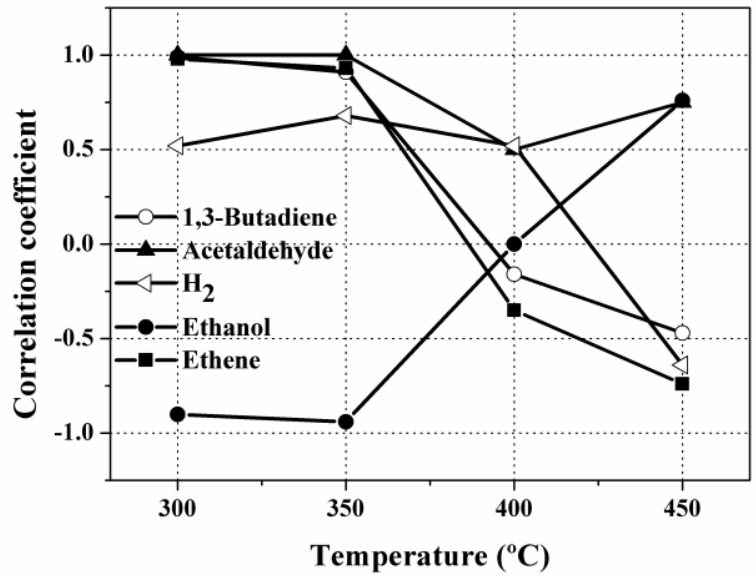

Figure 4.2.17 - Correlation coefficients between molar fractions of diethyl ether and of the remaining major compounds.

4.2.6.3 Correlations involving AcH and 1,3-BD

Correlation coefficients between molar fractions of AcH and of the other compounds are shown in Figure 4.2.18. Again, the positive correlation coefficients between AcH and ethanol, and AcH and DEE, highlight that AcH is consumed rapidly at 450 ºC. As 1,3-BD, hydrogen and ethene are produced at high rates at 450 ºC, correlation coefficients are negative in these cases. It is interesting to observe the relationship between 1,3-BD and AcH molar fractions, which clearly illustrate the modification of the relative rates of reaction. While from 300 to 400 ºC molar fractions of AcH and 1,3-BD were positively correlated, the correlation coefficient became negative at 450 ºC. This suggests that both 1,3-BD and AcH are formed in the system in the temperature range from 300 to 400 ºC, indicating that the acetaldehyde condensation can be the slowest reaction step in this temperature range. However, at 450 ºC the rate of AcH consumption increases sharply, resulting in negative correlation coefficients between AcH and 1,3-BD molar fractions. Therefore, it can be suggested that the slowest reaction step at 450 ºC is related to the ethanol dehydrogenation.

Finally, correlation coefficients between molar fractions of 1,3-BD and of other compounds are shown in Figure 4.2.19. The correlation coefficients between molar fractions of 1,3-BD and of other final products, such as hydrogen and ethene, are positive, indicating that these compounds are produced as reaction temperatures increase.

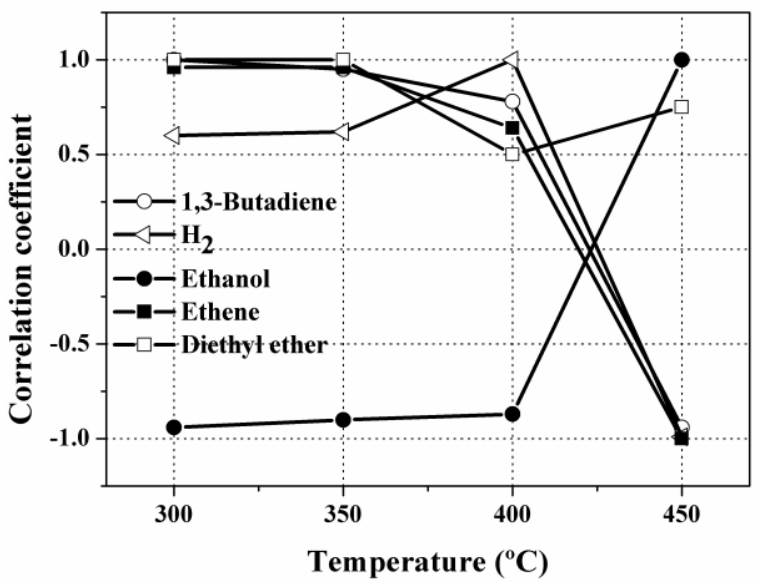

Figure 4.2.18 - Correlation coefficients between molar fractions of acetaldehyde and of the remaining major compounds.

It has been discussed whether hydrogen could participate in the crotonaldehyde reduction, instead of ethanol (BHATTACHARYYA and SANYAL, 1967). As pointed out by some authors (BHATTACHARYYA and SANYAL, 1967, ANGELICI *et al*., 2013), hydrogen participation is less probable and, therefore, should not be involved in the crotyl alcohol formation. The positive correlation coefficients between 1,3-BD and hydrogen in Figure 4.2.19 support this hypothesis. If hydrogen was involved in the crotonaldehyde reduction, hydrogen would be consumed and a negative correlation coefficient between 1,3-BD and hydrogen molar fractions would be expected.

The correlation analyses are in line with PCA results presented in the previous section, since the compounds that are also consumed at high rates at 450 ºC according to the previously discussed kinetic mechanism, that is, AcH and DEE, presented vector coefficients with the same sign of the vector coefficient of ethanol at this temperature, as shown in Table 4.2.6.

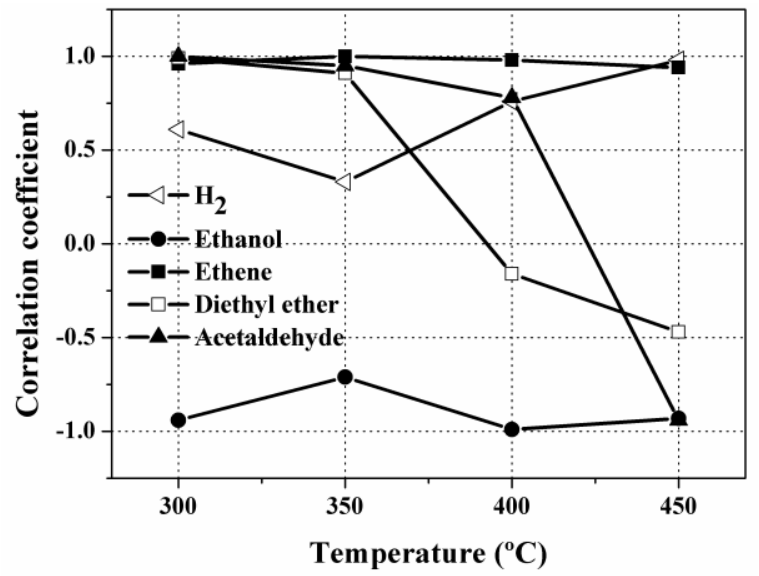

Figure 4.2.19 - Correlation coefficients between molar fractions of 1,3-butadiene and of the remaining major compounds.

4.2.7 Conclusions

In this section, it was shown that both reaction temperature and catalyst properties affected the behavior of the catalytic reaction fluctuations over MgO-SiO_2 catalysts significantly. Molar fraction fluctuations of distinct compounds in the output stream were not independent and were statistically different at distinct reaction conditions, making the usual constant and independent error assumptions invalid for quantitative data analysis. Furthermore, it was also shown that experimental fluctuations from the chromatographic measurement system were functions of the compound composition.

As the covariance matrix of catalytic reaction fluctuations could be discriminated from chromatographic measurement fluctuations, the covariance matrix of catalytic reaction fluctuations could be used for local microkinetic interpretation of the available data.

Particularly, correlation analyses performed with data obtained with the MgO-SiO2-(50:50) catalyst indicated that the ethanol to 1,3-BD reaction mechanism probably involves two distinct slow steps in the analyzed temperature range. From 300 to 400 ºC, acetaldehyde condensation is expected to limit the reaction rates, while ethanol dehydrogenation is expected to be the slowest reaction step at 450 ºC. Standard PCA reinforced the proposed kinetic interpretation and indicated that variability of catalyst

activity probably constitutes the most important source of experimental fluctuation in the analyzed reaction system.

Based on these previous results, the next step of the study was dedicated to the investigation of the potential improvement that the addition of ZrO_2 and ZnO over MgO-SiO_2 systems prepared by co-precipitation could cause on the 1,3-BD-yield, as presented in the next section.

4.3 ZrZn-Containing MgO-SiO_2 Systems Prepared by Co-precipitation for the Ethanol into 1,3-Butadiene Conversion

This section describes the investigation of using the co-precipitation method for preparation of ZrZn-containing magnesium silica oxide catalysts with different Mg-to-Si (Mg:Si) molar ratios for the ethanol conversion into 1,3-BD. In order to study in detail the role of the Mg-to-Si molar ratio, the performances of pure MgO-SiO_2-*x* systems were compared to performances of materials containing ZrO_2 and ZnO. Materials were prepared as described in Section 3.1.1 and 3.1.2, and the catalytic unit employed was Unit 2, described in Section 3.5.

4.3.1 The effect of the Mg:Si molar ratio

Initially, magnesium silica oxide catalysts prepared at different Mg:Si molar ratios were evaluated at 325 °C, using an ethanol weight hourly space velocity (WHSV) of 0.62 h^{-1}. At this condition, ethanol conversion was typically lower than 20 %, allowing for clear observation of the different catalytic properties among the catalysts samples.

Figure 4.3.1 shows the selectivity profile of the main carbon containing products, obtained after 3 h of time on stream, as a function of the Mg:Si molar ratio for (a) MgO-SiO_2 systems and (b) MgO-SiO_2 systems containing a fixed amount of ZrO_2 and ZnO, which had previously shown to be optimum for SiO_2 catalysts and are kept

constant in order to provide a reference for comparison to this previous work (JONES *et al*., 2011, LEWANDOWSKI *et al*., 2014). Profiles observed for ethene, diethyl ether (DEE) and acetaldehyde (AcH) show the same general trend as a function of the Mg:Si molar ratio. Whereas ethene and DEE selectivities decreased as the Mg:Si molar ratio increased, AcH selectivity showed a sharp increase, from less than 10 % with the 50:50 species to over 40 % with higher amounts of MgO. The decrease in the ethanol dehydration, along with the increase in the ethanol dehydrogenation, as the Mg:Si molar ratio increased is in agreement with a reduction of catalyst acidity, while basicity is boosted, as expected when the Mg:Si increases (NIIYAMA *et al*., 1972, OCHOA *et al*., 2016) and also in line with CO_2-TPD experiments presented in the previous section (Figure 4.2.1).

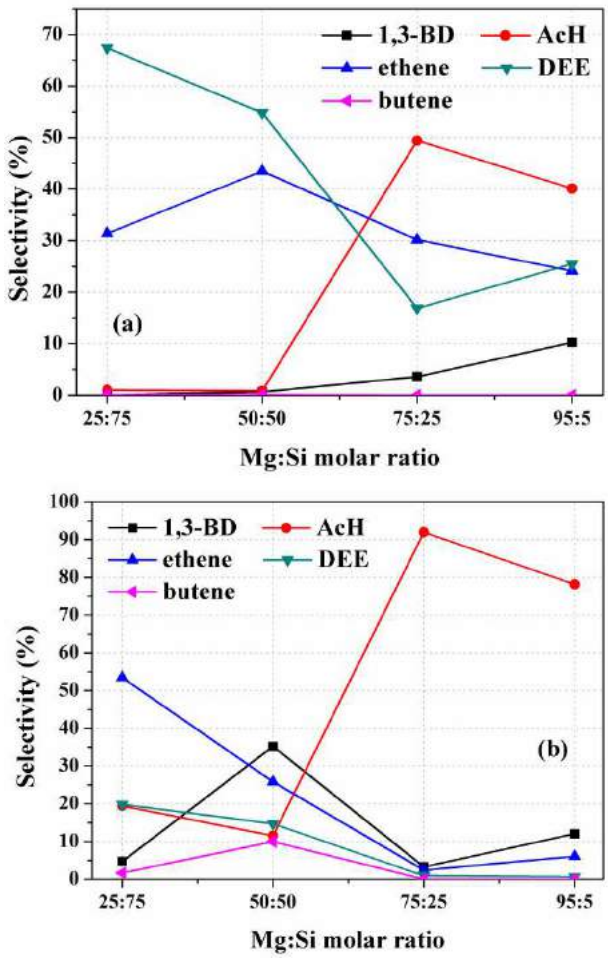

Figure 4.3.1 Mg:Si molar ratio effect on main carbon containing reaction products selectivities for (a) MgO-SiO_2 systems and (b) MgO-SiO_2 systems containing ZrO_2 and ZnO (T of 325 ºC, TOS of 3 h, WHSV of 0.62 h^{-1}, contact time of 4 s).

On the other hand, the effect of the Mg:Si molar ratio on 1,3-BD selectivity was different between $MgO\text{-}SiO_2$ systems and $MgO\text{-}SiO_2$ systems containing ZrO_2 and ZnO. While a smooth rise in 1,3-BD selectivity was verified as the Mg:Si molar ratio increased for pure $MgO\text{-}SiO_2$ samples, as shown in Figure 4.3.1 (a), the same trend was not observed for catalysts containing ZrO_2 and ZnO, as shown in Figure 4.3.1(b). Instead, a maximum in the 1,3-BD selectivity was obtained for the catalyst with the Mg:Si molar ratio equal to one.

The effect of the Mg:Si molar ratio for Zn(II) and Zr(IV) containing $MgO\text{-}SiO_2$ systems, using the wet-kneading method for $MgO\text{-}SiO_2$ preparation has been previously studied (JONES *et al*., 2011). In line with results presented in Figure 4.3.1, $MgO\text{-}SiO_2$ systems prepared by the wet-kneading method have shown different 1,3-BD selectivity behavior upon the addition of ZrO_2:ZnO to the catalyst. However, while a maximum in the 1,3-BD selectivity was observed at the Mg:Si molar ratio equal to 75:25 for the pure $MgO\text{-}SiO_2$ systems, an increase in 1,3-BD selectivity was observed as the Mg:Si molar ratio was increased for systems prepared by incipient wetness (that is, containing ZrO_2 and ZnO) (JONES *et al*., 2011). These results are in contrast with those reported here, as shown in Figure 4.3.1, emphasizing that the co-precipitation preparation procedure has dramatically changed the physicochemical properties of the catalyst, when compared to the wet-kneading procedure.

Figure 4.3.2 shows a comparison between 1,3-BD yields registered between pure and ZrO_2 and ZnO containing $MgO\text{-}SiO_2$ systems. For all Mg:Si molar ratios, the ZrO_2 and ZnO boosted catalyst activity to 1,3-BD. In particular, at the Mg to Si ratio equal to one, the 1,3-BD yield over the $ZrZn/MgO\text{-}SiO_2$ -(50:50) was fifty times higher than in its parent $MgO\text{-}SiO_2$ -(50:50) with no ZrO_2 and ZnO. It is assumed that ZnO is active for ethanol dehydrogenation, since oxidized Zn species (e.g., Zn^{2+}, Zn^{1+}) could act as Lewis centers associated to adjacent active oxygen species (O^-, O^{2-}) (JONES *et al*. 2011, DI COSIMO *et al*., 1998). On the other hand, besides catalyzing the *MPV* reduction of crotonaldehyde (JONES *et al*. 2011), incorporation of zirconia on silica results in formation of further Lewis acid sites and might induce Brønsted acidity of silanol groups, assisting self aldol addition (ORDOMSKY *et al*., 2010), which is believed to be the rate-limiting step of the reaction system. Figure 4.3.3 illustrates the surface mechanism proposed on ZrO_2/SiO_2 catalyst.

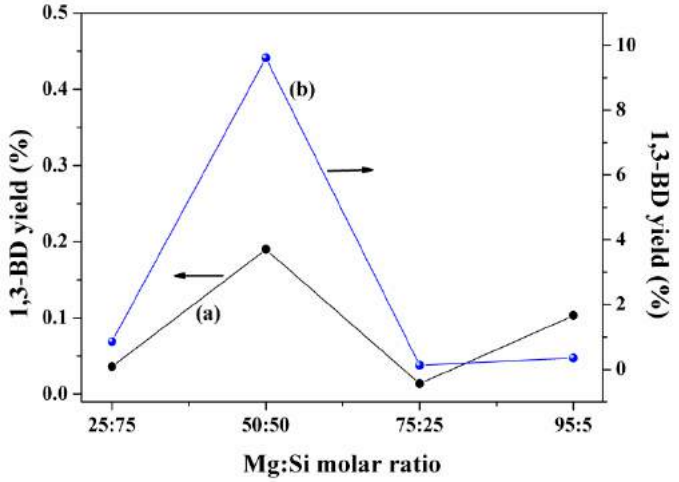

Figure 4.3.2 Mg:Si molar ratio effect on 1,3-BD yield (a) MgO-SiO_2 systems and (b) MgO-SiO_2 systems containing ZrO_2 and ZnO (T of 325 ºC, TOS of 3 h, WHSV of 0.62 h^{-1}, contact time of 4 s).

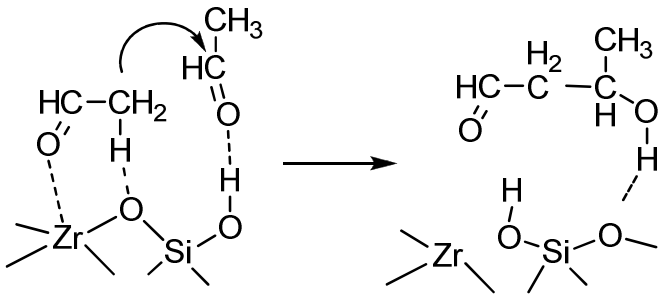

Figure 4.3.3 - Self aldol addition on ZrO_2/SiO_2 surface, according to ORDOMSKY *et al*. (2010).

Regarding textural properties, samples with higher Mg:Si molar ratio showed lower surface areas, when compared to the 50:50 and 25:75 ratios, which may indicate the formation of MgO particles in the pores of the samples, as shown in Table 4.3.1 (MAKSHINA *et al*., 2012, LEWANDOWSKI *et al*., 2014).

Moreover, diffraction patterns indicated samples with amorphous features, although the MgO periclase phase was observed in the MgO-SiO_2-(95:5) sample (peaks at Bragg angles of 37.0º, 43.0º, 62.4º) (JANSSENS *et al*., 2015), as shown in Figure 4.3.4. In particular, the ZrZn/MgO-SiO_2-(50:50) system presented broad peaks (at 25-30°, 33-39° and 58-62°) characteristic of magnesium silicate hydrates (BREW and GLASSER, 2005, LI *et al*., 2014). Since samples containing ZrO_2 and ZnO have shown similar pXRD patterns, when compared to the initial MgO-SiO_2-*x* support (for instance, compare diffraction patterns *c* and *d*), ZrO_2 and ZnO should be dispersed into the -Mg-

O-Si- network or their small loading was undetectable by pXRD. These results further highlight the effect of preparation method on catalyst properties, since MgO phase was observed even for Mg:Si molar ratio equal to 1, using a sol-gel technique (OCHOA *et al.*, 2016).

Table 4.3.1 - BET surface area of catalyst samples with different Mg-to-Si molar ratios.

Sample	Surface area (m^2/g)
MgO-SiO_2-(25:75)	328 ± 15 [a]
MgO-SiO_2-(50:50)	368 ± 4
MgO-SiO_2-(75:25)	14 ± 0.1
MgO-SiO_2-(95:5)	135 ± 0.1
ZrZn/MgO-SiO_2-(75:25)	31 ± 0.2
ZrZn/MgO-SiO_2-(50:50)	323 ± 7
ZrZn/MgO-SiO_2-(25:75)	107 ± 3

[a] Standard deviation denotes the value estimated from the B.E.T fitting to the N_2 physisorption data.

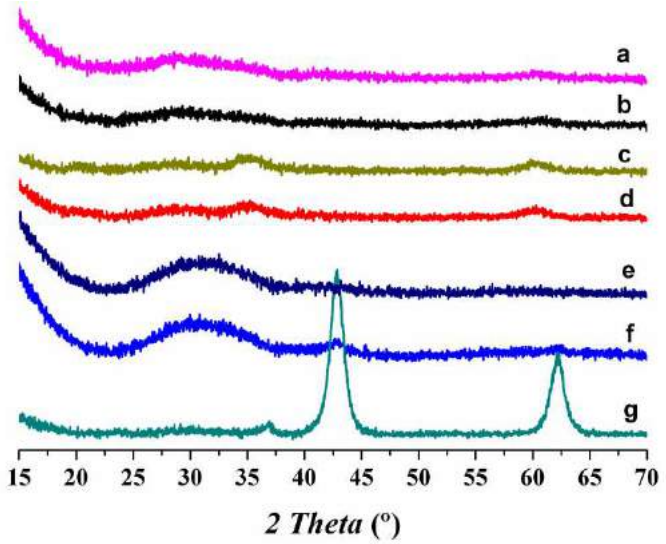

Figure 4.3.4 - XRD patterns of a) ZrZn/MgO-SiO_2-(25:75), b) MgO-SiO_2-(25:75), c) ZrZn/MgO-SiO_2-(50:50), d) MgO-SiO_2-(50:50), e) ZrZn/MgO-SiO_2-(75:25), f) MgO-SiO_2-(75:25), g) MgO-SiO_2-(95:5).

The local environment of the silicon atoms on the catalyst surface was investigated through ^{29}Si MAS NMR spectroscopy. A clear modification of silicon environments as a function of the Mg:Si molar ratio was suggested by ^{29}Si {^{1}H} CP MAS NMR experiments, as shown in Figure 4.3.5. Catalysts with higher amount of MgO, MgO-SiO_2-(95:5) and MgO-SiO_2-(75:25) samples, presented a single resonance with maxima around -71 ppm, indicating a high concentration of Q^1 species. Conversely, as the Mg:Si molar ratio was decreased, MgO-SiO_2-(50:50) and MgO-SiO_2-(25:75) samples, resonances maxima were shifted down field, to around -87 and -94 ppm, indicating an increase in Q^2 and Q^3 species (JANSSENS *et al.*, 2015, BREW and GLASSER, 2005, HARTMAN and MILLARD, 1990). In comparison with the wet-kneading method (LEWANDOWSKI *et al.*, 2014), Q^2 and Q^3 species were observed at the Mg:Si molar ratio equal to 75:25, and Q^2, Q^3 and Q^4 species were observed at the Mg:Si molar ratio equal to 1. Thus, the co-precipitation method used in this work seems to be more efficient for formation of Mg-O-Si linkages.

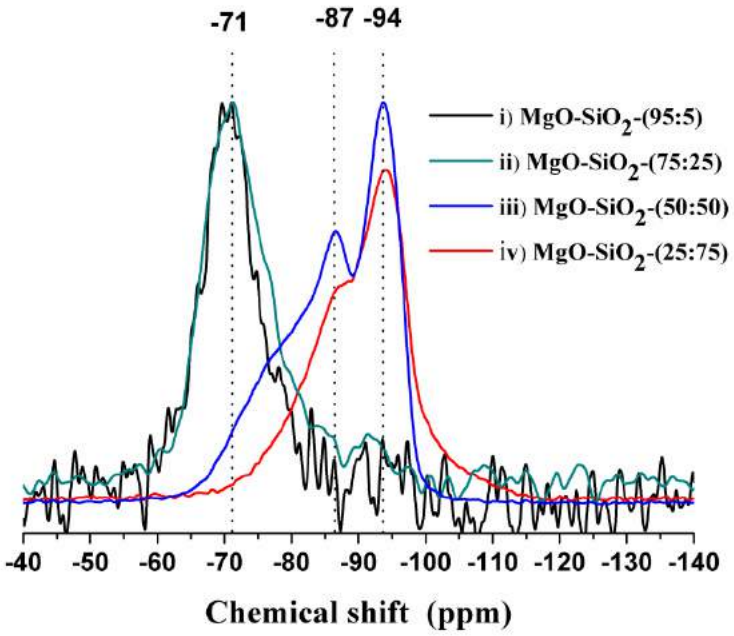

Figure 4.3.5 - $^{29}Si\{^{1}H\}$ CP MAS NMR spectra of catalysts i) MgO-SiO_2-(95:5), ii) MgO-SiO_2-(75:25), iii) MgO-SiO_2-(1:1), iv) MgO-SiO_2-(25:75).

Figure 4.3.6 illustrates typical silicon environments associated to species Q^1, Q^2, Q^3, and Q^4, for amorphous silica and their respective chemical shifts (JANSSENS *et al.*, 2015). Similar signals with chemical shift between -85 and -89 ppm and between -92

and -99 ppm were already reported for magnesium silicate systems and they were attributed to Q^2 and Q^3 species, respectively, as Si*(OMg)$(OSi)_2$(OH) and Si*(OMg)$(OSi)_3$ (JANSSENS *et al.*, 2015, BREW and GLASSER, 2005, HARTMAN and MILLARD, 1990). Thus, silicon environments from MgO-SiO_2 systems investigated in this work could be suggested as illustrated in the Figure 4.3.7. Moreover, the lack of signal at -110 in Figure 4.3.5 indicates the absence of silica in the catalyst structure, or the presence of an amount too small to be detected (BREW and GLASSER, 2005).

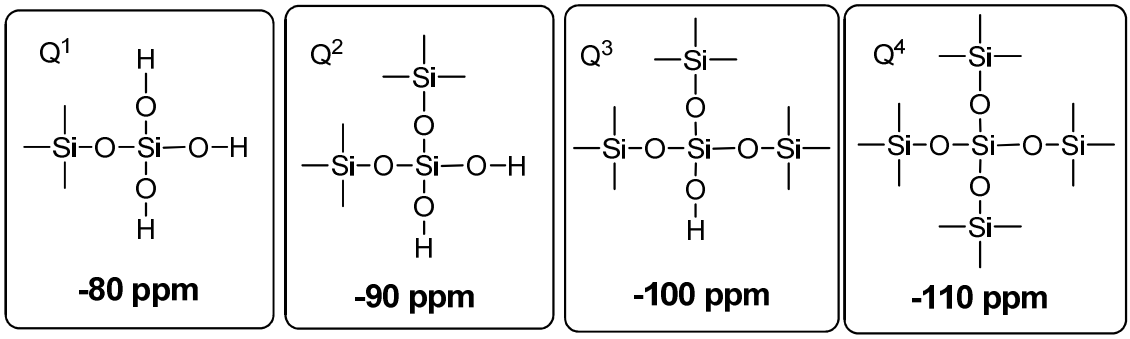

Figure 4.3.6 - Illustration of typical silicon environments for amorphous silica and their chemical shifts (JANSSENS *et al.*, 2015).

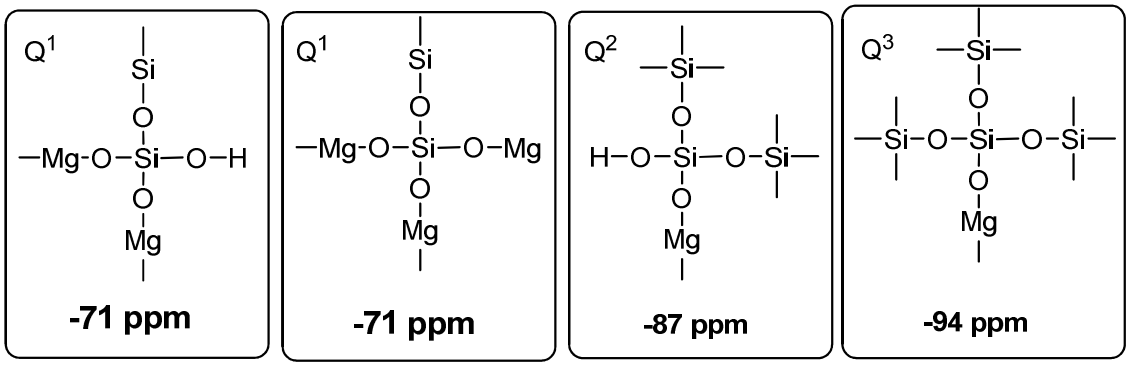

Figure 4.3.7 – Proposal for silicon environments for MgO-SiO_2 systems as characterized from Figure 4.3.5.

A similar behavior of increasing Mg-O-Si linkage concentration was verified for samples containing ZrO_2 and ZnO, as shown in Figure 4.3.8. However, the effect of ZrO_2 and ZnO catalyst doping on silicon environments was not as pronounced as observed for Mg:Si molar ratio. In fact, resonances maxima indicated similar

concentration of each silicon environment between pure and ZrO_2 and ZnO containing MgO-SiO_2 samples at the same Mg-to-Si molar ratio, as shown in Figures 4.3.9-4.3.11.

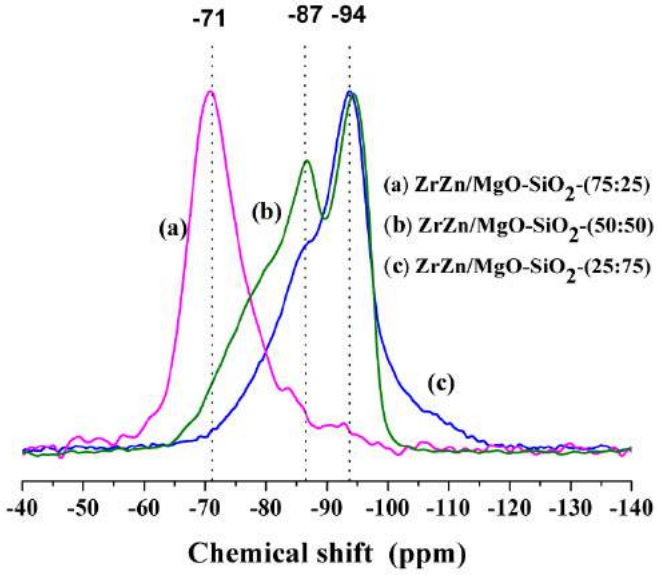

Figure 4.3.8 - $^{29}Si\{^1H\}$ CP MAS NMR spectra of catalysts (a) ZrZn/MgO-SiO_2-(75:25), (b) ZrZn/MgO-SiO_2-(50:50), and (c) ZrZn/MgO-SiO_2-(25:75).

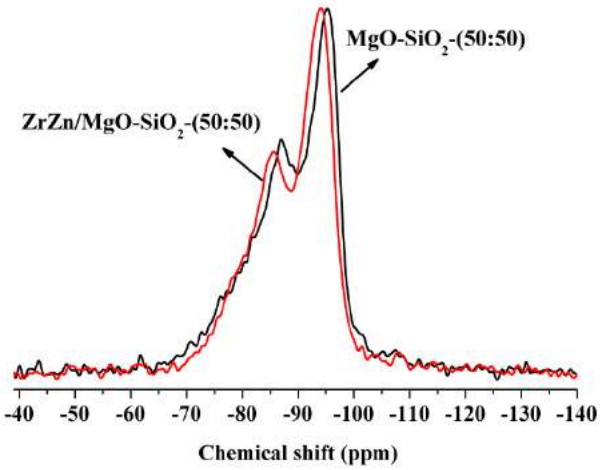

Figure 4.3.9 - ^{29}Si MAS NMR spectra of catalysts MgO-SiO_2-(50:50) and ZrZn/MgO-SiO_2-(50:50).

Thus, these results suggest that the higher concentration of Q^2 silicon environments observed in samples with the Mg-to-Si molar ratio equal to one was important to yield higher amounts of 1,3-BD. However, the participation of such sites, such as silanol Brønsted acid sites, on the overall reaction pathway of 1,3-BD formation

was likely not important, since very different catalytic performances were observed between samples MgO-SiO_2-(50:50) and ZrZn/MgO-SiO_2-(50:50). Therefore, the Mg-to-Si molar ratio equal to one resulted in the most suitable dispersion of Zr and Zn species, boosting 1,3-BD yield.

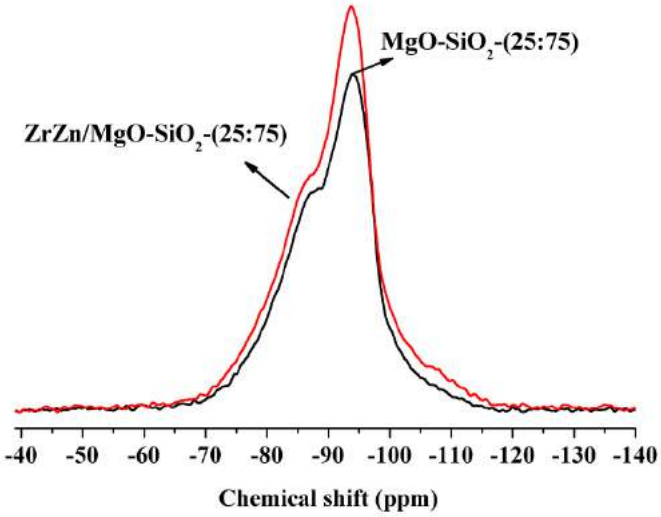

Figure 4.3.10 - $^{29}Si\{^{1}H\}$ CP MAS NMR spectra of catalysts MgO-SiO_2-(25:75) and ZrZn/MgO-SiO_2-(25:75).

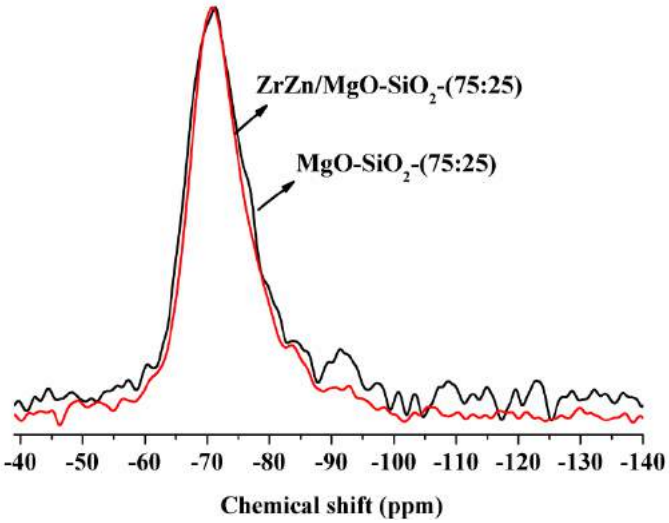

Figure 4.3.11 - $^{29}Si\{^{1}H\}$ CP MAS NMR spectra of catalysts MgO-SiO_2-(75:25) and ZrZn/MgO-SiO_2-(75:25).

The reproducibility of the dispersion degree of Zr and Zn species among different catalyst preparation batches was confirmed by ^{29}Si MAS NMR experiments, as shown in Figure 4.3.12. These results are in agreement with a general uniform

distribution of elements inside catalyst particles, as observed for the ZrZn/MgO-SiO_2-(50:50) sample through scanning electron microscopy with energy dispersive X-ray, as shown in Figure 4.3.13. Although a residual amount of Na was observed from catalyst preparation, as detailed in the following sections, these Na traces did not significantly affect catalyst activity.

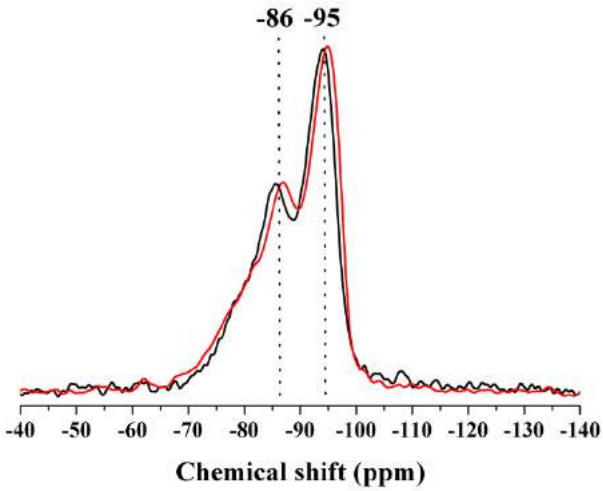

Figure 4.3.12 - ^{29}Si MAS NMR spectra of catalysts ZrZn/MgO-SiO_2-(50:50) prepared from different synthesis batches.

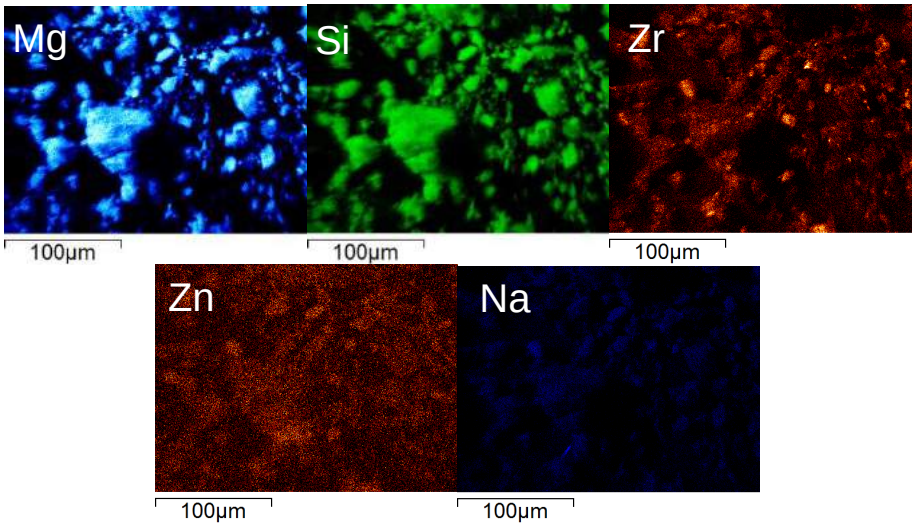

Figure 4.3.13 - Elemental mapping of the ZrZn/MgO-SiO_2-(50:50) catalyst.

Since the synergistic effect of ZrO_2 and ZnO on the MgO-SiO_2 system was more beneficial to 1,3-BD formation at the Mg:Si molar equal to one, this catalytic system was selected for further investigation. In the next section, the effect of reaction

temperature and ethanol flow rate over the ZrZn/MgO-SiO_2-(50:50) catalyst is discussed. In particular, the ethanol flow rate was investigated in order to assess the catalyst performance regarding 1,3-BD productivity (in $g_{bd}/g_{cat}.h$), a variable usually neglected (OCHOA *et al*., 2016, ANGELICI *et al*., 2014, KLEIN *et al*., 2016, CHAE *et al*., 2016), but fundamental to assess the potential of industrial applicability of this catalytic system.

4.3.2 Reaction Temperature and Spatial Velocity Effect

Initially, the effects of reaction temperature and WHSV were investigated in order to evaluate the catalyst performance and afford insights about the kinetic mechanism. In order to assess the possible existence of mass transfer limitation, catalytic reactions were performed at five different temperatures, 300, 325, 350, 375 and 400 ºC using an intermediate WHSV condition equal to 0.93 h^{-1}. Figure 4.3.14 (a) shows Arrhenius plots for ethene and acetaldehyde between 300 and 400 ºC. Apparent activation energy were estimated for the reaction temperature range between 300 and 375 ºC, as shown in Figure 4.3.14(b), as 97.7 and 77.2 kJ/mol for ethene and acetaldehyde formation, respectively, suggesting that the reaction rates of the main ethanol consumption reactions were not limited by diffusional resistances. Linear correlation coefficients were equal to 0.99. Carbon balances were equal to 89, 105, 110, 106 and 112 % for reactions performed at 300, 325, 350, 375 and 400 ºC, respectively.

The effect of reaction temperature and WHSV on ethanol dehydration products is shown in Figure 4.3.15. It must be noted that higher WHSV conditions correspond to higher ethanol molar fraction in gas phase and lower contact times simultaneously, since WHSV was modified by changing ethanol flow rate only, keeping catalyst mass and inert flow rate constant.

As expected, an increase in reaction temperature increased ethene selectivity, as shown in Figure 4.3.15(a), and decreased DEE selectivity, as shown in Figure 4.3.15(b), as ethanol dehydration to ethene is endothermic and to DEE is exothermic (ANGELICI *et al*., 2013, KNÖZINGER and KÖHNE, 1966). Although the mechanism of DEE formation is still discussed in the literature, regarding whether it involves acid-base pairs (JAIN and PILLAI, 1967, SHI and DAVIS, 1995), Brønsted acid sites and/or

Lewis acid sites (SHI and DAVIS, 1995), it is understood that DEE formation should involve the reaction of the two nearest chemisorbed ethanol moieties (ARAI *et al.*, 1967).

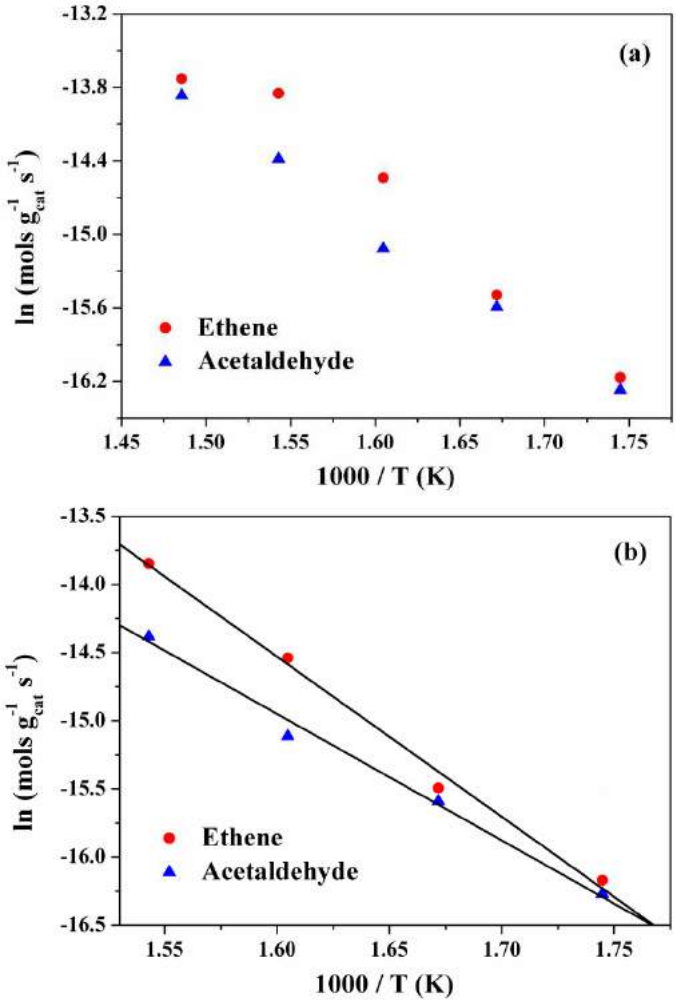

Figure 4.3.14 - Arrhenius plot for ethene and acetaldehyde from 300 to 400 ºC (a), and from 300 to 375 ºC (b). WHSV of 0.93 h^{-1}.

On the other hand, ethene formation should occur through a concerted mechanism, where the methyl hydrogen of the ethoxide species, chemisorbed on a Lewis (ARAI *et al.*, 1967) or Brønsted acid site (KNÖZINGER *et al.*, 1972), is abstracted by the adjacent Brønsted basic site. Indeed, using an alumina catalyst, ARAI *et al.* (1967) observed the increase of DEE formation as the concentration of surface ethoxide was increased, while ethene formation was suppressed. Therefore, the effects of WHSV on ethene and DEE selectivities observed in this work suggest the increase of

the concentration of chemisorbed ethanol species on the catalyst surface, with the concurrent increase in WHSV, since higher ethanol molar fractions were fed at higher WHSV conditions.

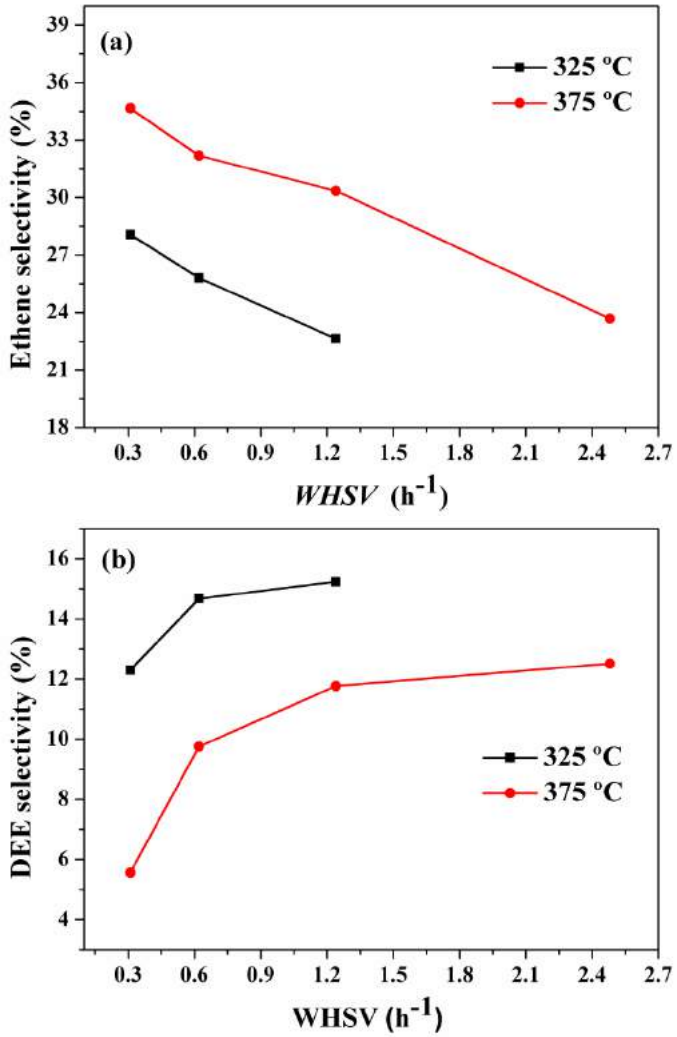

Figure 4.3.15 - WHSV and reaction temperature effects on (a) ethene and (b) DEE selectivities (ZrZn/MgO-SiO_2-(50:50), TOS of 3 h).

Figure 4.3.16 shows the effect of reaction temperature and WHSV on AcH and 1,3-BD selectivities. The AcH selectivity increases for both reaction temperatures as WHSV increases, as shown in Figure 4.3.16(a). Since ethanol dehydrogenation to AcH involves Brønsted basic sites and Lewis acid sites (DI COSIMO *et al*., 1998, GRUVER *et al*., 1995), these trends suggest a high concentration of active sites for ethanol dehydrogenation on the catalyst surface.

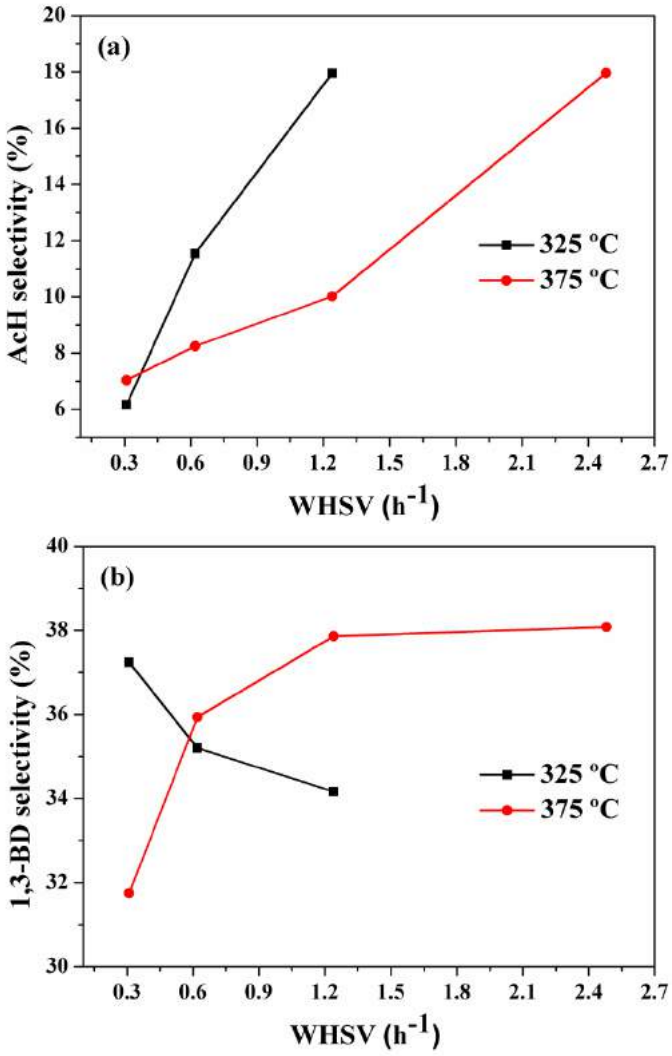

Figure 4.3.16 - WHSV and reaction temperature effects on (a) AcH and (b) 1,3-BD selectivities (ZrZn/MgO-SiO_2-(50:50), TOS of 3 h).

As discussed in Section 4.2, the AcH transformation involves 3-hydroxybutanal formation and its subsequent dehydration to crotonaldehyde (MAKSHINA *et al*., 2014, JONES *et al*., 2011). Whereas the aldol coupling is an endergonic reaction in the studied temperature range, which becomes more endergonic as reaction temperature increases (MAKSHINA *et al*., 2014), 3-hydroxybutanal dehydration to crotonaldehyde is favorable in this temperature range and becomes more favorable as the temperature increases. Thus, since ethanol dehydrogenation to AcH is favored thermodynamically as the reaction temperature increases, an excess of acetaldehyde in the system might

contribute to further AcH condensation, explaining its lower selectivities at 375 ºC (MAKSHINA *et al*., 2014).

1,3-BD selectivity presented different trends as functions of reaction temperature and WHSV, as shown in Figure 4.3.16(b). While at the higher temperature the increase of 1,3-BD selectivity with WHSV might be related to an excess of AcH in the system, at the lower temperature, contact time appears to affect 1,3-BD formation more dramatically. This same effect of contact time was observed by SUSHKEVICH *et al*. (2014), who evaluated the WHSV effect using an $Ag/ZrO_2/SiO_2$ system at 320 ºC. Besides, additional experiments varying the WHSV at 375 ºC and using the same ethanol molar fraction (the amount of catalyst remained constant and the gas flow and ethanol feed rate were both varied), indicated the same general trend observed at 325 ºC, as shown in Figure 4.3.17. This implies that the extra ethanol present in the higher WHSV processes facilitates the conversion to 1,3-BD, as observed previously (JONES *et al*., 2011).

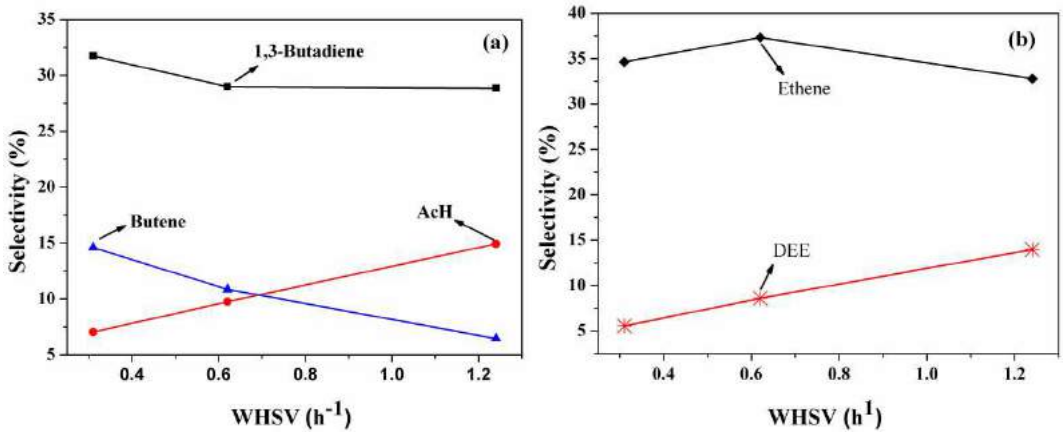

Figure 4.3.17 - Effect of WHSV on selectivity of the main carbonaceous products over the ZrZn/MgO-SiO_2-(50:50) system (375 ºC, TOS of 3 h, ethanol molar fraction of 0.4). (a) 1,3-butadiene (■), acetaldehyde (●) and butene (▲); (b) ethene (♦) and diethyl ether (✳).

Butene selectivity (1-butene, *cis*- and *trans*-2-butene) decreased smoothly as the WHSV was increased at both reaction temperatures, as shown in Figure 4.3.18. The formation of butene from ethanol is believed to occur through deoxygenation of butanal produced from crotyl alcohol isomerisation (MAKSHINA *et al*., 2014). Other studies

suggest butene as a butanol dehydration product, butanol being produced from the hydrogenation of butanal, which in turn might be obtained from the hydrogenation of the C=C double bond of crotonaldehyde (SUSHKEVICH *et al.*, 2015, LEÓN *et al.*, 2011). However, no traces of butanal or butanol were observed in this work, so that butene may be a product of 1,3-BD hydrogenation. Thus, the reduction in butene selectivity with WHSV can be explained by the reduction of the contact time of 1,3-BD in the reactor. This hypothesis was supported by an additional reaction experiment performed at 425 ºC, using a WHSV of 0.1 h^{-1}. At this condition, the contact time was equal to 6.6 s (and ethanol molar fraction at the inlet stream was equal to 0.2), and the smallest 1,3-BD selectivity was observed (4 %), whereas butene selectivity achieved its highest value (25 %).

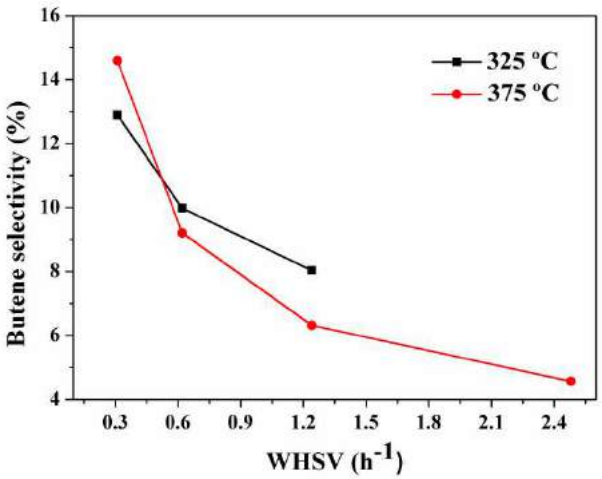

Figure 4.3.18 - WHSV and reaction temperature effect on butene selectivity (ZrZn/MgO-SiO_2-(50:50), TOS = 3 h).

Other minor products observed were ethane, acetone, propene and propane. Their combined selectivities did not achieve more than 7 % in all experiments. Traces of ethyl acetate, C5 (pentadienes and its isomers) and C6 (hexadienes) compounds were also identified in the output stream.

Regarding ethanol conversion, the increase of conversion was observed as reaction temperature increased, whereas the ethanol conversion dropped when the WHSV was raised, as shown in Figure 4.3.19. The higher WHSV increases the ethanol molar fraction in the gas stream, at the same time shortening the contact time, factors that might help to explain the reduced conversion.

Figure 4.3.20 shows the effect of reaction temperature and WHSV on the yields of the main carbon containing reaction products. Firstly, it is worth noting that the ethanol conversion increase that resulted from the temperature rise boosted 1,3-BD yields from 9-16 % at 325 ºC to 27-30 % at 375 ºC, within the same range of WHSV between 0.3 and 1.2 h^{-1}. Moreover, although the increase of the WHSV reduced the ethanol conversion, as shown in Figure 4.3.19, 1,3-BD yields were only reduced slightly. Thus, a linear increase of BD productivity (in $g_{BD}/g_{cat}\cdot h$) was obtained with the WHSV, as shown in Figure 4.3.21.

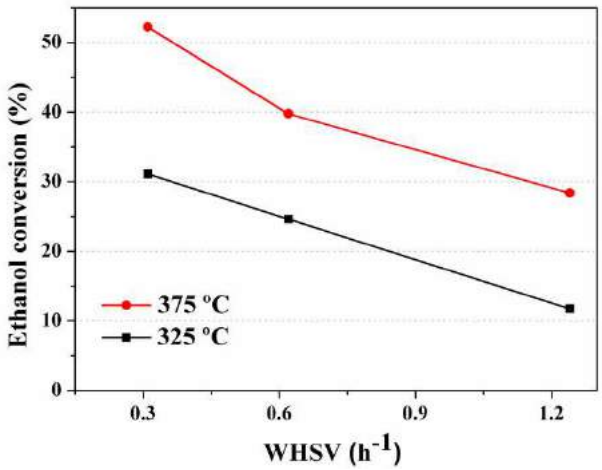

Figure 4.3.19 - WHSV and reaction temperature effects on ethanol conversion (ZrZn/MgO-SiO_2-(50:50), TOS of 3 h).

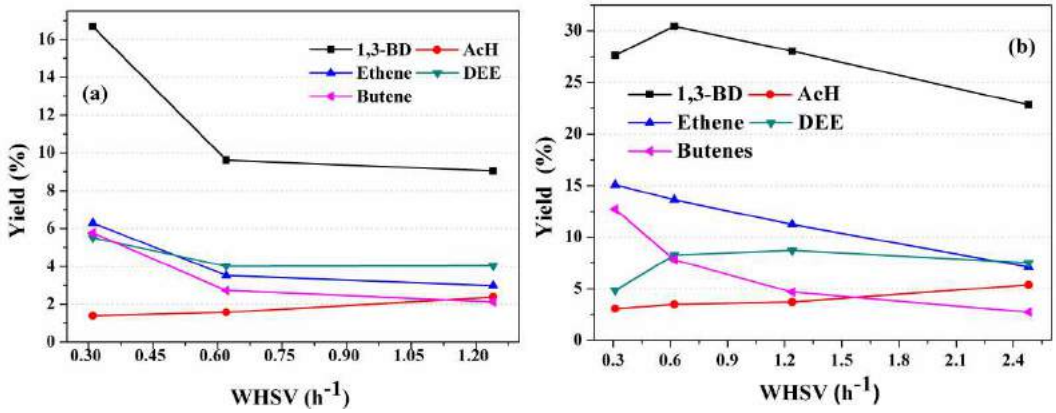

Figure 4.3.20 - Effect of WHSV on yields of the main carbon containing products at (a) 325 °C and (b) 375 °C. (ZrZn/MgO-SiO_2-(50:50), TOS of 3 h).

As discussed by MAKSHINA *et al*. (2012), catalytic data is usually reported at low ethanol concentrations and 1,3-BD productivities are usually too low to be

industrially relevant. 1,3-BD productivity values achieved in this work suggest that the ZrZn/MgO-SiO_2-(50:50) material prepared by co-precipitation is a promising catalyst for 1,3-BD production, as it presents high productivity with reasonable 1,3-BD selectivity, when compared to other catalytic systems (MAKSHINA *et al.*, 2012, BAYLON *et al.*, 2016). For instance, JANSSENS *et al.* (2015) reported productivity equal to 0.15 $g_{BD}/g_{cat}\cdot h$ over a catalyst based on Ag/MgO-SiO_2, at 400 ºC and WHSV of 1.2 h^{-1}. Using a lower temperature (320 ºC), but much higher WHSV (10.3 h^{-1}), SUSHCHEVICH *et al.* (2014) observed 0.23 $g_{BD}/g_{cat}\cdot h$ over a Ag/ZrO_2/SiO_2 system.

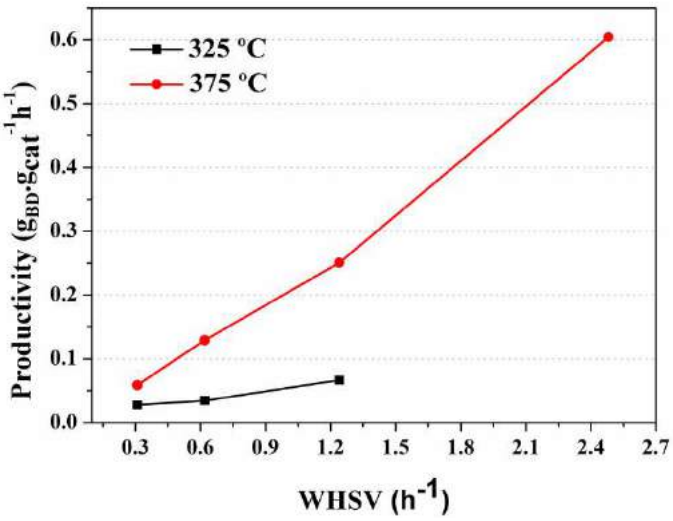

Figure 4.3.21 - Effect of WHSV and reaction temperature on 1,3-BD productivity ($g_{BD}/g_{cat}\cdot h$) on ZrZn/MgO-SiO_2-(50:50) catalyst (TOS of 3 h).

Additional experiments were performed in order to assess the reproducibility of the catalyst preparation procedure. In these experiments, reactions were performed at 350 ºC in order to evaluate experimental fluctuations at an average temperature value. Table 4.3.2 shows 1,3-BD yields and productivities obtained over ZrZn/MgO-SiO_2-(50:50) catalysts synthesized from four different preparation batches. The values observed are in agreement with results from Figures 4.3.20 and 4.3.21; thus, the observed variability should be related to intrinsic catalytic reaction fluctuations, as discussed in Section 4.2.

Finally, Table 4.3.2 also shows the number of days after the initial MgO-SiO_2-(50:50) calcination when reaction was performed, indicating no relationship between the MgO-SiO_2-(50:50) oxide age and the 1,3-BD yields and productivities. For instance,

if the age of the MgO-SiO_2-(50:50) oxide was important, higher 1,3-BD yields would be expected for sample from entry 4, and lower 1,3-BD yields for sample from entry 2.

Table 4.3.2 - 1,3-BD yields and productivities obtained over ZrZn/MgO-SiO_2-(50:50) catalysts from four different preparation batches. Reaction conditions were 350 ºC, WHSV of 0.93 h^{-1}, contact time of 3.0 s, ethanol molar fraction at inlet stream of 66.9 %, and TOS of 3 h.

Entry	Catalyst preparation batch[a]	Days after MgO-SiO_2 -(50:50) calcination	1,3-BD yield[b] (mol %)	1,3-BD productivity ($g_{BD}/g_{cat}\cdot h$)
1	1	18	22.0	0.14
2	1	20	20.2	0.13
3	2	15	24.1	0.16
4	3	12	23.2	0.15
5	3	14	15.4	0.10
6	3	15	16.2	0.11
7	4	14	17.7	0.12
Average			19.8	0.13
Standard deviation			3.5	0.02

[a] BET surface area among seven different preparation batches presented average of 364.5 m²/g with standard deviation of 24.5 m²/g and no correlation between surface area and 1,3-BD yield was observed. [b] Calculated with Eq. (3.5.3).

4.3.3 Conclusions

In this section, the effect of the Mg-to-Si molar ratio was investigated in the synthesis of magnesia silicate oxides prepared by co-precipitation for ethanol to 1,3-butadiene conversion. Catalysts were used as support for ZrO_2 and ZnO and ethanol conversion was studied in a wide range of WHSVs using two reaction temperatures. ^{29}Si MAS NMR data suggested that the co-precipitation method was more efficient for formation of Mg-O-Si linkages, compared to the traditional wet-kneading. Moreover, it was verified that the Mg:Si molar ratio equal to 1 was more suitable for 1,3-BD formation, while higher Mg:Si molar

ratios produced more acetaldehyde. High 1,3-BD productivities (in $g_{BD}/g_{cat} \cdot h$) were obtained with the ZrZn/MgO-SiO_2-(50:50) system, results that might be associated to the enhanced homogeneity of the catalyst properties.

Catalytic results supported the usual kinetic route of ethanol to 1,3-BD conversion, involving acetaldehyde condensation. However, although a suitable performance for ethanol to 1,3-BD conversion has been obtained over the ZrZn/MgO-SiO_2-(50:50) catalyst, this material presented reasonably high selectivities for ethanol dehydration products, ethene and DEE, and, thus, the acidic features of this system were modified through addition of the alkali metals Na, K and Li, as discussed in the next section.

4.4 Catalyst acidity modification through alkali metal addition

This section describes the investigation of the catalyst acidity modification through alkali metal doping. Materials were prepared as described in Sections 3.1.1, 3.1.2 and 3.1.3, and the catalytic unit employed was Unit 2, which is described in Section 3.5.

4.4.1 Sodium doping of ZrZn/MgO-SiO_2-(50:50) systems

Initially, ZrZn/MgO-SiO_2-(50:50) samples were doped with sodium. The effect of the Na_2O content on the selectivity for the main carbon containing products is shown in Figure 4.4.1(a). The increase in Na_2O content decreased the selectivities to ethene and DEE, while increasing the selectivities to 1,3-BD and AcH. Conversely, no significant change was observed to butene selectivity, which fluctuated around 10 %.

A positive linear relation was observed when 1,3-BD and AcH selectivities were considered as a function of Na_2O content, as shown in Figure 4.4.1(b), reaching 66 % for the combined 1,3-BD and AcH selectivities for the sample with the highest Na content. Also, a negative linear relation was obtained when ethene and DEE selectivities were considered as a function of catalyst Na_2O content, as shown in Figure 4.4.1(b).

Moreover, reduction of the ethanol conversion was observed as a function of the Na content, as shown in Figure 4.4.1(b), resulting in lower 1,3-BD yields and productivities, as shown in Table 4.4.1, entries 1-4. These trends were confirmed with a lower WHSV equal to 0.3 h^{-1}, entries 5-7 of Table 4.4.1. However, as discussed in Section 1.4, it should be emphasized that avoiding ethanol dehydration is of paramount importance in order to attain high 1,3-BD yields, since ethene is more thermodynamically stable than 1,3-BD.

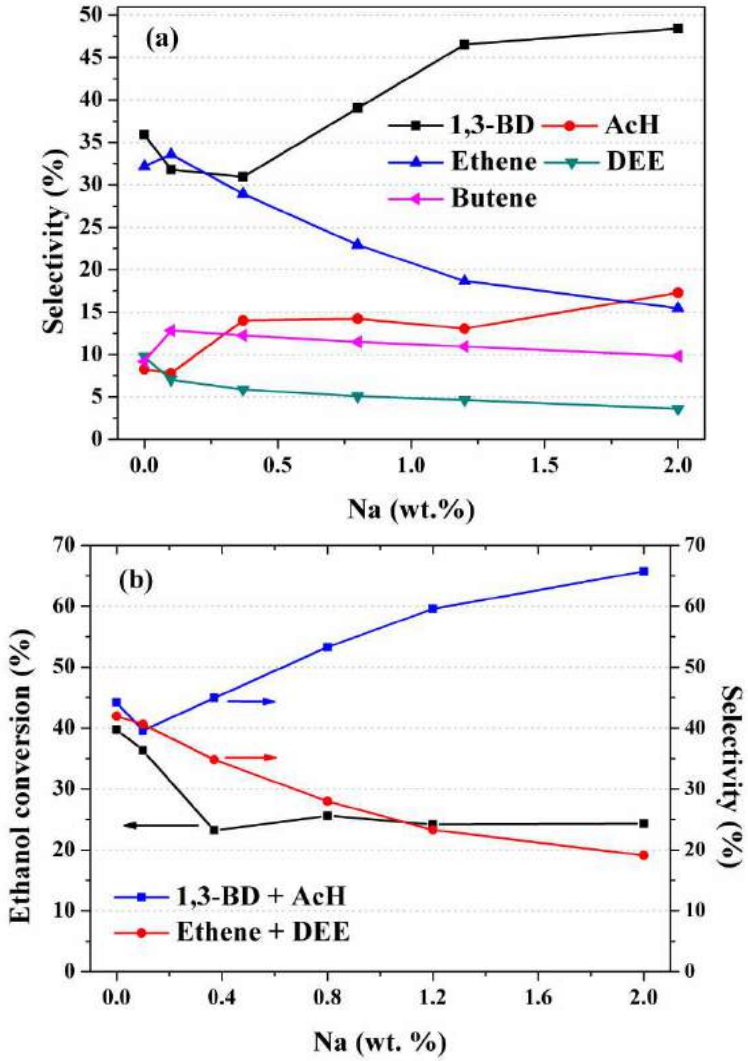

Figure 4.4.1 - (a) Effect of catalyst Na content on the selectivities of the main carbonaceous products and (b) comparison with ethanol conversion. (T of 375 °C, WHSV of 0.62 h^{-1}, TOS of 3 h).

The suppression of acid sites through Na doping was recently studied over $Zn_xZr_yO_z$ mixed metal oxides for the ethanol to 1,3-BD conversion (BAYLON *et al.*,

2016). An increase of the AcH and 1,3-BD selectivity and a decrease of ethene selectivity were observed for Na_2O containing samples. The catalytic results were rationalized through the reduction of the number of strong acid sites due to Na doping, which was observed through temperature programmed desorption of ammonia.

Table 4.4.1 - Effect of Na content on catalytic results over *y*-Na/ZrZn/MgO-SiO_2-(50:50) systems (TOS of 3 h, 375 °C).

Entry	Na (wt. %)	WHSV (h^{-1})[b]	X (%)	Selectivity (mol %)					Y_{BD}[a] (mol %)	P_{BD} (g_{BD}/g_{cat})
				1,3-BD	AcH	Ethene	DEE	Butene		
1	0	0.62	40	35.9	8.3	32.2	9.8	9.2	30.4	0.13
2	0.8	0.62	26	39.1	14.2	22.9	5.1	11.5	18.1	0.08
3	1.2	0.62	24	46.5	13.1	18.7	4.6	10.9	17.3	0.07
4	2.0	0.62	24	48.5	17.3	15.5	3.6	9.8	13.7	0.06
5	0	0.31	52	31.8	7.0	34.7	5.6	14.6	27.6	0.06
6	1.2	0.31	35	49.3	11.8	16.3	4.4	12.4	25.4	0.05
7	2.0	0.31	36	50.6	16.9	13.8	3.4	9.9	17.4	0.03

[a] Calculated with Eq. (3.5.3). [b] Contact times were equal to 3.7 and 5.1 s at the WHSV equal to 0.62 and 3.1, respectively.

In the present work, catalyst acidity of samples was investigated through ammonia adsorption followed by TPD experiments and IR measurements. Gases released during TPD experiments were monitored by mass spectroscopy, as shown in Figure 4.4.2.

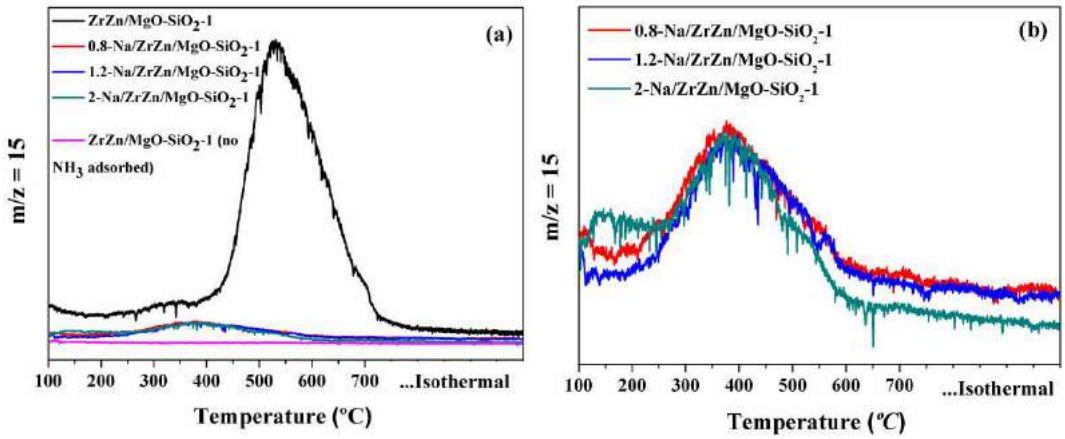

Figure 4.4.2 - NH_3-TPD profiles (a), and zoomed NH_3-TPD profiles for Na containing samples (b).

A significant reduction of the m/z signal attributed to NH_3 for ZrZn/MgO-SiO_2-(50:50) systems impregnated with sodium was observed, indicating the reduction of the number of acidic sites. A minor reduction of the number of acidic sites as the amount of sodium was increased was also indicated by NH_3-TPD experiments, as shown in Table 4.4.2. Furthermore, sodium containing samples presented peaks with maximum intensity at temperatures around 380 ºC, as shown in Figure 4.4.2(b), while the ZrZn/MgO-SiO_2-(50:50) system exhibited maximum peak intensity around 520 ºC. Therefore, the addition of sodium resulted in reduction of concentration and strength of acid sites. A reduction in the strength of acid sites from pure MgO to alkali metal doped MgO catalysts was also verified by CHOUDHARY *et al*. (1997).

Table 4.4.2 - Relative proportion of acid sites related to the m/z = 15 signal.

Catalyst Sample	%
ZrZn/MgO-SiO_2-(50:50)	100
0.8-Na/ZrZn/MgO-SiO_2-(50:50)	29.1
1.2-Na/ZrZn/MgO-SiO_2-(50:50)	28.1
2.0-Na/ZrZn/MgO-SiO_2-(50:50)	27.1

IR measurements after NH_3 adsorption supported NH_3-TPD conclusions, as shown in Figure 4.4.3. Infrared spectra are shown between 3900 and 2400 cm^{-1} in Figure 4.4.3(a) and between 1750 and 1300 cm^{-1} in Figure 4.4.3(b), for clarity.

When ammonia is adsorbed on a solid acid catalyst and its infrared spectra is recorded, the NH_4^+ protonated form, which would involve the association of ammonia with Brønsted acid sites, leads to bands near 1250 and 3130 cm^{-1}. Coordinately bonded NH_3, resulting from the interaction of ammonia with an electron-deficient metal atom, leads to bands near 1250, 1630 and 3330 cm^{-1}. However, the band near 1250 cm^{-1} may not be observable for samples containing SiO_2, which presents strong absorption from skeletal vibration below 1330 cm^{-1} (AUROUX and GERVASINI, 1990, ONO and HATTORI, 2015). Thus, the broad signal observed around 3300 cm^{-1}, as shown in Figure 4.4.3(a), could be ascribed to the superposition signal of coordinately bonded NH_3 and protonated form NH_4^+, whereas signals from Figure 4.4.3(b) would suggest the interaction of ammonia with Lewis acid sites.

Based on the previous paragraph, it can be concluded that IR measurements presented a clear reduction in the NH_3 stretching intensity, as the Na content was increased in the samples. In particular, weaker NH_3 signal was observed for the precursor MgO-SiO_2-(50:50) material, indicating that the ZrO_2 and ZnO addition increased the acidity of MgO-SiO_2-(50:50) to ZrZn/MgO-SiO_2-(50:50) system. Thus, sodium addition should deactivate Lewis acid sites associated to ZrO_2 and ZnO, contributing to the reduction of the ethanol dehydrated fraction and ethanol conversion.

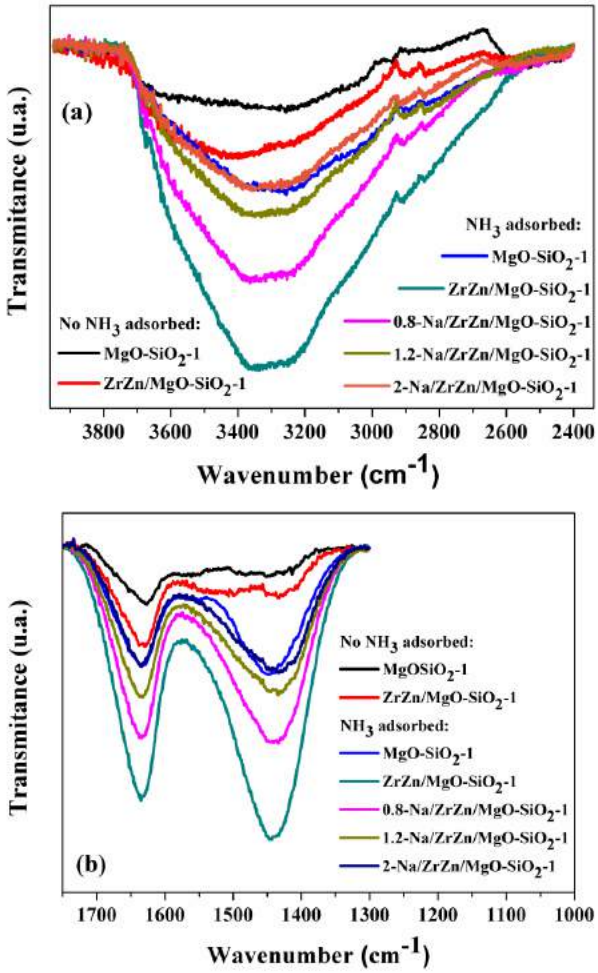

Figure 4.4.3 - IR spectra obtained after adsorption of NH_3 on MgO-SiO_2-1, ZrZn/MgO-SiO_2-1, 0.8-Na/ZrZn/MgO-SiO_2-1, 1.2-Na/ZrZn/MgO-SiO_2-1, and 2-Na/ZrZn/MgO-SiO_2-1samples. IR spectra of MgO-SiO_2-1 and ZrZn/MgO-SiO_2-1 are presented for comparison. Spectral regions were plotted separately between 3900 and 2400 cm^{-1} (a) and 1750 and 1300 cm^{-1} (b), for the sake of clarity.

The previous hypothesis was further supported by the basicity features of analyzed samples, which were characterized through IR measurements from $CHCl_3$ adsorption (TAMURA *et al.*, 2012, HUBER and KNÖZINGER, 1999), as shown in

Figure 4.4.4. On MgO, two bands at around 3011 and 2983 cm^{-1} are usually reported for the CH-stretching mode of $CHCl_3$ adsorbed and they are caused by two different kinds of adsorption species (HUBER and KNÖZINGER, 1999).

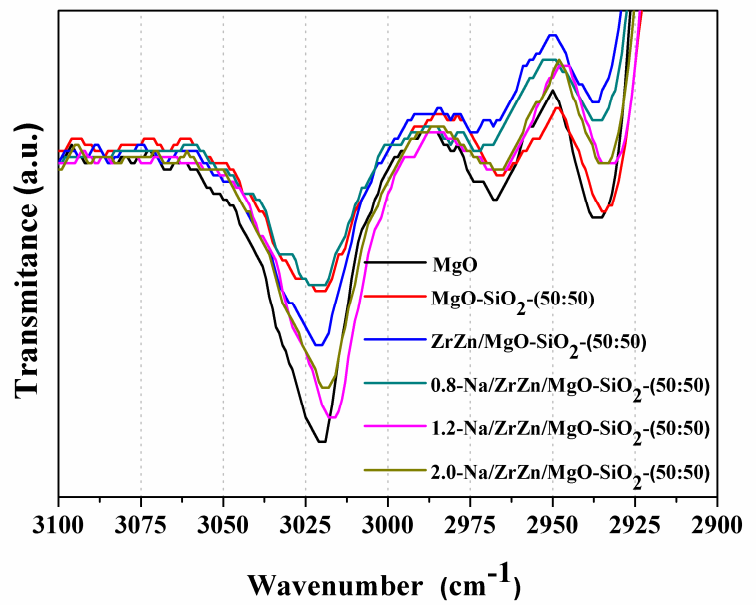

Figure 4.4.4 - IR spectra of adsorbed $CHCl_3$ on MgO, MgO-SiO_2-(50:50), ZrZn/MgO-SiO_2-(50:50), 0.8-Na/ZrZn/MgO-SiO_2-(50:50), 1.2-Na/ZrZn/MgO-SiO_2-(50:50) and 1.2-Na/ZrZn/MgO-SiO_2-(50:50) samples at 20 ºC.

Figure 4.4.5 shows possible interactions of trichloromethane with Lewis-acidic and Brønsted-basic sites. The CH-stretching at around 2983 cm^{-1} is associated to the hydrogen interaction with basic sites (a), and the CH-stretching at around 3011 cm^{-1} is related to the complex in which the chlorine atom and the hydrogen atom interact with both the Lewis-acid and the Brønsted-basic site simultaneously (b) (HUBER and KNÖZINGER, 1999).

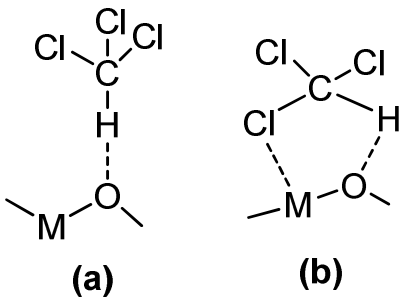

Figure 4.4.5 – Possible adsorbed $CHCl_3$ species on metal oxides (HUBER and KNÖZINGER, 1999).

Subtle differences in the $CHCl_3$ stretching intensities were observed among samples, Figure 4.4.4. A comparison with MgO suggested that samples containing higher alkali metal content (1.2 and 2 % wt.) may have a slightly higher basicity, when compared to the precursor MgO-SiO_2-(50:50) and the ZrZn/MgO-SiO_2-(50:50) system.

As expected, however, sodium addition modified textural properties of samples as well. Although no significant change on pore structure was indicated by N_2 adsorption-desorption isotherms, as shown in Figure 4.4.6, specific surface area reduced with the Na content, as shown in Table 4.4.3, probably due to Na_2O particle formation in the catalyst pores (MAKSHINA et al., 2012, LEWANDOWSKI et al., 2014). Thus, the reduction of the ethanol conversion can be associated mainly to the deactivation of acid sites and to the smaller access to active sites, as a result of surface area reduction.

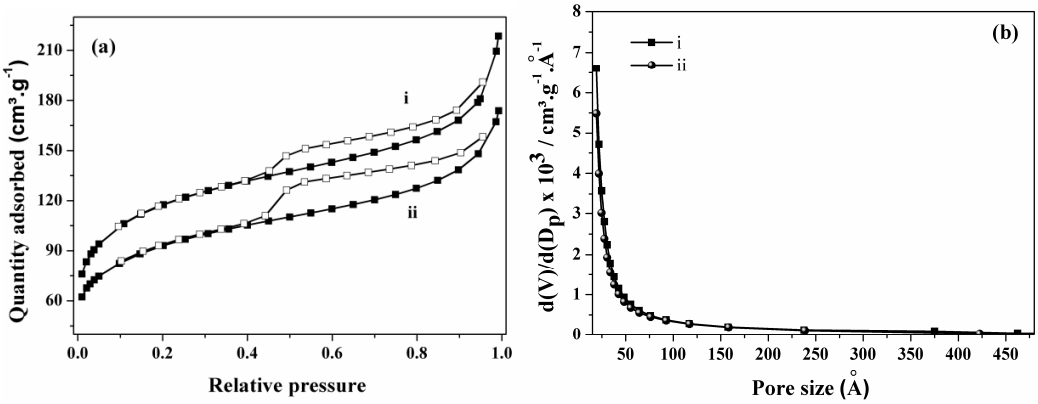

Figure 4.4.6 - N_2 adsorption (■)-desorption (□) isotherms (a) and pore size distributions (b) of i) ZrZn/MgO-SiO_2-(50:50) and ii) 1.2-Na/ZrZn/MgO-SiO_2-(50:50) catalyst samples.

Table 4.4.3 – BET surface areas and metal loadings of catalyst samples.

Entry	Sample	Surface area (m^2/g)	Metal loadings (wt. %)[b]		
			Na	Zr	Zn
1	ZrZn/MgO-SiO_2-(50:50)	323 ± 7 [a]	-	-	-
2	0.8-Na/ZrZn/MgO-SiO_2-(50:50)	198 ± 3	-	-	-
3	1.2-Na/ZrZn/MgO-SiO_2-(50:50)	219 ± 4	0.98	1.13	0.39
4	2-Na/ZrZn/MgO-SiO_2-(50:50)	61 ± 1	1.96	1.07	0.37

[a] Standard deviation denotes the value estimated from the B.E.T fitting to the N_2 physisorption data. [b] Metal loadings were assessed by ICP-OES.

It was observed that sodium doping up to the weight target of 2 % did not modify the overall structure of samples, as suggested by pXRD analysis, shown in Figure 4.4.7. In Figure 4.4.7, spectra from samples ZrZn/MgO-SiO_2-(50:50) and MgO-SiO_2-(50:50) are plotted together with samples containing sodium, for comparison.

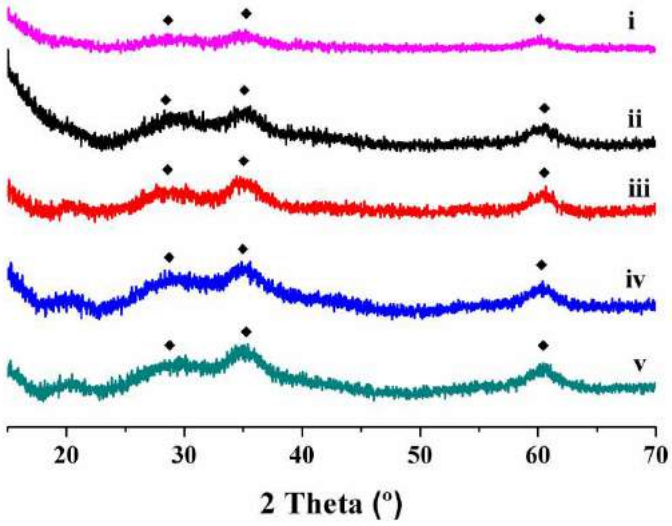

Figure 4.4.7 - pXRD patterns of i) MgO-SiO_2-(50:50), ii) ZrZn/MgO-SiO_2-(50:50), iii) 0.8-Na/ZrZn/MgO-SiO_2-(50:50), iv) 1.2-Na/ZrZn/MgO-SiO_2-(50:50) and v) 2-Na/ZrZn/MgO-SiO_2-(50:50). (♦) denotes magnesium silicate hydrate structure (BREW and GLASSER, 2005, LI *et al*., 2014).

It is important to mention that the metal loadings were confirmed by inductively coupled plasma optical emission spectroscopy (ICP-OES), Table 4.4.3. Na loadings of 0.98 and 1.96, Zn loadings of 0.39 and 0.37, and Zr loadings of 1.13 and 1.07 wt. % were observed for samples 1.2-Na/ZrZn/MgO-SiO_2-(50:50) and 2-Na/ZrZn/MgO-SiO_2-(50:50), respectively. Besides, the elemental dispersion of samples at specific locations on the catalyst particles was investigated through scanning electron microscopy with energy dispersive X-ray analysis. Table 4.4.4 shows the obtained average values.

Table 4.4.4 - Elemental dispersion of catalyst samples in weight %.[a]

Sample	Mg	Si	Zr	Zn	Na
ZrZn/MgO-SiO_2-1	32.1 ± 0.5	59.6 ± 2.2	6.3 ± 2.0	1.4 ± 0.4	0.6 ± 0.2
0.8-Na/ZrZn/MgO-SiO_2-1	31.8 ± 1.0	56.7 ± 2.0	7.6 ± 2.5	1.7 ± 0.4	2.2 ± 0.2
1.2-Na/ZrZn/MgO-SiO_2-1	31.5 ± 0.9	55.8 ± 0.5	7.2 ± 0.3	1.9 ± 0.6	3.7 ± 0.5
2-Na/ZrZn/MgO-SiO_2-1	31.8 ± 0.4	56.7 ± 0.5	6.5 ± 0.7	1.9 ± 0.3	3.2 ± 0.1

[a] Values of Mg, Si, Zr, Zn and Na were normalized to 100 and represent a dispersion measure only.

A general uniform distribution of Mg, Si, Zr, Zn, and Na was observed. However, higher scattering was observed for Zr, Zn and Na (compare standard deviations in Table 4.4.4), which may be due to the less uniform distribution of these compounds and/or related to a lower analytical sensitivity associated to the smaller concentration of these species. Moreover, Na doping was confirmed by analyses, which highlight the different Na_2O content among samples. The residual amount of Na observed in the ZrZn/MgO-SiO_2-(50:50) catalyst might be the result of incomplete removal of Na during catalyst washing.

Elemental distribution on the catalyst surface was also evaluated through EDX mapping analysis. Figure 4.4.8 shows element distribution for the 1.2-Na/ZrZn/MgO-SiO_2-(50:50) catalyst, emphasizing the homogenous chemical distribution of elements. Element distribution for samples 0.8-Na/ZrZn/MgO-SiO_2-(50:50) and 2-Na/ZrZn/MgO-SiO_2-(50:50) is shown in Figures 4.4.9-4.4.10. The dispersion homogeneity was verified through higher magnification, as shown in Figure 4.4.11.

Finally, the analysis of silicon environments by ^{29}Si MAS NMR spectroscopy suggested that the interaction of Na species with catalyst surface was not associated to Brønsted acidic silanol moieties, since no significant change on resonances was observed from the ZrZn/MgO-SiO_2-(50:50) system to the Na doped samples, as shown in Figure 4.4.12. Figure 4.4.12(a) shows spectra for catalysts i) MgO-SiO_2-(50:50), ii) ZrZn/MgO-SiO_2-(50:50), iii) 0.8-Na/ZrZn/MgO-SiO_2-(50:50), iv) 1.2-Na/ZrZn/MgO-SiO_2-(50:50) and v) 2-Na/ZrZn/MgO-SiO_2-(50:50).

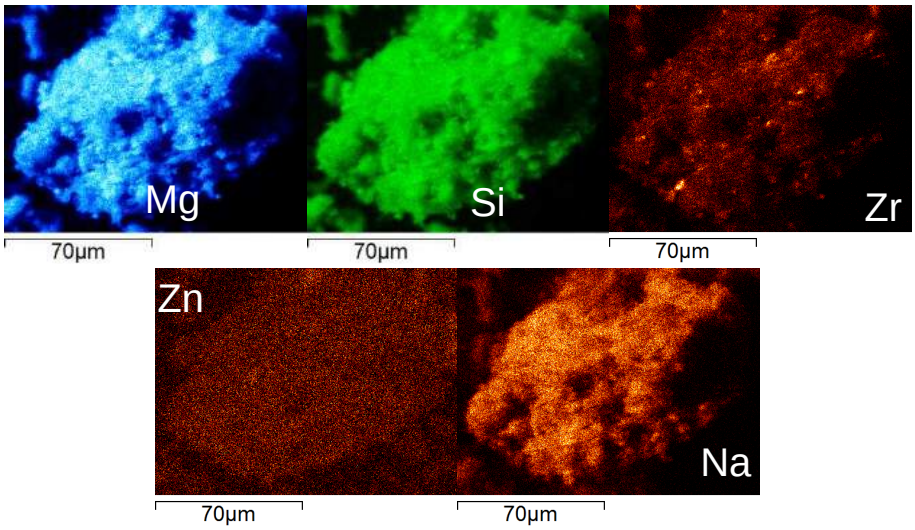

Figure 4.4.8 - Elemental mapping of the 1.2-Na/ZrZn/MgO-SiO_2-1 catalyst.

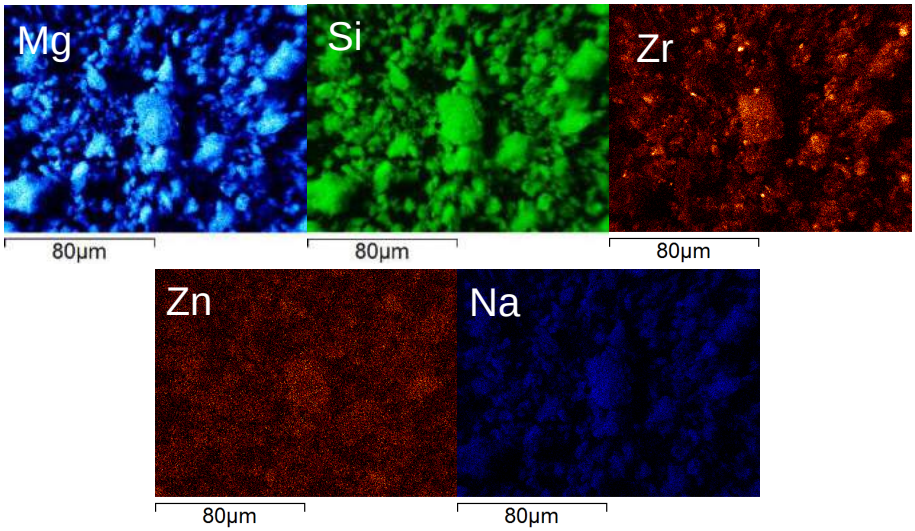

Figure 4.4.9 - Elemental mapping of the 0.8-Na/ZrZn/MgO-SiO_2-(50:50) catalyst.

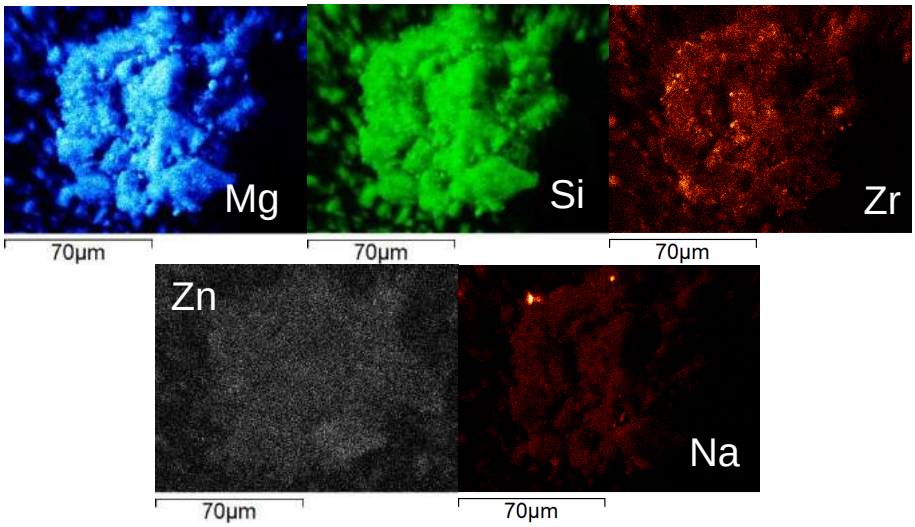

Figure 4.4.10 - Elemental mapping of the 2-Na/ZrZn/MgO-SiO_2-(50:50) catalyst.

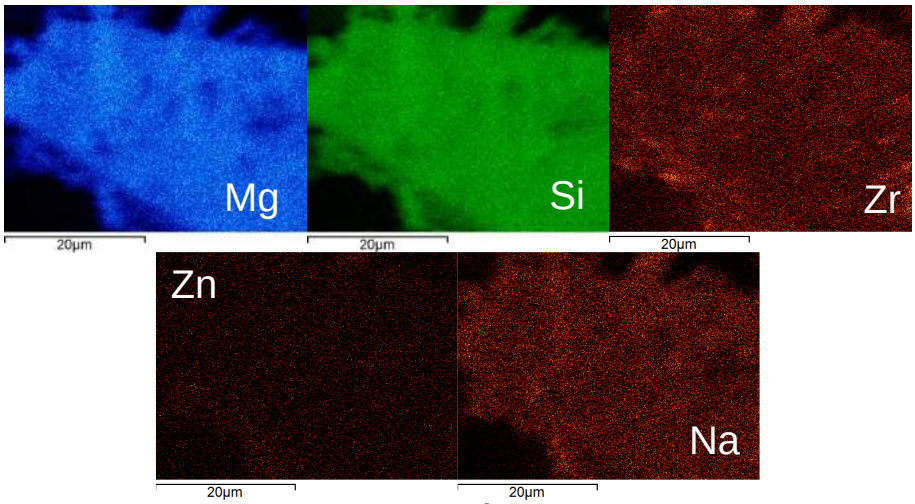

Figure 4.4.11 - Elemental mapping of the 1.2-Na/ZrZn/MgO-SiO_2-(50:50) catalyst using a higher magnification.

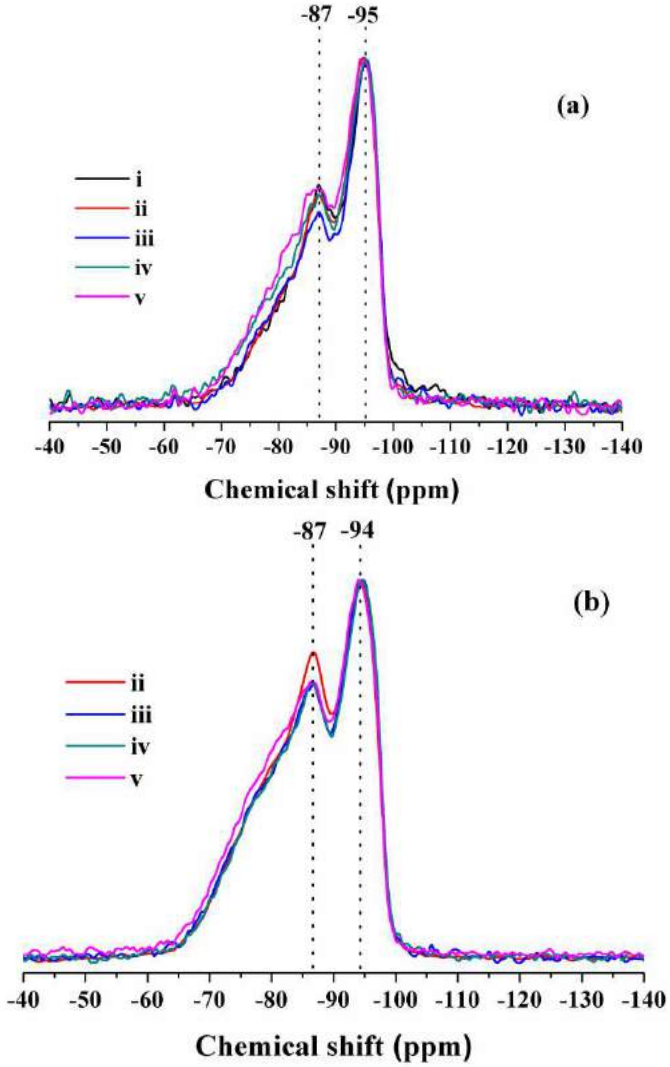

Figure 4.4.12 - ^{29}Si MAS NMR spectra of catalysts i) MgO-SiO_2-(50:50), ii) ZrZn/MgO-SiO_2-(50:50), iii) 0.8-Na/ZrZn/MgO-SiO_2-(50:50), iv) 1.2-Na/ZrZn/MgO-SiO_2-(50:50) and v) 2-Na/ZrZn/MgO-SiO_2-(50:50) (a) and ^{29}Si{^{1}H} CP MAS NMR spectra (b).

Spectra are in agreement with pXRD patterns. The two broad resonances with maxima around -87 and -95 ppm suggest the presence of -Mg-O-Si- linkages (JANSSENS *et al.*, 2015, BREW and GLASSER, 2005, HARTMAN and MILLARD, 1990), as discussed in Section 4.3. Moreover, ^{29}Si MAS spectra were confirmed by cross-polarization (CP) experiments, as shown in Figure 4.4.12(b). In this case, a shoulder at around -80 ppm was observed for all samples, which might be related to Q^1 species. ^{29}Si MAS spectra were fitted by a function containing two Gaussians in order to compute spectral areas and obtain the relative proportion of each silicon environment. The acquired data are summarized in Table 4.4.5. Only subtle differences were

observed between the relative proportion of Q^2 and Q^3 species, which are probably due to the intrinsic experimental fluctuation of the analysis.

Table 4.4.5 - Summary of ^{29}Si MAS NMR data. Numbers represent the relative proportion of each silicon environment.

Catalyst sample	Q^2 (-87 ppm)	Q^3 (-95 ppm)
i) $MgO\text{-}SiO_2$-1	78.1	21.9
ii) $ZrZn/MgO\text{-}SiO_2$-1	72.6	27.4
iii) 0.8-$Na/ZrZn/MgO\text{-}SiO_2$-1	71.4	28.6
iv) 1.2-$Na/ZrZn/MgO\text{-}SiO_2$-1	73.0	27.0
v) 2-$Na/ZrZn/MgO\text{-}SiO_2$-1	73.7	26.3

Therefore, the main effect of sodium doping may be related to the interaction of Na with Lewis acid sites related to ZrO_2 and ZnO, as also suggested by NH_3-TPD experiments and IR measurements from NH_3 adsorption.

The Na_2O effect on the catalytic properties was confirmed by an additional experiment where the process of Na addition was imitated using only water. Table 4.4.6 shows catalytic results obtained over this material, labelled as water/$ZrZn/MgO\text{-}SiO_2$-(50:50), and the data obtained over the $ZrZn/MgO\text{-}SiO_2$-(50:50), for comparison.

Although a slight reduction in the 1,3-BD yield and productivity could be observed for water/$ZrZn/MgO\text{-}SiO_2$-(50:50) samples, which is likely related to the reduction of specific catalyst surface area due to particle sinterisation after the additional calcination process, water addition did not avoid the ethanol dehydration, as ethene and DEE selectivities were very similar for the two samples, as shown in the Table 4.4.6.

Table 4.4.6 - Catalytic results for 3 h of time on stream, reaction temperature of 375 °C, WHSV of 0.62 h^{-1}, and contact time of 3.7 s.

Catalyst	X (%)	Selectivities (mol %)					Y_{BD} (mol. %)	P_{BD} (g_{BD}/ $g_{cat}\cdot h$)
		1,3-BD	AcH	Ethene	DEE	Butene		
$ZrZn/MgO\text{-}SiO_2$-(50:50)	40	35.9	8.3	32.2	9.8	9.2	30.4	0.13
Water/$ZrZn/MgO\text{-}SiO_2$-(50:50)	46	32.5	6.6	34.9	10.4	10.6	26.8	0.11

This result also suggests that the additional calcination step involved in the Na addition process (illustrated in Figure 3.1 as Calcination 3) was not responsible for the change of catalyst properties that resulted in the suppression of the ethanol dehydration, supporting the sodium doping effect, as expected. Therefore, the effect of removal of the calcination step after sodium doping (the third and final calcination steps, as described in Figure 3.1) was investigated.

From Figure 4.4.1 and Table 4.4.1, it can be was observed that the increase of the sodium loading to the ZrZn/MgO-SiO_2-(50:50) system increased the 1,3-BD selectivity. However, the 1,3-BD selectivity increase was only slight when the sodium loading was increased from 1.2 to 2.0 wt. % of Na. On the other hand, 1,3-BD yield and productivity were reduced more significantly due to the lower ethanol conversion achieved when sodium was added at loadings of 2.0 wt. %. Thus, the alkali metal loading of 1.2 wt. % was defined as the most suitable and kept constant in the following studies.

Table 4.4.7 compares results obtained for the initial 1.2-Na/ZrZn/MgO-SiO_2-(50:50) (entry 1 in Table 4.4.7) and the 1.2-Na/ZrZn/MgO-SiO_2-(50:50) sample prepared with no calcination step after sodium doping (entry 2 in Table 4.4.7).

Table 4.4.7 - Catalytic results over the 1.2-Na/ZrZn/MgO-SiO_2-(50:50) catalyst (TOS = 3 h, 375 °C, WHSV = 0.62 h^{-1}, and contact time equal to 3.7 s).

Entry	X (%)	Selectivities (mol. %)					Y_{BD} (mol. %)	P_{BD} ($g_{BD}/g_{cat}\cdot h$)
		1,3-BD	AcH	Ethene	DEE	Butene		
1 [a]	24	46.5	13.1	18.7	4.6	10.9	17.3	0.07
2 [b,c]	28	52.2	20.0	10.5	2.7	10.2	19.6	0.09
3 [d,e]	27	50.1	18.6	13.2	2.9	10.4	17.0	0.07

[a] BET surface area equal to 219 ± 4 m²/g. [b] No calcination after sodium doping. [c] BET surface area equal to 333 ± 3 m²/g. [d] Calcination temperature after sodium doping was 400 ºC. [e] BET surface area equal to 239 ± 2 m²/g.

A slight increase of the 1,3-BD selectivity, yield and productivity was obtained. However, there is a significant difference in the specific surface area (219 vs. 333 m²/g) of the two materials, which may contribute to the different performances. The beneficial effect of calcination step removal was confirmed by an additional experiment where the calcination temperature after the sodium doping was reduced to 400 ºC (entry 3 in Table

4.4.7). This procedure improved 1,3-BD selectivity and also resulted in higher surface area, when compared to the sample calcined at 500 ºC (entry 1 in Table 4.4.7).

A similar pXRD pattern with amorphous features, as presented in Figure 4.4.7, was observed for the 1.2-Na/ZrZn/MgO-SiO_2-(50:50) sample prepared with no calcination after alkali metal doping (pattern *ii*), as shown in Figure 4.4.13, indicating that Na_2O may be dispersed into the -Mg-O-Si- network or that the small loading was undetectable by pXRD. Moreover, the presence of Na_2O as a single phase was ruled out, since no signal at the Bragg angles of 46 º was observed (HARTMANN *et al.*, 2013).

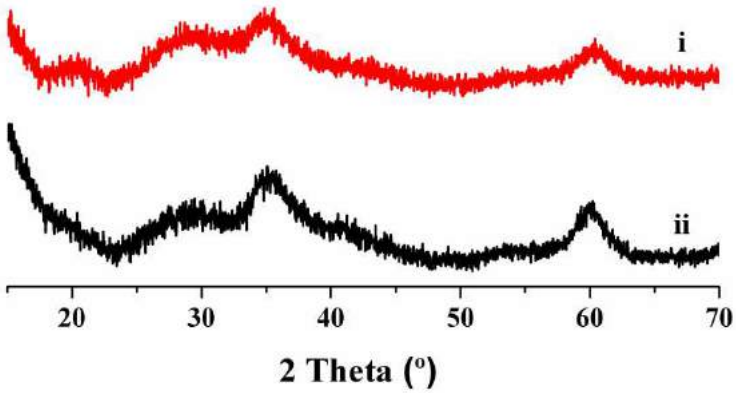

Figure 4.4.13 - XRD patterns of i) 1.2-Na/ZrZn/MgO-SiO_2-(50:50), and ii) 1.2-Na/ZrZn/MgO-SiO_2-(50:50) with no calcination after Na doping.

4.4.2 Acetaldehyde and Ethanol Co-feeding

Since acetaldehyde is an intermediary compound of the ethanol to 1,3-BD reaction, the effect of adding acetaldehyde to the feed was also evaluated. An ethanol-to-acetaldehyde feed ratio of 8:2 was employed, since this condition resulted in better catalytic performances in previous studies (JONES et al., 2011). Catalytic data is shown in Table 4.4.8.

As expected, the addition of AcH in the feed increased the amount of produced 1,3-BD (compare yields and productivities between entries 1 and 2, and entries 3 and 4 in Table 4.4.8). Moreover, ethanol dehydration to ethene was suppressed after AcH addition, in line with thermodynamic calculations (Section 1.4). Suppression is more pronounced catalysts containing Na_2O, as shown in Table 4.4.8 and 4.4.9.

Table 4.4.8 – Effect of adding AcH to the feed on catalytic results (TOS of 3 h, 375 °C, WHSV of 0.62 h^{-1} and contact time of 3.7 s).

Entry	Catalyst	X (%)	Selectivities (mol %)					Y_{BD} (mol. %)	P_{BD} (g_{BD}/ g_{cat}·h)
			1,3-BD	AcH	Ethene	DEE	Butene		
1	ZrZn/MgO-SiO_2-1	40	35.9	8.3	32.2	9.8	9.2	30.4	0.13
2	ZrZn/MgO-SiO_2-1[a]	32[c]	44.6	8.2	24.2	6.6	10.8	41.4	0.17
3	1.2-Na/ZrZn/MgO-SiO_2-1[b]	28	52.2	20.0	10.5	2.7	10.2	19.6	0.09
4	1.2-Na/ZrZn/MgO-SiO_2-1[a,b]	6.9[c]	44.7	34.1	5.8	1.2	9.89	25.4	0.10

[a] Acetaldehyde in the feed (8:2 ethanol to AcH feed ratio). [b] No calcination after sodium doping. [c] Acetaldehyde conversion was not calculated.

Table 4.4.9 - Effect of adding AcH to the feed on ethene and DEE yield (TOS of 3 h, 375 °C, WHSV of 0.62 h^{-1} and contact time of 3.7 s).

Entry	Catalyst	Yield (mol. %)	
		Ethene	DEE
1	ZrZn/MgO-SiO_2-1	13.6	8.3
2	ZrZn/MgO-SiO_2-1[a]	11.2	6.1
3	1.2-Na/ZrZn/MgO-SiO_2-1[b]	2.0	1.0
4	1.2-Na/ZrZn/MgO-SiO_2-1[a,b]	1.6	0.7

[a] Acetaldehyde in the feed (8:2 ethanol to AcH feed ratio). [b] No calcination after sodium doping.

4.4.3 Potassium and Lithium Doping of ZrZn/MgO-SiO_2-(50:50) systems

The acidity modification of the ZrZn/MgO-SiO_2-(50:50) system was also investigated using potassium and lithium. Table 4.4.10 shows catalytic results for these samples (entries 3 and 4). As observed for sodium doped samples, the addition of potassium and lithium was also effective for suppression of ethanol dehydration, leading to lower selectivities to ethene and DEE, when compared to the starting ZrZn/MgO-SiO_2-(50:50) material (which is shown again in the Table 4.4.10 as entry 1).

Similar catalytic performances were observed for samples doped with Na and K (compare entries 2 and 3 in Table 4.4.10). Conversely, the 1.2-Li/ZrZn/MgO-SiO_2-(50:50) sample presented lower 1,3-BD yield and productivity, which is in line with its lower BET surface area, equal to 81 m^2/g, when compared to the surface area of 1.2-Na/ZrZn/MgO-SiO_2-(50:50) and 1.2-K/ZrZn/MgO-SiO_2-(50:50) samples, equal to 219 and 243 m^2/g, respectively. CHOUDHARY *et al*. (1997) also verified similar trends of

specific surface area for alkali metal promoted MgO catalysts, which followed the order Li/MgO < Na/MgO < K/MgO, in agreement with results obtained in the present work. No significant difference was observed on the alkali metal doped catalyst structures, as suggested by the pXRD of samples and shown in Figure 4.4.14.

Table 4.4.10 – Alkali metal doping effect on catalytic results (TOS of 3 h, 375 °C, WHSV of 0.62 h^{-1} and contact time equal to 3.7 s).

Entry	Catalyst[a]	X (%)	Selectivities (mol %)					Y_{BD} (mol %)	P_{BD} (g_{BD}/ g_{cat}·h)
			1,3-BD	AcH	Ethene	DEE	Butene		
1	ZrZn/MgO-SiO_2-1[b]	40	35.9	8.3	32.2	9.8	9.2	30.4	0.13
2	1.2-Na/ZrZn/MgO-SiO_2-1[c]	24	46.5	13.1	18.7	4.6	10.9	17.3	0.07
3	1.2-K/ZrZn/MgO-SiO_2-1[d]	22	51.6	13.7	17.4	5.2	7.5	21.1	0.09
4	1.2-Li/ZrZn/MgO-SiO_2-1[e]	18	44.3	20.5	16.2	4.4	8.7	11.4	0.05

[a] BET surface area equal to [b] 323 ± 7, [c] 219 ± 4, [d] 243 ± 2, and [e] 81 ± 0.3 m^2/g.

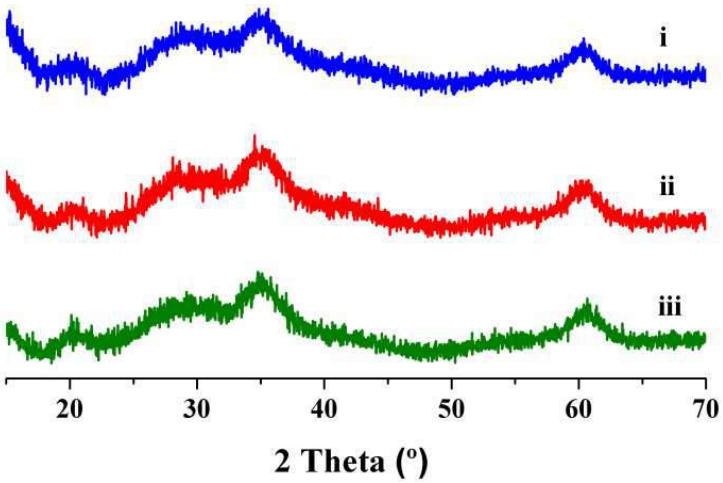

Figure 4.4.14 - pXRD patterns of i) 1.2-Na/ZrZn/MgO-SiO_2-(50:50) i) 1.2-K/ZrZn/MgO-SiO_2-(50:50) and ii) 1.2-Li/ZrZn/MgO-SiO_2-(50:50).

Thus, at this point, it could be argued if the alkali metal features exerted significant effect on the catalytic performance, or if the observed effects were related to the different amounts of added alkali metal, since samples were prepared with similar alkali metal loading in weight %. Indeed, given that the molecular weight of potassium is higher than the molecular weight of sodium that, in turn, is higher than the molecular weight of lithium, the number of lithium mols added to the catalyst was five times

higher than the number of potassium mols added and three times higher than the number of sodium mols added to the catalyst mixture.

This could help to explain the smallest surface area observed for lithium doped samples and the lower 1,3-BD yields and productivities. However, the addition of lithium, using the same number of mols used for potassium, resulted in a material with catalytic properties similar to the starting ZrZn/MgO-SiO_2-(50:50) system, entry 3 of Table 4.4.11. Thus, the increase in the 1,3-BD yield and productivity observed from lithium to potassium doped samples (considering the same weight loading and the same molar loading) suggest that the type of alkali metal is important.

Table 4.4.11 - Catalytic results for lithium doped samples (TOS of 3 h, 375 °C, WHSV of 0.62 h^{-1}, and contact time of 3.7 s).

Entry	Catalyst	Selectivities (mol %)					Y_{BD} (mol %)	P_{BD} ($g_{BD}/g_{cat}\cdot h$)
		1,3-BD	AcH	Ethene	DEE	Butene		
1	ZrZn/MgO-SiO_2-1	35.9	8.3	32.2	9.8	9.2	30.4	0.13
2	1.2-Li/ZrZn/MgO-SiO_2-1[a]	44.3	20.5	16.2	4.4	8.7	11.4	0.05
3	0.22-Li/ZrZn/MgO-SiO_2-1[b]	33.8	7.1	30.6	8.4	13.8	27.2	0.12

[a] BET surface area equal to 81 ± 0.3 m^2/g. [b] BET surface area equal to 267 ± 2 m^2/g.

These results are consistent with findings reported by SUSUKI *et al*. (1988), who treated hectorita with lithium, sodium and potassium and observed a higher fraction of ethanol dehydration to ethene and DEE for samples treated with lithium. According to the authors, the smaller atomic radius of lithium results in stronger Lewis acidity due to the higher electrostatic field associated to its smaller atomic size. Indeed, CHOUDHARY *et al*. (1997) observed that the amount of NH_3 chemisorbed at 100 ºC over Li/MgO, Na/MgO and K/MgO catalysts (in $\mu mol\cdot g^{-1}$) followed the order Li/MgO > Na/MgO > K/MgO, also suggesting that the addition of lithium results in higher acitidity. Thus, assuming that alkali metals at the catalyst surface act as Lewis acid sites, the slightly better performance observed for the potassium doped sample (entry 3 of Table 4.4.10) could be related to its weaker Lewis acidity, due to its higher atomic radius. However, the presence of different basic sites cannot be ruled out in order to explain the better observed performance for the potassium containing catalyst.

4.4.4 Calcination Steps Number Reduction

In Section 4.4.1, it was shown that the removal of the calcination step after the Na doping resulted in slightly higher 1,3-BD yield and productivity, as shown in Table 4.4.7. Thus, the effect of removing the calcination step before the Zr and Zn addition was also investigated, while simultaneously removing the calcination step after the alkali metal doping. The removed calcination steps are illustrated in Figure 3.1 as Calcination 1 and 3. Table 4.4.12 shows catalytic results for the ZrZn/MgO-SiO_2-(50:50) system and alkali metal doped samples prepared with only 1 calcination step (entries 1-4), and the alkali metal doped samples prepared with three calcination steps (entries 5-8), for the sake of comparison.

Table 4.4.12 – Effect of the number of calcination steps on catalytic results (TOS of 3 h, 375 °C, WHSV of 0.62 h^{-1} and contact time of 3.7 s).

Entry	Catalyst	X (%)	Selectivities (mol %)					Y_{BD} (mol %)	P_{BD} (g_{BD}/ g_{cat}·h)
			1,3-BD	AcH	Ethene	DEE	Butene		
1	ZrZn/MgO-SiO_2-1[a]	44	26.2	6.3	43.6	12.7	7.5	24.6	0.11
2	1.2-Na/ZrZn/MgO-SiO_2-1[a,b]	19	49.5	22.8	11.3	3.2	9.0	22.2	0.10
3	1.2-K/ZrZn/MgO-SiO_2-1[a,b]	26	55.1	17.1	12.2	3.5	7.9	27.1	0.12
4	1.2-Li/ZrZn/MgO-SiO_2-1[a,b]	19	47.7	17.0	13.4	2.6	13.7	15.9	0.07
5	ZrZn/MgO-SiO_2-1	40	35.9	8.3	32.2	9.8	9.2	30.4	0.13
6	1.2-Na/ZrZn/MgO-SiO_2-1	24	46.5	13.1	18.7	4.6	10.9	17.3	0.07
7	1.2-K/ZrZn/MgO-SiO_2-1	22	51.6	13.7	17.4	5.2	7.5	21.1	0.09
8	1.2-Li/ZrZn/MgO-SiO_2-1	18	44.3	20.5	16.2	4.4	8.7	11.4	0.05

[a] No calcination before Zr and Zn addition. [b] No calcination after alkali metal doping.

Regarding the ZrZn/MgO-SiO_2-(50:50) system, a slight enhancement of ethene and DEE selectivities was observed upon the removal of the calcination step (compare entries 1 and 5 of Table 4.4.12), suggesting the increase of the acidity of the catalyst or improvement of the access to active acid sites, as the BET surface area changed from 323 ± 7 m^2/g to 416 ± 3 m^2/g for the ZrZn/MgO-SiO_2-(50:50) system prepared with and without the calcination step before Zr and Zn addition, respectively.

For samples containing Na_2O, K_2O and Li_2O, the removal of the calcination steps was also beneficial to 1,3-BD yield and productivity (compare entries 2 and 6 for Na_2O, entries 3 and 7 for K_2O, and entries 4 and 8 for Li_2O containing samples). As observed for the ZrZn/MgO-SiO_2-(50:50) system, 1.2-Na/ZrZn/MgO-SiO_2-(50:50), 1.2-

K/ZrZn/MgO-SiO_2-(50:50) and 1.2-Li/ZrZn/MgO-SiO_2-(50:50) samples also presented an increase of the surface area due to the removal of the calcination steps, as shown in Table 4.4.13.

Table 4.4.13 - BET surface area of catalyst samples.

Sample	Surface area (m^2/g)	Calcination steps in preparation method (as Figure 3.1)	Total number of calcination steps
1.2-Na/ZrZn/MgO-SiO_2-(50:50)	219 ± 4	Calcination 1, 2 and 3	3
1.2-K/ZrZn/MgO-SiO_2-(50:50)	243 ± 2	Calcination 1, 2 and 3	3
1.2-Li/ZrZn/MgO-SiO_2-(50:50)	81 ± 0.3	Calcination 1, 2 and 3	3
ZrZn/MgO-SiO_2-(50:50)[a]	416 ± 3	Calcination 2	1
1.2-Na/ZrZn/MgO-SiO_2-(50:50)[a,b]	290 ± 2	Calcination 2	1
1.2-K/ZrZn/MgO-SiO_2-(50:50)[a,b]	305 ± 3	Calcination 2	1
1.2-Li/ZrZn/MgO-SiO_2-(50:50)[a,b]	210 ± 2	Calcination 2	1

[a] No calcination before Zr and Zn addition. [b] No calcination after alkali metal doping.

These results suggest that there is a relationship among 1,3-BD formation, acidic-basic concentration and site distribution on the catalyst surface, since 1,3-BD yield and productivity were strongly correlated with catalyst surface area for samples containing alkali metals, as shown in Figure 4.4.15.

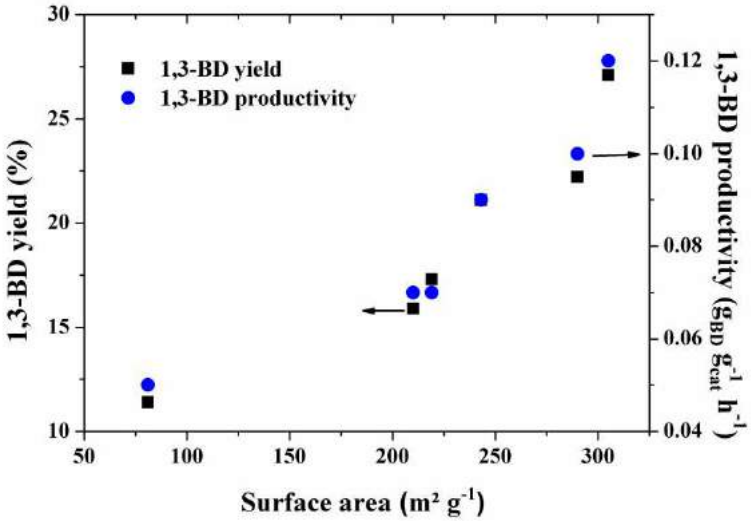

Figure 4.4.15 - Relationship between surface area, 1,3-BD yield (left) and 1,3-BD productivity (right) for 1.2-Na/ZrZn/MgO-SiO_2-(50:50), 1.2-K/ZrZn/MgO-SiO_2-(50:50) and 1.2-Li/ZrZn/MgO-SiO_2-(50:50) samples. Reactions performed as entries 2-4 and 6-8 in Table 4.4.12.

The effect of removing calcination steps was also investigated through ^{7}Li MAS NMR spectroscopy. The lithium doped 1.2-Li/ZrZn/MgO-SiO_2-(50:50) sample was submitted to ^{7}Li MAS NMR analysis due to its higher sensitivity, when compared to Na and K isotopes. Figure 4.4.16(a) shows spectra for samples 1.2-Li/ZrZn/MgO-SiO_2-(50:50) and 1.2-Li/ZrZn/MgO-SiO_2-(50:50) prepared with only 1 calcination step after ZrO_2 and ZnO addition. Although similar chemical shifts can be observed for both samples, the different lineshape, broader in the half width for the sample with higher number of calcination steps, as shown in Figure 4.4.16(b), and the different intensities of the spinning sideband distribution indicated the modification of the local environment of the lithium nuclei. Thus, the reduction of the number of calcination steps, affects the surface area and also produces other structural modifications on the samples.

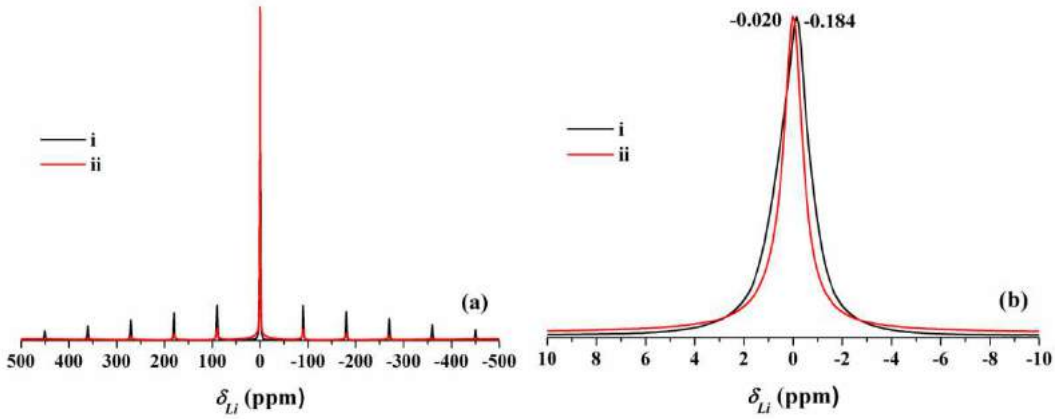

Figure 4.4.16 - ^{7}Li MAS NMR spectra of catalysts i) 1.2-Li/ZrZn/MgO-SiO_2-(50:50) and ii) 1.2-Li/ZrZn/MgO-SiO_2-(50:50) with no calcination step before Zr and Zn addition and after Li doping: (a) full spectra; (b) zoomed spectra.

The effect of removing calcination steps on the silicon environments was also evaluated. In this case, the sample studied was the 1.2-K/ZrZn/MgO-SiO_2-(50:50), since the potassium addition caused higher modification of the 1,3-BD yield and productivity for both numbers of calcination steps, as shown in Table 4.4.12, when compared to the lithium and sodium doped samples. For the sake of clarity, the preparation procedure of the 1.2-K/ZrZn/MgO-SiO_2-(50:50) system, involving only one calcination step, is explained in Section 3.1.4 and illustrated in Figure 3.2.

In Sections 4.3.1 and 4.4.1, ^{29}Si NMR experiments indicated that the alkali metal and Zr and Zr addition did not change silicon environments significantly. Conversely, the removal of the calcination steps exerted a more pronounced effect on the silicon environments, as shown in Figure 4.4.17, in line with ^{7}Li MAS NMR results.

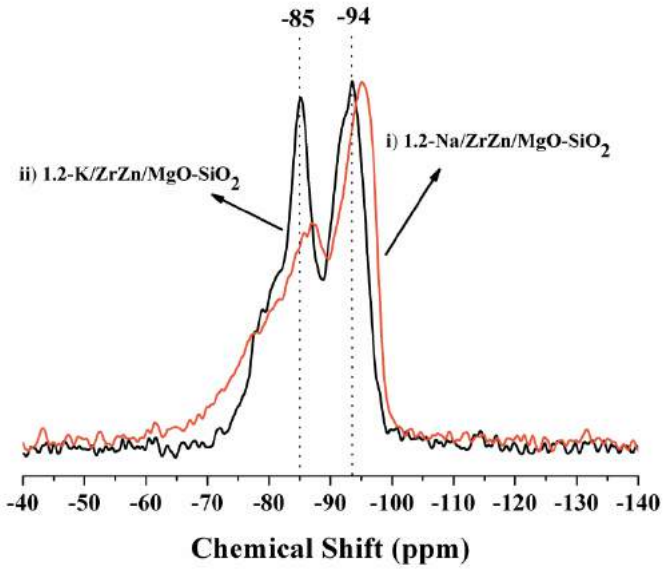

Figure 4.4.17 - ^{29}Si MAS NMR spectra of catalysts i) 1.2-Na/ZrZn/MgO-SiO_2-(50:50), and ii) 1.2-K/ZrZn/MgO-SiO_2-(50:50) sample prepared with no calcination before Zr and Zn addition and no calcination after alkali metal doping.

Moreover, although the purity of the KOH employed in the synthesis of potassium doped samples was equal to 90 % (see Section 3.1.3, as KOH contained 10 % of humidity), the presence of impurities in the 1.2-K/ZrZn/MgO-SiO_2 material was ruled out by SEM-EDX analyses, Appendix G. Elements were uniformly distributed on the surface of the catalyst, as indicated by the SEM-EDX elemental mapping and shown in Figure 4.4.18 and the elemental dispersions at specific locations of the catalyst particle, as shown in Table 4.4.14. Moreover, bulk loadings were confirmed by inductively coupled plasma optical emission spectroscopy (ICP-OES), leading to K, Zn and Zr loadings of 1.31, 0.57 and 1.68 wt%, respectively.

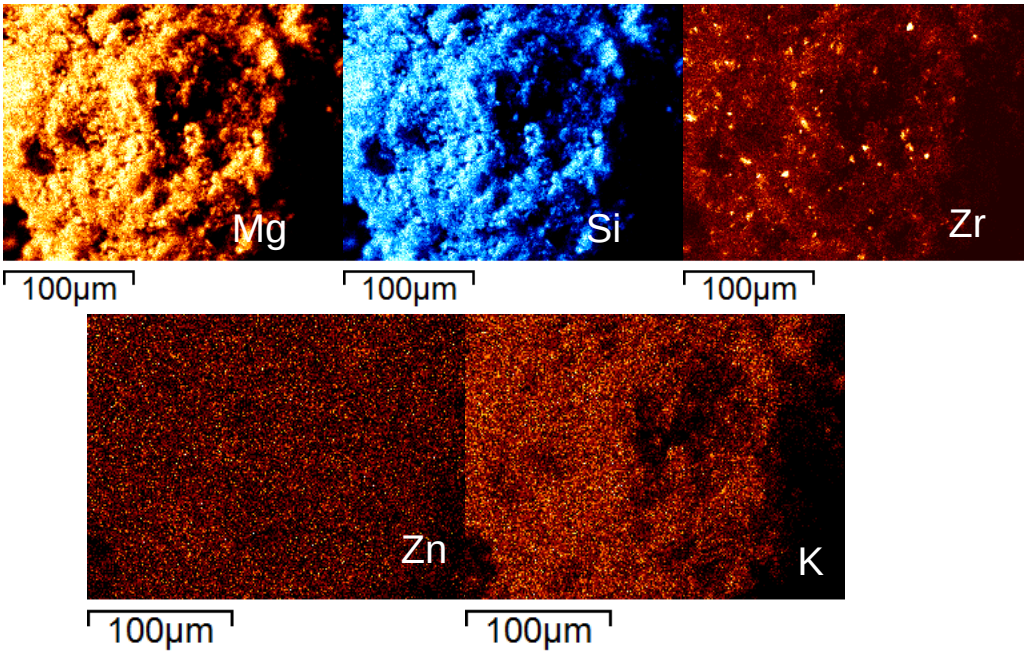

Figure 4.4.18 – Elemental mapping of the 1.2-K/ZrZn/MgO-SiO_2-(50:50) catalyst prepared with no calcination before Zr and Zn addition and no calcination after alkali metal doping.

Table 4.4.14 – Surface elemental dispersion of 1.2-K/ZrZn/MgO-SiO_2-(50:50) catalyst sample in weight. % [a,b].

Mg	*Si*	*Zr*	*Zn*	*K*
37.42 ± 0.50	52.79 ± 0.49	5.44 ± 0.55	1.69 ± 0.31	2.66 ± 0.20

[a] Elemental values were normalized to 100 and represent a dispersion measure only. [b] Catalyst prepared with no calcination before Zr and Zn addition and no calcination after alkali metal doping.

Regarding the sample crystallinity, the removal of the calcination steps did not modify the common amorphous structure of the sample, which presented the three broad peaks (at 25-30°, 33-39° and 58-62°) of Figure 4.4.19, characteristic of magnesium silicate hydrates (BREW and GLASSER *et al*., 2005, LI *et al*., 2014), as observed for previous samples, and shown in Figures 4.4.7, 4.4.13 and 4.4.14.

Finally, it was observed that the removal of the calcination steps did not modify the role of alkali metals, which is here rationalized as the neutralization of the strong acid sites of the catalyst, responsible for ethanol dehydration, as discussed in Section 4.4.1. Figure 4.4.20 shows the profiles obtained from NH_3-TPD experiments, which confirmed the reduction of the total catalyst acidity as the alkali metal was added.

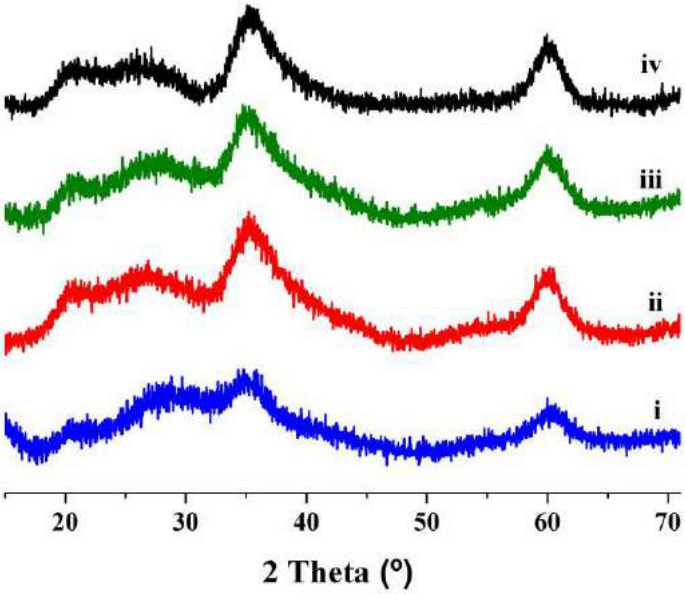

Figure 4.4.19 - XRD patterns of i) ZrZn/MgO-SiO_2-(50:50) (prepared with no calcination before Zr and Zn addition), ii) 1.2-Na/ZrZn/MgO-SiO_2-(50:50), iii) 1.2-K/ZrZn/MgO-SiO_2-(50:50) and iv) 1.2-Li/ZrZn/MgO-SiO_2-(50:50). Samples ii, iii and iv were prepared with no calcination before Zr and Zn addition and no calcination after alkali metal doping.

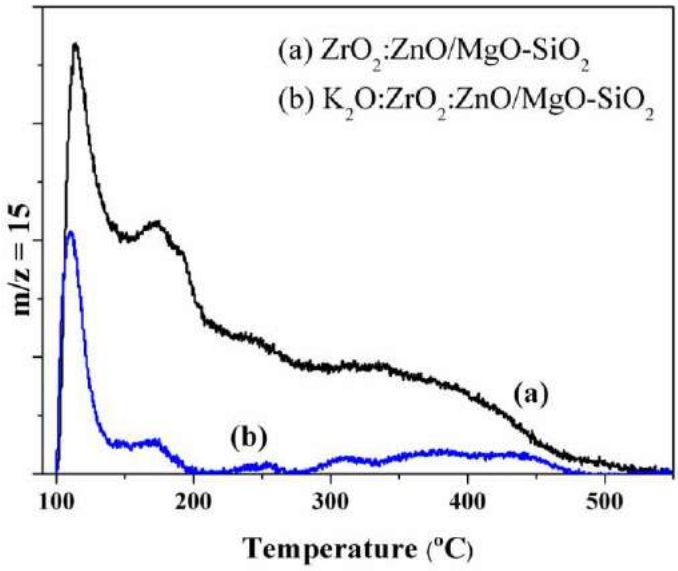

Figure 4.4.20 - NH_3-TPD profiles for the K_2O:ZrO_2:ZnO/MgO-SiO_2 catalyst and its ZrO_2:ZnO/MgO-SiO_2 precursor, both prepared with only one calcination step after Zr and Zn addition.

Three additional experiments were performed by varying the WHSV at 375 ºC and using the same ethanol molar fraction (by keeping the catalyst weight constant and varying simultaneously the gas flow and ethanol feed rate) and results suggested a

similar kinetic behavior, as observed for the ZrZn/MgO-SiO_2-(50:50) system at 325 ºC. As expected, the use of higher contact times was beneficial to 1,3-BD selectivity and yield, as shown in Table 4.4.15.

Table 4.4.15 - Catalytic results for 3 h of time on stream over the 1.2-K/ZrZn/MgO-SiO_2-(50:50) system prepared with no calcination before Zr and Zn addition and after alkali metal doping, at 375 °C and using ethanol feed molar fraction of 0.4.

WHSV (h^{-1})	τ (s)	X (%)	Selectivities (mol %)					Y_{BD} (mol %)	P_{BD} (g_{BD}/ g_{cat}. h)
			1,3-BD	AcH	Ethene	DEE	Butene		
0.31	5.1	44	57.8	12.9	10.3	2.5	10.3	37.2	0.07
0.62	2.5	35	55.9	19.2	10.2	2.78	7.5	20.1	0.09
1.24	1.3	26	44.6	30.9	7.5	2.36	5.0	13.1	0.12

Therefore, the modification of the acidity of the ZrZn/MgO-SiO_2-1 system prepared by co-precipitation, through addition of alkali metals, specially using K_2O, seems to constitute a promising – and cheap – catalyst alternative to maximize the 1,3-BD formation from ethanol conversion. Firstly, ethanol dehydration must be avoided, which is a thermodynamic requirement to achieve higher 1,3-BD yield. Then, unconverted ethanol and produced acetaldehyde must be recycled in the process, overcoming the lower ethanol conversion obtained with these systems.

4.4.5 Comparison with Literature Catalysts

Two literature catalysts, labelled as Cu/MgO-SiO_2 and CuZrZn/SiO_2, were synthesized and tested for the ethanol to 1,3-BD reaction in order to allow for the comparison with the catalyst developed in the present work. The preparation procedure for these materials is detailed in Section 3.1.5.

The measured surface areas were equal to 209 ± 3.6 m^2/g and 264 ± 5.2 m^2/g for the Cu/MgO-SiO_2 and CuZrZn/SiO_2 catalysts, respectively. Figure 4.4.21 shows the pXRD of the samples, which indicates the SiO_2 feature phase with maximum intensity at the Bragg angles between 20 and 25 º for the CuZrZn/SiO_2 sample (JONES *et al.*, 2011), whereas the Cu/MgO-SiO_2 catalyst showed a mixture of phases of magnesium silicate and MgO periclase phase, as expected (MAKSHINA *et al.*, 2012; ANGELICI *et al.*, 2014).

Figure 4.4.22 shows 1,3-BD selectivities (a) and 1,3-BD yields (b) obtained using the Cu/MgO-SiO_2, CuZrZn/SiO_2, and 1.2-K/ZrZn/MgO-SiO_2-(50:50) catalysts.

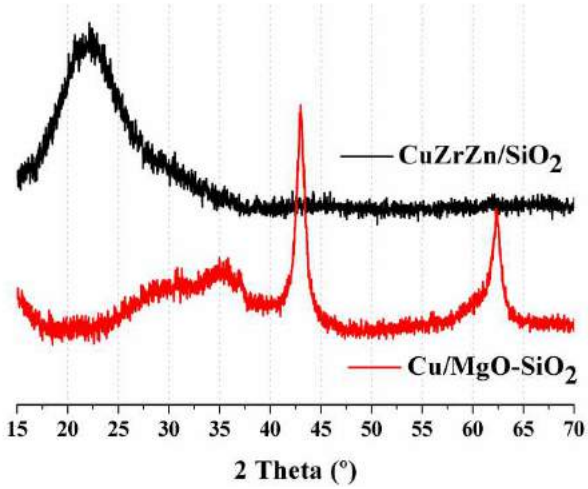

Figure 4.4.21 – pXRD spectra of Cu/MgO-SiO_2 and CuZrZn/SiO_2 catalysts samples.

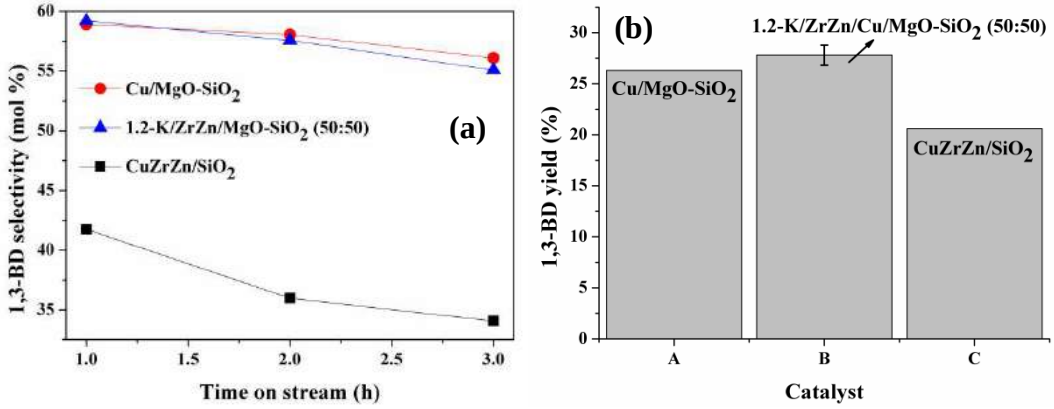

Figure 4.4.22 – Catalyst performance comparison: (a) 1,3-BD selectivity as a function of time on stream and (b) 1,3-BD yield. Reaction at 375 ºC and ethanol WHSV of 0.62 h^{-1}. For 1,3-BD yields, TOS was equal to 3 hours and the error bar denotes the absolute standard deviation obtained from duplicated reactions.

It can be seen that the Cu/MgO-SiO_2 and 1.2-K/ZrZn/MgO-SiO_2-(50:50) catalysts presented similar 1,3-BD selectivities as a function of time on stream, whereas the CuZrZn/SiO_2 system was inferior, at least for the reaction conditions evaluated in this work. However, the 1.2-K/ZrZn/MgO-SiO_2-(50:50) catalyst presented slightly better 1,3-BD yields, Figure 4.4.22(b). Thus, it is shown that the co-precipitation

method is suitable to prepare MgO-SiO_2 systems that may be used for the ethanol to 1,3-BD reaction, which is in contrast with the findings of ANGELICI *et al*. (2014, 2015).

4.4.6 Conclusions

In this section, it was shown that the modification of the catalyst acidity through alkali metals addition (Me = Na, Li and K) to the final materials leads to reduction of ethanol dehydration, boosting the 1,3-BD selectivity. A positive linear correlation was obtained for the combined 1,3-BD and acetaldehyde selectivities as a function of the catalyst Na content. Catalyst acidity modification was confirmed by NH_3-TPD and IR measurements after NH_3 adsorption, but ^{29}Si MAS NMR data indicated that the role of the alkali metal on the catalyst structure was not related directly to the interaction with Brønsted acidic silanol moieties. Since IR measurements after $CHCl_3$ adsorption indicated only subtle differences between catalysts basicity, the main effect of alkali metal doping is associated to the selective deactivation of Lewis acid sites related to ZrO_2 and ZnO.

Moreover, it was shown that catalyst properties can still be improved through reduction of the number of calcination steps during the catalyst preparation, resulting in higher surface areas, 1,3-BD yields and productivities. In particular, a strong correlation between surface area, 1,3-BD yield and productivity was observed for 1.2-Me/ZrZn/MgO-SiO_2-(50:50) samples. The best catalytic results were obtained with the 1.2-K/ZrZn/MgO-SiO_2-(50:50) material, achieving 72 mol% for the combined selectivity of 1,3-BD and acetaldehyde, at reasonable 1,3-BD yield and productivity level. Thus, the kinetic behavior of this catalytic system was investigated at different reaction conditions, as discussed in the next section.

4.5 Modelling the Effects of Reaction Temperature and Flow Rate on the Conversion of Ethanol to 1,3-Butadiene

In Section 4.2, the kinetic information contained in experimental fluctuations of ethanol to 1,3-BD conversion over the commonly used $MgO\text{-}SiO_2$ system was investigated. Acetaldehyde condensation was identified as the rate-limiting step between 300 and 400 ºC, but reaction variables effects were not quantified. In this section, reaction variables (temperature and WHSV) are rigorously investigated with help of a full factorial experimental design, as detailed in Section 3.6, allowing for identification and quantification of variable effects on catalytic activity. Catalyst performance was characterized in terms of the product distribution, 1,3-BD yields and productivities and reactions were performed using the catalytic Unit 2. The experimental study was performed with the 1.2-K/ZrZn/$MgO\text{-}SiO_2$-(50:50) system, which was prepared as described in Section 3.1.4 and had its properties discussed in Section 4.4, since this material was shown to provide high activity and selectivity to 1,3-BD, as detailed in the previous sections. This is the first study that evaluates the effect of these variables simultaneously on 1,3-BD formation from ethanol and was conducted in order to evaluate the kinetic mechanism over a wider range of reaction conditions.

4.5.1 Catalyst Stability over Reaction Time on Stream

Initially, catalyst deactivation was evaluated with a 48 h reaction test, at 350 ºC, WHSV equal to 0.62 h^{-1}, contact time equal to 3.8 s and ethanol molar fraction at the feed equal to 0.58. In this experiment (as well as in all reactions performed in this thesis), the catalyst bed was not diluted. The selectivities for the main carbon containing products are presented in Figure 4.5.1(a). The slight reduction of the 1,3-BD selectivity with time on stream was observed, which may be related to catalyst deactivation, potentially via active sites blocking due to coke formation, as suggested by the thermogravimetric analysis of the 48 h used catalyst, shown in Figure 4.5.2, and in line with the final dark color of the used catalyst, as shown in Figure 4.5.3.

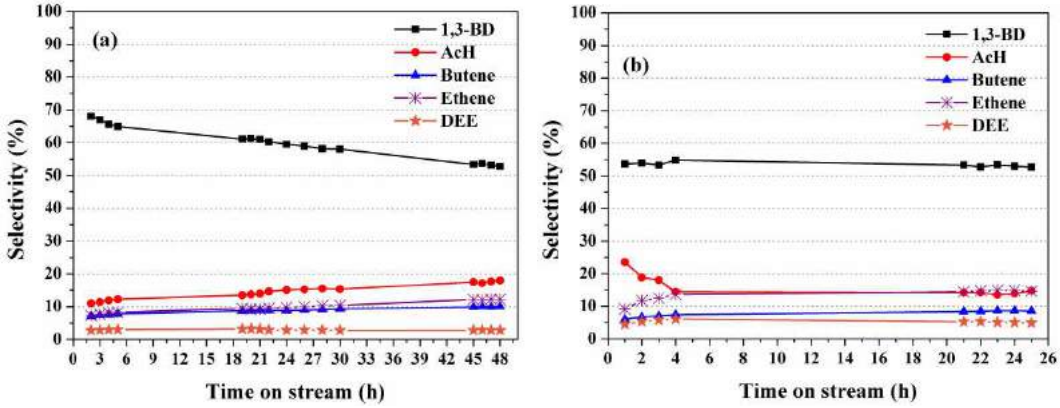

Figure 4.5.1 - Effect of time on stream on the selectivity of the main carbon containing products: (a) fresh catalyst; (b) recycled catalyst. (T of 350 ºC, WHSV of 0.62 h^{-1}, contact time of 3.8 s).

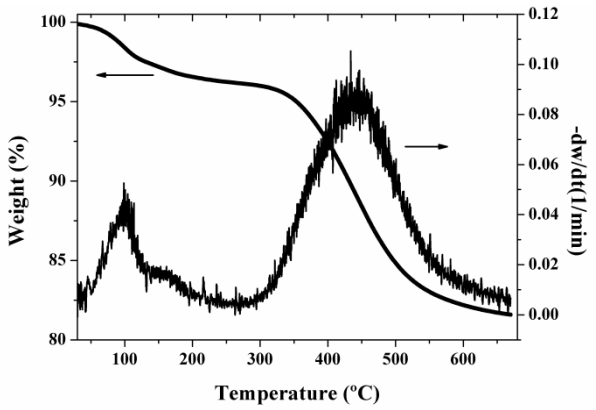

Figure 4.5.2 -Thermogravimetric analysis of the 48 h used catalyst. Only weight loss above 280 ºC was attributed as coke formation and it was calculated as 15.5 %.

Figure 4.5.3 – 1.2-K/ZrZn/MgO-SiO_2-(50:50) catalyst after 48 h of reaction use (left) and its image after regeneration (right).

The recyclability of the catalyst was also investigated. In order to assess this point, the catalyst used during the 48 h reaction test was regenerated (re-calcined in air, at 500 ºC, for 5 h, using a heating rate equal to 5 ºC/min) and re-tested for an additional period of 25 h, as shown in Figure 4.5.1(b). The BET surface area of the regenerated

material was equal to 259 ± 3 m²/g, whereas the initial fresh catalyst had BET surface area equal to 305 ± 3 m²/g. Catalyst recycling did not restore the full catalyst activity; in spite of that, the recycled catalyst showed constant and high selectivity to 1,3-BD during the test procedure.

Although the 1,3-BD selectivity was kept above 50 % during both long reaction tests, molar fractions quantified at the output reactor stream decreased more dramatically as a function of time. Figure 4.5.4 shows the molar fraction of the main carbon containing products for the fresh (a) and recycled catalyst (b) as a function of time on stream, suggesting that ethanol conversion was reduced as the result of catalyst deactivation. For instance, the calculated 1,3-BD yield was reduced from 26.5 %, after 3 h of time on stream, to 16.8 and 11.8 % after 25 and 48 h of time on stream for the fresh catalyst. For the recycled catalyst, the calculated reduction on 1,3-BD yield was smaller, from 19.3 %, after 3 h of time on stream, to 14.1 % after 25 h of time on stream.

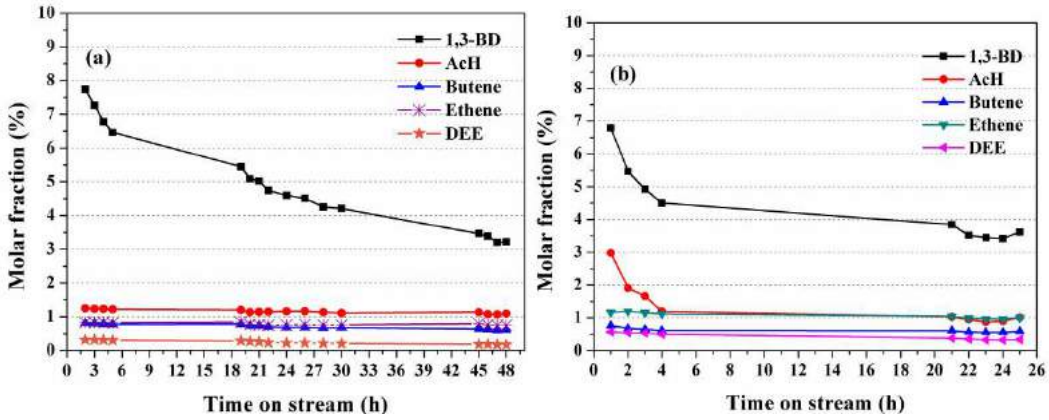

Figure 4.5.4 - Effect of time on stream on the molar fraction of the main carbon containing products: (a) fresh catalyst; (b) recycled catalyst. (T of 350 ºC, WHSV of 0.62 h^{-1}, contact time of 3.8 s).

However, the observed variability of product selectivities during the initial reaction hours were similar to the experimental fluctuations observed at the central point experiments, indicating that catalyst performances at initial reaction hours were not affected significantly by catalyst deactivation.

4.5.2 Activity Tests in the Designed Experimental Conditions

The designed experimental conditions afforded ethanol conversions ranging from 7 to 44 %, indicating that the variables imposed significant variation on the catalyst performance. The main carbon containing products were 1,3-BD, acetaldehyde (AcH), ethene, diethyl ether (DEE) and butene (1-butene, *cis*- and *trans*-2-butene). Other minor products were propene, propane, ethane, acetone, with combined selectivities below 5 %. Besides, traces of C5 and C6 compounds could also be detected. Table 4.5.1 shows ethanol conversions, selectivities of the main carbon containing products, 1,3-BD yields and productivities obtained in the designed experiments.

Table 4.5.1 - Catalytic results over the 1.2-K/ZrZn/MgO-SiO_2-(50:50) catalyst, for 3 h of time on stream, at the designed experimental conditions.

Exp.	T (ºC)	WHSV (h^{-1})	X (%)	Selectivity (mol. %)					Y_{BD} [a]	P_{BD} [b]
				1,3-BD	AcH	Ethene	DEE	Butene		
1	325	0.62	17.0	65.9	15.0	5.6	3.3	7.3	14.8	0.06
2	325	1.24	16.4	49.4	37.1	4.3	2.8	4.2	9.0	0.08
3	375	0.62	25.8	54.5	21.0	8.8	2.8	8.4	28.5	0.13
4	375	1.24	26.2	48.8	32.7	7.4	2.5	5.5	22.4	0.20
5	350	0.93	23.6	51.3	31.2	6.1	2.9	5.6	18.1	0.12
6	350	0.93	26.2	52.1	30.5	5.9	2.9	5.7	18.3	0.12
7	350	0.93	32.9	49.6	33.6	5.8	2.9	5.2	19.5	0.13
8	350	0.93	29.0	58.7	22.2	7.0	2.8	6.2	17.9	0.12
9	300	0.93	13.4	55.2	31.5	3.9	3.0	4.2	4.9	0.03
10	400	0.93	41.8	50.1	22.0	11.2	2.4	9.1	31.4	0.21
11	350	0.31	43.6	63.4	14.6	7.2	2.6	8.0	26.1	0.05
12	350	1.55	13.6	51.7	32.4	5.9	2.6	4.9	14.6	0.16
13	325	0.93	21.7	48.2	38.6	3.7	3.5	4.0	8.2	0.05
14	375	0.93	39.1	54.3	25.9	7.2	2.8	6.4	25.3	0.16
15	325	2.49	6.5	33.3	57.3	3.5	2.3	2.3	5.5	0.10
16	350	2.49	9.9	41.4	45.5	5.1	2.5	3.6	13.5	0.25
17	375	2.49	12.3	43.4	40.6	7.0	2.2	4.4	20.0	0.37
18	400	2.49	19.1	46.4	33.0	9.3	2.3	5.7	26.8	0.49

[a] Calculated as Eq. (3.5.3), in mol %. [b] In $g_{BD}/g_{cat} \cdot h$.

A list containing all components observed in the outlet reactor stream is presented in Appendix H. Additional information regarding contact time, ethanol molar fractions in the feed, molar fractions of the main carbonaceous products and carbon balances are reported in Table 4.5.2.

Table 4.5.2 - Additional catalytic results over the 1.2-K/ZrZn/MgO-SiO_2-(50:50) catalyst, for 3 h of time on stream, at the designed experimental conditions: contact time (τ), ethanol molar fraction fed (m_{EtOH}), quantified molar fractions, and carbon balances (C bal.).

Exp.	τ [a] (s)	m_{EtOH} (%)	Molar fraction [b] (%)					C bal. (%)
			1,3-BD	AcH	Ethene	DEE	Butene	
1	3.97	57.6	4.56	1.04	0.38	0.23	0.50	93.3
2	2.52	73.1	3.42	2.57	0.30	0.19	0.29	91.1
3	3.66	57.6	8.82	3.40	1.43	0.45	1.36	92.1
4	2.32	73.1	8.60	5.76	1.30	0.45	0.97	104.1
5	2.97	66.9	6.39	3.89	0.76	0.36	0.70	98.6
6	2.97	66.9	6.55	3.83	0.75	0.37	0.72	96.4
7	2.97	66.9	6.96	4.70	0.81	0.40	0.74	92.9
8	2.97	66.9	6.35	2.40	0.76	0.30	0.67	90.9
9	3.23	66.9	1.74	0.99	0.12	0.09	0.13	86.9
10	2.75	66.9	11.14	4.89	2.49	0.54	2.03	104.9
11	5.34	40.4	5.61	1.29	0.63	0.23	0.71	88.0
12	2.05	77.1	5.88	3.69	0.67	0.30	0.56	102.1
13	3.09	66.9	2.90	2.33	0.22	0.21	0.24	85.3
14	2.85	66.9	8.91	4.24	1.18	0.46	1.04	94.3
15	1.45	84.4	2.38	4.10	0.25	0.16	0.17	97.4
16	1.40	84.4	5.86	6.43	0.72	0.35	0.51	104.4
17	1.34	84.4	8.73	8.16	1.40	0.44	0.88	115.5
18	1.29	84.4	11.64	8.27	2.34	0.57	1.42	119.2

[a] τ: Contact time was calculated considering the mixture of ethanol and argon as an ideal gas at reaction temperature. [b] Molar fractions do not sum next to 100 % due to inert gas molar fraction, which was omitted.

The possible existence of mass transfer limitations was discarded from the estimation of the apparent activation energy, as shown in Figure 4.5.5. Since total flow changes with the WHSV, the assessment of mass transfer limitations was performed using the central condition (0.93 h^{-1}) for this variable, in order to perform this evaluation at an average WHSV value. Besides, catalyst particles were ground until fine powders were obtained in order to minimize internal pore diffusion limitations.

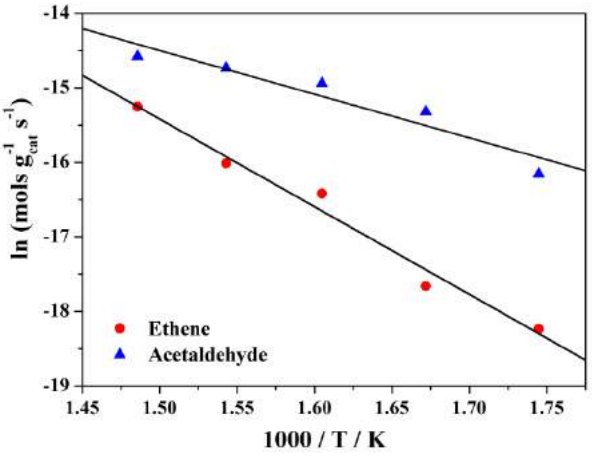

Figure 4.5.5 - Arrhenius plot for ethene and acetaldehyde from 300 to 400 ºC. Apparent activation energies were estimated as 98 and 45 kJ/mol for ethene and acetaldehyde formation, respectively. Linear correlation coefficients were equal to 0.98 and 0.91.

Catalytic results were also shown to be far from equilibrium conditions, as indicated by calculated equilibrium compositions at the analyzed reaction conditions, shown in Figure 4.5.6.

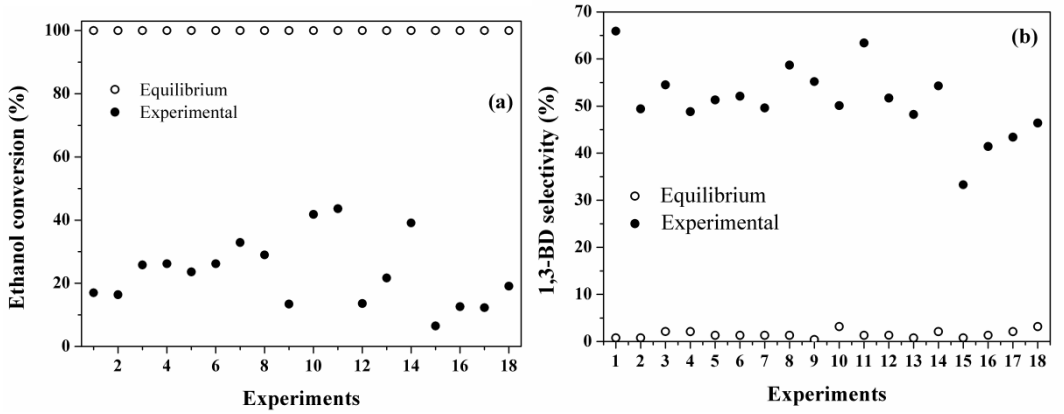

Figure 4.5.6 – Comparison between experimental (●) and values expected at equilibrium conditions (○) for ethanol conversion (a) and 1,3-BD selectivity.

Equilibrium calculations were performed for the ethanol to 1,3-BD conversion and allowing for formation of ethene, diethyl ether and butene (1-butene) as by-products at 1 atmosphere. Temperatures and ethanol feed (m_{EtOH}) used for equilibrium simulations were the same ones described in Tables 4.5.1 and 4.5.2. Compositions were calculated through the Gibbs energy minimization method, discussed in Appendix A. Numerical simulations are in accordance to the previous thermodynamic analysis, shown in Section 1.4.

Catalysts used in Experiments 7, 10 and 14 (Table 4.5.1) were analyzed after reaction trials by thermogravimetric analysis in order to characterize possible carbon formation on the catalyst surface. The observed weight losses (10.1, 9.8 and 9.5 %) were attributed to carbon deposition during reactions performed at 400, 375 and 350 ºC, respectively, as shown in Figure 4.5.7. This is a clear indication of coke deposition and possible catalyst deactivation.

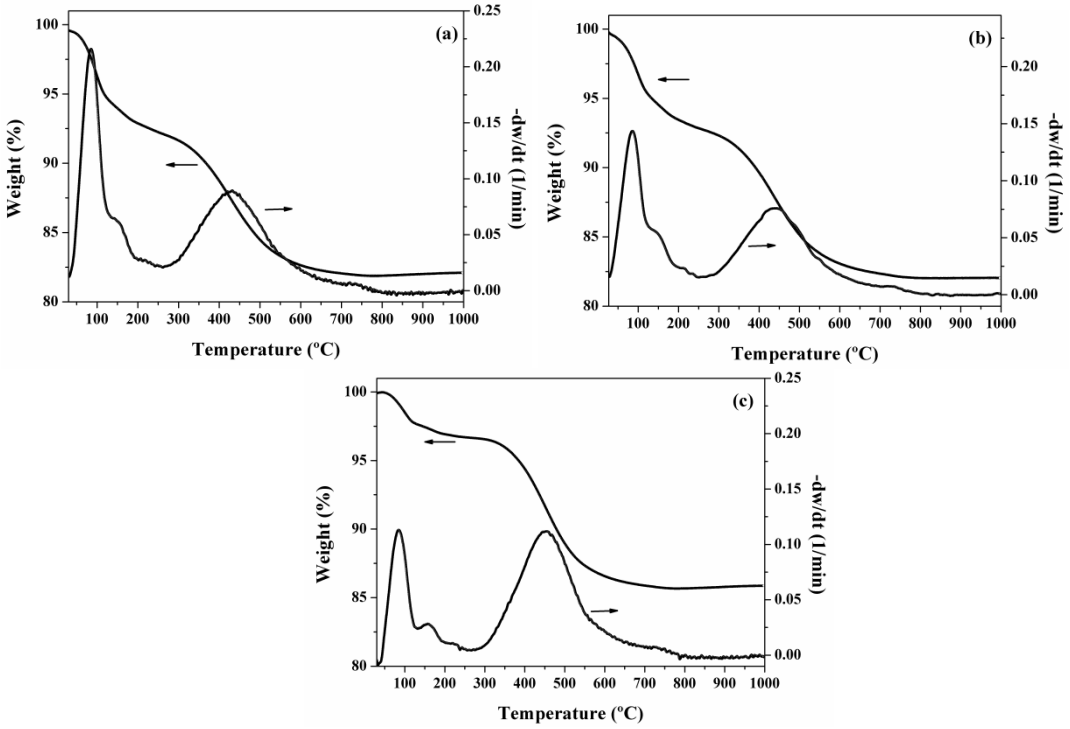

Figure 4.5.7 -Thermogravimetric analyses of used catalysts in Experiments 7 (a), 14 (b), and 10 (c). Weight losses above 280 ºC were attributed to carbon formation.

4.5.3 Modelling of the Effects of Reaction Temperature and Flow Rate on the Conversion of Ethanol to 1,3-Butadiene

Ethanol conversions, product selectivities, 1,3-BD yields and productivities were correlated to reaction variables using Eq. (3.6.2). For ethanol conversions, Figure 4.5.8 shows experimental data and values calculated with the empirical model described in Eq. (4.5.1), where lines denote constant WHSV values. The experimental standard deviation was equal to 4.0 % and the linear correlation coefficient was equal to 0.89. As expected, ethanol conversion increased with reaction temperature and decreased with the WHSV, as also observed over the ZrZn/MgO-SiO_2-(50:50) system, in the Section 4.2. It is important to emphasize that higher WHSV values correspond to higher ethanol molar fractions in the feed and lower contact times.

$$X = (26.68 \pm 1.41) + (6.02 \pm 1.23) \cdot x_1 - (3.68 \pm 0.57) \cdot x_2 \quad (4.5.1)$$

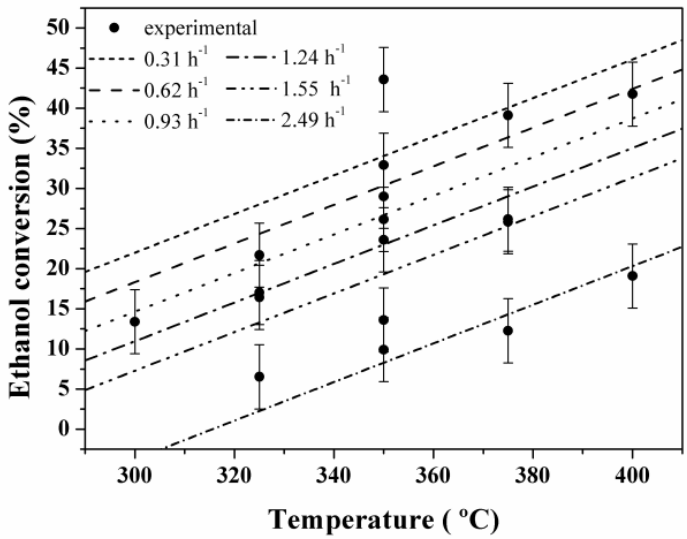

Figure 4.5.8 - Experimental values (●) and empirical model for ethanol conversion (r = 0.89). Lines represent constant ethanol WHSV.

Figure 4.5.9(a) shows the experimental ethene selectivities and the values calculated with the model described in Eq. (4.5.2), which led to a linear correlation coefficient of 0.97. Ethene selectivity ranged from 3.5 to 11.2 % with the standard deviation of 0.57 %. Temperature was the most influential variable on ethene selectivity, presenting a linear and quadratic influence within the investigated

experimental region. WHSV, in turn, exerted a linear and negative effect on the ethene selectivity, suggesting that reduction of contact time (or richer ethanol molar fraction in the feed) can cause the decrease of the ethene selectivity.

$$S_{Ethene} = (6.44 \pm 0.15) + (1.72 \pm 0.13) \cdot x_1 - (0.26 \pm 0.06) \cdot x_2 + (0.29 \pm 0.09) \cdot (x_1^2 - 14/15) \quad (4.5.2)$$

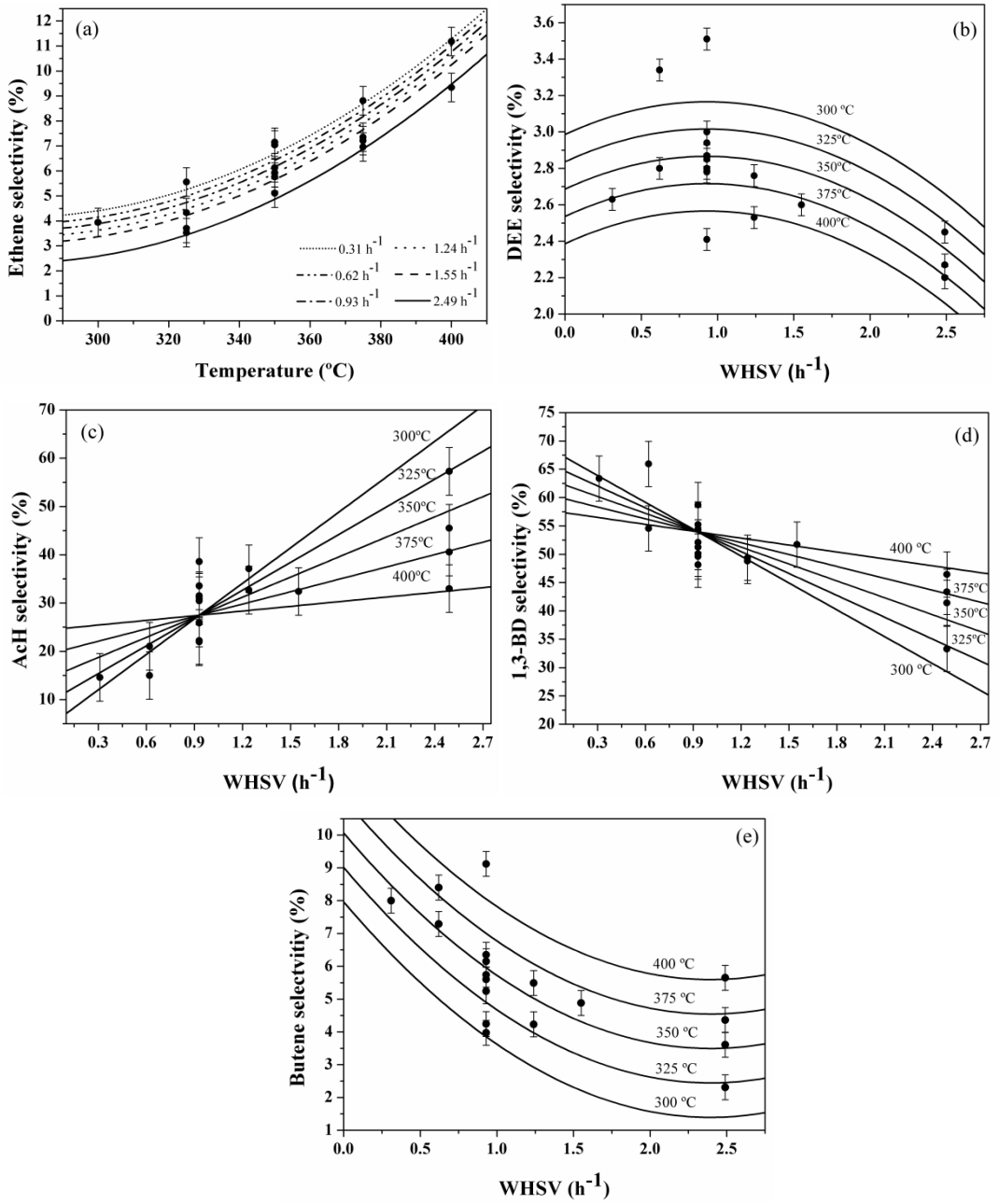

Figure 4.5.9 - Experimental values (●) and empirical model selectivities for: (a) ethene (r = 0.97); (b) DEE (r = 0.82); (c) AcH (r = 0.89); (d) 1,3-BD (r = 0.88); (e) butene (r = 0.94). In (a), lines represent constant WHSV. In (b), (c), (d) and (e), lines represent isotherms. Experimental selectivities are as described in Table 4.5.1.

For DEE selectivity, obtained data varied in a narrow range, from 2.2 to 3.5 %, with a standard deviation of 0.06 %. The empirical model described in Eq. (4.5.3) indicated that the linear effect of temperature is the most important one, although the WHSV exerted a nonlinear influence on DEE selectivity. Thus, the DEE selectivity decreased with the increase of temperature, showing a point of maximum as a function of the WHSV. This behaviour is illustrated in Figure 4.5.9(b), where the lines represent the isotherms.

$$S_{DEE} = (2.85 \pm 0.06) - (0.15 \pm 0.05) \cdot x_1 - (0.02 \pm 0.005) \cdot (x_2^2 - 12/15) \quad (4.5.3)$$

Similar effects of reaction temperature and WHSV on selectivities of ethanol dehydration products were observed over the ZrZn/MgO-SiO_2-(50:50) system, shown in Section 4.3. It can be rationalized that the increase of ethanol molar fraction in the feed can promote DEE formation due to the higher concentration of surface ethoxide species, which can suppress the formation of ethene. However, when the WHSV reached higher values, selectivity to DEE was reduced due to the increase of the AcH selectivity, as shown in Figure 4.5.9(c).

Figure 4.5.9(c) shows the experimental data and calculated values of AcH selectivities as functions of WHSV. AcH selectivities ranged from 14.6 to 57.3 % and with a standard experimental deviation of 4.9 %. AcH selectivities increased with the linear increase of WHSV and decreased with the interaction effect observed between WHSV and temperature, as described in Eq. (4.5.4).

$$S_{AcH} = (27.47 \pm 1.33) + (4.30 \pm 0.56) \cdot x_2 - (1.65 \pm 0.44) \cdot x_1 \cdot x_2 \quad (4.5.4)$$

Thus, results suggest that ethanol dehydrogenation can be facilitated at the catalyst surface, since the lower contact times associated with higher WHSV values cause the increase of the AcH selectivities. Besides, results presented in Figure 4.5.9(c) also suggest that AcH was the primary product, since selectivities were high even at low contact times. These high selectivity values also suppressed DEE formation, as discussed in the previous paragraph. These results are also in agreement with results discussed previously in Section 4.3. The interaction effect between WHSV and

temperature on AcH selectivity may be associated with the higher AcH to 1,3-BD conversions as temperature increases (MAKSHINA *et al*., 2014, JONES *et al*., 2011).

The effect of reaction variables on 1,3-BD selectivities, however, indicates a clear relationship between AcH and 1,3-BD. 1,3-BD selectivities ranged from 33 to 66 % and the standard experimental deviation was equal to 3.99 %. The empirical model of Eq. (4.5.5) presented a linear correlation coefficient of 0.88, as illustrated in Figure 4.5.9(d). This graph is similar to that obtained for AcH selectivities; however, opposite effects were observed (that is, WHSV affected linearly and negatively 1,3-BD selectivities, whereas the interaction effect was positive). Thus, these results suggest that the AcH condensation can be the slowest reaction step, since selectivities of AcH and 1,3-BD present opposite trends.

$$S_{BD} = (53.92 \pm 0.99) - (3.08 \pm 0.42) \cdot x_2 + (0.91 \pm 0.33) \cdot x_1 \cdot x_2 \quad (4.5.5)$$

However, in order to increase 1,3-BD selectivities it is not only necessary to decrease the WHSV, as it results in the increase of the butene selectivities. Butene selectivities ranged from 2.3 to 9.1 % and the standard deviation was equal to 0.38 %. The empirical model described by Eq. (4.5.6) led to a linear correlation coefficient of 0.94 and is illustrated in Figure 4.5.9(e). The WHSV exerts a fundamental role on the evolution of butene selectivities, affecting these values linearly and non-linearly. Temperature, in turn, exerted only a weak linear influence. Therefore, it is possible to identify a point of minimum for butene selectivities at each reaction temperature, as shown in Figure 4.5.9(e). As also verified over the ZrZn/MgO-SiO_2-(50:50) system, as shown in Section 4.3, no traces of butanal or butanol were observed in the output reactor stream, suggesting that butene may result from the 1,3-BD hydrogenation.

$$S_{Butene} = (6.04 \pm 0.17) + (1.05 \pm 0.15) \cdot x_1 - (1.04 \pm 0.18) \cdot x_2 + (0.11 \pm 0.04) \cdot (x_2^2 - 12/15) \quad (4.5.6)$$

However, analyses of the reaction variable effects on product molar fractions resulted in much more accurate relationships, with linear correlation coefficients of 0.99, 0.96, 0.95, 0.99 and 0.98 for ethene, DEE, AcH, 1,3-BD and butene, respectively,

as shown in Figure 4.5.10. This is because selectivities are strongly affected by fluctuations of molar fractions of all reaction products.

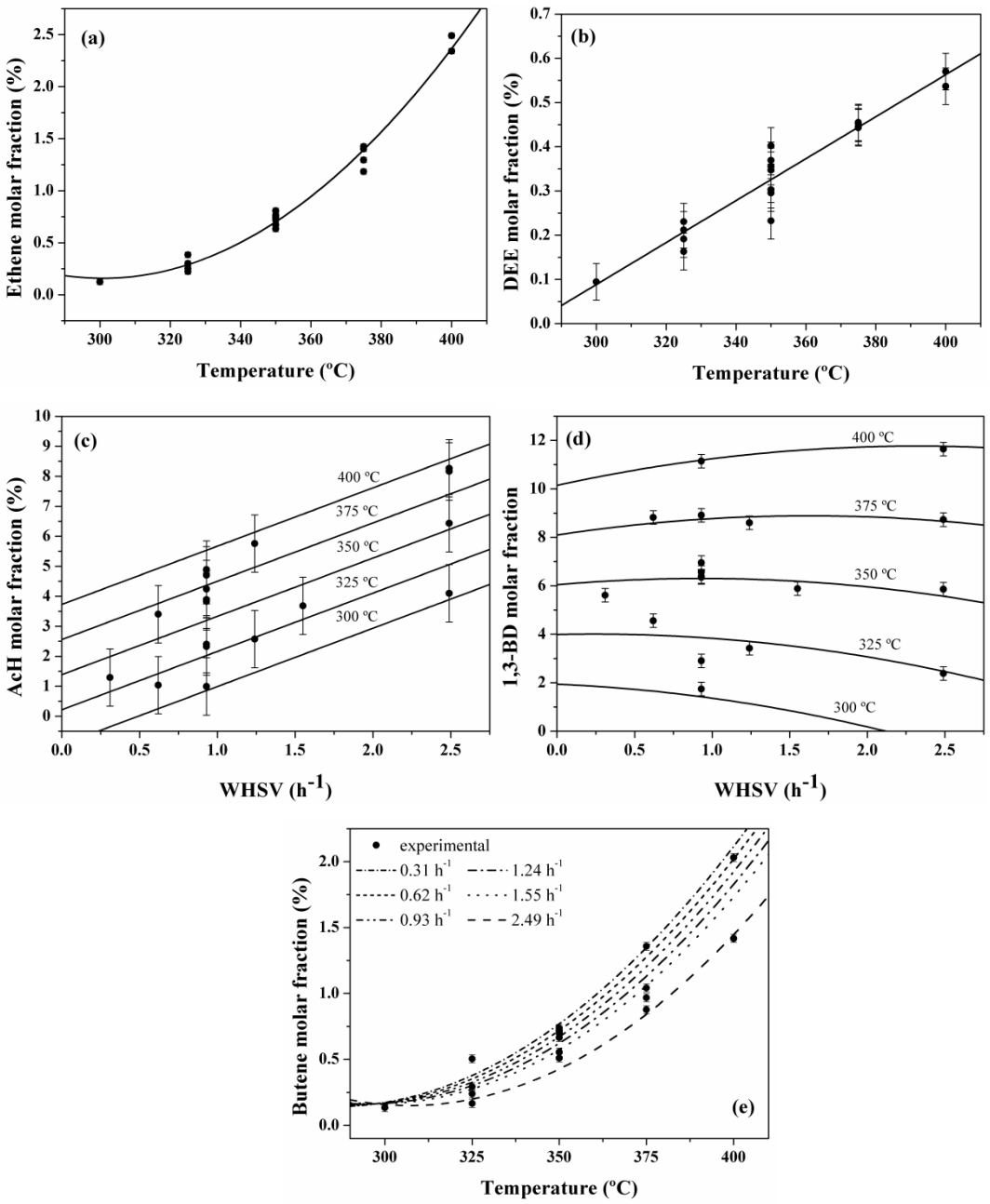

Figure 4.5.10 - Experimental values (●) and empirical model molar fraction for: (a) ethene (r = 0.99); (b) DEE (r = 0.96); (c) AcH (r = 0.95); (d) 1,3-BD (r = 0.99); (e) butene (r = 0.98). Experimental molar fractions are as described in the Table 4.5.2.

As a consequence, variances of selectivities are higher than variances of molar fractions, contributing to the lower quality of fittings presented in Figure 4.5.9.

The molar fractions of ethanol dehydration products, ethene and DEE, were not significantly affected by the WHSV, with temperature being the only variable responsible for changes in these molar fractions. Figure 4.5.10(a-b) shows the experimental and empirical model for ethene and DEE molar fraction, as described in Eq. (4.5.7) and (4.5.8). On the other hand, AcH molar fractions increased as functions of WHSV and temperature, as described by Eq. (4.5.9) and illustrated in Figure 4.5.10(c), highlighting the dehydrogenation capacity of this catalytic system.

$$m_{Ethene} = (0.83 \pm 0.02) + (0.55 \pm 0.02) \cdot x_1 + (0.14 \pm 0.02) \cdot (x_1^2 - 14/15) \quad (4.5.7)$$

$$m_{DEE} = (0.33 \pm 0.008) + (0.12 \pm 0.008) \cdot x_1 \quad (4.5.8)$$

$$m_{AcH} = (3.2 \pm 0.19) + (1.17 \pm 0.17) \cdot x_1 + (0.60 \pm 0.08) \cdot x_2 \quad (4.5.9)$$

$$m_{BD} = (6.28 \pm 0.12) + (2.44 \pm 0.12) \cdot x_1 + (0.13 \pm 0.04) \cdot x_1 \cdot x_2 - (0.029 \pm 0.01) \cdot (x_2^2 - 12/15) \quad (4.5.10)$$

$$m_{Butene} = (0.76 \pm 0.03) + (0.44 \pm 0.03) \cdot x_1 - (0.049 \pm 0.01) \cdot x_2 - (0.02 \pm 0.01) \cdot x_1 \cdot x_2 + (0.09 \pm 0.02) \cdot (x_1^2 - 14/15) \quad (4.5.11)$$

1,3-BD molar factions, in turn, increased with temperature and with the interaction effect between temperature and WHSV, being also affected negatively by the nonlinear WHSV effect. Thus, it is possible to identify a point of maximum in the 1,3-BD molar fraction for each reaction temperature, as shown in Figure 4.5.10(d). Finally, butene molar fractions were adjusted by a function containing the linear effects of temperature and WHSV and the quadratic effect of temperature, as shown in Eq. (4.5.11) and Figure 4.5.10(e).

It is important to note that all effects from Eq. (4.5.1-4.5.11) were shown to be statistically significant, within 95 % confidence level, when all data were used to estimate models parameters. Thus, although some error bars cross more than one statistical model line (see Figure 4.5.8, Figure 4.5.9 (a,c,d) and Figure 4.5.10(c)), all reported variable effects are meaningful – and valid – since they were determined using the whole experimental set. For instance, in Figure 4.5.10(c) at WHSV equal to 2.5 h^{-1} despite the fact that values at 400 ºC are not significantly different from the values predicted at 375 ºC, a significant increase in the AcH molar fraction was observed as temperature increased from 300 ºC to 350 ºC and from 350 ºC to 400 ºC. Consequently,

it can be concluded that an increase in the temperature leads to a significant increase in the AcH molar fraction.

The results obtained with the molar fractions highlight some of the advantages related to the use of experimental designs for identification and quantification of variable effects. All molar fractions of products increased linearly with temperature, which is directly related to the increase of the ethanol conversion. However, it is possible to observe that this effect was more pronounced for the 1,3-BD molar fractions, which presented a linear temperature effect equal to 2.44, as shown in Eq. (4.5.10), followed by the effects on AcH, ethene, butene and DEE molar fractions. This suggests that reduction of DEE selectivities with temperature may be related to the faster increase of the molar fractions of the remaining products, when compared to the molar fractions of DEE. Additionally, since the WHSV exerted no significant effect on ethene and DEE molar fractions, the WHSV effect on ethene and DEE selectivities can be understood as a consequence of the observed WHSV effect on 1,3-BD, AcH and butene molar fractions.

Eq. (4.5.1-4.5.11) also indicates that higher WHSV conditions are beneficial for 1,3-BD production, as AcH and 1,3-BD molar fractions are favored by this variable. This suggests that the catalyst surface should be rich in active sites for ethanol dehydrogenation, since the increase of the ethanol molar fraction in the feed (using higher WHSV) resulted in higher AcH molar fractions. Furthermore, the behavior of 1,3-BD and AcH molar fractions supports the hypothesis that the AcH condensation step constitutes the slowest reaction step, as also concluded from product selectivity analysis. Therefore, efforts should be driven to indentify AcH condensation sites and determine how they depend on the catalyst preparation conditions, in order to further optimize catalyst properties and maximize 1,3-BD production.

At this point, it is important to emphasize that Eq. (4.5.1-4.5.11) can be used to describe catalytic performance within experimental ranges and should be used with care for extrapolations. Nevertheless, the proposed models describe catalyst activity very well inside the selected experimental region, unveiling the kinetic rate-limiting step in the commonest range of experimental conditions reported in the literature and fully justifying the utilization of the proposed statistical approach. Moreover, as in a phenomenological model that presents different kinetic parameters (activation energy and pre-exponential factor) depending on the employed catalyst, the parameters from

Eq. (4.5.1-4.5.11) should be re-estimated when evaluating different active catalysts for the ethanol to 1,3-BD reaction. However, the approach presented in this work is broadly applicable and highlights the importance of a full statistical study.

The effects of reaction variables on 1,3-BD yields and productivities were also evaluated. 1,3-BD yields, as defined in Eq. (3.5.3), ranged from 4.9 to 31.4 % and had standard deviation of 0.73 %. Data could be fitted using a function containing the linear effect of temperature and the linear and quadratic effect of WHSV, as shown in Eq. (4.5.12) and Figure 4.5.11(a).

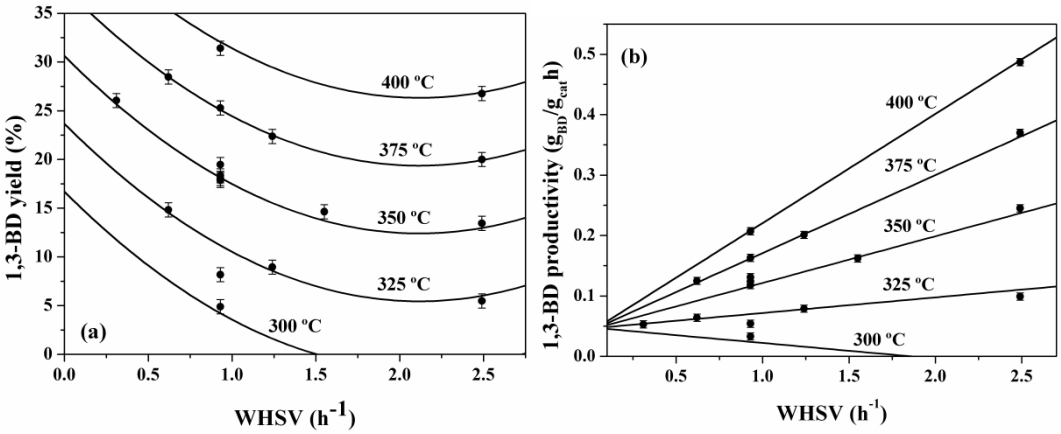

Figure 4.5.11 - Experimental and empirical model for: (a) 1,3-BD yield (r = 0.99); (b) 1,3-BD productivity (r = 0.99).

As pointed previously in Section 4.3, catalyst performance is usually assessed at low ethanol flow rates, resulting in too low 1,3-BD productivities to be industrially significant. The quantification of reaction variables effects on 1,3-BD yield showed, however, that WHSV affected 1,3-BD yields linearly and nonlinearly, being possible to obtain reasonably high 1,3-BD yields under high WHSV conditions, thus increasing the industrial viability of this system.

$$Y_{BD} = (18.45 \pm 0.26) + (6.96 \pm 0.23) \cdot x_1 - (2.99 \pm 0.27) \cdot x_2 + (0.39 \pm 0.06) \cdot (x_2^2 - 12/15) \quad (4.5.12)$$

Figure 4.5.11(b) shows experimental 1,3-BD productivities and values calculated with an empirical model, as a function of WHSV. Productivities ranged from 0.06 to 0.49 $g_{BD}/g_{cat}{\cdot}h$ and the standard deviation was equal to 0.006 $g_{BD}/g_{cat}{\cdot}h$. 1,3-BD

productivities increased as a linear function of temperature and WHSV, being favored by the interaction effect, as shown in Eq. (4.5.13) and Figure 4.5.11(b).

$$P_{BD} = (0.116 \pm 0.002) + (0.046 \pm 0.002) \cdot x_1 + (0.024 \pm 0.001) \cdot x_2 + (0.016 \pm 0.001) \cdot x_1 \cdot x_2 \quad (4.5.13)$$

Finally, as WHSV was modified by varying ethanol flow rate only, it is not possible to distinguish between contact time and ethanol composition effects on the discussed models. Thus, WHSV effects represent somehow the influence of both variables.

4.5.4 Principal Component Analysis

Molar fractions observed at central point experiments (Exps 5-8, in Table 4.5.2) were evaluated in respect to the variability. Table 4.5.3 shows the principal directions calculated with PCA analysis, suggesting that few common sources of fluctuation perturbed experimental data, in line with results presented in Section 4.2. Moreover, the correlation matrix of this data set, shown in Table 4.5.4, highlights the relationship between ethanol and the main carbonaceous products. Correlation coefficients among products are all positive, as also observed in Section 4.2 for replicates performed at 350 ºC (see Figures 4.2.13, 4.2.15-4.2.18).

Table 4.5.3 - Principal directions computed with standard PCA tools at central point. Numbers represent correlations coefficients between the factor (eigenvector) and the original direction of variable fluctuation.

	Temperature at 350 ºC		
	Factor 1	Factor 2	Factor 3
Ethanol	0.61	**0.77**	-0.21
1,3-BD	**-0.98**	-0.17	0.13
AcH	**-0.91**	0.39	-0.16
Ethene	**-0.79**	-0.50	-0.35
DEE	**-0.94**	0.34	0.004
Butene	**-0.91**	0.38	0.18
Eigenvalue	4.48	1.28	0.24
Explained Variance (%)	74.6	21.3	4.1

Numbers in bold denote correlation coefficients higher than 0.7.

Table 4.5.4 – Molar fraction correlation matrix from central experiments obtained at 350 ºC (Exps 5-8, Table 4.5.2).

	Ethanol	1,3-BD	AcH	Ethene	DEE	Butene
Ethanol	1.00	-0.75	-0.22	-0.79	-0.30	-0.29
1,3-BD	-0.75	1.00	0.80	0.81	0.86	0.84
AcH	-0.22	0.80	1.00	0.58	0.99	0.94
Ethene	-0.79	0.81	0.58	1.00	0.57	0.46
DEE	-0.30	0.86	0.99	0.57	1.00	0.98
Butene	-0.30	0.84	0.94	0.46	0.98	1.00

Conversely, whereas in Section 4.2 it was concluded that the hypothesis of constant experimental error throughout the whole experimental region should be avoided, since experimental fluctuations depend on reaction conditions such as temperature and catalyst properties, in this section it is assumed that experimental fluctuations are constant and equal to the value measured at the central experimental conditions (Exp 5-8 of Table 3.2). Such hypothesis was assumed to be valid because measurement of experimental variances in each reaction condition of the plain would result in an unfeasible number of experiments. Regardless, the rigorous statistical approaches employed to analyze experimental data allows for significant reduction of the impact of measurement errors on obtained results. As a consequence, it became possible to evaluate the main effects, the quadratic effects and the variable interaction effects exerted by the investigated variables on catalyst performances with minimum uncertainty and minimum number of experiments. Thus, the obtained results are very significant, as they indicate the effects of process conditions on catalyst performance, as needed when one is interested in designing reaction processes. However, it is true that obtained data depend on the catalyst, although this is also true when one proposes fundamental kinetic models to describe available kinetic data, as in general kinetic parameters cannot be transported from one catalyst to the other. Finally, in order to propose a kinetic model one needs to understand the effects of processing variables on catalyst performance, as it was pursued here.

4.5.7 Conclusions

In this section, the effects of temperature and ethanol WHSV on the performances of ethanol to 1,3-BD reactions were investigated with the aid of a statistical experimental design. Catalytic results, ethanol conversions, product selectivities, 1,3-BD yields and productivities were correlated with reaction variables, allowing for identification and quantification of variable effects on the 1,3-BD formation.

The interaction effect between temperature and WHSV was very important for 1,3-BD molar fractions, selectivities and productivities. Thus, evaluation of catalyst performance in terms of the “change-one-factor-at-a-time” method should be thought carefully, so as not to erroneously assign a change in selectivity to one variable and not two acting in a cooperative manner. Moreover, the nonlinear effects of WHSV on 1,3-BD molar fractions and yields were significant, indicating that high WHSV conditions can clearly benefit the 1,3-BD formation with the investigated catalyst system.

Further, the results indicate the existence of a strong relationship between acetaldehyde and 1,3-BD selectivities, as well as their respective molar fractions, suggesting that conversion of acetaldehyde to 1,3-BD constitutes the rate determining step of the reaction mechanism. As a consequence, efforts should be driven to indentify AcH condensation sites and determine how they depend on catalyst preparation conditions, in order to allow for optimization of catalyst properties and maximize 1,3-BD production. Moreover, given the obtained empirical model responses, the investigation of 1,3-BD production at higher temperatures and WHSV's should be considered. In particular, as WHSV was modified by varying ethanol flow rate only, it was not possible to distinguish between contact time and ethanol composition effects on the catalyst activity. Thus, contact time and ethanol feed composition should be studied independently. Finally, catalyst stability for longer times on stream should be pursued in order to become feasible the industrial application of the proposed catalyst.

5. CONCLUSIONS AND RECOMMENDATIONS

In the present work, the synthesis of multifunctional magnesia silicate oxides MgO-SiO_2 catalysts prepared by the co-precipitation method was investigated for the ethanol to 1,3-butadiene conversion.

Experimental fluctuations were characterized in a wide range of reaction temperatures, using two MgO-SiO_2 catalyst systems (with Mg:Si molar ratios of 50:50 and 95:5) with distinct properties. Both reaction temperature and catalyst features were important to explain experimental fluctuations, which were not constant. Moreover, molar fraction fluctuations of distinct compounds in the output stream were correlated, indicating that the usual constant and independent error assumption should be avoided for quantitative data analysis. Thus, the least-squares objective function should be avoided in parameter estimation procedures. Reaction experimental fluctuations were discriminated from intrinsic chromatographic measurement fluctuations and, thus, the kinetic information contained in the covariance matrix was extracted. Particularly, correlation analyses performed with data obtained with the MgO-SiO_2-(50:50) catalyst indicated that the ethanol to 1,3-BD reaction mechanism probably involves two distinct slow steps in the analyzed temperature range. From 300 to 400 ºC, acetaldehyde condensation is expected to limit the reaction rates, while ethanol dehydrogenation is expected to be the slowest reaction step at 450 ºC. Standard PCA reinforced the proposed kinetic interpretation and indicated that variability of catalyst activity probably constitutes the most important source of experimental fluctuation in the analyzed reaction system.

The effect of the Mg-to-Si molar ratio was investigated in the synthesis of MgO-SiO_2 catalysts prepared by co-precipitation. Catalysts were used as support for ZrO_2 and

ZnO and ethanol conversion was studied in a wide range of WHSVs using two temperatures. ^{29}Si MAS NMR data suggested that the co-precipitation method was more efficient for formation of Mg-O-Si linkages, when compared to the traditional wet-kneading method. Moreover, the Mg-to-Si molar ratio equal to 1 was more suitable to 1,3-BD formation, while higher Mg-to-Si molar ratios produced more acetaldehyde. High productivities (in g_{BD}/g_{cat}.h) were obtained with the ZrZn/MgO-SiO_2-(50:50) system, results that might be associated to the homogeneity of the catalysts properties.

Catalytic results supported the usual kinetic route of ethanol to 1,3-BD conversion involving acetaldehyde condensation. However, although a suitable performance for ethanol to 1,3-BD conversion have been obtained over the ZrZn/MgO-SiO_2-(50:50) catalyst, this material presented reasonably high selectivities for ethanol dehydration products, ethene and DEE; thus, the acidic features of this system were modified through the addition of the alkali metals Na, K and Li.

The catalyst acidity modification through alkali metals addition (Me = Na, Li and K) to the final materials allowed for reduction of the fraction of dehydrated ethanol, while boosting 1,3-BD selectivity. A positive linear relation was obtained for the combined 1,3-BD and acetaldehyde selectivities as a function of the catalyst Na content. Catalyst acidity modification was further confirmed by NH_3-TPD and IR measurements from NH_3 adsorption, but ^{29}Si MAS NMR data indicated that the role of the alkali metal on the catalyst structure was not related to its interaction with Brønsted acidic silanol moieties. Since IR measurements from $CHCl_3$ adsorption indicated only subtle differences between catalysts basicity, the main effect of alkali metal doping might be associated to the selective deactivation of Lewis acid sites related to ZrO_2 and ZnO. As a suggestion for future work, the evaluation of sodium washing removal after the aging time of the initial MgO-SiO_2 system could be investigated, since this could simplify catalyst preparation procedure.

It was shown that catalyst properties can still be improved through the reduction of calcination steps during the catalyst preparation, resulting in higher surface areas, 1,3-BD yields and productivities. In particular, a strong correlation between surface area, 1,3-BD yield and productivity was observed for 1.2-Me/ZrZn/MgO-SiO_2-(50:50) samples. The best catalytic results were obtained with the 1.2-K/ZrZn/MgO-SiO_2-(50:50) material, achieving 72 mol % for the combined selectivity of 1,3-BD and acetaldehyde, at reasonable 1,3-BD yield and productivity level. This material also

presented the highest surface area among the alkali metal doped samples. Thus, in order to improve the catalyst properties, efforts should be driven to increase the catalyst surface area, while keeping the acid-basic sites distribution constant. In order to do that, the catalyst preparation method could be modified. For instance, structure-directing agents and/or surfactants could be employed in order to produce ordered mesoporous magnesium silicate materials with higher surface areas, as performed during preparation of ordered mesoporous silicas, such as SBA-15. The synthesis of nanoparticles and/or nanowires of magnesium silicates could also bring improvements to the 1,3-BD production from ethanol, since nanocatalysts might combine the advantages of high surface area and high porosity, increasing the availability of surface active sites, while simultaneously improving heat transfer rates. These factors could prevent catalyst deactivation by sinterization and by active sites blocking due to formation of carbon deposits.

The 1.2-K/ZrZn/MgO-SiO_2-(50:50) system was investigated at different reaction conditions, with the aid of a statistical experimental design. Catalytic results, ethanol conversions, product selectivities, 1,3-BD yields and productivities were correlated with reaction variables, temperature and WHSV, allowing for identification and quantification of variable effects on the 1,3-BD formation.

The interaction effect between temperature and WHSV was very important for 1,3-BD molar fractions, selectivities and productivities. Thus, evaluation of catalyst performance in terms of the “change-one-factor-at-a-time” method should be thought carefully, so as not to erroneously assign a change in selectivity to one variable and not two acting in a cooperative manner. Moreover, the nonlinear effects of WHSV on 1,3-BD molar fractions and yields were significant, indicating that high WHSV conditions can clearly benefit the 1,3-BD formation with the investigated catalyst system.

Obtained results indicate the existence of a strong relationship between acetaldehyde and 1,3-BD selectivities, as well as their respective molar fractions, suggesting that conversion of acetaldehyde to 1,3-BD constitutes the rate determining step of the reaction mechanism, in line with the information contained in the covariance matrix of experimental fluctuations. As a consequence, efforts should be driven to indentify AcH condensation sites and determine how they depend on catalyst preparation conditions, in order to allow for optimization of catalyst properties and maximization of 1,3-BD production. For instance, a study investigating the modification

of ZrO_2, ZnO and K_2O contents, simultaneously, could also bring additional insights about the role of the distinct active sites on the 1,3-BD formation.

Given the obtained empirical model responses, the investigation of 1,3-BD production at higher temperatures and WHSV's should be considered. In particular, as WHSV was modified by varying ethanol flow rate only, it was not possible to distinguish between contact time and ethanol composition effects on the catalyst activity. However, it could be noted that high ethanol molar fractions and low contact time could improve 1,3-BD selectivity (even though the contact time effect is nonlinear, because at some point 1,3-BD will be converted to butenes). Thus, the study of contact time, temperature and ethanol feed composition should be investigated independently.

Finally, catalyst stability for longer times on stream should be pursued for the industrial application of the proposed system to become feasible. Once catalyst sinterization can be avoided, carbonaceous products deposits could be eliminated by cycles of regeneration with oxygen. However, other factor that could contribute to catalyst deactivation is the ablating of alkali metal surface, especially if they are added to the final catalyst through incipient wetness impregnation. Thus, other catalyst preparation techniques should be investigated, such as the solution combustion synthesis, which could produce materials that are more resistant to degradation (GHOSE *et al*., 2014).

In order to improve the process, it is still required to develop a fundamental kinetic model involving the reactor mass balance and the reaction steps. Once the reaction system is described (involving the estimation of the kinetic parameters), operational variables can be properly manipulated to find the reaction condition that maximizes 1,3-BD yield and selectivity. Thus, one can see that there is much work to be done in order to make the ethanol to 1,3-BD reaction more efficient and economically feasible.

6. REFERENCES

ALBERTON, A. L. *Estimação de parâmetros e planejamento de experimentos: Estudo de incertezas e funções de informação*. PhD. Dissertation, PEQ/COPPE/UFRJ, Rio de Janeiro, RJ, Brazil, 2010.

ALBERTON, A.L., SCHWAAB, M., SCHMAL, M., PINTO, J.C. "Experimental errors in kinetic tests and its influence on the precision of estimated parameters. Part I-Analysis of first-order reactions", *Chemical Engineering Journal*, v. 155, p. 816-823, 2009.

ALBERTON, A. L., SCHWAAB, M., LOBÃO, M. W. N., PINTO, J. C. "Experimental design for the joint model discrimination and precise parameter estimation through information measures", *Chemical Engineering Science*, v. 66, p. 1940-1952, 2011.

ANGELICI, C., WECKHUYSEN, B. M., BRUIJNINCX, P. C. A. "Chemocatalytic conversion of ethanol into butadiene and other bulk chemicals", *ChemSusChem*, v. 6, p. 1595-1614, 2013.

ANGELICI, C., MARJOLEIN, E. Z., WECKHUYSEN, B. M., BRUIJNINCX, P. C. A. "Effect of preparation method and CuO promotion in the conversion of ethanol into 1,3-Butadiene over SiO_2-MgO catalysts", *ChemSusChem*, v. 7, p. 2505-2515, 2014.

ANGELICI, C., VELTHOEN, M. E. Z., WECKHUYSEN, B. M., BRUIJNINCX, P. C. A. "Influence of acid-base properties on the Lebedev ethanol-to-butadiene process catalyzed by SiO_2-MgO materials", *Catalysis Science & Technology*, v. 5, p. 2869-2879, 2015.

ARAI, H., TAKE, J.-I., SAITO, Y., YONEDA, Y. "Ethanol dehydration on alumina catalysts I. The thermal desorption of surface compounds", *Journal of Catalysis*, v. 9, p. 146-153, 1967.

ARNDT, S., LAUGEL, G., LEVCHENKO, S., HORN, R., BAERNS, M., SCHEFFLER, M., SCHLÖGL, R., SCHOMÄCKER, R. "ACritical Assessment

of Li/MgO-Based Catalysts for the Oxidative Coupling of Methane", *Catalysis Reviews: Science and Engineering*, v. 53:4, p. 424-514, 2011.

AUROUX, A., GERVASINI, A. "Microcalorimetric study of the acidity and basicity of metal oxide surfaces", *The Journal of Physical Chemistry*, v. 94, p. 6371-6379, 1990.

BARD, Y. *Nonlinear Parameter Estimation*, New York, Pergamon Press, 1974.

BAERDEMAEKER, T. D., FEYEN, M., MÜLLER, U., YILMAZ, B., XIAO, F.-S., ZHANG, W., YOKOI, T., BAO, X., GIES, H., DE VOS, D. E. "Bimetallic Zn and Hf on silica catalysts for the conversion of ethanol to 1,3-butadiene", *ACS Catalysis*, v. *5*, p. 3392-3397, 2015.

BASTIANI, R., 2001. *Condensação aldólica do citral com a acetona*. Tese de M.Sc., PEQ/COPPE/UFRJ, Rio de Janeiro, RJ, Brasil.

BAYLON, R. A. L., SUN, J., WANG, Y. "Conversion of ethanol to 1,3-butadiene over Na doped $Zn_xZr_yO_z$ mixed metal oxides", *Catalysis Today*, v. 259, p. 446-452, 2016.

BHATTACHARYYA, S. K., GANGULY, N. D. "One-step catalytic conversion of ethanol to butadiene in the fixed bed. I. Single-oxide catalysts", *Journal of Applied Chemistry*, v. 12, p. 97-104, 1962a.

BHATTACHARYYA, S. K., GANGULY, N. D. "One-step catalytic conversion of ethanol to butadiene in the fixed bed. II. Binary and ternary oxide catalysts", *Journal of Applied Chemistry*, v. 12, p. 105-110, 1962b.

BHATTACHARYYA, S. K., AVASTHI, B. N. "One-step catalytic conversion of ethanol to butadiene in a fluidized bed", *I&EC Process design and development*, v. 2, nº1, p. 45-51, 1963.

BHATTACHARYYA, S. K., AVASTHI, B. N. "Catalytic conversion of ethanol to butadiene by two-step process in a fluidized bed", *Journal of Applied Chemistry*, v. 16, p. 239-244, 1966.

BHATTACHARYYA, S. K., SANYAL, S. K. "Kinetic study on mechanism of the catalytic conversion of ethanol to butadiene", *Journal of Catalysis*, v. 7, p. 152-158, 1967.

BOX, G. E. P., HUNTER, J. S., HUNTER, W. G., *Statistics for Experimenters – Design, Innovation, and Discovery*. 2 ed. New Jersey, John Wiley & Sons, 2005.

BOX, G. E. P., HUNTER, W. G., HUNTER, J. S., *Statistics for Experimenters – An Introduction to Design, Data Analysis, and Model Building*. John Wiley & Sons, New York, 1978.

BREW, D.R.M., GLASSER, F.P. "Synthesis and characterisation of magnesium silicate hydrate gels", *Cement and Concrete Research*, v. 35 p. 85-98, 2005.

BRUICE, P. Y., *Organic Chemistry*. 4 ed. Cleveland, Prentice Hall, 2004.

BRUIJNINCX, P. C. A., WECKHUYSEN, B. M. "Shale Gas Revolution: An Opportunity for the Production of Biobased Chemicals?", *Angewandte Chemie International Edition*, v. *52*, p. 11980-11987, 2013.

CALLEJA, G., DE LUCAS, A., VAN GRIEKEN, R. "Co/HZSM-5 catalyst for syngas conversion: influence of process variables", *Fuel*, v. 74, p. 445-451, 1995.

CAREY, F. A., *Organic Chemistry*. 4 ed. Boston, *Mc Graw Hill*, 2001.

CERQUEIRA, H. S., RAWET, R., PINTO, J. C. "The influence of experimental errors during laboratory evaluation of FCC catalysts", *Applied Catalysis A*, v. 181, p. 209-220, 1999.

CESPI, D., PASSARINI, F., VASSURA, I., CAVANI, F. "Butadiene from biomass, a life cycle perspective to address sustainability in the chemical industry", *Green Chemistry*, v. 18, p. 1625-1638, 2015.

CHAE, H.-J., KIM, T.-W., MOON, Y.-K., KIM, H.-K., JEONG, K.-E., KIM, C.-U., JEONG, S.-Y. "Butadiene production from bioethanol and acetaldehyde over tantalum oxide-supported ordered mesoporous silica catalysts". *Applied Catalysis B: Environmental*, v. 150-151, p. 596-604, 2014.

CHIEREGATO, A., OCHOA, J. V., BANDINELLI, C., FORNASARI, G., CAVANI, F., MELLA, M. "On the chemistry of ethanol on basic oxides: revising mechanisms and intermediates in the Lebedev and Guerbet reactions", *ChemSusChem*, v. 8, p. 377-88, 2015.

CHOUDHARY, V. R., RANE, V. H., PANDIT, M. Y. "Comparison of alkali metal promoted MgO catalysts for their surface acidity/basicity and catalytic activity/selectivity in the oxidative coupling of methane", *Journal of Chemical Technology and Biotechnology*, v. 68, p. 177-186, 1997.

CORSON, B. B., STAHLY, E. E., JONES, H. E., BISHOP, H. D. "Butadiene from ethyl alcohol - Study of the variables of operation", *Chemical and Engineering Chemistry*, v. 41, p. 1012-1017, 1949.

CORSON, B. B., JONES, H. E., WELLING, C. E., Hinckley, J. A., Stahly, E. E. "Butadiene from ethyl alcohol – Catalysis in the one and two step processes". *Industrial and Engineering Chemistry*, v. 42, p. 359-373, 1950.

DEAN, J. A. *Lange's Handbook of Chemistry*, 14th ed., New York, McGraw-Hill, 1992.

DELHOMME, C., WEUSTER-BOTZ, D., KÜHN, F. E. "Succinic acid from renewable resources as a C_4 building-block chemical - a review of the catalytic possibilities in aqueous media", *Green Chemistry*, v. 11, p. 13-26, 2009.

DI COSIMO, J. I., DÍEZ, V. K., XU, M.; IGLESIA, M., APESTEGUÍA, C. R. "Structure and surface and catalytic properties of Mg-Al basic oxides", *Journal of Catalysis*, v. 178, p. 499-510, 1998.

DI COSIMO, J. I., DÍEZ, V. K., XU, M., IGLESIA, E., APESTEGUÍA, C. R. "Gas-phase hydrogen transfer reduction of α,β insaturated ketones on Mg-based catalysts", *Journal of Molecular Catalysis A: Chemical*, v. 222 p. 87-96, 2004.

EZINKWO, G. O., TRETJAKOV, V. F., TALYSHINKY, R. M., ILOLOV, A. M., MUTOMBO, T. A. "Creation of a continuous process for bio-ethanol to butadiene conversion via the use of a process initiator", *Catalysis Communications*, v. 43, p. 207-212, 2014.

EDGAR, T.F., HIMMELBLAU, D.M., LASDON, L.S. *Optimization of Chemical Processes*, 2 ed. New York, McGraw-Hill, 2001.

FRANCKAERTS, J., FROMENT, G. F. "Kinetic study of the dehydrogenation of ethanol", *Chemical Engineering Science*, v. 19, p. 807-818, 1964.

FROMENT, G.F., BISCHOFF, K.B., DE WILDE, J. *Chemical reactor analysis and design*, 3 ed. United States, John Wiley & Sons, Inc., 2011.

GALADIMA, A., MURAZA, O. "Revisiting the oxidative coupling of methane to ethylene in the golden period of shale gas: A review", *Journal of Industrial and Engineering Chemistry*, v. 37, p.1-13, 2016.

GAO, M., LIU, Z., ZHANG, M., TONG, L. "Study on the mechanism of butadiene formation from ethanol", *Catalysis Letters*, v. 144, p. 2071-2079, 2014.

GHOSE, R., "Catalysts for oxidative coupling of methane and solution combustion method for the production of the same", *Patent US 2014/00806699A1*, 2014.

GRUVER V., SUN, A., FRIPIAT, J. J. "Catalytic properties of aluminated sepiolite in ethanol conversion", *Catalysis Letters*, v. 32, p. 359-364, 1995.

HAN, Z., LI, X., ZHANG, M., LIU, Z., GAO, M. "Sol-gel synthesis of ZrO_2-SiO_2 catalysts for the transformation of bioethanol and acetaldehyde into 1,3-butadiene", *RSC Advances*, v. 5, p. 103982-103988, 2015.

HARRIS, D.C. *Quantitative chemical analysis*, 7 ed. New York, W.H. Freeman and Company, 2006.

HARTMAN, J.S., MILLARD, R.L. "Gel synthesis of magnesium silicates: a ^{29}Si magic angle spinning NMR study", *Physics and Chemistry of Minerals*, v. 17, p, 1-8, 1990.

HARTMANN, P., BENDER, C.L., SANN, J., DÜRR, A.K., JANSEN, M., JANEK, J., ADELHELM, P. "A comprehensive study on the cell chemistry of the sodium superoxide (NaO_2) battery", *Physical Chemistry Chemical Physics : PCCP*, v. 15, p. 11661-72, 2013.

HSU, K., LI, K. "Extractive distillation process for recovering butadiene from C4 hydrocarbon mixtures", *Patente Industrial US8252150B1*, 2012.

HUBER, G. W., IBORRA, S., CORMA, A. "Synthesis of Transportation Fuels from Biomass: Chemistry, Catalysts, and Engineering", *Chemical Reviews*, v. 106, p. 4044-4098, 2006.

HUBER, S., KNÖZINGER, H. "Adsorption of CH-acids on magnesia an FTIR-spectroscopic study", *Journal of Molecular Catalysis A: chemical*, v. 141, p. 117-127, 1999.

JANSSENS, W., MAKSHINA, E.V., VANELDEREN, P., DE CLIPPEL, F., HOUTHOOFD, K., KERKHOFS, S., MARTENS, J.A., JACOBS, P.A., SELS, B.F. "Ternary Ag/MgO-SiO_2 catalysts for the conversion of ethanol into butadiene", *ChemSusChem*, v. 8, p. 994-1008, 2015.

JAIN, J. R., PILLAI, C. N. "Catalytic dehydration of alcohols over alumina mechanism of ether formation", *Journal of Catalysis*, v. 9, p. 322-330, 1967.

JOHANN, T., SCHINDLER, G.-P., BRODHAGEN, A., CRONE, S., BENFER, R., HILL, T., DUDA, M. "Method for the production of butadiene", *Patente industrial US167661A1*, 2007.

JONES, H. E., STAHLY, E. E., CORSON, B. B. "Butadiene from ethanol. Reaction mechanism", *Journal of the American Chemical Society*, v. 71, p. 1822-1828, 1949.

JONES, M. D., KEIR, C. G., DI IULIO, C., ROBERTSON, R. A. M., WILLIAMS, C. V., APPERLEY, D. C. "Investigations into the conversion of ethanol into 1,3-butadiene", *Catalysis Science & Technology*, v. 1, p. 267-272, 2011.

KALSI, P. S. *Organic Reactions, Stereochemistry and Mechanism through solved problems*. 4 ed. Nova Deli, *New age International Ltda*, 2006.

KAMPMEYER, P. M., STAHLY, E. E. "Butadiene from ethyl alcohol – Improved production processes", *Industrial and Engineering Chemistry*, v. 41, p. 550-555.

KITAYAMA, Y., SATOH, M., KODAMA, T. "Preparation of large surface area nickel magnesium silicate and its catalytic activity for conversion of ethanol into buta-1,3-diene", *Catalysis Letters*, v. 36, p. 95-97, 1996.

KITAYAMA, Y., SHIMIZU, K., KODAMA, T., MURAI, S., MIZUSIMA, T., HAYAKAWA, M., MURAOKA, M. "Role of intracrystalline tunnels of sepiolite for catalytic activity", *Studies in Surface Science and Catalysts*, v. 142, p. 675, 2002.

KLEIN, A., KEISERS, K., PALKOVITS, R. "Formation of 1,3-butadiene from ethanol in a two-step process using modified zeolite-β catalysts", *Applied Catalysis A*, v. 514, p. 192-202, 2016.

KNÖZINGER, H., BÜHL, H., KOCHLOEFL, K. "The dehydration of alcohols on, alumina XIV. Reactivity and Mechanism", *Journal of Catalysis*, v. 24, p. 57-68, 1972.

KNÖZINGER, H., KOCHLOEFL, K., MEYE, W. "Kinetics of the bimolecular ether formation from alcohols over alumina", *Journal of Catalysis*, v. 28, p. 69-75, 1973.

KNÖZINGER, H., KÖHNE, R. "The Dehydration of Alcohols over Alumina I. The Reaction Scheme", *Journal of Catalysis*, v. 5, p. 264-270, 1966.

KVISLE, S., AGUERO, A., SNEEDEN, R.P.A. "Transformation of ethanol into 1,3-butadiene over magnesium oxide/silica catalysts", *Applied Catalysis*, v. 43, p. 117-131, 1988.

KURTI, L., CZAKÓ, B., *Strategic applications of named reactions in organic synthesis*. 1 ed. New York, Elsevier Academic Press, 2005.

LARENTIS, A. L., BENTES Jr., A. M. P., RESENDE, N. S., SALIM, V. M. M., PINTO, J. C. "Analysis of experimental errors in catalytic tests for production of synthesis gas", *Applied Catalysis A*, v. 242 p. 365-379, 2003.

LARENTIS, A. L., RESENDE, N. S., SALIM, V. M. M., PINTO, J. C. “Modeling and optimization of the combined carbon dioxide reforming and partial oxidation of natural gas”, *Applied Catalysis A: General*, v. 215, p.211-224, 2001.

LARINA, O.V., KYRIIENKO, P.I., SOLOVIEV, S.O. “Ethanol conversion to 1,3-butadiene on ZnO/MgO-SiO_2 catalysts: effect of ZnO content and MgO:SiO_2 ratio”, *Catalysis Letters*, v.145, p. 1162-1168, 2015.

LEBEDEV, S. V. “Improvements in or relating to the preparation of diolefinas directly from alcohols”. *Patent US-331482*, 1930.

LEÓN, M., DÍAZ, E., ORDÓÑEZ, S. “Ethanol catalytic condensation over Mg-Al mixed oxides derived from hydrotalcites”, *Catalysis Today*, v. 164, p. 436-442, 2011-a.

LEÓN, M., DÍAZ, E., VEGA, A., ORDÓÑEZ, S., AUROUX, A. “Consequences of the iron–aluminium exchange on the performance of hydrotalcite-derived mixed oxides for ethanol condensation”, *Applied Catalysis B: Environmental*, v. 102, p. 590-599, 2011-b.

LEÓN, M., DÍAZ, E., BENNICI, S., VEJA, A. ORDÓNEZ, S., AUROX, A. “Adsorption of CO_2 on hydrotalcite-derived mixed oxides: sorption mechanisms and consequences for adsorption irreversibility”, *Industrial & Engineering Chemistry Research*, v. 49, p. 3663-3671, 2010.

VEGA, A., ORDÓÑEZ, S., AUROUX, A. “Consequences of the iron–aluminium exchange on the performance of hydrotalcite-derived mixed oxides for ethanol condensation”, *Applied Catalysis B: Environmental*, v. 102, p. 590-599, 2011-b.

LEWANDOWSKI, M., BABU, G.S., VEZZOLI, M., JONES, M.D., OWEN, R.E., MATTIA, D., PLUCINSKI, P., MIKOLAJSKA, E., OCHENDUSZKO, A., APPERLEY, D.C. “Investigations into the conversion of ethanol to 1,3-butadiene using MgO:SiO_2 supported catalysts”, *Catalysis Communications*, v. 49, p. 25-28, 2014.

LI, Z., ZHANG, T., HU, J., TANG, Y., NIU, Y., WEI, J., YU, Q. “Characterization of reaction products and reaction process of MgO-SiO_2-H_2O system at room temperature”, *Construction and Building Materials*, v. 61, p. 252-259, 2014.

MAKSHINA, E.V., DUSSELIER, M., JANSSENS, W., DEGRÈVE, J., JACOBS, P.A., SELS, B.F. “Review of old chemistry and new catalytic advances in the on-purpose synthesis of butadiene”, *Chemical Society Reviews*, v. 43, p. 7917-53, 2014.

MAKSHINA, E. V., JANSSENS, W., SELS, B.F., JACOBS, P.A. "Catalytic study of the conversion of ethanol into 1,3-butadiene", *Catalysis Today*, v. 198, p. 338-344, 2012.

NELE, M., VIDAL, A., BHERING, D. L., PINTO, J. C., SALIM, V. M. M. "Preparation of high loading silica supported nickel catalyst: simultaneous analysis of the precipitation and aging steps", *Applied Catalysis A: General*, v. 178, p. 177-189, 1999.

NIIYAMA, H., MORII, S., ECHIGOYA, E. "Butadiene formation from ethanol over silica-magnesia catalysts", *Bulletin of the Chemical Society of Japan*, v. 45, p. 655-659, 1972.

OBRADOVIĆ, A., THYBAUT, J. W., MARIN, G. B. "Oxidative coupling of methane: opportunities for microkinetic model-assisted process implementations", *Chemical Engineering & Technology*, v. 39, 1996-2010, 2016.

OCHOA, J.V., BANDINELLI, C., VOZNIUK, O., CHIEREGATO, A., MALMUSI, A., RECCHI, C., CAVANI, F. "An analysis of the chemical, physical and reactivity features of MgO-SiO_2 catalysts for butadiene synthesis with the Lebedev process", *Green Chemistry*, v. 18, p. 1653-1663, 2016.

ODIAN, G., *Principles of polymerization*. 4 ed. New York, John Wiley & Sons, Inc., 2004.

OHNISHI R., AKIMOTO, T., TANABE, K. "Pronounced catalytic activity and selectivity of MgO-SiO_2-Na_2O for synthesis of 1,3-butadiene from ethanol", *Journal of the Chemical Society, Chemical Communication*, p. 1613, 1985.

ONO, Y., HATTORI, H. *Solid acid catalysis – From fundamentals to applications*. CRC Press, Taylor & Francis Group, 2015.

ORDOMSKIY, V. V., SUSHKEVICH, V. L., IVANOVA, I. I. "One-step method for butadiene production", *Patent WO-015340A1*, 2012.

ORDOMSKY, V. V., SUSHKEVICH, V. L., IVANOVA, I. I. "Study of acetaldehyde condensation chemistry over magnesia and zirconia supported on silica", *Journal of Molecular Catalysis A: Chemical*, v. *333*, p. 85-93, 2010.

PEREGO, C., PERATELLO, S. "Experimental methods in catalytic kinetics", *Catalysis Today*, *v. 52*, p. 133-145, 1999.

PÉREZ, C. N., *Condensação aldólica de citral com acetona sobre catalisadores sólidos básicos*. Tese de M.Sc., PEQ/COPPE/UFRJ, Rio de Janeiro, RJ, Brasil, 1997.

PERRY, R. H., GREEN, D. W. "*Perry's Chemical Engineers' Handbook*", The McGraw-Hill Companies, Inc., 1999.

PETERS, M. W., TAYLOR, J. D., MANZER, L. E., HENTON, D. E. "Methods of preparing renewable butadiene and renewable isoprene", *Patente Industrial US0216958 A1*, 2010.

PINTO, J. C., LAGE, P. L. C. *Métodos Numéricos em Problemas de Engenharia Química*. 1 ed. Rio de Janeiro, E-papers, 2001.

PINTO, J. C., LOBÃO, M. W., ALBERTON, A. L., SCHWAAB, M., EMBIRUÇU, M., MELO, S. V. "Critical analysis of kinetic modeling procedures", *International Journal of Chemical Reactor Engineering*, v. 9, article A87, 2011.

PINTO, J. C., SCHWAAB, M. *Análise de Dados Experimentais I, Fundamentos de Estatística e Estimação de Parâmetros*. 1 ed. Rio de Janeiro, E-Papers, 2007.

POLING, B. E., PRAUSNITZ, J. M., O'CONNELL, J. P., *The Properties of Gases and Liquids*. 5 ed. New York, McGraw-Hill, 2001.

POSADA, J. A., PATEL, A. D., ROES, A., BLOK, K., FAAIJ, A. P. C., PATEL, M. K. "Potential of bioethanol as a chemical building block for biorefineries: Preliminary sustainability assessment of 12 bioethanol-based products", *Bioresource Technology*, v. 135, p. 490-499, 2013.

QUATTLEBAUM, W. M., TOUSSAINT, W. J., DUNN, J. T. "Deoxygenation of certain aldehydes and ketones: preparation of butadiene and styrene", *Journal American of Chemical Society*, v. 69, p. 593-599, 1947.

RAÍZEN SUSTAINABILITY REPORT, 2011-2012, Available in: https://www.raizen.com.br/sociedade-e-sustentabilidade/relatorios, Searched on Feb, 2013.

RAWET, R., CERQUEIRA, H. S., PINTO, J. C. The influence of covariances during laboratory evaluation of FCC catalysts, *Applied Catalysis A,* v. 207, p. 199-209, 2001.

RENEWABLE FUELS ASSOCIATION, U.S. Department of Energy, "Global ethanol production", Available in: http://www.afdc.energy.gov/data/10331. Searched on 5 May. 2015.

REN, T., PATEL, M., BLOK, K. "Olefins from conventional and heavy feedstocks: energy use in steam cracking and alternative processes", *Energy*, v. *33*, p. 817-833, 2008.

ROUQUEROL, F.; ROUQUEROL, J.; SING, K. *Adsorption by Powders and Porous Solids*. San Diego: Academic Press, pp. 191, 1999.

SCHWAAB, M., BISCAIA, Jr., E. C., MONTEIRO, J. L., PINTO, J. C. "Nonlinear parameter estimation through particle swarm optimization", *Chemical Engineering Science*, v. 63, p. 1542-52, 2008b.

SCHWAAB, M., MONTEIRO, J.L., PINTO, J.C. "Sequential experimental design for model discrimination taking into account the posterior covariance matrix of differences between model predictions", *Chemical Engineering Science*, v. 63, p. 2408-19, 2008a.

SCHWAAB, M., PINTO, J. C., *Análise de Dados Experimentais II, Planejamento de experimentos*. 1 ed. Rio de Janeiro, E-Papers, 2011.

SCHWAAB, M., SILVA, F.M., QUEIPO, C.A., BARRETO Jr., A.G., NELE, M. PINTO, J.C. "A new approach for sequential experimental design for model discrimination", *Chemical Engineering Science*, v. 61, p. 5791-5806, 2006.

SEKIGUCHI, Y., AKIYAMA, S., URAKAWA, W., KOYAMA, T., MIYAJI, A., MOTOKURA, K., BABA, T. "One-step catalytic conversion of ethanol into 1,3-butadiene using zinc-containing talc", *Catalysis Communications*, v. 68, p. 20-24, 2015.

SHI, B., DAVIS, B. H. "Alcohol dehydration: mechanism of ether formation using an alumina Catalyst", *Journal of Catalysis*, v. 157, p. 359-367, 1995.

SHI, X., TANG, X., LI, Y. "Random copolymers of propylene with 1,5-hexadiene containing only cyclopentane units in main chain and tailoring structure and mechanical properties of the copolymers", *Polymer*, v. 52, p. 3053-3058, 2011.

SCHEID, A. J., BARBOSA-COUTINHO, E., SCHWAAB, M., SALAU, N. P. G., COSTA, V. C. *Gas phase reaction equilibrium calculator software*.

SMITH, J. M., VAN NESS, H. C., ABBOTT, M. M., *Introduction to chemical engineering thermodynamics*. 7 ed. United States, The McGraw-Hill Companies, Inc. 2005.

SPENCE, L.R. U., PARK, E., BUTTERBAUGH, D. J., KUNDIGER, D. G. "Catalytic process for producing butadiene", *Patent US-2438464*, 1948.

STAHLY, E. E., JONES, H. E., CORSON, B. B. "Butadiene from ethanol – Utilization of by-product ethyl acetate", *Industrial and Engineering Chemistry*, v. 40, p. 2301-2303, 1948.

STATSOFT Inc., 2325 East 13th Street, Tulsa, OK, USA, 1995.

SUSHKEVICH, V.L., IVANOVA, I.I., ORDOMSKY, V.V., TAARNING, E. “Design of a metal-promoted oxide catalyst for the selective synthesis of butadiene from ethanol”, *ChemSusChem*, v.7, p. 2527-36, 2014.

SUSHKEVICH, V.L., IVANOVA, I.I., TAARNING, E. “Ethanol conversion into butadiene over Zr-containing molecular sieves doped with silver”, *Green Chemistry*, p. 17, p. 2552-59, 2015.

SUZUKI, E., IDEMURA, S., ONO, Y. “Catalytic conversion of 2-propanol and ethanol over synthetic hectorite and its analogues”, *Applied clay science*, v. 3, p. 123-134, 1988.

SZCZERBA, J., PROROK, R., ŚNIEŻEK, E., MADEJ, D., MAŚLONA, K. “Influence of time and temperature on ageing and phases synthesis in the MgO-SiO_2-H_2O system”, *Thermochimica Acta*, v. 567, p. 57-64, 2013.

TAMURA, M., SHIMIZU, K.-I., SATSUMA, A. “Comprehensive IR study on acid/base properties of metal oxides”, *Applied Catalysis A*, v. *433-434*, 135-145, 2012.

TOUSSAINT, W. J., CHARLEATON, S., DUNN, J. T. “Process for making diolefinas”, *Patent US-2421361*, 1947.

TSUCHIDA, T., KUBO, J., YOSHIOKA, T., SAKUMA, S., TAKEGUCHI, T., UEDA, W. “Reaction of ethanol over hydroxyapatite affected by Ca/P ratio of catalyst”, *Journal of Catalysis*, v. 259, p. 183-189, 2008.

VAABEL, A. S., KALIBERDO, L. M., DUBENKOVA, L. B., KUVAKINA, P. R. “Dehydrodimerization of propylene on bismuth-phosphorus oxide catalysts”, *Petroleum Chemistry U.S.S.R.*, v. 14, p. 159-167, 1973.

WANG, B., LONG, Y.-Y., LI, Y.-G., MEN, Y.-F., LI, Y.-S. “Cyclic olefin copolymers of propylene with asymmetric Si-containing α,ω-diolefins: The tailored thermal and mechanical properties”, v. 61, p. 108-114, 2015.

WHITE, W. C. “Butadiene production process overview”, *Chemico-Biological Interactions*, v. 166, p. 10-14, 2007.

Appendix A – Thermodynamic Methods

Two approaches were employed to obtain equilibrium compositions. In both cases, the mixture was assumed to follow the as ideal gas law and the system pressure was assumed to be 1 atm. The standard-state was defined for the reference temperature of 298 K, T_o, and the reference pressure of one atmosphere (101325 Pa).

In the first approach, the method of the equilibrium constants was employed. According to this method, the set of reactions is defined and, for each reaction *j*, the equilibrium constant, K_j, in the case of an ideal gas mixture, is defined according to Eq. (A.1), (SMITH, 2007).

$$K_j - \prod \left(y_i P\right)^{v_{ij}} = 0 \qquad \text{(A.1)}$$

According to Eq. (A.1), y_i denotes the molar fraction of the chemical species *i* at the equilibrium, *P* is the system pressure, and v_{ij} is the stoichiometric coefficient for species *i* in *j* reaction, which is positive for products and negative for reactants. Thus, considering the reaction mechanism of Table A1, the equilibrium constants for each reaction *j* could be described as shown in the right column of Table A.1.

Table A.1 – Reaction mechanism considered for calculations of Gibbs energy changes and compositions.

Reaction	***j***	K_j
$CH_3CH_2OH + CH_3CHO \rightarrow C_4H_6 + 2H_2O$	(1)	$K_1 - \frac{(y_{BD})\left(y_{H_2O}^2\right)}{(y_{EtOH})(y_{AcH})}P = 0$
$CH_3CH_2OH \rightarrow CH_3CHO + H_2$	(2)	$K_2 - \frac{(y_{AcH})\left(y_{H_2}\right)}{(y_{EtOH})}P = 0$
$CH_3CH_2OH \rightarrow C_2H_4 + H_2O$	(3)	$K_3 - \frac{\left(y_{C_2H_4}\right)\left(y_{H_2O}\right)}{(y_{EtOH})}P = 0$
$2CH_3CH_2OH \rightarrow (C_2H_5)_2O + H_2O$	(4)	$K_4 - \frac{(y_{DEE})\left(y_{H_2O}\right)}{\left(y_{EtOH}^2\right)} = 0$
$C_4H_6 + H_2 \rightarrow C_4H_8$	(5)	$K_5 - \frac{\left(y_{C_4H_8}\right)}{\left(y_{C_4H_6}\right)\left(y_{H_2}\right)}\frac{1}{P} = 0$

For each temperature, *T*, the equilibrium constant was calculated with help of Eq. (A.2), where *R* is the universal gas constant and ΔG_j^0 denotes the Gibbs energy variation for reaction *j* (SMITH, 2007), which is defined according to Eq. (A.3). In Eq. (A.3), *NC* is the number of compounds of reaction *j*, and G_i^0 is the standard Gibbs energy for species *i*, calculated with Eq. (A.4).

$$K_j = \exp\left(-\frac{\Delta G_j^0}{RT}\right) \tag{A.2}$$

$$\Delta G_j^0 = \sum_{i=1}^{NC} \nu_{ij} G_i^\circ \tag{A.3}$$

In Eq. (A.4), H_i° denotes the standard enthalpy of formation for species *i*, and G_i° is the standard Gibbs energy of formation of species *i*, shown in Table A.1.

$$G_i^\circ = H_i^\circ - \frac{T}{T_\circ}(H_i^\circ - G_i^\circ) + R\int_{T_\circ}^{T} \frac{Cp_i^\circ}{R} dT - RT\int_{T_\circ}^{T} \frac{Cp_i^\circ}{R}\frac{dT}{T} \tag{A.4}$$

Table A.1 – Standard enthalpy and Gibbs energy of formation (25 ºC and 101325 Pa) (POLING, 2001).

Compound	$H_i^\circ\,(kJ/mol)$	$G_i^\circ\,(kJ/mol)$
Ethanol	-234.95	-167.73
Acetaldehyde[a]	-166.2	-133.0
1,3-Butadiene	110.0	150.6
Ethene	52.50	68.48
Diethyl ether	-250.80	-120.70
H_2	0	0
Water	-241.81	-228.42
1-Butene	-0.54	70.37

[a] Data from PERRY and GREEN (1999).

The relationship between the heat capacity and the temperature was calculated with Eq. (A.5), where the required parameters are shown in Table A.2.

$$\frac{Cp^\circ}{R} = a_0 + a_1 \cdot T + a_2 \cdot T^2 + a_3 \cdot T^3 + a_4 \cdot T^4 \tag{A.5}$$

Table A.2 –Heat capacity parameters for Eq. (A.5) (POLING, 2001).

Compound	$\mathbf{a_0}$	$\mathbf{a_1} \cdot 10^3$	$\mathbf{a_2} \cdot 10^5$	$\mathbf{a_3} \cdot 10^8$	$\mathbf{a_4} \cdot 10^{11}$
Ethanol	4.396	0.628	5.546	-7.024	2.685
Acetaldehyde	1.693	17.978	-0.616	0	0
1,3-Butadiene	3.607	5.085	8.253	-12.371	5.321
Ethene	4.221	-8.782	5.795	-6.729	2.511
Diethyl Ether	4.612	37.492	-1.87	1.316	-0.698
H_2	2.883	3.681	-0.772	0.692	-0.213
Water	4.395	-4.186	1.405	-1.564	0.632
1-Butene	4.389	7.984	6.143	-8.197	3.165

Besides the five equations in Table A.1, three additional equations were defined for the mass balances of each element *k*, as shown in Eq. (A.6), where n_i is the number of mols of species *i* at equilibrium, $n_{i,0}$ is the initial number of mols of species *i*, $a_{i,k}$ is the number of atoms of the *k* element per molecule of species *i*, and *NC* is the number of compounds. Since the molar fraction is related to the number of mols, as defined in Eq. (A.7), eight equations must be solved simultaneously in order to determine the compositions of the eight compounds from Table A.1.

$$\sum_{i=1}^{NC} a_{i,k} \left(n_i - n_{i,0} \right) = 0 \tag{A.6}$$

$$y_i = \frac{n_i}{\sum_{i=1}^{NC} n_i} \tag{A.7}$$

The set of nonlinear algebraic equation was solved numerically using the Newton-Raphson method (PINTO and LAGE, 2001), with tolerance of 10^{-13} and maximum number of iterations of 100.

In the second approach, the compounds at the equilibrium mixture were defined, instead of the reaction set, and the Gibbs energy was minimized (SMITH *et al*., 2007). The calculation was performed with the GPREC gas phase reaction equilibrium calculation software (SCHEID *et al*., 2017). Both calculation approaches resulted in the same composition results, which validate the obtained numerical results.

Appendix B- XRD from empty holder

This appendix presents the diffractogram from the polymethyl methacrylate sample holder employed, showing an interference signal at the Bragg angles between 10 and 15 º.

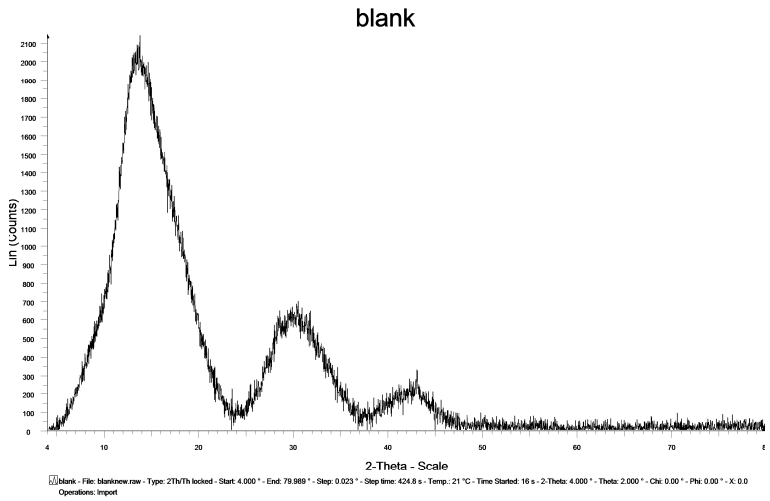

Figure B.1 – XRD from the employed empty holder.

Appendix C- Chromatographic Methods

In the catalytic **Unit 1**, the inlet injector chamber was kept at 100 ºC. The first column, the Molsieve 5Å, was kept at 95 ºC, and the inlet pressure was kept at 30 psi. The second column, PLOT Q, was kept at 140 ºC and the inlet pressure was kept at 20 psi. Finally, the third columns OV-1, was kept at 55 ºC, at the inlet pressure of 25 psi. After the end of each run, the column pressure was increased to 40 psi, in order to remove residual compounds before the next run. Thermal conductivity detectors were employed in all cases.

In the catalytic **Unit 2**, the injector chamber was kept at 200 ºC. The following temperature program was used during the analysis run: (*i*) the column temperature was kept at 35 ºC during the initial 7 min of analysis run; (*ii*) then, the temperature was raised up to 150 ºC, by using a heating rate of 20 ºC/min; (*iii*) after achieving 150 ºC, the oven was heated to 250 ºC, at the heating rate of 15 ºC/min; (*iv*) the temperature was kept constant at 250 ºC for 6 min. The inlet pressure was equal to 11.46 psi. The column flow was of 1.3 mL/min (the split ratio was equal to 10 to 1, and the carrier gas was Helium) and the injection volume was equal to 1 μL. For the hydrogen-air flame in the flame ionization detector (FID), the H_2 flow rate was kept at 30 mL/min and the air flow was kept at 400 mL/min. The chamber of the FID was kept at 300 ºC.

Appendix D- Experimental Calibration Data

This appendix presents experimental calibration details regarding the catalytic Unit 1 and 2.

Unit 1

Ethanol, diethyl ether, crotonaldehyde and crotyl alcohol calibration was performed using a saturator kept at a fixed temperature, through which N_2 was bubbled. The outlet saturator stream was diluted with a second N_2 stream in order to achieve lower molar fractions. The molar fraction in the outlet saturator stream was calculated using the Antoine's equation (SMITH *et al*, 2007), Eq. (D.1) and Eq. (D.2). Antoine's equation parameters used are shown in Table D.1.

$$\ln P^{sat} = A - \frac{B}{T + C} \tag{D.1}$$

$$y_i = \frac{P^{sat}}{P^{tot}} \tag{D.2}$$

Table D.1 - Antoine's equation parameters used for ethanol, diethyl ether and crotonaldehyde.

	A	**B**	**C**
Ethanol [a]	16.90	3795.17	230.92
Diethyl ether [a]	14.07	2511.29	231.20
Crotonaldehyde[b]	22.91	4255.95	271.57

[a] SMITH *et al*., (2007).

[b] For crotonaldehyde, data of vapor pressure at different temperatures, Table D.2, was used in order to calculate the Antoine's equation parameters, using least-squares estimation procedure.

Table D.3 shows ethanol molar fractions and the measured chromatographic areas, which were employed to calibrate the GC instrument and to estimate measurement fluctuations. For calibration, the molar fraction was defined as the independent variable and was assumed to be known with high precision. Moreover, chromatographic measurements were assumed as independent from each other and to follow the normal distribution. Thus, the response factor was estimated using the

weighted least squares estimation procedure and using all experimental data (PINTO and SCHWAAB, 2008).

Table D.2 – Crotonaldehyde vapor pressures at different temperatures.[a,b]

Temperature (ºC)	Vapor pressure (kPa)
20.00	4266
33.80	7697
35.40	8257
39.70	10000
42.60	11500
50.20	15989
50.60	16284
57.70	21643
58.60	22414
64.00	27599
64.30	27899
69.20	33505
69.40	33750
73.15	38693
74.20	40119
77.60	45185
78.40	46509
81.60	51896
82.80	54106

[a] BOUBLÍK, T., FRIED, V., HÁLA, E., *The vapour pressures of pure substances*, 2 ed. New York, Elsevier, 1984.

[b] WARADZIN, W., SKUBLA, P., *Chem. Prum*., v. 23, p. 556, 1973.

Table D.3 –Experimental ethanol calibration data [a].

Molar fraction (%)	Chromatographic areas				
	Injection 1	Injection 2	Injection 3	Injection 4	Injection 5
5.80	47495.12	47451.85	47611.43	48128.80	47470.34
4.26	35577.89	36734.95	35542.30	36391.55	35739.32
2.10	17180.82	17616.31	17745.94	17777.90	17560.40
0.89	7550.21	7437.89	7522.66	7629.51	7524.75
0.53	4497.47	4543.71	4415.99	4452.60	4409.54

[a] Saturator was kept at 20 ºC.

Figures D.1 and D.2 show experimental chromatographic areas as a function of the molar fraction and the linear model fits with the estimated response factors for the different compounds. Tables D.4 and D.15 show the experimental calibration data.

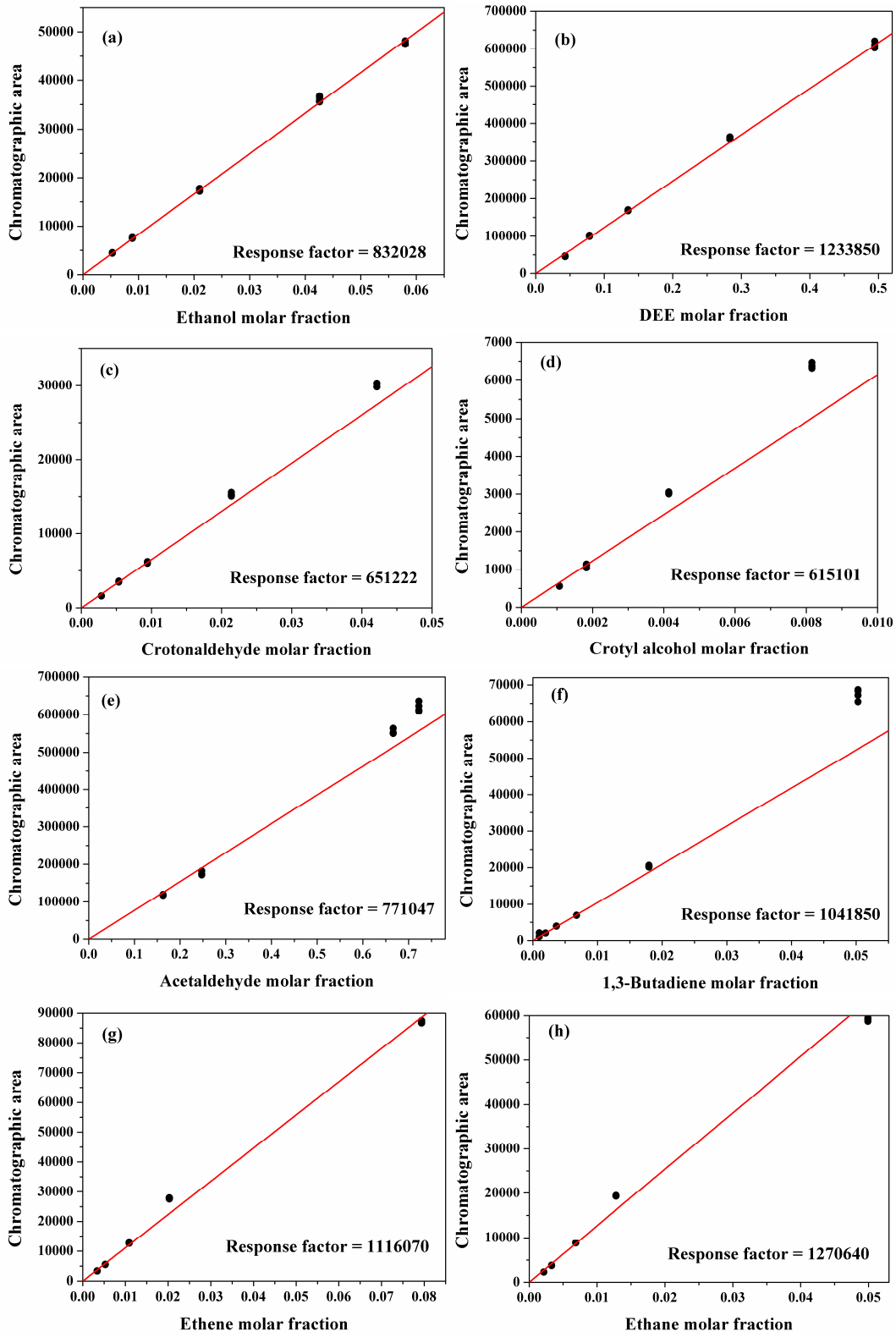

Figure D.1 – Experimental chromatographic areas (●) and response fits (-).

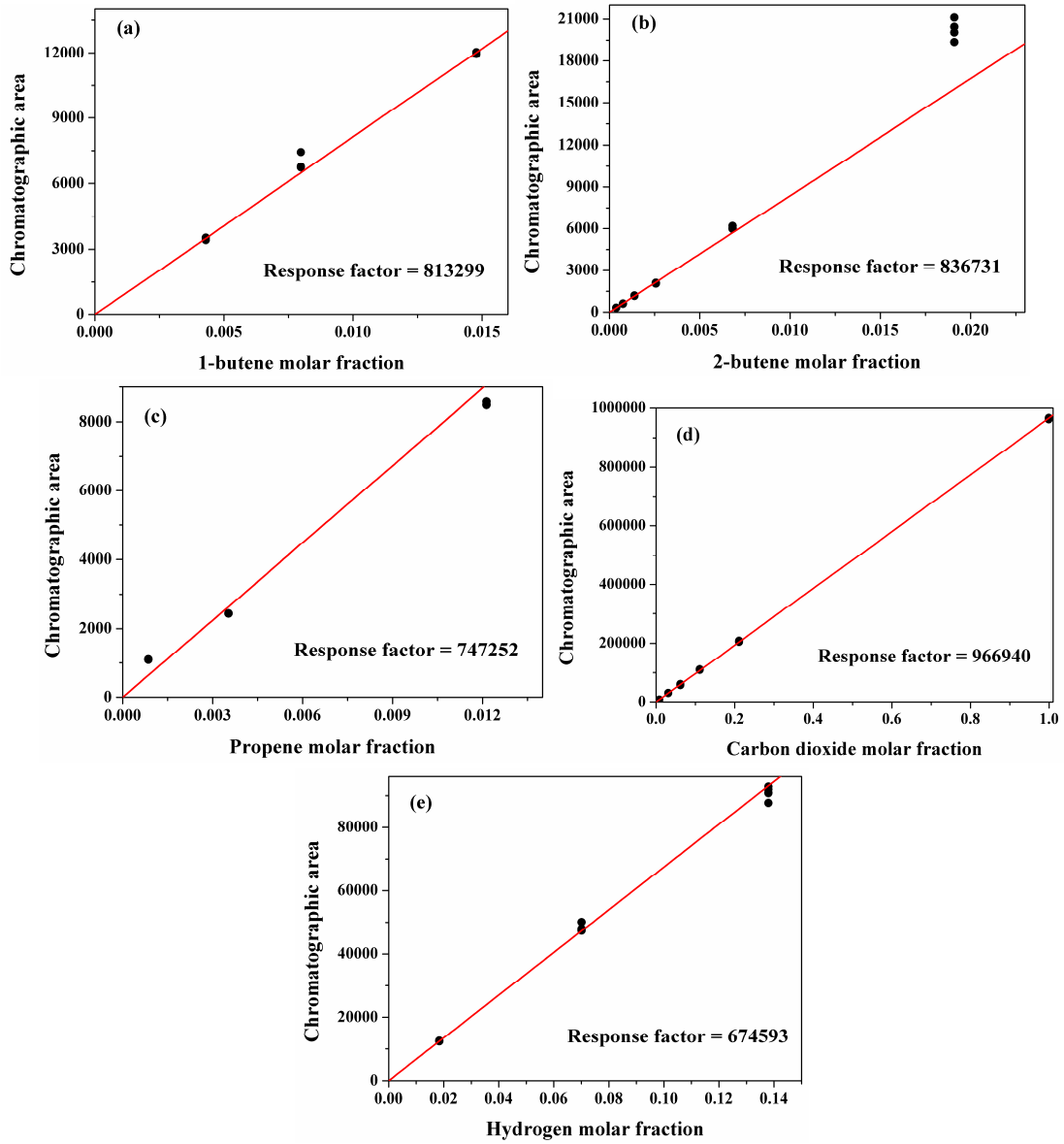

Figure D.2 – Experimental chromatographic areas (●) and response fits (-).

Table D.4 – Experimental diethyl ether data [a].

Molar fraction (%)	Chromatographic areas				
	Injection 1	Injection 2	Injection 3	Injection 4	Injection 5
49.47	603363.96	610584.08	603053.06	610118.96	621166.89
28.34	357368.91	358969.92	364326.96	363237.58	
13.49	169994.27	167353.59	169796.69	170324.92	
7.86	102774.12	98832.24	98998.84	101978.93	
4.30	44920.32	46935.04	46215.43	46810.43	46458.42

[a] Saturator was kept at 16 ºC.

Table D.5 – Experimental crotonaldehyde calibration data [a].

Molar fraction (%)	Chromatographic areas				
	Injection 1	Injection 2	Injection 3	Injection 4	Injection 5
4.21	29812.02	30304.82	30249.12	30326.92	30271.39
2.14	15269.73	15571.78	15173.47	15057.20	15078.80
0.94	6072.36	6234.79	6064.48	5997.89	6012.51
0.54	3474.41	3467.53	3447.33	3471.42	3595.59
0.29	1592.91	1601.35	1585.41	1610.52	1633.23

[a] Saturator was kept at 21 ºC.

Table D.6 – Experimental crotyl alcohol calibration data [a].

Molar fraction (%)	Chromatographic areas				
	Injection 1	Injection 2	Injection 3	Injection 4	Injection 5
0.816	6353.36	6318.30	6359.29	6470.11	6390.99
0.414	3056.40	3007.38	3032.40		
0.183	1044.07	1122.40	1144.70	1109.14	
0.107	555.87	562.62	558.01		

[a] Saturator was kept at 25 ºC.

Table D.7 - Experimental acetaldehyde calibration data[a].

Molar Fraction (%)	Chromatographic areas			
	Injection 1	Injection 2	Injection 3	Injection 4
72.26	636006.87	609955.02	623161.06	612264.57
66.65	563654.57	552182.63	550188.58	
24.73	182080.77	174429.85	171665.78	
16.29	118225.81	117852.21	120034.68	

[a] Pure gas acetaldehyde was diluted with a second stream of N_2.

Table D.8 – Experimental 1,3-butadiene calibration data [a].

Molar fraction (%)	Chromatographic areas				
	Injection 1	Injection 2	Injection 3	Injection 4	Injection 5
5.030	65472.35	67249.65	68389.57	68720.25	
1.796	20129.30	20230.80	20591.75	20365.09	20431.87
0.676	6933.95	6950.57	6911.18	6915.69	6908.27
0.365	3946.52	3968.33	3990.31	3965.99	3970.15
0.197	2055.73	2035.21	2047.91	2040.98	2053.30
0.100	1102.21	2097.13	1095.70	1104.45	1102.41

[a] A gas mixture constituted by 2-butene (1.91 vol.%), 1-butene (2.90 vol.%) and 1,3-butadiene (5.03 vol.%) (diluted in N_2) was used. Lower molar fractions were obtained by dilution with N_2.

Table D.9 - Experimental ethene calibration data [a].

Molar fraction (%)	Chromatographic areas				
	Injection 1	Injection 2	Injection 3	Injection 4	Injection 5
7.94	87069.86	87480.88	86711.25		
2.03	27689.29	27771.00	27548.43	27903.13	27918.91
1.09	12803.34	12683.63	12665.81	12641.49	12832.82
0.53	5546.04	5595.10	5592.08	5527.44	5560.90
0.34	3417.61	3368.04	3374.84	3389.77	

[a] A gas mixture constituted by ethane (4.99 vol.%), ethene (7.94 vol.%), propane (12.28 vol.%), propene (2.0 vol.%), and n-butane (2.97 vol.%), diluted in N_2 was used. Lower molar fractions were obtained by dilution with N_2.

Table D.10 – Experimental ethane calibration data [a].

Molar fraction (%)	Chromatographic areas				
	Injection 1	Injection 2	Injection 3	Injection 4	Injection 5
4.990	58698.06	59118.19	59417.24		
1.279	19289.11	19385.76	19323.19	19373.51	19422.85
0.686	8874.92	8852.53	8839.50	8843.72	8839.96
0.330	3819.77	3762.07	3802.36		
0.215	2310.78	2292.29	2299.69	2299.22	

[a] A gas mixture constituted by ethane (4.99 vol. %), ethene (7.94 vol. %), propane (12.28 vol. %), propene (2.0 vol. %), and n-butane (2.97 vol. %), diluted in N_2 was used. Lower molar fractions were obtained by dilution with N_2.

Table D.11 – Experimental 1-butene calibration data.

Molar fraction (%)	Chromatographic areas			
	Injection 1	Injection 2	Injection 3	Injection 4
1.478	12040.64	11957.89	11946.29	
0.798	6765.96	6732.06	7436.07	
0.430	3520.54	3420.00	3421.90	3421.19

[a] A gas mixture constituted by 1-butene (11.0 vol. %), propene (9.03 vol. %) and 1-pentene (9.05 vol. %) (diluted in N_2) was used. Lower molar fractions were obtained by dilution with N_2.

Table D.12 – Experimental 2-butene calibration data [a].

Molar fraction (%)	Chromatographic areas				
	Injection 1	Injection 2	Injection 3	Injection 4	Injection 5
1.910	19362.53	20049.01	20456.96	21119.28	
0.682	6028.02	5979.66	6019.06	6189.76	6032.77
0.257	2050.67	2105.30	2041.52	2046.45	2038.74
0.139	1180.66	1195.67	1169.48	1163.85	1164.08
0.075	611.50	610.91	620.19	599.08	602.82
0.038	324.19	329.43	323.08	320.46	321.27

[a] A gas mixture constituted by 2-butene (1.91 vol. %), 1-butene (2.90 vol. %) and 1,3-butadiene (5.03 vol. %) (diluted in N_2) was used. Lower molar fractions were obtained by dilution with N_2.

Table D.13 – Experimental propene calibration data [a].

Molar fraction (%)	Chromatographic areas			
	Injection 1	Injection 2	Injection 3	Injection 4
1.213	8578.61	8486.47	8496.57	
0.353	2442.35	2443.86	2434.65	2434.35
0.086	1100.17	1098.1	1093.48	1101.78

[a] A gas mixture constituted by ethane (4.99 vol. %), ethene (7.94 vol. %), propane (12.28 vol. %), propene (2.0 vol. %), and n-butane (2.97 vol. %), diluted in N_2 was used. Lower molar fractions were obtained by dilution with N_2.

Table D.14 – Experimental carbon dioxide calibration data [a].

Molar fraction (%)	Chromatographic areas				
	Injection 1	Injection 2	Injection 3	Injection 4	Injection 5
99.90	966645.74	961708.50	963582.79	961840.94	
21.12	208800.78	209030.91	204446.59	207753.80	207944.59
11.11	112131.71	109871.91	109483.46	108946.20	110349.97
6.20	56754.91	58944.42	59540.10	60176.68	61304.07
3.10	30199.75	30455.41	30601.45	29929.84	30886.38
0.83	8025.15	7923.71	7922.56	7976.72	8046.57

[a] A pure CO_2 gas cylinder and a gas mixture constituted by hydrogen (13.8 vol. %), carbon monoxide (7.9 vol. %), and carbon dioxide (6.2 vol. %) diluted in N_2 were used. Lower molar fractions were obtained by dilution with N_2.

Table D.15 – Experimental hydrogen calibration data [a].

Molar fraction (%)	Chromatographic areas				
	Injection 1	Injection 2	Injection 3	Injection 4	Injection 5
13.80	87720.94	90775.16	90980.20	91954.43	92839.20
7.01	47782.63	47286.70	50110.12	47925.08	47986.47
1.84	12499.29	12321.75	12553.52	12364.20	12385.75

[a] A gas mixture constituted by hydrogen (13.8 vol. %), carbon monoxide (7.9 vol. %), and carbon dioxide (6.2 vol. %) diluted in N_2 was used. Lower molar fractions were obtained by dilution with N_2.

Finally, Table D.16 summarizes the estimated response factors and the respective standard deviations.

Table D.16 – Estimated response factors and standard deviations for the different compounds.

Compound	*Response factor estimated*	*Standard deviation*
Acetaldehyde	$7.71047 \cdot 10^5$	$3.09089 \cdot 10^3$
Ethanol	$8.32028 \cdot 10^5$	$1.57051 \cdot 10^3$
1,3-Butadiene	$1.04185 \cdot 10^6$	$8.71383 \cdot 10^2$
1-Butene	$8.13299 \cdot 10^5$	$1.88646 \cdot 10^3$
2-Butene	$8.36731 \cdot 10^5$	$2.05876 \cdot 10^3$
Crotyl alcohol	$6.15101 \cdot 10^5$	$1.43965 \cdot 10^3$
Crotonaldehyde	$6.51222 \cdot 10^5$	$1.46285 \cdot 10^3$
Carbon dioxide	$9.66940 \cdot 10^5$	$9.94292 \cdot 10^2$
Ethene	$1.11607 \cdot 10^6$	$1.34275 \cdot 10^3$
Ethane	$1.27064 \cdot 10^6$	$7.44625 \cdot 10^2$
Diethyl ether	$1.23385 \cdot 10^6$	$3.00038 \cdot 10^3$
Propene	$7.47252 \cdot 10^5$	$5.4452 \cdot 10^4$
Hydrogen	$6.74593 \cdot 10^5$	$2.11090 \cdot 10^3$

Unit 2

In Unit 2, a gas mixture containing comprising ethene (1.0 vol. %), 1,3-butadiene (1.0 vol. %), 1-butene (0.5 vol. %), diethyl ether (0.25 vol. %) and acetaldehyde (0.25 vol. %) was employed to calculated the response factors. In this case, two measures were performed. Table D.17 shows chromatographic areas and Table D.18 shows the calculated response factors. Response factors for propene, ethane, propane, and acetone were assumed to follow Eq. (D.1-D.4), respectively.

Table D.17 – Experimental calibration data – Unit 2.

	Chromatographic areas		Response Factor (RF)
	Injection 1	Injection 2	
Ethene (1.0 vol. %)	65578869.0	68741315.0	67160092.0
1-butene (1.0 vol %)	84852884.0	87005067.0	171857951.0
DEE (0.25 vol. %)	35192654.0	35480904.0	141347116.0
Acetaldehyde (0.25 vol. %)	10283276.0	10686004.0	41938560.0
1,3-butadiene (1.0 vol. %)	176727627.0	182035591.0	179381609.0

b (D.1)

$$\mathrm{RF}_{\mathrm{ethane}} = \frac{RF_{ethene} + RF_{propene}}{2} \quad \text{(D.2)}$$

$$RF_{propane} = \frac{RF_{ethane} + RF_{propene}}{2} \quad \text{(D.3)}$$

$$RF_{acetone} = \frac{RF_{ethene} + RF_{Acetaldehyde}}{2} \quad \text{(D.4)}$$

Appendix E- Powder X-Ray Diffractograms

In this appendix, pXRD from Mg-Al mixed oxides derived from hydrotalcites are presented, Figure E.1 and E.2 (b), as well as their hydrotalcite precursors, Figure E.1 and E.2 (a). Figure E.1 and E.2 show diffraction patterns for the materials prepared at the Mg-to-Al molar ratio equal to 3 and 5, respectively.

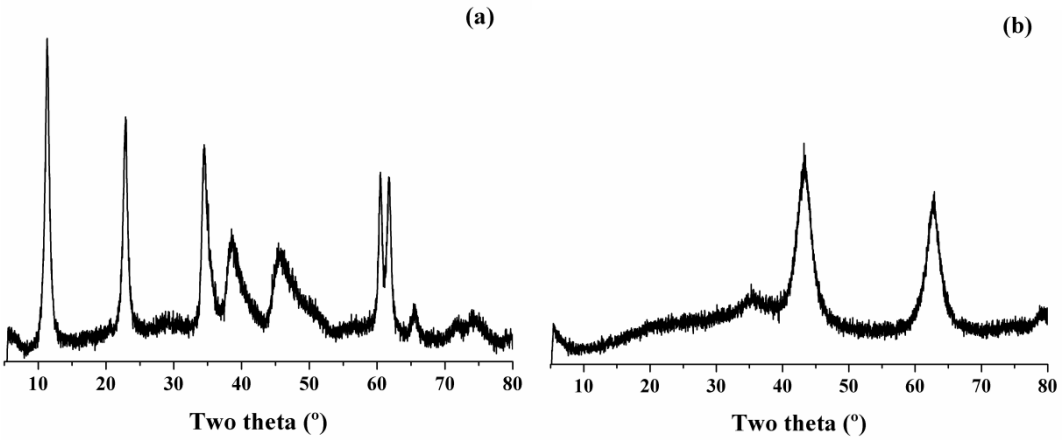

Figure E.1 – pXRD patterns of the Mg-Al mixed oxide (b) and its precursor (a) hydrotalcite, prepared at the Mg-to-Al molar ratio equal to 3.

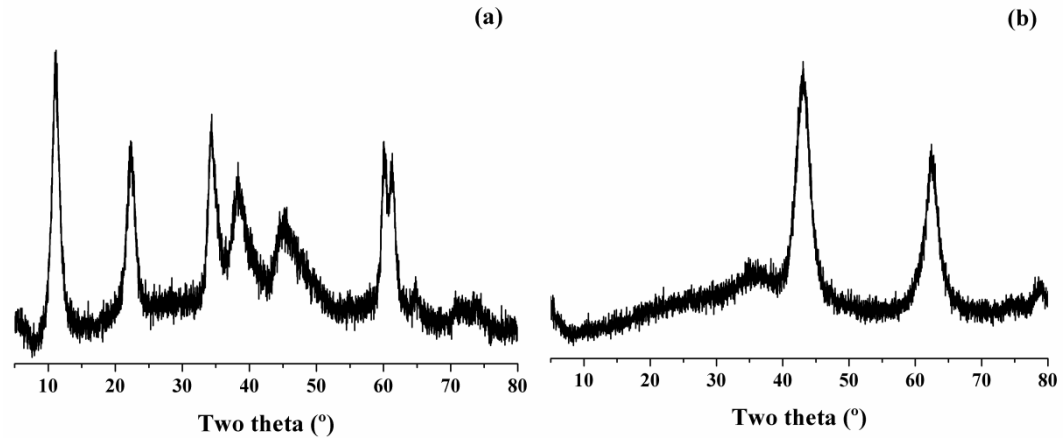

Figure E.2 – pXRD patterns of the Mg-Al mixed oxide (b) and its precursor (a) hydrotalcite, prepared at the Mg-to-Al molar ratio equal to 5.

The diffraction patterns of uncalcined samples, Figure E.1 and E.2 (a), presented intensities at the Bragg angles of 11.7, 23.6, 34.7, 39.1, 46.3, 60.2, and 61.8 º, which are characteristic of hydrotalcites phase. As expected, after calcination, the MgO periclase phase was observed, Figure E.1 and E.2 (b) (LEÓN *et al*., 2010).

Appendix F- CO_2-TPD profiles

This appendix presents the CO_2-TPD profiles for the MgO-SiO_2-(50-50) (a) and MgO-SiO_2-(95:5) (b) samples in the whole temperature range analyzed.

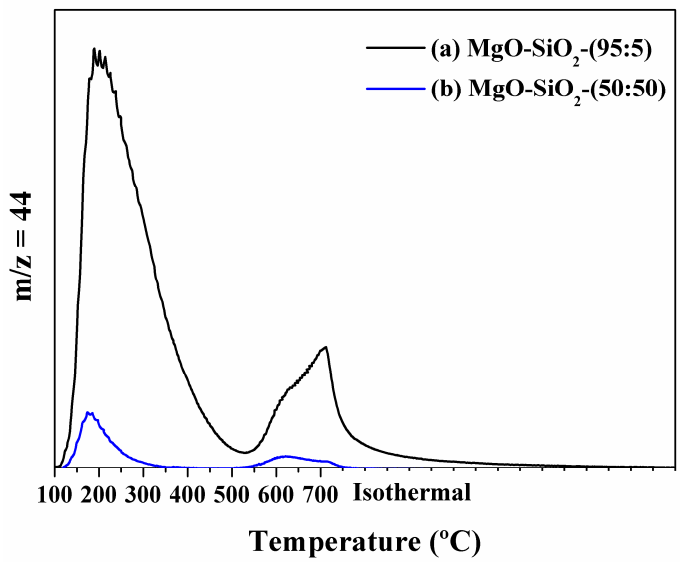

Figure F.1 - CO_2-TPD profiles for the MgO-SiO_2-(50-50) (a) and MgO-SiO_2-(95:5) (b) samples.

Appendix G – Energy-Dispersive X-Ray Spectra

This appendix presents the energy-dispersive X-ray spectrum obtained for the Copper sample used in the analysis optimization, Figure G.1, as well the spectrum acquired for the samples ZrZn/MgO-SiO_2, Figure G.2, and 1.2-K/ZrZn/MgO-SiO_2, Figure G.3. The related microscopy images are also presented. Results presented in Table 4.4.4 and 4.4.14 represent, thus, an average of at least five spots from the microscopy images. For each spot, a spectrum was generated, and the weight and atomic % values for each element were calculated. The intensity of each peak is proportional to the number of photons emitted by the element, and thus, to its concentration. However, results presented in Table 4.4.4 and 4.4.14 were normalized to remove the amount of carbon and oxygen.

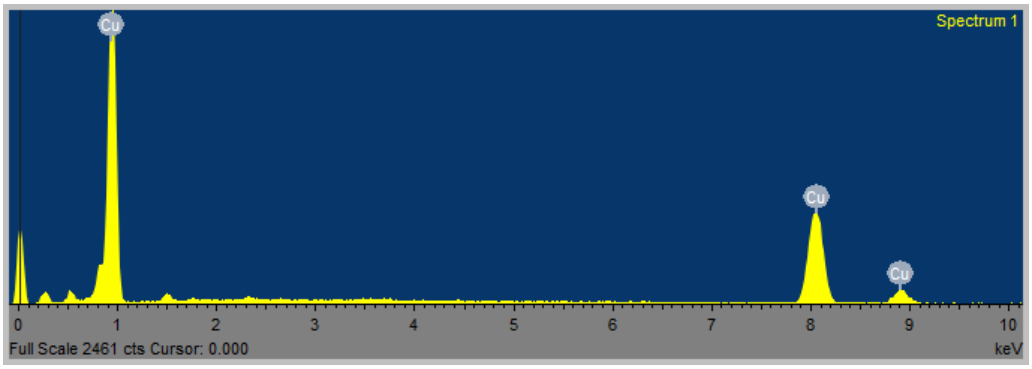

Figure G.1 - Energy-dispersive X-ray spectrum obtained for the Copper sample used in the analysis optimization. The characteristic X-ray emission energies (in keV) for Cu are located at $K\beta_1$ = 8.904, $K\alpha_1$ = 8.047, $L\beta_1$ = 0.948, and $L\alpha_1$ = 0.928, (DEAN, 1992).

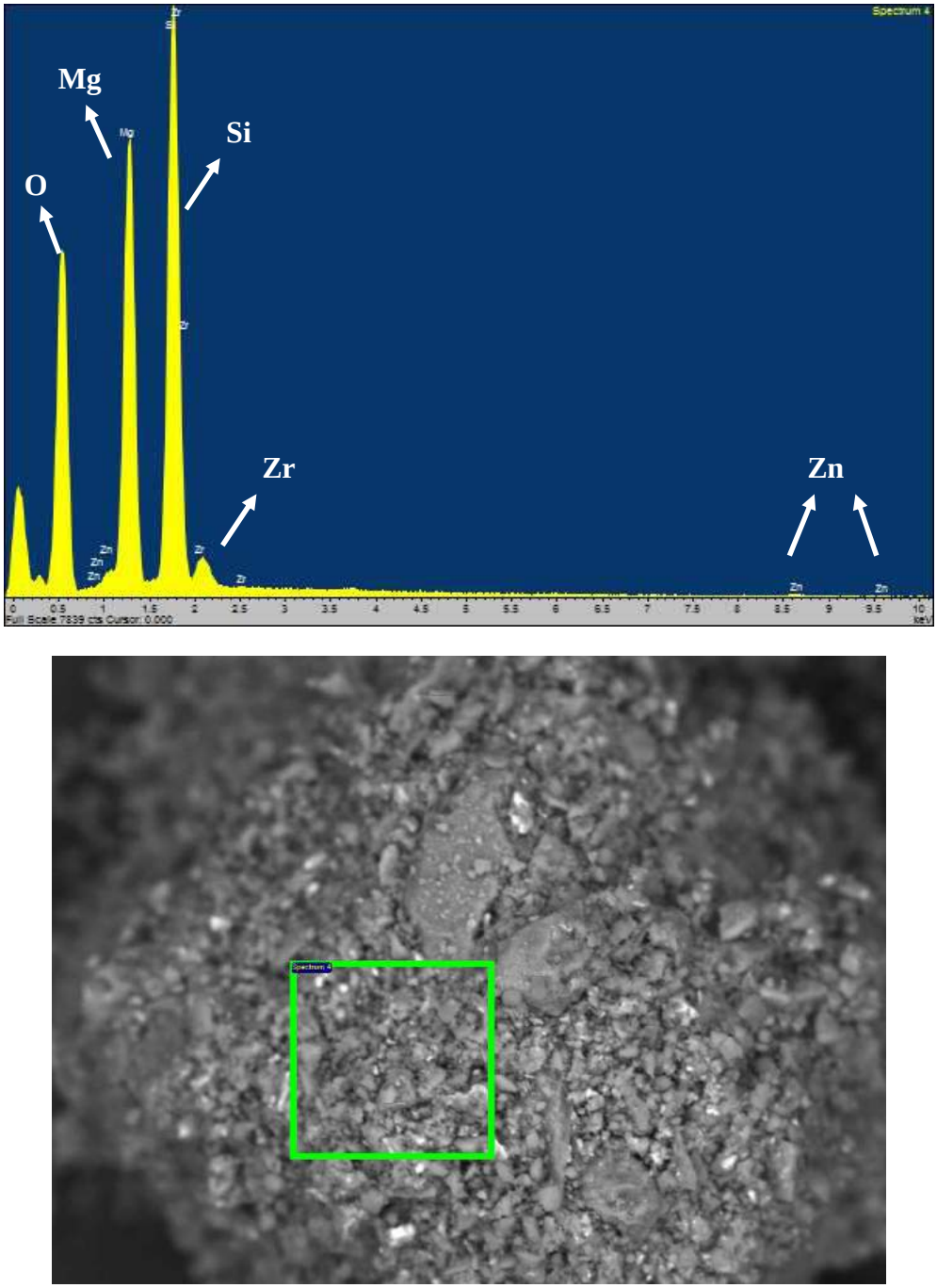

Figure G.2 - Energy-dispersive X-ray spectrum (top) and microscopy image (bottom) obtained for the ZrZn/MgO-SiO_2 sample. The spectrum was recorded between 0 and 10.1 keV. The characteristic X-ray emission energy (in keV) of Zn, at $L\beta_1$ = 1.032 and $L\alpha_1$ = 1.009, may be overlapped by those ones from Na, at $K\beta_1$ = 1.067 and $K\alpha_1$ = 1.041 (DEAN, 1992).

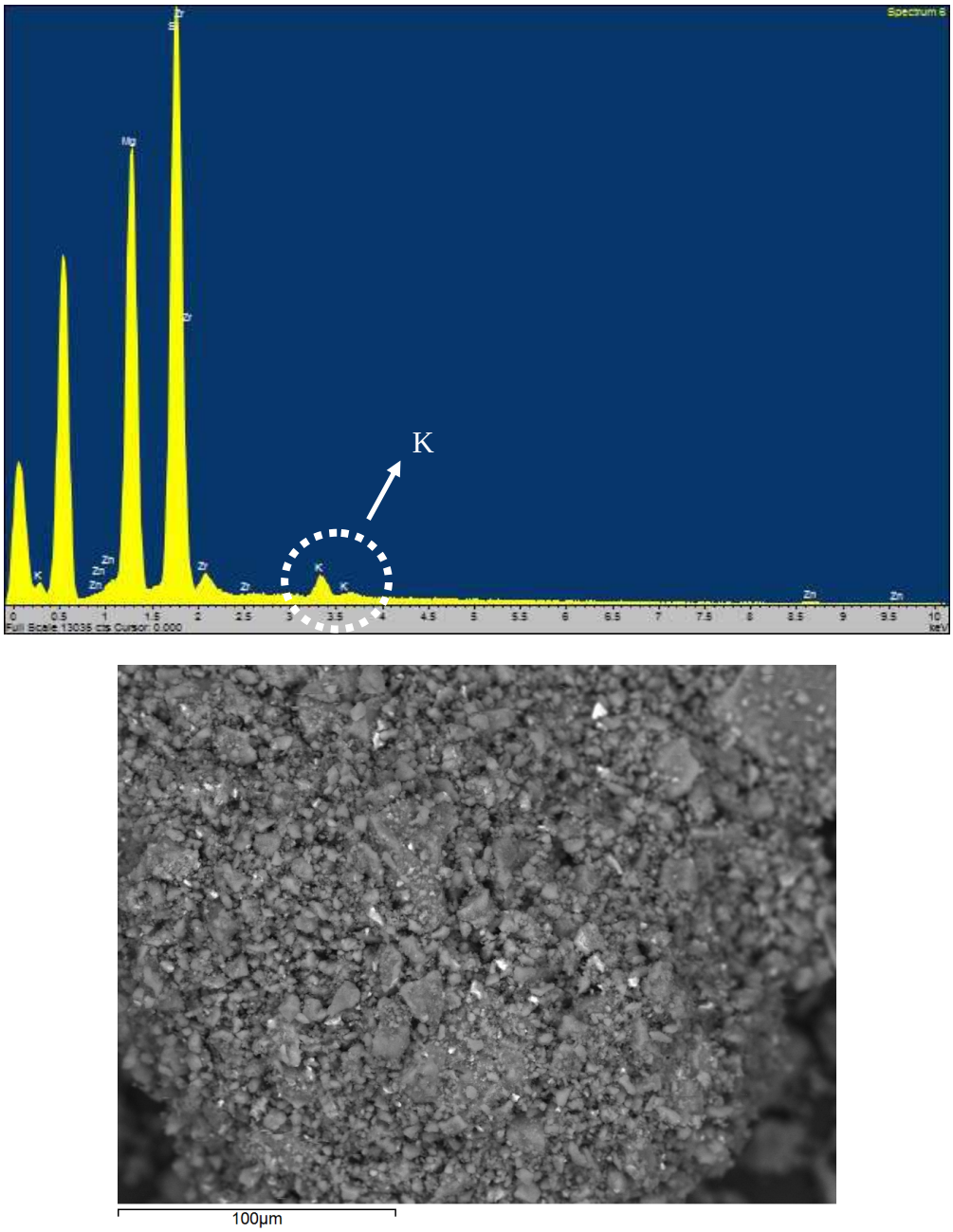

Figure G.3 - Energy-dispersive X-ray spectrum (top) and microscopy image (bottom) obtained for the 1.2-K/ZrZn/MgO-SiO_2. The characteristic X-ray emission energy (in keV) of Zn, at $L\beta_1$ = 1.032 and $L\alpha_1$ = 1.009, may be overlapped by those ones from Na, at $K\beta_1$ = 1.067 and $K\alpha_1$ = 1.041 (DEAN, 1992). X-ray emission energies are as described in the Figure G.2, with the additional emission intensity observed for potassium at $K\beta_1$ = 3.589 and $K\alpha_1$ = 3.313 (DEAN, 1992).

Appendix H – Outlet Reactor Components

This appendix presents a detailed list of components obtained over the 1.2-K/ZrZn/MgO-SiO_2-(50:50) catalyst, for 3 h of time on stream. This list was built from experimental data obtained at 400 ºC and WHSV equal to 0.92 h^{-1} , experiment from entry 10, Table 4.5.1, and it is a good representation of the outlet stream composition obtained over all reaction conditions presented in the Table 4.5.1.

Table H.1 – Typical components observed at the outlet reactor stream obtained over the 1.2-K/ZrZn/MgO-SiO_2-(50:50) catalyst[a].

Component	Retention time (min)
ethene	6.17
Ethane	7.95
Propene	12.59
Propane	12.94
Acetaldehyde	14.26
1-butene	15.21
1,3-butadiene	15.24
Trans-2-butene	15.54
Cis-2-butene	15.68
Ethanol	15.9
Acetone	16.94
Ethyl ether	17.5
2-pentene	17.67
1,2-Dimethylcyclopropane	17.76
1,4-pentadiene	17.99
1,3-pentadiene	18.07
Ethyl acetate	19.12
2,4-hexadiene	19.40
3-hexene	19.50
1,4-hexadiene	19.58
3-methyl-2-pentene	19.66
2-methyl-1,3-pentadiene	19.87
1,3,5-hexatriene	20.12

[a] No signal for acetylene was observed, indicating that this compound was not produced in significant amounts in the experiments.